DISSERTATION

Exploring Pedestal Structure and Stability: Insights from Shaping and β_{pol} Variations in ASDEX Upgrade

Ausgeführt zum Zwecke der Erlangung des akademischen
Grades einer Doktorin der technischen Wissenschaften

unter der Leitung von
Univ.-Prof. Dr. Friedrich Aumayr
und
Univ.-Prof. Dr. Elisabeth Wolfrum

eingereicht an der TU Wien
Fakultät für Physik
Institut für Angewandte Physik (E134)

von
Dipl.-Ing.in Lidija Radovanović

Wien, 10. Februar 2025

(Lidija Radovanović)

Kurzfassung

Zukünftige Fusionsreaktoren des Tokamak-Typs werden höchstwahrscheinlich im Hoch-Einschlussmodus (H-Mode) betrieben, einem Regime, das den Einschluss durch die Bildung eines steilen Druckgradienten am Plasmarand verbessert. Diese Randregion, die auch noch das Pedestal genannt wird, spielt eine entscheidende Rolle für die gesamte Plasmaperformance. Ein höherer Pedestaldruck führt zu einem erhöhten Druck im Kern des Reaktors, was wiederum die Fusionsreaktionsraten steigert und den Energiegewinn verbessert. Andererseits kann die in dieser steilen Gradientenregion gespeicherte freie Energie randlokalisierte Moden (Edge Localised Modes - ELMs) antreiben, die zu Energie- und Teilchenverlusten führen. Unter bestimmten Pedestalbedingungen können diese jedoch unterdrückt werden. Daher ist das Verständnis der physikalischen Mechanismen, die die Pedestalstruktur bestimmen, von zentraler Bedeutung für die Optimierung der Plasmaperformance.

In dieser Arbeit wurden Experimente an ASDEX Upgrade durchgeführt, um systematisch zu untersuchen, wie die Plasmageometrie und der normierte poloidale Druck β_{pol} das Pedestalverhalten beeinflussen. Diese Parameter wurden gewählt, da sie beide die kinetische Ballooning-Moden (KBMs) beeinflussen, die als etablierte Hypothese für die Bestimmung der Pedestalbreite gelten. Eine Reihe gezielter Entladungen wurde analysiert, die jeweils darauf ausgelegt waren, die Auswirkungen dieser beiden Größen zu isolieren. Drei Entladungen mit unterschiedlichem β_{pol} wurden durchgeführt, wobei jede zwei Phasen mit unterschiedlichem Plasmaquerschnitt enthielt, in denen β_{pol} konstant gehalten wurde. Dadurch ergaben sich sechs verschiedene Datensätze. Ein breites Spektrum experimenteller Diagnostikverfahren und rechnergestützter Methoden wurde eingesetzt, um kinetische Profile zu rekonstruieren, das magnetohydrodynamische (MHD) Gleichgewicht und die Stabilität zu bestimmen und die Transportprozesse innerhalb des Pedestals zu analysieren. Besonderes Augenmerk lag auf der Rolle lokaler idealer Ballooning-Moden (IBMs), die hier als Stellvertreter für KBMs betrachtet wurden, sowie auf den Bedingungen, die den Zugang zum zweiten Stabilitätsregime ermöglichen.

Die Ergebnisse zeigen, dass die Pedestalbildung nicht durch einen einzelnen Transportmechanismus gesteuert wird, sondern durch das Zusammenspiel mehrerer Instabilitäten in verschiedenen Bereichen des Pedestals, die Dichte und Temperatur von Ionen und Elektronen unterschiedlich beeinflussen. Besonders hervorzuheben ist die stabilisierende Wirkung der lokalen magnetischen Verscherung, die KBMs unterdrückt und somit die Dichtepedestalstruktur beeinflussen kann. Der obere Bereich des Pedestals wird weitgehend von KBMs reguliert. Sie beeinflussen sowohl die Dichte, indem sie die Pedestalbreite festlegen, als auch den turbulenten Ionentransport auf dem oberen Teil des Pedestals. Eine zentrale Erkenntnis ist, dass der Zugang zum zweiten Stabilitätsregime eine entscheidende Rolle für die Festlegung der Pedestalbreite spielt. Dies zeigt sich insbesondere im oberen Pedestalbereich, wo sich die ballonungskritischste Region radial verschiebt, abhängig

davon, ob der Zugang zur zweiten Stabilität gegeben ist.

Ein tiefergehendes Verständnis der mikroturbulenten Transportmechanismen wurde durch gyrokinetische lokale lineare Simulationen mit GENE gewonnen. Diese bestätigten, dass KBMs im oberen Pedestalbereich dominieren, während ITG-Turbulenz in der äußeren Plasmakern vorherrscht. Die Simulationen zeigten außerdem, dass Shaping-Effekte primär zur Stabilisierung von KBMs beitragen, mit dem stärksten Einfluss dort, wo der Druckgradient am steilsten ist – was die Bedeutung der zweiten Stabilität weiter unterstreicht. Darüber hinaus wurde gezeigt, dass Elektronentemperaturgradient-Moden (ETGs) im Pedestal vorhanden sind, die eine charakteristische Temperaturlängenskala vorgeben und damit die Elektronenwärmediffusivität bestimmen.

Die Ergebnisse verdeutlichen die Notwendigkeit, das Pedestal als ein System miteinander verbundener, aber unterschiedlicher Komponenten zu betrachten, anstatt als ein einzelnes Druckpedestal. Die Pedestals von Ionen- und Elektronentemperatur sowie der Dichte entwickeln sich nach unterschiedlichen Mechanismen und reagieren unterschiedlich auf Shaping und Variationen von β_{pol}. Dies legt nahe, dass globale Skalierungsgesetze möglicherweise nicht ausreichen, um das Pedestalverhalten in zukünftigen Anlagen vorherzusagen, ohne eine detailliertere, regionsspezifische Beschreibung zu berücksichtigen.

In dieser Arbeit wurde eine Reihe komplementärer Analysemethoden eingesetzt, um eine solide Grundlage für zukünftige Forschungsarbeiten zu schaffen. Zukünftige Untersuchungen sollten die hier beobachteten Trends anhand eines breiteren Datensatzes validieren und deren Auswirkungen auf prädiktive Modellierungen weiter erforschen. Ein tieferes Verständnis des KBM-Verhaltens unter verschiedenen Plasmabedingungen wird entscheidend für die Optimierung der Pedestalperformance in zukünftigen Fusionsanlagen sein.

Abstract

Future fusion reactors of the tokamak type will most likely operate in high-confinement mode (H-mode), a regime that enhances confinement through the formation of a steep pressure gradient at the plasma edge. This edge region, known as the pedestal, plays a crucial role in determining overall plasma performance. Higher pedestal pressure leads to increased core pressure, which in turn boosts fusion reaction rates and improves energy gain. On the other hand, the free energy stored in this steep gradient region can drive edge localised modes (ELMs), which cause energy and particle loss. These can be mitigated under specific pedestal conditions. Therefore, understanding which physical mechanisms govern the pedestal structure is crucial for optimising plasma performance.

In this thesis, experiments were conducted on ASDEX Upgrade to systematically investigate how plasma shape and the normalised poloidal pressure β_{pol} influence pedestal behaviour. The parameters are selected because they both affect kinetic ballooning modes (KBMs), which are a well-established hypothesis for determining the pedestal width.

A series of dedicated discharges were analysed, each designed to isolate the effects of the two quantities. Three discharges at varying β_{pol} were conducted, each with two shaping phases where β_{pol} is kept constant, yielding six distinct datasets. A wide range of experimental diagnostics and computational techniques were employed to reconstruct kinetic profiles, determine the magnetohydrodynamic (MHD) equilibrium and stability, and assess transport processes within the pedestal. Particular attention was given to the role of local ideal ballooning modes (IBMs), used here as a proxy for KBMs, and to the conditions enabling access to the second stability regime.

The results demonstrate that pedestal formation is not governed by a single transport mechanism but rather by the interplay of multiple instabilities across different pedestal regions, affection density and temperature of ions and electrons differently. Importantly, the study highlights the stabilising role of local magnetic shear, which can suppress KBMs and thereby impact the density pedestal structure. The top of the pedestal is largely regulated by KBMs. They are shown to influence both density, setting the width of its pedestal, and turbulent ion heat transport in the pedestal top region. A key finding is that access to the second stability regime plays a decisive role in setting the pedestal width. This is particularly evident at the pedestal top, where the most ballooning-unstable region shifts radially depending on second stability access.

Further insight into microturbulent transport mechanisms was obtained through local linear gyrokinetic simulations with GENE, which confirmed that KBMs dominate at the pedestal top, whereas ITG turbulence prevails in the outer core. The simulations also verified that shaping effects primarily stabilise KBMs, with the strongest impact occurring where the pressure gradient is steepest - further emphasising the role of second stability. Electron temperature gradient modes, which are thought to impose a well-defined temperature gradient length, determining the electron heat diffusivity, are also shown to be

present in the pedestal.

The results underscore the necessity of treating the pedestal as a system of coupled but distinct components, rather than a single pressure pedestal. Ion and electron temperature pedestals, as well as the density pedestal, evolve according to different governing mechanisms and respond differently to shaping and β_{pol} variations. This implies that global scaling laws may be insufficient for predicting pedestal behaviour in future devices without a more detailed, region-dependent description.

In this thesis, a range of complementary analytical methods are employed to provide a solid foundation for future work, which should validate the observed trends across a broader dataset and exploring their implications for predictive modelling. A deeper understanding of how KBMs behave in different plasma conditions will be crucial for optimising pedestal performance in future fusion devices.

Сажетак

Енергетски реактори типа токамака ће највероватније радити у режиму високог задржавања (Х-мода), који побољшава задржавање плазме формирањем стрмог градијента притиска на ивици плазме. Ова гранична област, позната као педестал, игра кључну улогу у одређивању целокупног перформанса плазме. Већи притисак педестала доводи до повећања притиска у језгру, што заузврат побољшава стопе фузионих реакција и повећава енергетски добитак. Са друге стране, слободна енергија акумулирана у овом региону са стрмим градијентом може покренути ивичне локализоване модове (ЕЛМови), који узрокују губитке енергије и честица. Ови губици могу бити ублажени под одређеним условима педестала. Због тога је разумевање физичких механизама који одређују структуру педестала од суштинског значаја за оптимизацију перформанса плазме.

У овом раду су спроведени експерименти на АСДЕКС Апгрејд токамаку како би се систематски испитало како облик плазме и нормализовани полоидални притисак β_{pol} утичу на понашање педестала. Ови параметри су одабрани јер оба утичу на кинетичке балунасте моде (КБМ), који представљају добро утврђену хипотезу за одређивање ширине педестала.

Анализирана је серија посебно дизајнираних пражњења, при чему је свака конфигурација осмишљена да изолује утицај ова два параметра. Изведена су три пражњења са различитим вредностима β_{pol}, при чему је свако имало две фазе различитог облика, али са константним β_{pol}, што је резултирало са шест различитих скупова података. Коришћен је широк спектар експерименталних дијагностичких техника и рачунарских метода за реконструкцију кинетичких профила, одређивање магнетохидродинамичког (МХД) равнотежног стања и стабилности, као и анализу транспортних процеса унутар педестала. Посебна пажња посвећена је улози локалних идеалних балунастих мода (ИБМ), који су овде коришћени као посредник за КБМ, и условима који омогућавају приступ другом режиму стабилности.

Резултати показују да формирање педестала није вођено једним транспортним механизмом, већ сложеном интеракцијом више нестабилности у различитим регионима педестала, што различито утиче на густину и температуру јона и електрона. Посебно је истакнута стабилизујућа улога локалног магнетног смицања, које може сузбити КБМове и тиме утицати на структуру густинског педестала. Горњи део педестала углавном регулишу КБМови. Они утичу како на густину, одређујући ширину педестала, тако и на турбулентни транспорт јонске топлоте у горњем региону педестала. Кључни закључак је да приступ другом режиму стабилности има одлучујућу улогу у дефинисању ширине педестала. Ово је посебно евидентно на врху педестала, где се најнестабилнија балунаста област помера радијално у зависности од приступа другој стабилности.

Дубљи увид у механизме микротурбулентног транспорта добијен је кроз локалне

линеарне гирокинетичке симулације коришћењем ГЕНЕ кода, које су потврдиле да КБМови доминирају у горњем делу педестала, док ИТГ турбуленција преовлађује у спољном делу центра плазме. Симулације су такође потврдиле да ефекти облика плазме углавном стабилизују КБМове, са најјачим утицајем у региону са најстрмијим градијентом притиска – што додатно наглашава улогу друге стабилности. Утврђено је и присуство нестбилности електронског температурног градијента (ЕТГ), за које се сматра да одређују карактеристичну дужину градијента температуре и тиме дефинишу електронску топлотну дифузивност.

Ови резултати истичу неопходност третирања педестала као система међусобно повезаних, али различитих компоненти, уместо као јединственог педестала притиска. Педестали јонске и електронске температуре, као и густине, развијају се у складу са различитим механизмима и различито реагују на промене облика плазме и β_{pol}. Ово указује на то да глобални закони скалирања можда нису довољни за предвиђање понашања педестала у будућим уређајима без детаљнијег, регионално зависног описа.

У овој дисертацији примењен је низ комплементарних аналитичких метода како би се поставила чврста основа за будућа истраживања. Наредни радови би требало да верификују овде уочене трендове на ширем скупу података и истраже њихове импликације на предиктивно моделирање. Дубље разумевање понашања КБМова у различитим плазменим условима биће од кључног значаја за оптимизацију перформанса плазме у будућим фузионим уређајима.

Table of Contents

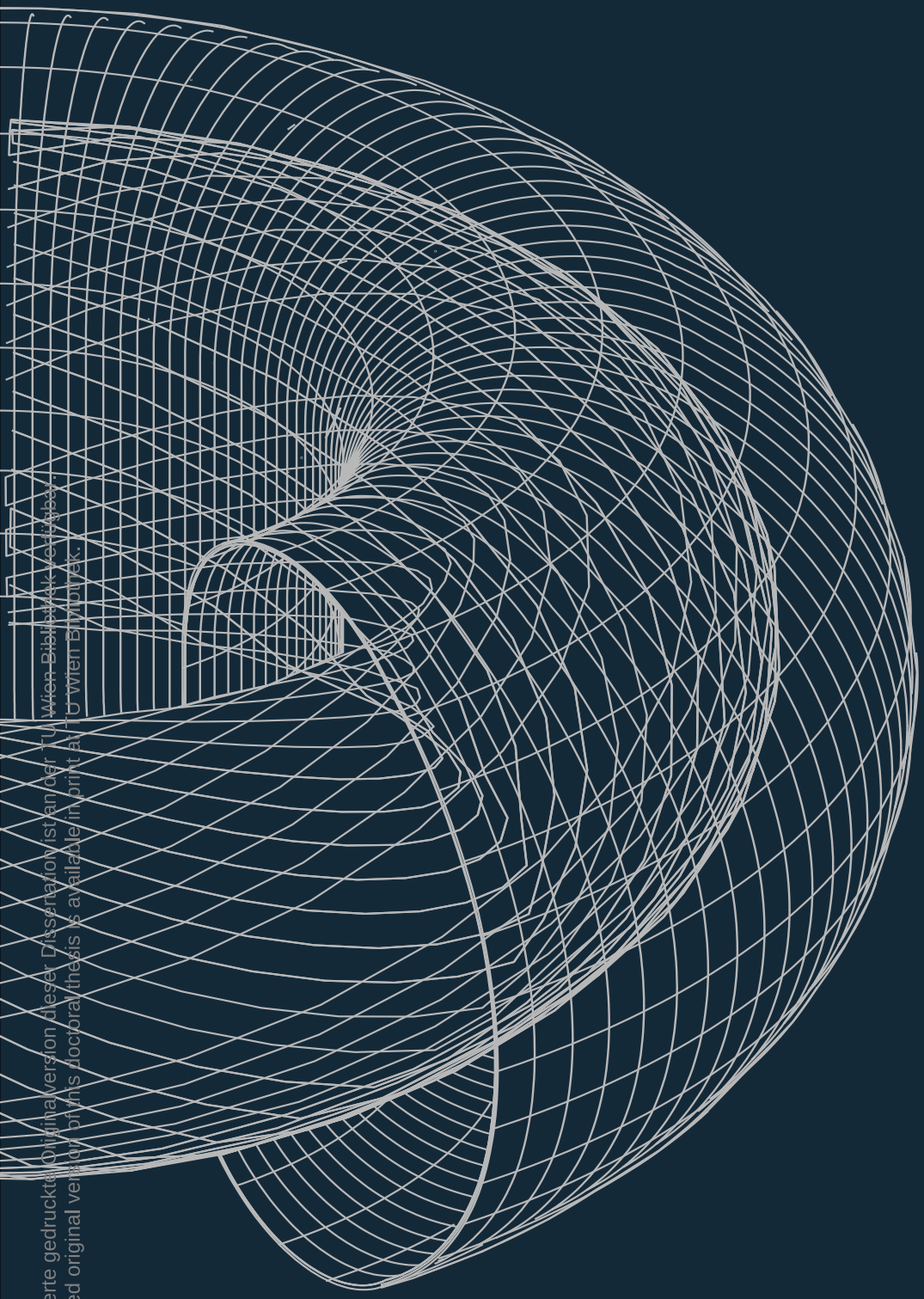

INTRODUCTION

1 Introduction

1.1 Why Fusion?

Nuclear fusion, the physical process that powers the stars, has long been praised as a potential solution to humanity's energy challenges. Despite immense advancements, fusion has yet to be realised as a viable energy source. It can be seen as a very optimistic pursuit, with concerns raised about its feasibility and practicality in the near future. The technological, economic, and infrastructural hurdles that must be overcome are substantial, and fusion is unlikely to provide a quick solution for the pressing climate crisis. To tackle these environmental issues, it is essential to invest in renewables, re-think nuclear fission, electrify industries, and, most importantly, make the reduction of emissions the top priority — without which, all other endeavours will fall short.

However, despite significant efforts, and impressive improvements, it seems unlikely that renewable energy sources will be able to fully replace fossil fuels by the end of the century. [1] With the growing energy demand, we will likely need to rely on every available energy source, possibly including fusion, if we are to secure a sustainable future. Fusion offers the potential for nearly limitless energy from abundant fuel sources, with minimal waste and no direct greenhouse gas emissions during operation. This makes it a crucial area of research, even if it does not come in time to avert the initial effects of climate change, future generations will still need an energy source that is both sustainable and scalable. In the long term, fusion has the potential to transform our global energy systems, making it a pursuit worth the continued investment and effort.

One of the most significant advantages of nuclear fusion as a commercial energy source, is that, once operational, it produces no direct greenhouse gas emissions, making it an inherently clean source of energy. There are, however, emissions associated with the construction and maintenance of fusion power plants, as well as the production of fuel. While these emissions are inevitable, they are relatively minimal compared to the emissions from conventional energy sources. Additionally, the long-term benefits of the clean energy output far outweigh the initial environmental impact, particularly as the technology matures and the global energy mix transitions to more sustainable sources.

Nuclear fusion is often considered a safer alternative to nuclear fission, because it cannot produce a chain reaction; as much as controlled fusion is powerful, it is also very fragile: if the burning fuel touches the reactor walls, the fuel instantly cools and the reaction naturally shuts down. Even though this contact can damage the reactor components, the effect is manageable and

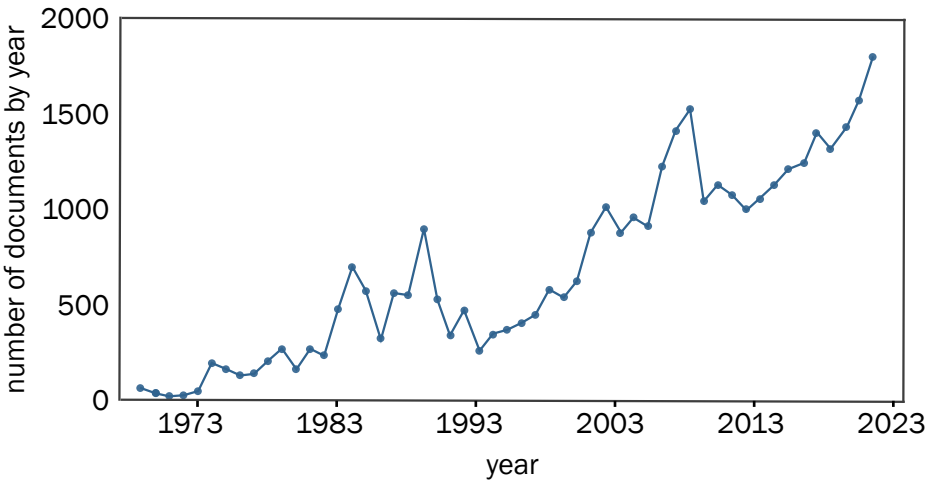

Figure 1.1: Number of the scientific works on nuclear fusion in Scopus database, 1968–2023. Source: Scopus database (2023). Figure adapted from [2]

does not pose a direct risk to human safety. Fusion also does produce some radioactive waste, it is however significantly less hazardous than fission waste. The materials that become radioactive in fusion reactors lose their radioactivity relatively quickly, typically becoming safe to handle within around 100 years [3, 4]. As a result, fusion waste poses a significantly more manageable long-term challenge. Fusion holds another large advantage over fission in terms of nuclear non-proliferation, as the safeguarding measures are considerably simpler and more straightforward [5](and unfortunately this is a topic to consider).

Fusion offers additional benefits, including its weather-independence, which makes it a highly reliable and stable energy source, capable of delivering base load energy. It also has very high energy density, and therefore requires far less space than many renewable energy sources.

Perhaps most importantly, fusion fuel is incredibly inexpensive — based on abundant resources that are relatively equally distributed — meaning that if the technology is fully developed and construction costs are reduced, fusion could become a highly cost-effective energy source. A key challenge in fusion energy is ensuring a reliable fuel supply. Deuterium is abundant in seawater, but tritium must be produced in a reaction of lithium with neutrons from the fusion reaction. While lithium is plentiful on Earth, the demand for lithium batteries is depleting the reserves on land. However, there is a large amount of lithium in seawater, but efficiently extracting it is still a developing technique. Additionally, beryllium is needed to multiply neutrons. These hurdles, though important, are technical obstacles that could be overcome with continued research, opening the door to a sustainable and almost limitless fuel supply, which would be worth the efforts.

Fusion offers immense potential, but it is clear that it is still not within reach. One of the reasons for this is that fusion research is extending the limits of established technology and science, which often leads to unforeseen challenges, unexpected costs, and delays. Nonetheless, in recent years we have seen remarkable progress in fusion research, showing a growing interest and

expanding of knowledge in this field. Figure 1.1 illustrates the growing interest in fusion research, showing a steady annual increase in academic publications on the subject since 1968, a clear sign of both rising engagement and encouraging progress in the field.

Several major developments have marked recent fusion advancements. In 2022, the National Ignition Facility (NIF), the largest ignition fusion experiment, achieved a major result in inertial confinement fusion by generating more fusion energy from the fuel pellet than was delivered to it [6]. Although the lasers are highly inefficient, this achievement represents a significant milestone for fusion science. In 2021, the Joint European Torus (JET)[7], a magnetic confinement fusion device with tokamak configuration, set a record for Deuterium-Tritium plasma, reaching 59 megajoules of fusion energy in a single pulse, where most of it was produced in a five-second time window [8, 9] — a major achievement in magnetic confinement fusion. After 40 years of operation, JET is being decommissioned, and the recently operational JT60-SA, which achieved its first plasma in 2023, is now the largest active tokamak [10, 11]. It is an advanced spherical tokamak with superconducting coils, intended to study the plasma in 100 s high power discharges, an exciting step forward in fusion research. A goal of JT60-SA is to also complement the research which will be conducted at ITER [12, 13], the future largest tokamak, currently under construction. ITER is an ambitious international mega-project, and it is a crucial step towards fusion energy, on the way to completion. Although delays have been inevitable, this project represents an unprecedented global collaboration, intended to achieve a deuterium-tritium plasma with fusion energy exceeding the heating energy by a factor of 10. ITER is also going to be used to test various approaches to generating fuel, expand experience with long pulse operation and pave the road for the first demonstration power plant DEMO [14, 15]. Another promising project is SPARC [16, 17], a privately funded compact tokamak using impressive high temperature superconducting technology. It is expected to also yield about 10 times more fusion than heating energy. SPARC is not the only privately funded fusion company, as a wave of fusion start-ups is coming up in recent years. There are currently 45 private companies with over 7 billion in private funding [18]. Some of these ventures are possibly overly optimistic in their concepts or timelines, and most will face similar challenges as more conventional tokamak devices, such as reducing plasma-wall interactions, developing fuel-breeding capabilities, and overcoming turbulence. Still, these start-ups represent a very dynamic parallel effort, fostering new ideas across the field.

As evidenced by the various advanced projects outlined, fusion research is very much alive and well. I hope this snapshot of the current moment in fusion research has convinced the reader that the work presented in this manuscript contributes to a field of immense value, playing a role in the ongoing journey towards a sustainable and transformative energy future.

1.2 Nuclear Fusion

Fusion involves merging of atomic nuclei, and in the following, the basic principles of physics behind fusion reaction are explained.

Atomic nuclei are positively charged and

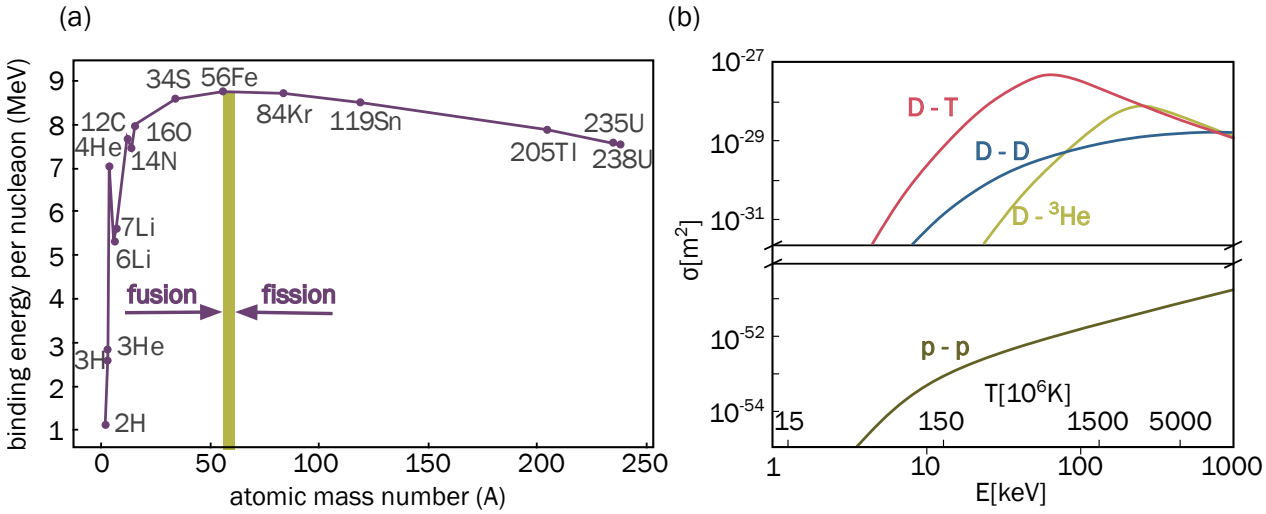

Figure 1.2: a) Binding energy per nucleon (in MeV) as a function of atomic mass number for selected nuclei. The yellow vertical line highlights the region of particularly stable nuclei. Nuclei with smaller mass numbers release energy through fusion, while those with larger mass numbers release energy through fission. b) Collision cross-sections for hydrogen isotope fusion reactions as a function of kinetic energy (in keV), with the corresponding temperature shown for reference.

repel each other, however if they come close enough, they can overcome the electrostatic repelling force and fuse into a new nucleus due to the strong nuclear force. The mass of the resulting nucleus is different from the sum of the two original nuclei, a phenomenon known as the mass defect. This mass defect is crucial, as it is the source of the energy released during the process, according to the principle of mass-energy equivalence $E = mc^2$ (where $c \approx 3\times10^8$m/s is the speed of light). The same principle applies to both fusion and fission reactions.

This process works both ways because of the varying binding energies of different nuclei, which are shown in figure 1.2a. Energy is released either by fusing lighter elements with a mass number less than approximately 60, where the binding energy per nucleon is the highest, or by splitting heavier elements with larger mass numbers. The most significant difference is in the binding energies between hydrogen and helium makes the fusion of hydrogen isotopes an ideal candidate for use in a fusion reactor.

The probability of particle interactions is commonly expressed by their collision cross-section (figure 1.2b). Among fusion reactions involving different hydrogen isotopes, the reaction between deuterium and tritium does not only exhibit the highest probability at the lowest temperature, but also releases the largest amount of energy, making it the most efficient fusion reaction

$$^2\mathrm{D} + ^3\mathrm{T} \rightarrow ^4\mathrm{He}(3.5\,\mathrm{MeV}) + \mathrm{n}(14\,\mathrm{MeV})$$

When deuterium (D) and tritium (T) nuclei fuse, their combined mass is greater than the combined mass of the resulting helium-4 (He) nucleus and the neutron, which corresponds to about 17.5 MeV of energy. According to the conservation of momentum, this energy is split between the He-4 nucleus and the neutron, with the helium carrying 3.5 MeV and the neutron 14 MeV. The kinetic energy produced by

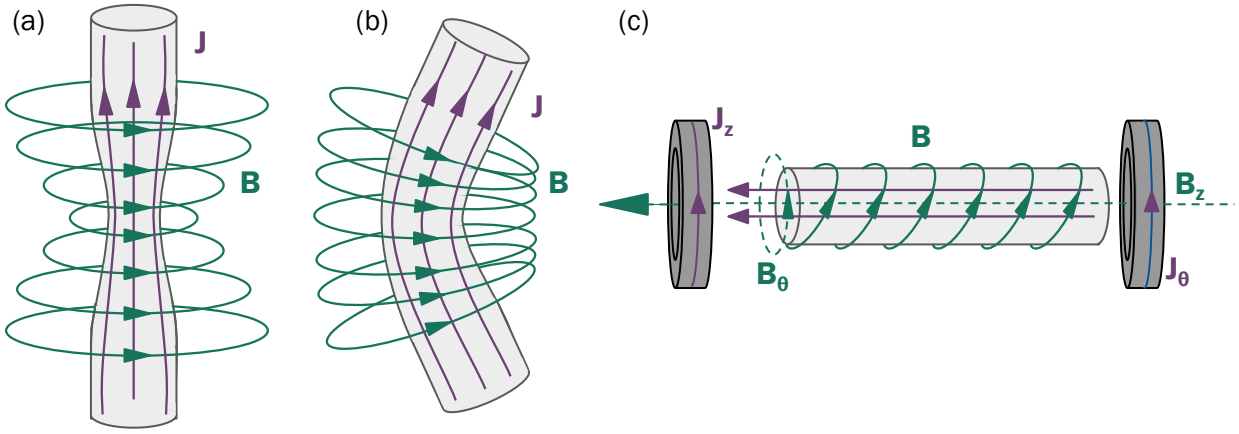

Figure 1.3: Plasma column with a plasma current $\vec{J}$ (purple arrows) and its induced magnetic field $\vec{B}$ (green arrows) in a) sausage instability, b) kink instability, and c) Z-pinch configuration.

the fusion reaction can be converted into heat, which can then be transformed into mechanical energy and eventually electricity through thermodynamic processes.

To achieve fusion, the fuel particles, in this case deuterium and tritium, must have sufficient kinetic energy to overcome the Coulomb barrier due to their positive charges. This high energy is typically reached by heating the particles to extremely high temperatures, as described by the kinetic theory of gases. Though the temperature required for the D–T fusion reaction is lower than for other fusion reactions, it still requires temperatures on the order of 100 million degrees Kelvin (or Celsius, for it does not make a whole lot of difference at these temperatures).

At these extreme temperatures, matter exists in a highly ionised state known as plasma, where the gas is composed of ions and electrons. Due to the intensity of the heat, no material can directly withstand contact with this plasma. However, a key advantage of plasma is that it by definition consists of charged particles, which allows it to be manipulated and controlled using magnetic fields.

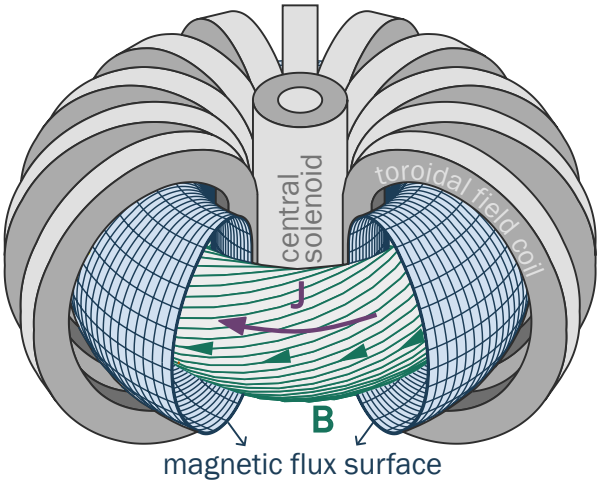

Figure 1.4: Drawing of a tokamak: Central solenoid that generates the toroidal plasma current $\vec{J}$, marked with the purple arrow. The poloidal magnetic field, that is induced from $\vec{J}$, together with the toroidal magnetic field produced by the toroidal field coils, create the magnetic field $\vec{B}$, marked with green arrows. The blue surface, illustrated as a net, shows one of the surfaces with a constant magnetic flux.

1.3 Magnetic Confinement

When a charged particle with charge q and velocity $\vec{v}$ enters an electric field $\vec{E}$ and a

magnetic field $\vec{B}$, it experiences the Lorentz force

$$\vec{F} = q(\vec{v} \times \vec{B} + \vec{E}) \quad (1.1)$$

Therefore, we can use electric and magnetic fields to control particles and confine the plasma. By running a current through the plasma, we induce a magnetic field that helps contain it. However, several instabilities can arise: for instance, if the radius of the plasma column locally decreases, the current density and the magnetic pressure increase, leading to a "sausage instability" (figure 1.3a). Similarly, a slight bend in the column can cause a "kink instability" (figure 1.3b). By adding an axial magnetic field, we can create a so-called screw pinch, where helical magnetic field lines stabilise the plasma (figure 1.3c). Yet, in linear configurations, there are significant losses at the plasma edge. A solution to this is to close the system in a toroidal (doughnut-shaped) form, giving us the tokamak configuration shown in figure 1.4. In a tokamak, the plasma current is induced by the central solenoid with increasing current, that acts as the primary coil of a transformer, whereas the plasma serves as the secondary coil. The plasma current then induces the poloidal magnetic field needed to confine and stabilise the plasma within the tokamak. The superposition of the toroidal and the poloidal magnetic fields, results in helical field lines. The safety factor q=m/n characterises the helical configuration of a tokamak by describing the ratio of toroidal to poloidal rotations a magnetic field line completes before closing on itself, where m represents the number of poloidal turns and n the toroidal turns. The aspect ratio □=R/a defines the relationship between the major radius R of the torus and the minor radius a of the plasma column.

The tokamak design remains the most thoroughly researched approach in magnetic confinement fusion.

Overview of ASDEX Upgrade

Figure 1.5: Inside the machine vessel of ASDEX Upgrade. Source: [19]

This project was conducted on one of the leading tokamak experiments, Axially Symmetric Divertor Experiment Upgrade (ASDEX Upgrade). The Axially Symmetric Divertor Experiment Upgrade (ASDEX Upgrade, or AUG) is a tokamak located at the Max Planck Institute for Plasma Physics in Garching, Germany, where it has operated since 1991. A photograph of the inside of AUG vessel is shown in figure 1.5. Experiments on ASDEX Upgrade are primarily focused on advancing the understanding of various plasma phenomena and refining fusion reactor engineering for future applications, primely ITER.

In the AUG experiment, a typical plasma has a major radius $R_0 \approx 1.65\,\mathrm{m}$ and a minor radius $a \approx 0.5\mathrm{m}$ and the plasma is confined with a toroidal magnetic field reaching up to 3 T and a plasma current of 1.6 MA. As of 2025, AUG operates with two divertor systems, which redirect the outer edge of confined plasma towards collection plates. To simplify the operation and reduce activation of plasma-facing components from neutron fluxes, the experiment does not use tritium, but rather deuterium, hydrogen,

and helium. The particle density is approximately $10^{20}m^{-3}$ and total mass of the fuel is only around 3 mg. Meanwhile, the entire system—including the vessel, coils, diagnostic and heating equipment, and supporting structures weighs about 800 tonnes. Through various heating methods, that sum up to about 35MW, the plasma achieves temperatures of 100 million degrees. In section 3, the specifics of heating techniques and the plasma diagnostics used in this project will be outlined.

1.4 Plasma Structure and Confinement Regimes

Divertor Configuration

In figure 1.7, a cross-section of the tokamak plasma is shown. The dashed gray lines visible in the diagram on the left represent the surfaces of constant magnetic flux. Along these lines, kinetic quantities such as plasma density, temperature, and pressure are equalised rapidly due to fast transport processes. As a result, when examining plasma properties, we often use a normalised radial coordinate as the x-axis, which is 0 at the plasma centre and 1 at the last closed flux surface, and show different flux surface averaged quantities on the y-axis as it is shown on the right diagram of figure 1.7 where for example a sketch of plasma pressure profiles is shown.

The last closed flux surface, marked with the thick red line in figure 1.7, is also called the separatrix, as it separates the confined plasma from the outer plasma region. In ASDEX Upgrade and many other devices, a plasma configuration known as the divertor is employed. In this configuration, the separatrix forms an X-point in the poloidal magnetic field, beyond which the field lines become open and connect to the divertor plates (shown in gray in 1.7).

The region just outside the separatrix, where particles are directed toward the divertor target, is called the scrape-off layer Scrape Off Layer (SOL) and it is marked as the green region in the left diagram of figure 1.7. The SOL is relatively narrow because the particle and transport parallel to the magnetic field lines is very rapid. The heat flux and particle load on the divertor pose a significant challenge for future fusion reactors, as they have the potential to damage the plasma facing materials. However, it is possible to create a high neutral particle pressure above the divertor. When ions collide with this cloud of neutrals, due to the charge exchange, recombination and eventual radiation, energy can be dissipated enough to not damage the divertor.

H-Mode and Pedestal

When the heating power applied to the plasma exceeds a certain threshold, the plasma promptly transitions from the Low confinement mode (L-mode) to the High confinement mode (H-mode) [20] depicted in figure 1.7. Increased confinement is primarily due to the formation of a transport barrier within a few centimetres of the plasma edge just inside the separatrix. The transport barrier is formed as a radial electric field E_r is formed, which leads to a sheared $E \times B$ drift. This sheared plasma flow deforms the turbulent eddies, draining the energy out of the turbulent vortices, and reduces their heat and particle transport perpendicular to the flux surfaces [21–24] as it is sketched in figure 1.6. Reduced turbulent transport leads to the steepening of the pressure profile in this region, which is referred to as pedestal - it elevates the stiff core profiles, as if they were lifted on

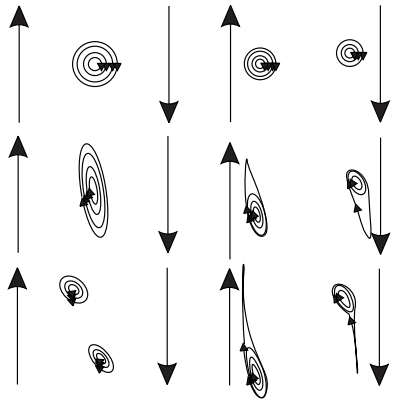

Figure 1.6: Sketch of zonal flow generation and the resulting turbulence decorrelation. Panels on the left illustrate the conventional mechanism, where eddies are disrupted and torn apart. Panels on the right show the vortex thinning mechanism, where eddies are absorbed and dominated by the zonal flow. Figure adapted from [25]

a pedestal. Changes in the pedestal are of critical importance, as they directly influence the entire plasma behaviour. Since the effects of the pedestal extend to the plasma core, optimising the pedestal structure is essential for achieving optimal confinement. Different mechanisms that influence the pedestal structure are in the focus of this thesis.

ELMs

Steep gradient regions at the plasma edge are essential for improved confinement, but they come with significant trade-offs. The strong pressure gradient regions can drive a certain type of quasi-periodic Magnetohydrodynamics (MHD) instabilities, known as Edge Localized Modes (ELMs) [26]. These events lead to the collapse of the pedestal (dashed light blue line in figure 1.7), resulting in the rapid release of energy and particles into the SOL, which then quickly reaches the divertor plates. The deposited energy is manageable in the current machines, however in future fusion devices ELMs could quickly lead to severe damage to the plasma facing components [27, 28]. More detailed mechanism of an ELM crash will be further explored in section 2.1.3.

1.5 Thesis Motivation and Outline

As the H-mode offers significantly better confinement, it is expected to be critical for future fusion reactors, however it comes with challenges. ELMs, particularly in future machines like ITER, pose a major risk for the plasma facing components.

Because of this, significant focus has been put on developing different operational regimes where ELMs are suppressed or mitigated, but the high confinement and performance of the H-mode is sustained [29]. The developed experimental techniques and their theoretical background are diverse, but in almost all of them the pedestal physics plays a decisive role.

Therefore, understanding, predicting, and controlling the pedestal structure and its stability are highly important for optimising plasma performance.

Simplified, we can describe the pedestal with a combination of its gradient and its width. Multiple approaches are used to model and predict this structure, with the EPED [30] model being the most regularly used one, and more recently, integrated modelling with engineering parameters (IMEP) on ASDEX Upgrade [31, 32]. These two approaches have in common that they both determine the pedestal width and height using the intersection between two limitations: first, the MHD stability and second, some transport constraint.

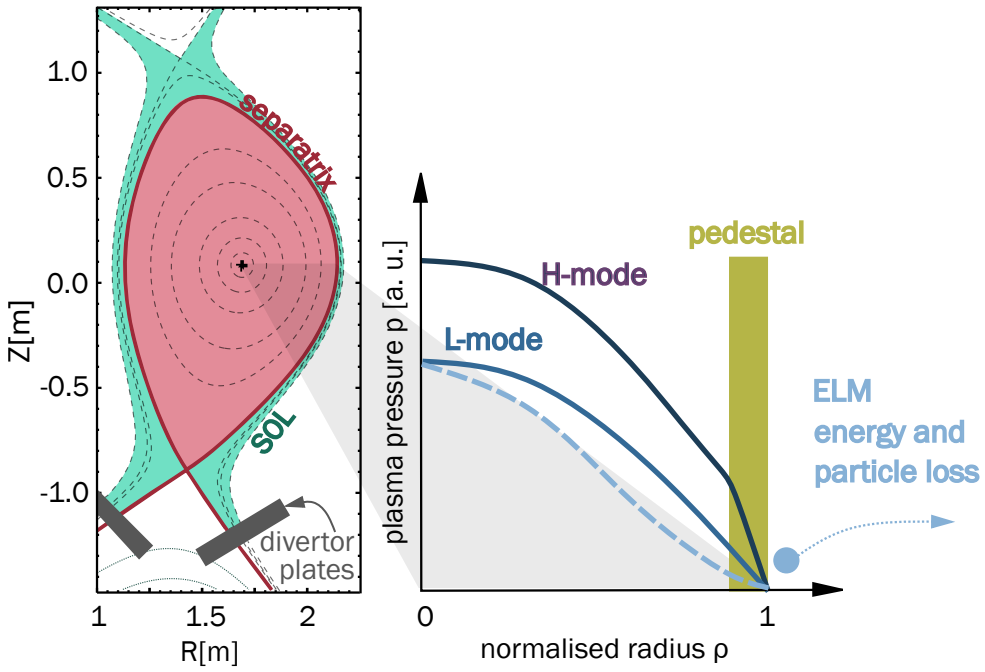

Figure 1.7: A cross-section of a tokamak, on the left, with marked last closed flux surface (separatrix), Scrape Off Layer (SOL) and the divertor plates. On the right the normalised radius ρ_{pol} is projected and three typical plasma pressure profiles p are sketched in blue. The characteristic steep gradient region, the pedestal, is marked as the yellow vertical stripe.

In both models, the MHD constraint is based on the ideal peeling-ballooning stability limit, which when exceeded triggers an ELM [33, 34]. This limit can be used to determine the maximum pedestal height and width just prior to an ELM onset. However, this approach does not capture stability limits within the pedestal between ELMs, and it poses challenges in predicting pedestal structures in ELM-free regimes.

The IMEP modelling approach determines the transport constraint by transport simulations to calculate the pedestal top pressure for a given pedestal width, as detailed in [31]. These simulations are informed by empirical observations from [35], which demonstrate that the electron temperature gradient length $T_e/\nabla T_e$ in real space coordinates, scaled to the machine size, remain constant across multiple tokamaks (AUG, JET, and DIII-D). This scaling is robust across diverse plasma shapes, heating powers, and electron densities, suggesting that a type of turbulent instability, the electron temperature gradient modes (ETGs), may set this limit, though this has not been conclusively proven.

On the other hand, the EPED model derives its transport limitation from the observed relation between the pedestal width (Δ_{ped}) and the β_{pol}, the poloidal component of the normalised plasma pressure $\beta_N = \langle p \rangle / p_{mag}$, where $\beta + N$ represents the ration of global plasma pressure $\langle p \rangle = \langle n k_B T \rangle$ and the magnetic pressure $p_{mag} = B^2/2\mu_0$. The hypothesis is that a specific instability, the kinetic ballooning mode (KBM), enforces a limit on the critical normalised pressure gradient. In this framework, β_{pol} contributes both to the pressure gradient drive of the mode, and its current stabilisation, because an increase in pressure gradient also leads

to generation of the so-called bootstrap current. This leads to a dependence of $\Delta_{ped} = D * \sqrt{\beta_{pol}}$. While this model is mostly effective, its predictive power is limited by the dependence of D on various parameters, such as operational regime, plasma shaping, and collisionality, making it difficult to forecast the pedestal width without experimental data to determine D. This issue is addressed by calculating the exact Kinetic Ballooning Mode (KBM) stability. The pedestal is considered to be ballooning-critical if more than 50% of it becomes unstable [36]. However, the distribution of KBM modes across the pedestal can significantly vary, as will be shown in this thesis, and the ballooning-critical method may not always provide an accurate assessment. Another drawback is that the model assumes identical temperature profiles for electrons and ions, which is frequently not observed in experiments, as will be further discussed in this work.

In addition, the EPED model has been used to establish a connection between KBMs, MHD, and pedestal width, particularly in the inter-ELM evolution of the pedestal observed on MAST [37]. More recent studies on ASDEX Upgrade, examining pedestals in an ELM-free Quasi Contiuous Exhaust Regime (QCE) regime, have shown that ideal $n \rightarrow \infty$ ballooning modes — commonly used as proxies for KBMs—are near the stability boundary in the pedestal [38, 39], further underlining their significance.

In this thesis, the aim is to investigate these aspects further, and the study is structured as follows.

Chapter 2 provides the theoretical background, covering the full scope of the analyses performed in the following chapters. It includes an overview of plasma physics, the MHD model, equilibrium and stability, as well as plasma transport and gyrokinetics. Additionally, the numerical codes used in this study are introduced.

Chapter 3 details the experimental setup at ASDEX Upgrade, describing the device and the used diagnostics, the design of the experiments, their execution, and the workflow followed throughout the study. The experiments are motivated by the investigation of ballooning modes and the normalised poloidal pressure, β_{pol}. For this reason, β_{pol} was chosen as one of the control parameters, while the other key parameter is plasma shape. Shape modifications influence the local magnetic shear, which in turn affects ballooning modes, making them a central aspect of the study.

Chapter 4 presents the experimental results, focusing on direct measurements from ASDEX Upgrade. This includes the pedestal structure for various quantities, radial electric field measurements, and equilibrium properties.

In Chapter 5, the focus shifts to analysing kinetic ballooning modes (KBMs), using local ideal ballooning modes as a proxy. A detailed investigation is conducted to determine their radial location, their relation to the pedestal top, and how changes in plasma shape modify local magnetic shear, thereby influencing ballooning modes and ultimately affecting the pedestal structure.

Chapter 6 extends this analysis to ELM-synchronised data, examining how different pedestal quantities, such as density and ion/electron temperatures, evolve during an ELM cycle. A key aspect is understanding the role of ideal local MHD stability and its access to second stability throughout the cycle.

Finally, Chapter 7 connects transport and gyrokinetic analyses to the MHD results. Instead of focusing solely on MHD stability, this chapter explores how heat and particle transport behave in the plasma. Gy-

rokinetic simulations provide insights into microturbulence in the pedestal, identifying dominant modes and their potential impact on transport. Additionally, while local ideal ballooning modes are used as a KBM proxy, microturbulence analysis helps assess the validity of this assumption.

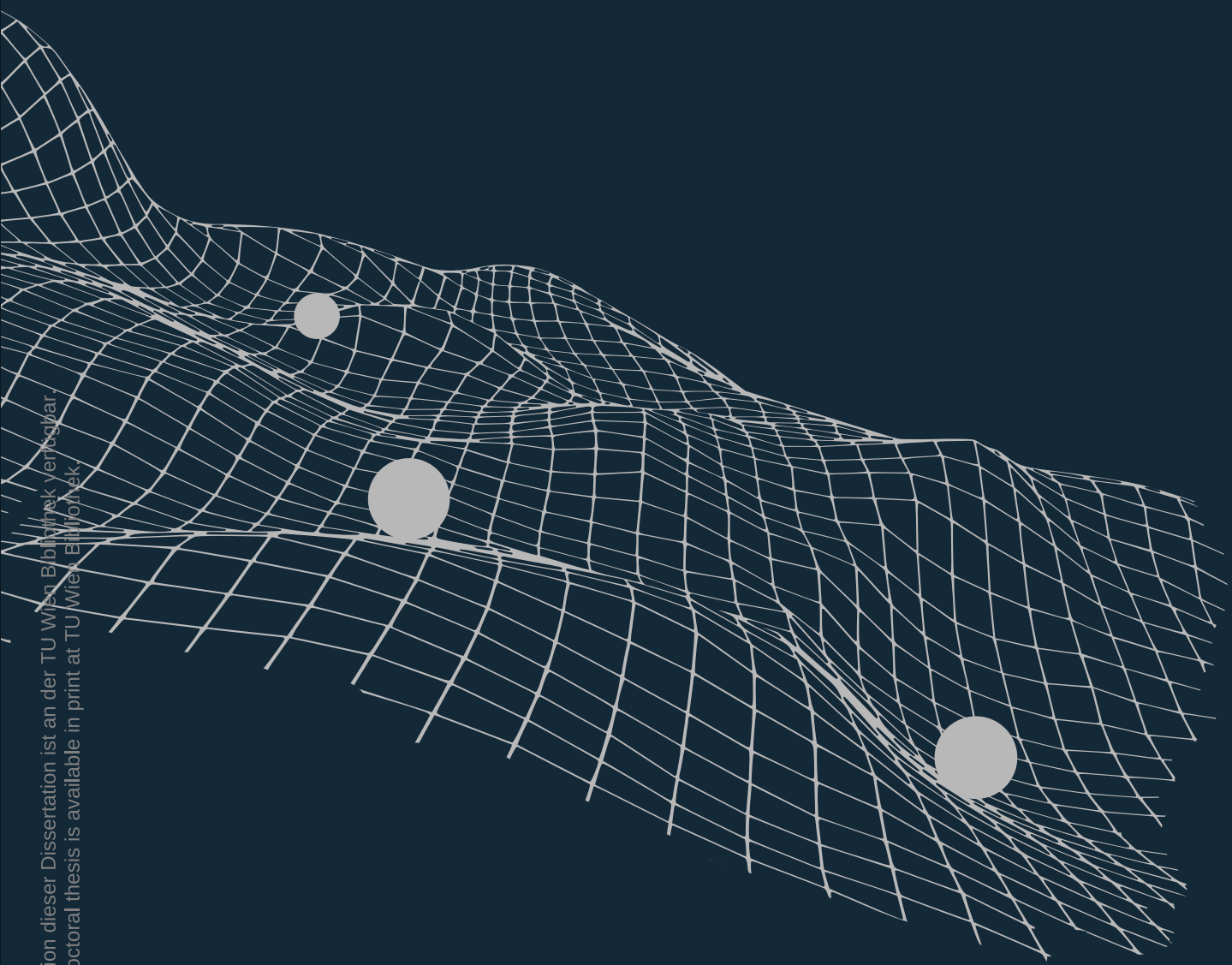

THEORETICAL AND NUMERICAL BACKGROUND

2 Theoretical and Numerical Background

If not stated differently, all the equations, sketches of derivations, and other concepts in this chapter are interpreted using a combination of several text books [40–46].

Single Particle Motion

As shortly outlined in Section 1.3, the fundamental principle of magnetic confinement originates from the equation of motion for a charged particle in an electromagnetic field. A charged particle, subjected to both electric fields $\vec{E}$ and magnetic fields $\vec{B}$, experiences the Lorentz force $\vec{F}_L$, which describes the motion of an individual charged particle as:

$$\vec{F}_L = m\frac{d\vec{v}}{dt} = q(\vec{E} + \vec{v} \times \vec{B}), \tag{2.1}$$

where m is the particle mass, $\vec{v}$ is the velocity of the particle and q is the particle charge. The spatial and temporal properties of the electric and the magnetic field determine the trajectory of the particle. Because the magnetic fields in a tokamak are strong and dominate in the particle transport, the particle dynamics can be effectively decomposed into two main components - parallel to the magnetic field lines and perpendicular to the magnetic field lines. Simplified, in absence of the electric field

$$m\frac{d\vec{v}_\perp}{dt} = q\left(\vec{v}_\perp \times \vec{B}\right) \tag{2.2}$$

$$m\frac{d\vec{v}_\parallel}{dt} = 0. \tag{2.3}$$

These equations show that the perpendicular velocity causes the particle to gyrate around the magnetic field lines in uniform circular motion, whereas the parallel velocity remains constant, meaning the particle follows the field lines without acceleration. This is the foundation of magnetic confinement, where charged particles are constrained to follow helical paths along the magnetic field lines. In this way, it is possible to split the single particle movement into the movement of the guiding centre (shown in yellow in figure 2.1) and the gyrating motion around this centre (shown as a spiral in figure 2.1). The gyrating motion is then described with its characteristic gyrofrequency $\omega_c = qB/m$ and Larmor radius $\rho_L = v_\perp/\omega_c = mv_\perp/qB$. Due to their difference in charge, the equations indicate that electrons and ions gyrate in opposite directions, and because of the different masses, the electrons gyrate faster and with a smaller radius than the ions. The Larmor gyration is also characterised by its magnetic moment, $\mu = mv_\perp^2/2B$ which stays constant if the magnetic field is static or if its rate of change is sufficiently slow in

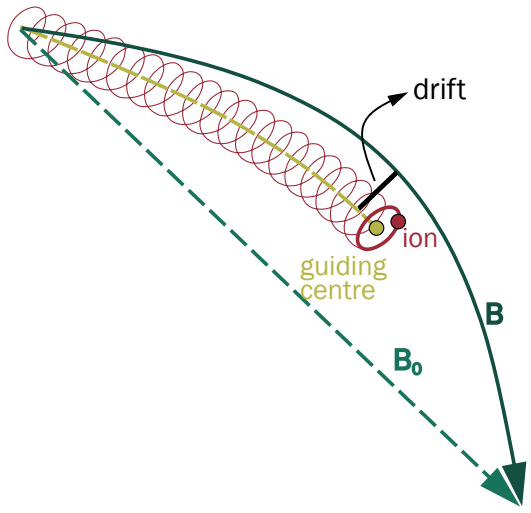

Figure 2.1: Sketch of the particle trajectories. The dashed green line shows the equilibrium magnetic field, $\vec{B}_0$ and the darker, full green line represents the perturbed magnetic field $\vec{B}$. Particle motion is split into the motion of its guiding centre, shown in yellow, and its gyration around it, shown in red. The yellow dashed line, showing the guiding centre motion, does not follow the magnetic field line exactly, which is indicated as a drift. Figure reproduced from [47]

comparison to the gyro-motion.

Approximating the particle motion with the motion of the guiding centre can be used in cases of sufficiently small spatial and temporal variations of $\vec{B}$, that is if $B/\nabla B >> \rho_L$ and $\dot{B}/B << \omega_c$, which generally holds true in fusion plasmas. The system is however still more complex since the magnetic field is not uniform, electric fields play an important role, gradients in pressure develop and there are other forces that could influence the plasma. These forces change the path that the particle is following and result in drifts.

Drifts

If a particle experiences an additional external force $\vec{F}_{ext}$ that has a component perpendicular to $\vec{B}$, it leads to the drift motion v_d of the guiding centre described as:

$$\vec{v}_d = \frac{1}{q}\frac{\vec{F}_{ext} \times \vec{B}}{B^2}. \qquad (2.4)$$

This causes the particle to move in a trajectory that is not perfectly aligned with the magnetic field, the deviations of this trajectory is marked with a black line in figure 2.1. Depending on the properties of the force acting on the particle, various types of drifts can arise, the most important of which are outlined in the following subsections, and their directions for a typical ASDEX Upgrade configurations are sketched in figure 2.2.

E×B Drift

In presence of a time-independent electric field $\vec{E}$, an electric force $\vec{F}_E = q\vec{E}$ acts on the particle and generates the drift velocity v_d

$$\vec{v}_d = \vec{v}_{E\times B} = \frac{\vec{E} \times \vec{B}}{B^2}. \qquad (2.5)$$

This drift is very important for stabilisation of microscopic turbulences and consequently large scale plasma behaviour. More on this interplay will be outlined in section 2.1.3. Because the force is charge - dependent, it cancels out with q in (2.4), and the resulting drift is charge - independent, moving both ions and electrons in the same direction.

∇B drift

In a tokamak, the magnetic field gradient is oriented in the direction of the major radius ($B \propto 1/R$). This gradient gives rise to a force acting on the particle, expressed as:

$$F = -\mu\nabla B \qquad (2.6)$$

By substituting this force into the general drift formula (2.4), we obtain the drift velocity v_d:

$$\vec{v}_d = \vec{v}_{\nabla B} = \frac{mv^2(\nabla B \times \vec{B})}{2qB^3}, \qquad (2.7)$$

The ∇B drift depends directly on the charge of the particle and its kinetic energy, which means that it leads to charge separation, resulting in the further E × B drift.

Curvature Drift

The curvature drift arises when a charged particle moves along curved magnetic field lines, and experiences a centrifugal force. If the curvature radius of the magnetic field line R_c is assumed to be constant, then the centrifugal force associated with it is defined as

$$\vec{F}_{curv.} = m\bar{v}_{\parallel}^2 \frac{\vec{R}_c}{R_c^2}, \qquad (2.8)$$

and the drift caused by it is expressed as

$$\vec{v}_d = \vec{v}_c = \frac{mv_{\parallel}^2}{qB^3} \nabla B \times \vec{B} \qquad (2.9)$$

Curvature drift also leads to charge separation and therefore also an electric field, further causing the E × B drift, which is the motivation why a poloidal magnetic field is introduced in the magnetic confinement concepts.

Diamagnetic Drift

Diamagnetic drift is an exception from the previously mentioned drifts, because it is not a guiding centre drift, and it does not occur for single particles, but rather, it is a collective phenomenon. It is generated in the presence of pressure gradient ∇p perpendicular to the magnetic field and results in

$$\vec{v}_d = \vec{v}_{dia} = -\frac{\nabla p \times \vec{B}}{qnB^2}, \qquad (2.10)$$

where n is the particle density. Because of the charge separation, the diamagnetic drift generates a current, called the diamagnetic current j_{dia}.

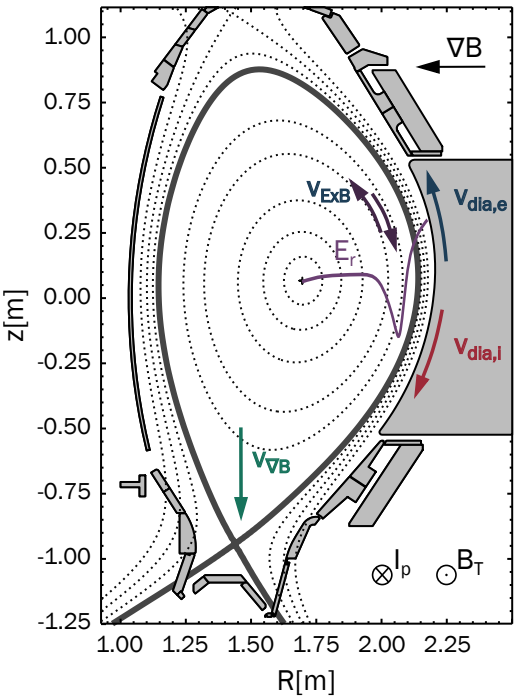

Figure 2.2: Drifts and their direction in a typical ASDEX Upgrade configuration. Diamagnetic drift for electrons and ions is shown in blue and red, respectively. The radial electric field E_r and the corresponding E × B drifts are shown in purple. The ∇B drift is marked in green.

Complexity of Multiscale Dynamics

For a single particle, we can comfortably rely on the good old Newtonian equations of motion. When electromagnetic coupling is introduced, Maxwell's equations are the key tool, allowing us to describe the interactions between particles. In principle, this covers everything we need. However, not only do we lack knowledge of the initial conditions for each particle, but attempting to

solve a system of 10^{20} coupled equations, needed to describe individual particles, is computationally unfeasible. To address this challenge, alternative approaches are employed, relying on distributions and statistical methods to describe the system in manageable terms. These approaches are summarized in figure 2.3.

Instead of tracking each individual particle, we can consider a distribution f_a of particle species a, and study its time evolution as $\frac{d}{dt}f_a(t,\vec{x},\vec{v}) = f_{coll}$, with f_{coll} being the collisions term. In a limit of very fast processes in plasmas, which occur on timescales much shorter than the time between two collisions, we can neglect the collisions entirely, leading to the construction of a collisionless distribution function $\frac{d}{dt}f_a(t,\vec{x},\vec{v}) = 0$ where $\vec{x}$ is the position and $\vec{v}$ the velocity. Assuming that the gravitational force is much weaker than the Lorentz force, which is generally true in fusion plasmas (not so much in astrophysical plasmas), allows us to expand this equation of motion, the so-called Vlasov equation, to:

$$\frac{df_a}{dt} = \frac{\partial f_a}{\partial t} + \vec{v}\cdot\nabla f_a + \frac{q}{m}\left(\vec{E} + \vec{v}\times\vec{B}\right)\cdot\frac{\partial f_a}{\partial \vec{v}} = 0. \tag{2.11}$$

The fields $\vec{E}$ and $\vec{B}$ are determined using Maxwell's equations. With this framework, we no longer need to manage the overwhelming 10^{20} equations individually, however, the Vlasov equation is not universally applicable.

This description works particularly well for phenomena on small, fast timescales, where collisions are excluded. To extend its applicability to larger scales or slower processes, we can bring back the collision term, replacing the zero on the right-hand side. Still, by doing so, the model captures a greatly extensive range of plasma behaviours, as shown in yellow in figure 2.3. This is unnecessarily impractical for describing larger phenomena, where further simplifications in the model can be made, especially because the computational cost of solving these fully kinetic equations for larger spatial and temporal time scales is unrealistic. Instead, we can further specialise to develop more specific modelling tools.

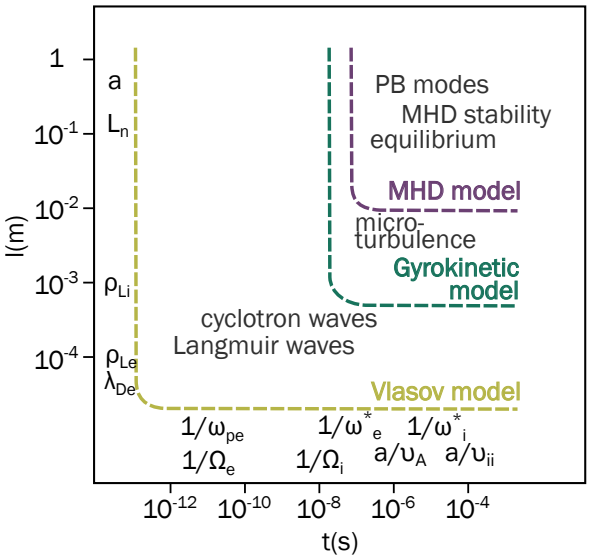

Figure 2.3: Fusion plasmas exhibit a vast range of spatio-temporal scales - represented on the y and x axes respectively - necessitating the use of different models such as Vlasov (yellow), gyrokinetic (green), and MHD (purple), depending on the phenomena of interest. Key parameters included on the x and y scales for reference are the plasma oscillation frequency (ω_p), cyclotron frequency (Ω_s), and diamagnetic rotation frequency (ω^*_s), along with characteristic scales like the Alfvén velocity (v_A), ion–ion collision frequency (v_{ii}), Debye length (λ_D), Larmor radius (ρ_L, equilibrium density scale length (L_n), and plasma size (a), where s represents the particle species. The range of velocity for each model is above and right of the dashed line. Figure adapted from [48].

The next step in simplifying the Vlasov-Maxwell equation system, while retaining its applicability, is gyrokinetics (marked in

green in figure 2.3). This approach splits the particle motion into the gyro motion and the motion of the guiding centre, as illustrated in figure 2.1. By doing so, the 6D differential equation is reduced to 5D in strongly magnetised plasmas, as the gyration around magnetic field lines is averaged out. Instead of tracking the full particle trajectory, we follow the guiding centre motion along magnetic field lines and its drifts. This method is particularly well-suited for studying microturbulence, as it operates on appropriate scales and neglects high-frequency phenomena or very small structures. Additionally, various collision operators can be incorporated into the model to enhance its accuracy and applicability.

Another approach is to scale up to even slower and larger phenomena, which enables neglecting the behaviour of individual particles and treating the plasma as a continuum. This involves assuming that the characteristic structures are sufficiently large and collisions occur far more frequently than the dynamic processes under consideration. The crucial assumption is that the distribution function f_a is a Maxwellian distribution. This shift allows us to move beyond the Vlasov equation and adopt magnetohydrodynamics (MHD), which combines standard hydrodynamics with electrodynamics (range shown in purple in figure 2.1). This framework is particularly suited for analysing large-scale plasma properties, such as the magnetic equilibrium, stability, and macroscopic MHD modes. Various flavours of this model exist, ranging from resistive to ideal MHD, single or multi-fluid formulations where different species are treated separately.

Regardless of the approach - gyrokinetics or MHD - further simplifications can be made by either linearising the system, and/or focusing on local phenomena instead of the global plasm. While such approximations save computational resources, they come at the expense of limiting the range of applicability. A major challenge in plasma physics arises from the fact that processes at vastly different scales occur simultaneously and are interdependent, as it is illustrated in figure 2.3. To grasp how large the range of scales is: length scale range spans an equivalent of 1 m to 10 km and timescale ranges equivalent to 1 s to 4 years. Currently, no model or computational framework can fully capture all these scales at once. This necessitates splitting the problem into manageable parts, often requiring the use of different models to describe overlapping phenomena. Additionally, small-scale processes can influence large-scale behaviour and vice versa, complicating the picture further.

This interplay of scales presents a particular challenge when it comes to describing the pedestal, which is the main focus of this thesis. Many of the same physical phenomena — such as transport, stability, and turbulence — occur at different scales and all play critical roles in shaping pedestal physics. To address this complexity, I will start by discussing large-scale processes, beginning with MHD, and then progressively delve into smaller-scale phenomena. This will include collisional transport of particles and heat, turbulence, microturbulence, and finally the gyrokinetic framework used to describe it.

A perfectly didactic thread of all the physics included is probably impossible to achieve[1], nonetheless I will try to give some

[1] In reality, as anyone who has written a scientific text probably very well knows, the process of acquiring relevant information is much more unstructured, exploratory, often abstract and even at some point intuitive. Organising this knowledge into a coherent narrative is a continually evolving process, and this thesis represents yet another iteration of my ongoing practice.

logical structure for discussing these interconnected phenomena. So, bear with me as we traverse this multiscale path!

2.1 Magnetohydrodynamics

2.1.1 MHD Plasma Description

In Magnetohydrodynamics, we assume that the distribution function f_a is a Maxwellian distribution, which allows us to integrate over velocity space and leads us to hydrodynamic equations. This is very useful because we can find relations between macroscopic quantities in the plasma and model it as a fluid. We again assume the force acting on the particle to be the Lorentz force (2.1), where we calculate $\vec{E}$ and $\vec{B}$ with Maxwell [2] equations and neglect gravity.

Averaging (2.11) over velocity space involves multiplying the equation of motion by v^k and then integrating over d^3v, a process that generates the so-called moments. The zeroth moment provides information about mass, the first about momentum, and the second about energy. As we go through these moments, it is important to clarify a subtle distinction, that is important for the comprehension of the following section. The equation of motion (2.11) itself is a differential equation describing the evolution of the distribution function f_a. When we take moments of the equation of motion, we mostly have to take moments of f_a which are calculated as

$$\int \vec{v}^k f_a \, d^3v = n_a \langle \vec{v}^k \rangle. \tag{2.12}$$

.

To avoid confusion, the notation *f-moment* refers to the moment of f_a, and it is thereby distinguished from *moment* of the equation of motion (2.11).

So let us take now the **zeroth** moment of (2.11). The first term in the equation is the zeroth f-moment:

$$\int \frac{\partial f_a}{\partial t} d^3v = \frac{\partial}{\partial t} \int f_a d^3v = \frac{\partial n_a}{\partial t}. \tag{2.13}$$

The second term of (2.11) is the first f-moment:

$$\int \vec{v} \cdot \nabla f_a d^3v = \nabla \cdot (n_a v_a), \tag{2.14}$$

and the partial integration of the third term, the force term, reduces to 0. This gives us the zeroth moment of the equation of motion, and that is the equation of continuity:

$$\frac{\partial n_a}{\partial t} + \nabla(n_a v_a) = 0 \tag{2.15}$$

We already observe an important detail to keep in mind for later: the zeroth moment equation (2.15) involves velocity, which corresponds to the first moment. Next, we calculate the **first** moment of (2.11) where we multiply each term with v and integrate as $\int d^3v$. Doing this for the first term, we have the now familiar first f-moment. In the second term, however, we get the second f-moment, that benefits from decomposing the particle velocity $\vec{v}$ into its fluid velocity $\vec{u}$ and thermal motion $\vec{w}$. While thermal motion $\vec{w}$ is zero when averaged linearly, as it was the case in the first f-moment, a quadratic average yields thermal energy, resulting in the relation

[2] Yes, the same James Clerk Maxwell that also figured out our distribution function. In his 48 years, he did some of the most important physics in history, and he also wrote poetry, which is absolutely hilarious. One of the poems he wrote when he was 22 has the title "*Lines written under the conviction that it is not wise to read Mathematics in November after one's fire is out*", and as a fellow young physicist writing this chapter on a rainy November evening, I must admit, I tend to agree with James. https://allpoetry.com/James-Clerk-Maxwell

$$\frac{1}{2}m_\alpha \int \vec{w}^2 f_\alpha d^3v = \frac{3}{2}n_\alpha k_B T_\alpha = \frac{3}{2}p_\alpha, \tag{2.16}$$

where p_α represents the scalar pressure and k_B the Boltzmann constant. The situation is actually somewhat more intricate; in addition to scalar pressure, we must also account for viscosity. Thus, the total pressure tensor is expressed as

$$\mathbf{P} = p_\alpha \mathbf{1} + \mathbf{\Pi}, \tag{2.17}$$

where $\mathbf{1}$ is the unity tensor and $\mathbf{\Pi}$ encompasses the off diagonal terms related to viscosity. With these definitions, for the second term of (2.11) we have:

$$\int \vec{v}\cdot\vec{v}\cdot\nabla f_a d^3v = \nabla\cdot(n_a\vec{v}\cdot\vec{v}) + \frac{1}{m_a}\nabla\cdot\mathbf{P}. \tag{2.18}$$

In the third term, velocity integration and spatial differentiation can be exchanged, which results in force multiplied with the zeroth f-moment. Using all previous assumptions, the final form of the first moment of (2.11) gives us the force balance equation

$$\underset{①}{m_a n_a \frac{d\vec{v}_a}{dt}} = \underset{②}{-\nabla\cdot\mathbf{P}_a} + \underset{③}{n_a q_a\left(\vec{E} + \vec{v}_a \times \vec{B}\right)} + \underset{④}{\mathbf{R}_{a,b}}. \tag{2.19}$$

The term on the left side of the equation marked with 1 is the inertia, term 2 is pressure force, including viscosity, term 3 is the Lorentz force and term 4 $\mathbf{R_{a,b}}$ is the friction term between particles of two different species.

We note once more that the force balance equation includes the pressure tensor, $\mathbf{P}$, which arises from the second moment, so averaging over $\vec{v}^2$, much like velocity — the first moment — appears in the zeroth moment equation. This highlights that progressing further by considering the second moment of the equation of motion will still not suffice to close the system of equations, because it will contain a term from the third moment. To address this, we must introduce additional assumptions about the system energy to determine $\mathbf{P}$, instead of progressing with moment calculations. Specifically, we take the adiabatic closure of the system as

$$\frac{d}{dt}\left(\frac{p_a}{\rho_a^\gamma}\right) = 0. \tag{2.20}$$

where $\rho_a = n_a m_a$ is the mass density and γ is the adiabatic constant.

Now that we have connected the distribution function to the macroscopic fluid variables with the equation of continuity (2.15), force balance (2.19) and equation of state (2.20), we must incorporate the role of electromagnetism. To do this, we introduce the relevant electromagnetic equations, starting with reduced Ohm's law for plasmas:

$$\vec{E} + \vec{v} \times \vec{B} = \frac{1}{\sigma}\vec{j}. \tag{2.21}$$

where $\vec{j}$ is the current density and σ the electric resistivity. We then proceed to Maxwell's equations, which govern the behaviour of electric and magnetic fields:

$$\mu_0\vec{j} = \nabla \times \vec{B} \tag{2.22}$$

$$\frac{\partial\vec{B}}{\partial t} = -\nabla \times \vec{E} \tag{2.23}$$

$$\nabla \cdot \vec{B} = 0 \tag{2.24}$$

including Ampère's law (2.22), Faraday's law of induction (2.23), and Gauss's law of magnetism (2.24).

Solving this set of seven differential equations is a highly complex task. The problem can be further simplified, using several simplifying assumptions. Due to the much smaller mass of electrons compared to ions, we assume that the plasma centre of mass is in the ions, and the presence of additional plasma components, such as impurities, can be accounted for through correction terms. The plasma is assumed to be quasi-neutral, meaning it contains an equal amount of positive and negative charges distributed homogeneously, so it appears electrically neutral on a macroscopic scale. Additionally, the pressure is assumed to be isotropic so that $\nabla \cdot \mathbf{P}$ is reduced to ∇p.

Summarizing the key assumptions underlying the ideal MHD model:

- The description of the plasma is continuum based, and the behaviour of individual particles is therefore not explicitly considered. In the context of the MHD model, the Larmor radius is assumed to be much smaller than any characteristic length scale of interest.
- Maxwellian Temperature Distribution: The plasma is assumed to have a Maxwellian temperature distribution, based on the premise that the timescales of interest are much longer than the particle collision times, or equivalently, that the spatial scale of the plasma is much larger than the mean free path of particles. This condition is generally satisfied in the direction perpendicular to magnetic field lines, but not necessarily along them. Consequently, MHD is limited to describing dynamics perpendicular to the field lines.
- Ideal Conductivity: Assuming the plasma is an ideal conductor, the electrical conductivity σ in equation (2.21) approaches infinity. As a result, resistance is effectively zero, and no energy dissipation occurs. This forms the basis of the ideal MHD model. In cases where electrical resistance is included, it is treated within the framework of the resistive MHD model.

2.1.2 Equilibrium

As outlined in previous sections, the tokamak configuration relies on external coils surrounding the chamber to generate a toroidal magnetic field. A strong electric current flows through these coils, inducing the magnetic field as described by Ampère's law:

$$\int B_{\varphi,} \, ds = \mu_0 I, \tag{2.25}$$

which leads to the expression:

$$B_\varphi(R) = \frac{\mu_0 I}{2\pi R}. \tag{2.26}$$

This equation shows that the toroidal magnetic field strength B_φ is inversely proportional to the major radius R. Consequently, the region closer to the inner side of the torus is referred to as the high-field side (HFS), while the outer region is known as the low-field side (LFS).

The poloidal magnetic field, in contrast, is determined by the toroidal plasma current and the configuration of the poloidal field coils. Since the plasma resistivity decreases at high temperatures, the toroidal current density peaks at the plasma centre, where the electron temperature is highest.

For the plasma to reach equilibrium, all forces must balance such that the plasma velocity remains constant, ensuring a stationary system. By setting $\partial/\partial t = 0$ and considering plasma rotation velocities small compared to the sound speed, we obtain

the force balance equation

$$\vec{j} \times \vec{B} = \nabla p. \tag{2.27}$$

We can also re-write this equation using Ampere's law for current density and obtain

$$\nabla p = \frac{1}{\mu_0}(\nabla \times \vec{B}) \times \vec{B} = -\nabla \frac{B^2}{2\mu_0} + \frac{1}{\mu_0}(\vec{B} \cdot \nabla)\vec{B} = \underset{①}{-\nabla \frac{B^2}{2\mu_0}} + \underset{②}{\frac{B^2}{\mu_0}\vec{\kappa}}. \tag{2.28}$$

Here we introduced curvature $\vec{\kappa}$ defined as

$$\vec{\kappa} = \frac{\vec{B}}{B} \cdot \nabla \frac{\vec{B}}{B} \qquad \text{with } |\vec{\kappa}| = \frac{1}{R_c}, \tag{2.29}$$

We see that there are two restorative mechanisms on the right-hand side of the equation: there is the magnetic pressure that counteracts the field line compression, marked as 1, and there is the field line tension, which opposes the bending of the field lines, marked as 2. The interaction between the plasma displacement and the restoring forces generates oscillations in the plasma, leading to either compressional or shear Alfvén waves, depending on the nature of the restorative force.

First, let us consider the case where the plasma is compressed homogeneously in a direction perpendicular to the magnetic field lines, with no variation along the field lines. This scenario gives rise to compressional Alfvén waves, which are longitudinal waves. The phase velocity of these waves is given by

$$v_{ph} = \sqrt{\frac{\gamma p_0}{\rho_0} + \frac{B_0^2}{\mu_0 \rho_0}} \tag{2.30}$$

where γ is the adiabatic constant, ρ is the mass density and the subscript 0 denotes that this is an equilibrium value. The first term on the right-hand side represents the kinetic contribution, and the second term corresponds to the magnetic contribution.

If the normalised pressure, $\beta_{pol} = \frac{2\mu_0 p}{B^2}$, is much greater than 1 ($\beta \gg 1$), the phase velocity of the wave approaches the plasma sound speed, $c_s = \sqrt{\gamma p_0/\rho_0}$. Conversely, if $\beta_{pol} \ll 1$, the wave propagates at the Alfvén velocity, $v_A = B_0/\sqrt{\mu_0 \rho_0}$, which corresponds to the magnetic pressure contribution. In general, the phase velocity results from a combination of both kinetic and magnetic contributions.

Shear Alfvén waves, on the other hand, are characterised by incompressible motion and therefore lack any kinetic contribution. As a result, their phase velocity is equal to the Alfvén velocity, v_A. This velocity plays a crucial role in plasma behaviour, as it sets the "natural" timescale for inertial effects, given by $\tau_A = L/v_A$, which in fusion plasmas is typically on the order of 1–10 microseconds.

Alfvén waves mostly have a stabilising effect on the plasma because they are a sink of free energy that the perturbation needs to grow. However, they can also be excited by various mechanisms, including the presence of a population of fast particles in the plasma.

From the equilibrium force balance (2.27), follows that the magnetic field is perpendicular to the pressure gradient, satisfying $B \cdot \nabla p = 0$. This shows that the pressure remains constant along a magnetic field line. Similarly, the current density is also perpendicular to the pressure gradient, leading to $j \cdot \nabla p = 0$.

These relations allow the definition of a coordinate system based on surfaces of constant magnetic flux. The magnetic flux function satisfies:

$$B \cdot \nabla \psi = 0, \tag{2.31}$$

where ψ is the magnetic flux function. This condition implies that the magnetic field lines lie within these surfaces. The flux surfaces are nested around the magnetic axis at the centre of the plasma.

The radial coordinate that is often used in the pedestal studies normalised poloidal flux, which ranges from 0 at the magnetic axis to 1 at the separatrix. It is defined as

$$\psi_N = \frac{\psi - \psi_0}{\psi_{sep} - \psi_0}, \tag{2.32}$$

and its square root, mostly used in this thesis, called the poloidal normalised ratio

$$\rho_{pol} = \sqrt{\psi_N}, \tag{2.33}$$

where ψ is the magnetic flux, ψ_0 is the flux value at the magnetic axis, and ψ_{sep} is the flux at the separatrix.

Due to the high particle velocities and low density, the mean free path of particles along the magnetic field lines is long, allowing temperature gradients on a flux surface to average out quickly. In the framework of ideal MHD, where the pressure gradient remains constant on a flux surface, the pressure p is also constant on that surface. The relationship $p \propto nT$ connects the pressure, density n, and temperature T, indicating that density can also be assumed constant on a flux surface.

Consequently, it is typically sufficient to analyse only the poloidal cross-section of p, T, and n. This approach reduces the description of these parameters in the axisymmetric tokamak geometry to one dimension.

The equilibrium condition of a plasma, which represents the balance between the pressure gradient, poloidal currents, toroidal currents, and magnetic fields, is expressed by the two-dimensional Grad Shafranov (GS) equation:

$$\Delta^*\psi = -F\frac{dF}{d\psi} - \mu_0 R^2 \frac{dp}{d\psi} = -\mu_0 R j_\varphi, \tag{2.34}$$

where ψ is the poloidal magnetic flux, F is the poloidal current function, μ_0 is the vacuum permeability, R is the major radius, p is the plasma pressure, and j_φ is the toroidal current density.

In this context, Δ^* is defined as:

$$\Delta^* \equiv R^2 \nabla \cdot \left(\frac{\nabla}{R^2} \right) = R\frac{\partial}{\partial R}\left(\frac{1}{R}\frac{\partial}{\partial R} \right) + \frac{\partial^2}{\partial Z^2}, \tag{2.35}$$

and $F(\psi)$ represents the diamagnetic profile, given by:

$$F(\psi) = RB_\varphi = \frac{\mu_0}{2\pi} I_{pol}, \tag{2.36}$$

where R is the major radius, B_φ is the toroidal magnetic field, μ_0 is the vacuum permeability, and I_{pol} is the poloidal current, and ψ indicates that the quantity is a flux function. For simplicity, we will consider the last closed flux surface and the nested surfaces within it as circular around the central axis, R_0 as shown in the top panel of figure 2.4. The pressure depends only on the flux surface and remains constant along the magnetic field lines. When we observe the whole toroidal structure, the inner flux surfaces of the tokamak have a smaller area compared to the outer ones, and an outward force arises, pushing the plasma towards the larger surfaces. Additionally, the peaked plasma current generates a force that further expands the torus. These outward forces are counteracted by a vertical magnetic field. The total poloidal magnetic field generated by the plasma and vertical field coils creates a weaker radial field on the outside compared to the inside of the torus. This difference results in a shift of the centres of the flux surfaces outward,

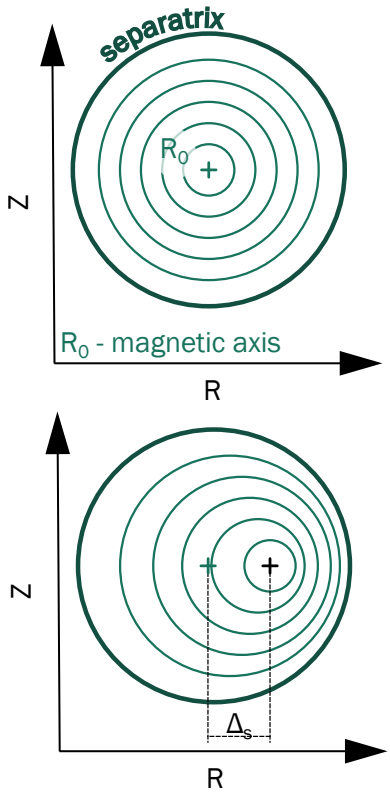

Figure 2.4: A sketch of the concept of Shafranov shift. In the upper panel, a perfectly concentric magnetic flux surfaces are shown with marked separatrix and the magnetic axis R_0. In the lower panel, the effect of Shafranov shift is shown, where the magnetic flux surfaces consequently create a shift Δ_s to the LFS.

an effect known as the Shafranov shift, marked as Δ_s in the bottom panel of figure (2.4), and it is calculated as

$$\Delta_s = -\frac{r}{R_0}(B_{pol} + \frac{1}{2}l_i), \tag{2.37}$$

showing that the Shafranov shift is proportional to the normalised plasma pressure β_{pol} and the current peaking l_i that describes the ratio of plasma pressure to magnetic pressure as

$$\beta_{pol} = \frac{\text{plasma pressure}}{\text{magnetic pressure}} = \frac{\langle p \rangle}{B_{pol}^2/2\mu_0}. \tag{2.38}$$

Radial force balance and E_r

Having introduced the radial force balance equation in (2.19) and the fundamentals of the equilibrium, it is a good moment to take a short detour from MHD equilibrium and stability, and introduce an equation, that will later be central to our analysis.

We consider that the plasma is stationary and in thermodynamic equilibrium, so $\frac{\partial v}{\partial t} = 0$, and we also assume isotropic pressure and negligible viscosity. In this case, equation (2.19) is reduced to

$$\nabla p_a = n_a q_a(\vec{E} + \vec{v} \times \vec{B}). \tag{2.39}$$

with n_a here being the particle density and q_a the particle charge. If we take the cross product with $\vec{B}/B$, we obtain the perpendicular velocity of species *a*:

$$v_{\perp,a} = -\frac{\nabla p_a \times B}{n_a q_a B^2} + \frac{E \times B}{B^2} = v_{dia} + v_{E\times B} \tag{2.40}$$

so the perpendicular velocity of species *a* is the sum of its diamagnetic and E × B drifts. As we have shown in section 2.1.2, the pressure and the plasma current are flux functions, meaning that in our model, they don't have a gradient along the magnetic field line. In the radial direction, however, an electric field can arise due to the radial transport of electrons and ions. Utilizing (2.39) in axisymmetric coordinate system (R,θ,φ) where θ is the poloidal and the toroidal angle[3], we get the equation for the radial electric field E_r for species *a*:

$$E_r = \frac{\nabla_r p_a}{n_a q_a} + v_{\perp,a} B = \\ = \frac{\nabla_r p_a}{n_a Z_a e} - v_{\varphi,a} B_\theta + v_{\theta,a} B_\varphi. \tag{2.41}$$

[3] If the reader has troubles remembering which Greek letter denotes poloidal and which toroidal angle, the convention is *not* Theta - *T*oroidal, *P*hi - *P*oloidal, but the exact opposite, just to keep things interesting and make sure tokamak physics does not get too simple.

where Z_a is the charge number of species *a* and e is the elementary charge, B_φ and B_θ are toroidal and poloidal magnetic field, and v_φ and v_θ represent the toroidal and poloidal velocities.

There are a variety of mechanisms that contribute to the emergence of E_r, coming either from toroidal and poloidal plasma rotation, or from charge separation. The most commonly recognised mechanisms are ion orbit losses, turbulent Reynolds stress, and toroidal torque from neutral beam injection. The radial electric field is particularly strong at the plasma edge.

2.1.3 MHD Stability

Now, we have established that the plasma is in an equilibrium if the forces acting on it equal out. The question of stability is then how the system responds if the equilibrium is disturbed by a perturbation: if the disturbance is damped and the system returns to the equilibrium, it is stable; if the disturbance persists without change, it is marginally stable; and if the disturbance grows, the system is unstable, and this instability is also referred to as mode[4]. Depending on the complexity of the system, this stability can be linear or non-linear. A mechanical analogy for this concept is illustrated in figure 2.5. Consider a ball subjected only to gravitational force. If a displacement perturbation is introduced, different scenarios of stability arise. In figure 2.5a, the system is linearly unstable, meaning the perturbation causes the displacement to grow. In figure 2.5d, the system is linearly stable but non-linearly unstable, where if the perturbation is large enough, it eventually leads to instability. Figure 2.5b represents a stable system, where the perturbation is counteracted, and if we assume some dissipative mechanism, like for example friction, the system eventually loses energy and returns to the equilibrium after an oscillation around it. In contrast, figure 2.5e shows a system that is linearly unstable but non-linearly stable. Finally, in figure 2.5c, the system is marginally stable, where the perturbation neither grows, now damps, while in figure 2.5f, it is marginally stable in the linear sense but becomes unstable non-linearly if the perturbation is large enough. In a fusion reactor, the plasma is constantly perturbed on both large and small scales, and the key question is whether these perturbations remain small or grow due to some fundamental drive.

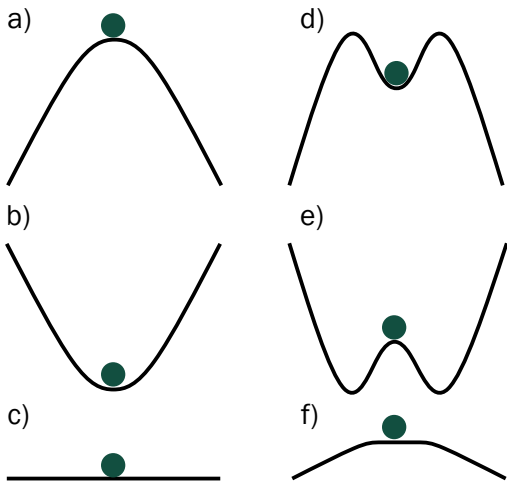

Figure 2.5: Drawing of different stability concepts on an example of mechanical system with a ball on a surface with only gravity acting on the ball. In the left column in a) an unstable system is shown, in b) a stable system and in c) a marginally stable system. In the right column, non-linear systems are shown. In d) a linearly stable and non-linearly unstable system is shown, in e) linearly unstable and non-linearly stable and in f) a linearly marginally stable, and non-linearly unstable system.

[4] So far, we have had three different uses of the word *mode*: H or L mode - regime; edge localised mode - empirically observed loss of energy and particles; and here mode is an unstable solution of our system

Linear analysis begins by considering small perturbations and focuses on identifying the conditions under which the instability can occur in the first place. In such cases, the subsequent evolution of the plasma due to non-linear effects is disregarded. This simplification involves linearising the MHD equations by decomposing all variables into the sum of two components: an equilibrium value and a small perturbation. For instance:

$$A = A_0 + A_1$$

$$AB = A_0B_0 + A_0B_1 + A_1B_0 + A_1B_1$$

in which index 0 is the equilibrium, or background quantity, and index 1 is the fluctuating perturbation in the system. When the equations are expressed in this form, the first terms, A_0B_0, represents the equilibrium, which is stationary and has no time dependence ($\partial/\partial t = 0$). The final term, A_1B_1, can be neglected due to the assumption that the perturbation is small. While equilibrium states are time-independent, the evolution of the perturbation over time serves as the formal criterion for determining the stability of the system.

In the linear approximation, this allows us to use the wave ansatz to further describe the perturbed quantity as

$$A(r,t) = A_0(r) + A_1(r,t) = A_0(r) + A_1(r)e^{i\omega t},$$

where ω represents the eigenvalues that need to be calculated to gain information about the stability. It is important to note that ideal MHD does not account for any dissipation in the system. This implies that when a perturbation is introduced, without any damping, it would oscillate indefinitely around the equilibrium state in the most stable scenario. On the other hand, if the system is unstable, the perturbation would grow exponentially.

Since ω is generally a complex number, it can be expressed as:

$$e^{-i\omega t} = e^{-i(Re(\omega)+iIm(\omega))t} = e^{-iRe(\omega)t}e^{Im(\omega)t}. \tag{2.42}$$

If the imaginary parts of all eigenvalues ω are negative or zero, the perturbation will oscillate, and the system is considered MHD stable. Conversely, any eigenvalue with a positive imaginary part will cause exponential growth of the perturbation, and make the system unstable. Qualitatively, it is assumed that if the conditions for instability are present, the instability will inevitably manifest, as it can grow exponentially from the micro-fluctuations inherent in the initial state.

Alternatively, one can follow a different analysis: the mechanical analogy in figure 2.5 illustrates how the stability and potential energy are related. If the perturbation decreases the potential energy W, the kinetic energy will drive the perturbation away from the equilibrium state A_0. Otherwise, if the potential energy gets increased by the perturbation, the system will oscillate around the initial state. If some dissipation mechanism is included, it will eventually relax and stabilise back into the equilibrium state.

This approach is called the energy principle, and it is a very useful analysis tool for gaining insight in linear MHD stability. We introduce a displacement vector $\vec{\xi}(x)$ as

$$\frac{d\vec{\xi}}{dt} = \vec{v}_1.$$

The potential energy change that results from this displacement is given by the volume integral

$$\delta W = -\frac{1}{2}\int \vec{\xi}\cdot\vec{F}d^3x \tag{2.43}$$

with $\vec{F}$ being the force caused by the displacement. The energy functional generally consists of its fluid component W_f that describes the bulk plasma, the surface component W_s characterising the plasma-vacuum interface and the contribution from the vacuum W_v. For this purpose, we set the current on the surface of the plasma to zero and assume that the mode sits far enough from the surface, the last two contributions to the energy functional are neglected it is therefore simplified to its fluid term:

$$\delta W_F = \frac{1}{2}\int_{\text{Volume}} \Big(\underbrace{\frac{|B_{1\perp}|^2}{2\mu_0}}_{1} + \underbrace{\frac{B_{0\perp}^2}{2\mu_0}|\nabla\cdot\xi_\perp + 2\xi_\perp\cdot\vec{\kappa}|^2}_{2} + \underbrace{\gamma p_0|\nabla\cdot\xi|^2}_{3} - \underbrace{2(\xi_\perp\cdot\nabla p_0)(\vec{\kappa}\cdot\xi_\perp^*)}_{4} - \underbrace{\frac{j_{0\parallel}}{B_0}(\xi_\perp^*\times\vec{B}_0)\cdot\vec{B}_1}_{5} \Big) dV \tag{2.44}$$

where ξ^* stands for the complex conjugate of the displacement vector, and the direction perpendicular and parallel to the equilibrium magnetic field has the subscript $\perp$ and $\parallel$. The equilibrium values are subscripted with 0 and the perturbed values by 1. Equation (2.44) can be split into two different parts: in the first and second line, the terms 1, 2 and 3 are all positive and therefore contribute to the increase of the potential energy - meaning that they are restorative forces that act stabilising on the perturbation. They all have a connection to plasma waves: contribution 1 is the magnetic pressure that corresponds to the shear Alfvén wave, term 2 to the compressional Alfvén waves and the third is the adiabatic compression of the ideal plasma related to the soundwaves. The last

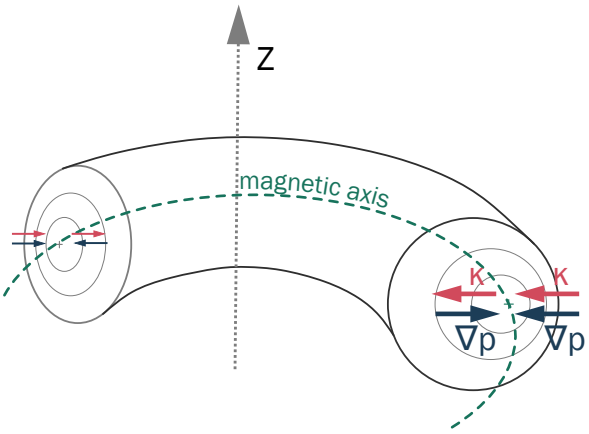

Figure 2.6: Illustration of the concept of "good" and "bad" curvature in a tokamak. The curvature κ is always directed towards the centre of the torus, while the pressure gradient ∇p is pointed towards the magnetic axis. As the result, on the high field side they cancel each other out, while on the low field side they are showing in the same direction, and destabilising the mode.

two contributions to the equation, marked with 4 and 5, can be positive or negative, and depending on their sign, either stabilise or destabilise the perturbation. The driving mechanisms are the pressure gradient ∇p_0 and the parallel current density $j_{0\parallel}$. In term 4, the sign is determined by the mutual orientation of the pressure gradient, ∇p, and the curvature, κ, sketched in figure 2.6. The curvature vector always points toward the centre of the tokamak, while ∇p points toward the magnetic axis. Consequently, at the low-field side (LFS), these vectors are parallel, resulting in a negative, destabilising contribution, whereas at the high-field side (HFS), they are antiparallel, leading to a positive, stabilising term in (2.44). Curvature is commonly described as "good" or "bad" depending on its influence on plasma stability.

The final term introduces instabilities driven by current density, which align parallel to the equilibrium magnetic field. Desta-

bilising effects are strongest on surfaces where q is rational. On such resonant surfaces, the perturbation aligns with the magnetic field lines, amplifying the instability as the stabilising effect of magnetic field line bending disappears.

From the negative terms of the energy functional, two primary types of instability emerge: pressure-driven modes and current-driven modes. One could assume that the goal of the ideal MHD stability analysis is to find an operational point in the parameter space that is not affected by any instability and has as high as possible plasma performance. While this is generally true, certain instabilities can be manageable to some extent and may even enhance plasma performance, depending on their location and extent. Therefore, the primary objective is to achieve a thorough understanding of the pedestal and its stability, rather than striving for complete stability under all conditions.

Pressure Driven Modes

Equation (2.44) shows that an MHD instability either originates from the pressure gradient or from the parallel current density. The pressure driven instabilities depend on the orientation of the pressure gradient and the magnetic field curvature. Because the mutual orientation of these vectors causes the instability to localise on the LFS, these modes are called *ballooning* modes. But first, we set the toroidal geometry aside, and focus on a more general case. In the MHD framework, illustrated in figure 2.7, a layer of plasma with higher pressure can interchange with a layer of lower pressure. If this exchange reduces the potential energy by shortening the magnetic field lines. The reduction in potential energy that results from the magnetic field line shortening enables the perturbation to grow. The destabilising energy term for pressure-driven modes is expressed as

$$\Delta W_d \sim -\frac{dp}{dr}\frac{R_c}{\kappa^2}, \tag{2.45}$$

where R_c represents the destabilising curvature. The stabilising term, which arises from the energy associated with field line bending, is given by

$$\Delta W_s \sim k_{\parallel}\frac{B_T^2}{\mu_0}\kappa^2. \tag{2.46}$$

Here, $k_{\parallel}$ denotes the parallel component of the propagation vector. At the resonant surfaces, the stabilising energy vanishes, allowing pressure-driven modes to propagate slowly with long wavelengths along field lines where there is no line bending, and rapidly with short wavelengths in the perpendicular direction. As a result, these modes become strongly localised in radially narrow regions around resonant surfaces, where $q = \frac{m}{n}$ is a rational number.

For further simplification, the extreme case where $n \to \infty$ is considered. In this limit, the radial extent of the modes approaches zero. Stability is thus calculated independently for each flux surface. This type of analysis will be of great significance in the rest of this thesis and will be referred to as *local* ballooning stability.

The calculations are performed in a coordinate system (ψ, θ, ζ), where ψ represents the flux surface, θ is the poloidal angle, and ζ is the toroidal angle. The perturbation quantity is introduced as $X = RB_\theta\xi_\psi$. The curvature κ is decomposed into normal and parallel components in this coordinate system, commonly referred to as the normal κ_n and geodesic κ_g curvature, respectively. An expression for ΔW is reformulated in the new coordinate system, incorporating the previously introduced definitions of the

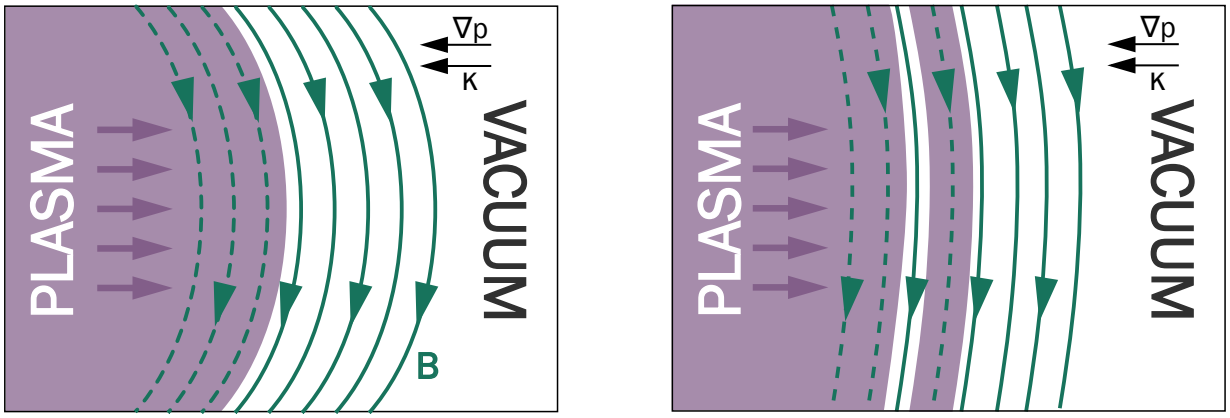

Figure 2.7: Interchange instability in the bad curvature region where the curvature κ and the pressure gradient ∇p are both pointing in the same direction. In the left panel, the initial state of the system is shown. In the right panel, because it is energetically favourable, the high pressure plasma region interchanges with the vacuum region, leading to lower potential energy due to shortening of the magnetic field lines. Here, vacuum is used as an example, however the same process can happen at any pressure gradient.

relevant terms, to assess the stability of localised pressure-driven modes:

$$\Delta W = \pi \int d\chi\, d\psi\, J \left[\frac{B^2}{R^2 B_p^2} \left| k_\parallel X \right|^2 + \right.$$
$$+ R^2 B_p^2 \left| \frac{1}{n} \frac{\partial}{\partial \psi} k_\parallel X \right|^2 - 2\mu_0 \frac{dp}{d\psi} \left(\frac{\kappa_n}{R B_p} |X|^2 - \right.$$
$$\left. \left. - i \frac{\mu_0 I_{pol} \kappa_g}{B^2} \frac{X}{n} \frac{\partial X^*}{\partial \psi} \right) \right], \quad (2.47)$$

with poloidal current I_{pol}, and toroidal wave number n. Similarly to equation (2.44), the stabilising terms representing field line bending are the first and the second term, containing only positive contributions. In the third and the fourth term, the orientation of the normal and geodesic curvatures relative to the pressure gradient again determine the sign and, consequently, their effect on stability.

In the simplified cylindrical geometry of a screw pinch, field lines curve poloidally but remain straight axially. A trial function for this geometry can be substituted into the energy functional, yielding the Suydam criterion, which states that the plasma is stable if

$$\frac{8\mu_0 p' r}{B_z^2} < \left(\frac{r q'}{q} \right)^2. \quad (2.48)$$

Here, the right-hand side represents the stabilising effect of magnetic shear, defined as

$$s = \frac{r q'}{q}. \quad (2.49)$$

In toroidal geometries, however, the problem becomes more complex due to the additional curvature that must be accounted for. The resulting toroidal counterpart to the Suydam criterion is the Mercier criterion. For a tokamak that possesses a large aspect ratio and a circular cross-section, the criterion simplifies to:

$$-\frac{8\mu_0 \nabla p}{r B_T^2} (1 - q^2) < \left(\frac{q'}{q} \right)^2. \quad (2.50)$$

The pressure gradient ∇p typically remains negative throughout the plasma profile, with

pressure peaking at the core. Consequently, if $q > 1$, which must be the case for other stability reasons, the left-hand side of the inequality will invariably be negative, thereby ensuring the stability of the plasma. However, it is important to note that this criterion is merely a necessary condition.

To comprehensively consider the toroidal geometry, one must account for modes that are not perfectly aligned with the magnetic field lines. Such misaligned modes can couple, leading to a small but finite $k_{\parallel}$. As a result, perturbations may localise in regions of unfavourable curvature, where their influence exceeds that of pure interchange modes. These localised instabilities, predominantly manifesting on the low-field side (LFS), are referred to as ballooning modes.

Given a finite poloidal coordinate χ, ensuring the necessary periodicity of the function is challenging. To resolve this, an extended poloidal coordinate l is introduced, which corresponds to the arc length along a surface. This technique, known as the ballooning transformation [49], yields the following expression:

$$\frac{\partial}{\partial l}\left[\frac{(k_n^2 + k_t^2)B_p}{B^2}\frac{\partial X}{\partial l}\right] + \\ + \frac{2\mu_0 R}{B^2}\frac{dp}{d\psi}(k_t^2\kappa_n - k_t k_n \kappa_g)X = 0. \quad (2.51)$$

In this formulation, k_t and k_n denote the mode propagation wave numbers in the tangential and normal directions, respectively. The stability of the system is determined by the behaviour of the solution: if X rapidly decays for $l \to \infty$ or $l \to -\infty$ without reaching zeros, this indicates a ballooning stable plasma; otherwise, the presence of zeros suggests instability.

In practice, the stability of ballooning modes is typically assessed through numerical methods. However, for a large aspect ratio tokamak with a circular cross-section, an explicit approach is feasible. While such an analysis involves significant simplifications, it offers valuable conceptual clarity about the behaviour of ballooning modes. The result can be summarised by the following equation:

$$\frac{\partial}{\partial\theta}\left[(1+\Lambda^2)\frac{\partial X}{\partial\theta}\right] + \alpha(\Lambda\sin\theta + \cos\theta)X = 0, \quad (2.52)$$

where

$$\Lambda = s\theta - \alpha\sin\theta. \quad (2.53)$$

In this expression, θ represents the poloidal angle of a circular cross-section, s is the surface-averaged global magnetic shear, and α is the normalised pressure gradient, which causes destabilisation. The parameter α is defined as:

$$\alpha = -\frac{2\mu_0}{(2\pi)^2}\frac{\partial V}{\partial\psi}\left(\frac{V}{2\pi^2 R_0}\right)^{1/2}\frac{\partial p}{\partial\psi}, \quad (2.54)$$

for general tokamak geometry, or in a more simplified form, for a large aspect ratio tokamak with circular flux surfaces.

$$\alpha = -\frac{2\mu_0 R_0}{B^2 q^2}\frac{\partial p}{\partial r}. \quad (2.55)$$

The impact of s and α is visualised on an s-α diagram (see figure 2.8), where the stability boundaries are plotted. This diagram divides the parameter space into three distinct regions, categorising the stability of ballooning modes based on these two key parameters.

The first stability region is characterised by high magnetic shear (s) combined with a low-pressure gradient (α). In this regime, the stabilising influence of favourable average curvature dominates. Enhanced shear increases field line bending, which strengthens stability, whereas a rising pressure gradient works in the opposite direction by enhancing instability. However, stability can

also be achieved under conditions of low average shear, giving rise to the so-called second stability region.

Although the magnetic shear is treated as a flux surface averaged quantity in prior equations, its value can vary significantly at a local level. This variability is expressed in the s−α equilibrium through the term αsinθ (see equation 2.53), which accounts for the local modification of the shear along a flux surface due to the Shafranov shift. In regions of unfavourable curvature, the shear may become locally large and negative, reducing the averaged value. Despite this reduction, negative shear can stabilise ballooning modes, as it is actually s^2 that contributes to the stabilisation (see the first term of equation (2.51) This stabilising effect creates a magnetic well, offering an explanation for the presence of the second stability region.

The region of instability separates the two stable regimes in the s−α diagram when the flux surfaces are circular and perfectly concentric (illustrated in green in figure 2.8). However, when the Shafranov shift is included, it modifies the s−α equilibrium by shifting the unstable region upward in the diagram. This shift allows a direct connection between the first and second stability regions (depicted in red in figure 2.8). Moreover, by varying the shaping parameters of the plasma, the size of this connecting region can be further increased, shown with the darker striped red region in figure 2.8, enhancing the accessibility of the second stable region.

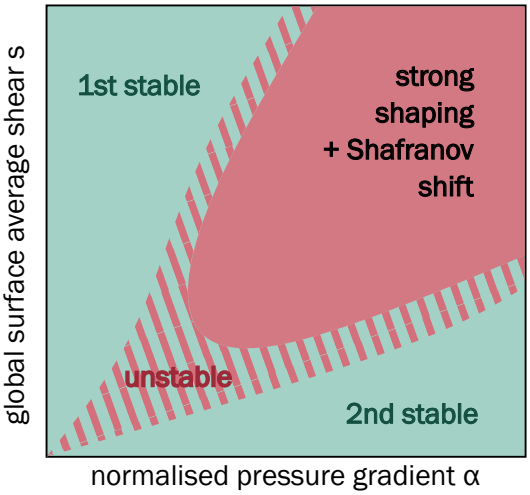

Figure 2.8: Schematic representation of the ballooning stability in an s-α diagram. The two stable regions are shown in green, and the unstable in red. The striped area shows the unstable region if Shafranov shift and higher shaping are taken into account.

Current Driven Modes

While pressure-driven modes, especially ballooning modes, have been discussed in detail due to their critical role in this particular work, especially in the context of the chapters 5 and 6, it is important to briefly address current-driven modes. Though their direct impact on stability may not be the primary focus of this thesis, their relevance becomes apparent when considering the coupling of a particular kind of current driven mode, the peeling mode, with ballooning modes. This coupling can significantly influence plasma behaviour, particularly in the edge and pedestal regions, and current driven modes in this context become significant. In equation (2.44), our initial focus was on the term involving the pressure gradient. We now analyse the second term, which describes instabilities driven by the parallel component of the plasma current $j_{\parallel}$, along the magnetic field lines. These current-driven instabilities can arise even in plasmas with zero pressure gradient. However, such scenarios are not particularly relevant for our study. At the plasma edge, where this thesis heavily focuses, a certain kind of current develops, called the bootstrap current, as a direct consequence of the pressure gradient. The

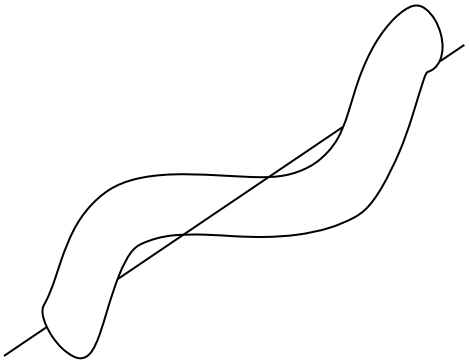

Figure 2.9: Drawing of a plasma column "kinking" around a magnetic field line. Figure adapted from [41].

mechanism leading to this current is discussed in section 2.2.1 about the collisional transport. For now, it is important to know that the bootstrap current is proportional to ∇p. Thus, the coupling of pressure gradients and consequent current becomes the primary interest in this context.

Current-driven instabilities are commonly referred to as kink instabilities (sketched in figure 2.9) named for the characteristic deformation of the plasma column, as illustrated earlier in figure 1.3. Depending on the location of this kinking deformation, these instabilities are classified as either internal or external kink modes. A specific type of external kink instability is the peeling mode, which usually occurs at the edge of the plasma.

Analogous to the ballooning modes, one can derive an energy functional for the peeling modes and determine their stability by minimising this functional. This analysis yields the peeling stability criterion:

$$\alpha\left(\frac{r}{R}\left(1-\frac{1}{q^2}\right)+s\Delta_s'-f_t\frac{Rs}{2r}\right)> \\ > Rqs\frac{j_{\|driven}}{B} \quad (2.56)$$

where we introduced the normalised pressure gradient α in equation (2.54), s is the magnetic shear defined in (2.49), Δ_s' is the amount of Shafranov shift illustrated in figure 2.4, f_t is the fraction of trapped particles, further explained in 2.1.2. Here $j_{\|driven}$ is the parallel current density, but without the bootstrap current and Pfirsch-Schlüter current contribution, which has, due to its dependency on α, been moved to the left side of the inequality.

The first term in (2.56) is the Mercier contribution to the stabilisation. The second is the stabilising Pfisrsch-Schlüter term that is strongly affected by the Shafranov shift. The third term is negative, and therefore destabilising, and it is the bootstrap current contribution to the drive of the peeling mode. We can read from this that the pressure gradient α can stabilise the peeling modes, however this stabilisation is limited on one side due to the bootstrap contribution to the current density, and on the other side due to the ballooning modes. This coupling between peeling and ballooning modes plays a crucial role in the dynamics of the pedestal.

Mode Coupling and ELMs

The analysis of ballooning and peeling modes has provided insight into the stability limits of plasma at the edge, where both the pressure gradient and current density define the stable operating region, as illustrated in figure 2.10. The peeling boundary is characterised by modes with relatively low toroidal mode numbers, typically $n<5$, whereas the ballooning boundary is associated with mode numbers $n>15$.

The dynamic process where the operational point moves in this j-α space describes to a large extent an ELM cycle. At the plasma edge, steep gradients form due to the suppression of turbulent transport, as outlined in the introduction. These gradients in temperature and density combine

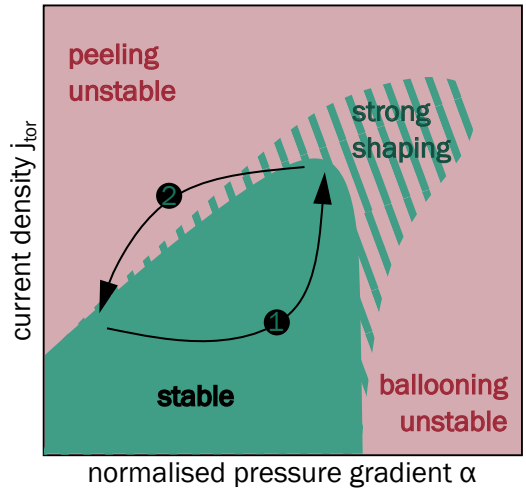

Figure 2.10: Peeling-ballooning stability model to explain an ELM cycle. The red shows the unstable and green the stable regions. The striped area is the stable region if the plasma has strong shaping. The numbers note three stages of an ELM cycle: 1 - an increase in the normalised pressure gradient, 2 - build up of the bootstrap current, 3 - an ELM crash.

to create a steep pressure gradient. As the pedestal pressure gradient builds up, the stability trajectory moves towards higher α, toward the ballooning stability limit. This increase in pressure gradient causes the bootstrap current to develop, leading to the onset of peeling modes. At this point, the coupling between peeling and ballooning modes takes place, a highly abrupt process that triggers a collapse of the pedestal and resets the cycle. The region of stability in the j-α space can be extended by shaping, so that higher values of normalised pressure gradient and current can be reached.

This model is well established [33, 34], and has been particularly successful in describing the ELM cycle, specifically for large type-I ELMs. Nonetheless, the peeling-ballooning model does not fully account for other ELM types, which are governed by different mechanisms. Despite its limitations, the coupling between peeling and ballooning modes remains critical, as it underpins the basic mechanism behind ELM cycles.

2.1.4 Codes

A large part of the analysis in this thesis focuses on the local $n \to \infty$ ideal ballooning stability that was numerically calculated with HELENA code[50, 51], for which an overview is given in this section. Global peeling-ballooning stability was also calculated with the code MISHKA [52] that will also be briefly described.

HELENA

To obtain higher-resolution equilibrium flux surfaces, the HELENA code [50, 51] is used to solve the Grad-Shafranov (GS) equation (2.34) for a toroidal axisymmetric plasma with a fixed boundary. The GS equation is normalized using three scaling parameters: the plasma boundary minor radius a as the length scale, the vacuum magnetic field B_0 at the plasma centre R_0, and the total poloidal flux per radian at the plasma boundary. These parameters normalize the pressure gradient $p(\psi)$, the diamagnetic profile $F(\psi)$, the toroidal current density $\langle j_{tor}\rangle(\psi)$, and the total plasma current I_P.

Additionally, the plasma boundary coordinates, originally in (R, z), are scaled relative to a as $x = (R - R_0)/a$ and $y = z/a$. This normalization transforms the GS equation into a dimensionless form:

$$\Delta\psi = -\frac{1}{\varepsilon}(1+\varepsilon x)^2 p'(\psi) - \frac{1}{\varepsilon}F(\psi)F'(\psi) = \\ = -\frac{1}{\varepsilon}(1+\varepsilon x) j_{tor} \quad (2.57)$$

where $\varepsilon = a/R_0$ is the aspect ratio and $'$ denotes a derivative along ψ. From the equation (2.57) it is evident that solving it requires a combination of two out of four possible input profiles: the diamagnetic

profile $F(\psi)F(\psi)'$, the pressure gradient p, the toroidal current density j_{tor} or alternatively the safety factor q.

The problem is then solved by the finite elements method, where in each element, a coordinate system is locally formulated in such way, that the straight field line configuration is achieved. The function is then interpolated using the bicubic Hermite element functions, so that inside the element boundaries the function is continuous.

Because HELENA is a fixed boundary solver, it also requires a predefined last closed flux surface, additionally to the inputs listed. The last closed flux surface naturally lies inside the separatrix, and it therefore defines the computational domain avoiding the X point. As an initial guess, HELENA makes a set of nested flux surfaces simply as down-scaled plasma boundaries, and then iteratively solves the GS equation until it converges to a flux surface grid that is sufficiently accurate, given the input profiles.

Aside from reconstructing the equilibrium, HELENA also provides a range of outputs concerning the MHD. The most important output for this thesis is the marginal ballooning stability for local Ideal Ballooning Mode (IBM)s. In HELENA, Suydam method[5], developed for a cylinder, is applied to the ballooning equation (2.47)[53].

The MHD energy functional is written as

$$\delta W = \int_0^L \left[F(l) \left(\frac{df}{dl} \right)^2 + G(l) f^2 \right] dl \tag{2.58}$$

with F(l) and G(l) representing functions that depend on the pressure profile and the magnetic field and f is the amplitude of the perturbed displacement. In the cylinder, l is the radial variable and L is the plasma column radius.

[5] Not to be confused with Suydam criterion given in equation (2.48).

The variables are then replaced by their centred finite difference expressions and arranged to complete squares, resulting in

$$\delta W = \sum_{i=0}^{N} \alpha_i (b_i)^2 \tag{2.59}$$

$$\alpha_i = A_{i,i} - \frac{A_{i-1,i}^2}{\alpha_{i-1}} \tag{2.60}$$

$$b_i = f_i + \frac{A_{i,i+1}}{\alpha_i} f_{i+1} \tag{2.61}$$

where the coefficients $A_{i,j}$ are given as

$$A_{i,i} = \frac{1}{\Delta l}(F_{i-1/2} + F_{i+1/2}) + \frac{\Delta f}{4}(G_{i-1/2} + G_{i+1/2}) \tag{2.62}$$

If all coefficients α_i in equation (2.59) are positive, δW remains positive, which means that the plasma is stable. On the other hand, because in the model resistivity is set to 0, any α_i coefficient that is negative indicates that a part of the spectrum has an exponential growth without dissipation, and eventually it dominates the solution. The plasma is then considered to be unstable. Thus, it is not necessary to solve for the eigenfunctions b_i; calculating the coefficients α_i suffices. However, in toroidal geometry, L approaches infinity, resulting in an ever-increasing number of α_i coefficients. Consequently, the Suydam method becomes as computationally intensive as conventional numerical methods for solving this problem in toroidal geometry. To make this approach practical, a maximum value for L must be established.

The procedure in the toroidal geometry then works as follows: First a large value of L is taken (about 10^3) and the stability is checked on all flux surfaces with a large step Δl. Next, surfaces that are around the stability boundary, obtained in the previous

step, are analysed again using a smaller mash size. This iteration is continued until the stability boundary remains the same for the further reduced Δl.

This method is integrated into HELENA, and it enables very efficient calculation of the ballooning stability, allowing for easy testing of different scenarios. Its application makes a detailed analysis of the topics discussed in chapters 5 and 6 possible.

MISHKA

To calculate the peeling-ballooning stability, we use the MISHKA code [52]. This code employs the set of linearised MHD equations, where the resistivity of the plasma is neglected, and only ideal MHD is employed. The method assumes small perturbations and treats the plasma as a single fluid, implying a net charge density of zero. The problem is also simplified by assuming the equilibrium velocity is zero and considering only a pressure perturbation p_1, rather than separately accounting for density and temperature variations. Additionally, plasma pressure is assumed to be isotropic, so only the scalar p is used.

By linearising the previously described MHD equations, the following eigenvalue equation is obtained:

$$\lambda \rho_0 \vec{v}_1 = \frac{1}{\mu_0}(\nabla \times \vec{B}_0) \times (\nabla \times \vec{A}_1) - \frac{\vec{B}_0}{\mu_0} \times (\nabla \times \nabla \times \vec{A}_1) - \nabla p_1 \quad (2.63)$$

$$\lambda p_1 = -(v_1 \nabla) p_0 - \Gamma p_0 (\nabla \cdot \vec{v}_1) \quad (2.64)$$

$$\lambda \vec{A}_1 = \vec{v}_1 \times \vec{B}_0 \quad (2.65)$$

Here, λ is the eigenvalue, and the perturbed magnetic field $\vec{B}_1$ is expressed in terms of the perturbed vector potential $\vec{A}_1$ as $\vec{B}_1 = \nabla \times \vec{A}_1$. The parameter Γ is the adiabatic constant. The perturbed velocity is denoted by $\vec{v}_1$, while p_0 and p_1 represent the equilibrium and perturbed pressures, respectively. The equilibrium mass density is given by ρ_0.

Equation (2.63) is derived from the force balance equation (2.19) and Ampère's law (2.22); equation (2.64) originates from the adiabatic equation (2.20) and the mass continuity equation (2.15); and equation (2.65) is obtained from Faraday's law (2.23), Ohm's law (2.21), and Ampère's law (2.22).

The MISHKA code solves this eigenvalue problem for $\vec{A}_1$, $\vec{v}_1$, and p_1, providing insights into the stability of the system. The growth rate is determined as $\gamma = \mathrm{Re}(\lambda) \pm \mathrm{Im}(\lambda)$. In ideal MHD, the eigenvalue λ is purely real, meaning the instability grows without oscillating. Thus, the growth rate can be directly obtained from the eigenvalue.

Next, one can apply the j-α routine. Here, the toroidal current density j_{tor} and the normalised pressure gradient α are scaled in a certain range (for example multiply each ∇p and $j_t$or profile with $[0.6, 0.8, 1, 1.2, 1.4]$), creating a grid of input combinations. The unscaled profiles are referred to as the operational point. For each grid point, the equilibrium is re-determined for the scaled profile of j and α and the growth rate is computed.

At some point, the growth rate begins to increase rapidly with small changes in j or α. This typically occurs when $\gamma = 0.04\,\omega_A$, where, ω_A is the Alfvén frequency. While this threshold is somewhat arbitrary, it generally aligns well with observations. However, it is important to also carefully examine the growth rate behaviour to confirm that this value truly represents the stability limit.

2.2 Plasma Transport

We have now described the MHD framework that provides us a robust basis with its macroscopic description of plasma equilibrium, global dynamics and stability. We have however made several simplifying assumptions, more specifically, we have neglected the finer, small-scale processes at play. Additionally, we have focused on the pressure and have not committed much of our attention to different ways that density and temperature can change individually and how the particles and heat are transported across magnetic surfaces. In real plasmas, transport phenomena - both collisional and turbulent - play a critical role in determining overall plasma performance. These processes govern the movement of particles, momentum, and energy across magnetic flux surfaces, influencing the evolution of kinetic profiles.

In the following section, we shift our focus to the mechanisms of transport in magnetized plasmas. These processes complement the model laid out by the ideal MHD and provide the underlying drivers of observed phenomena such as pedestal formation at the plasma edge.

2.2.1 Collisional Transport

Even though charged particles are restricted by the magnetic fields, because of the radial transport, they can move across the magnetic flux surfaces. The processes responsible for the radial outward transport of particles and energy are generally categorised as either collisional or turbulent.

In a plasma, density and temperature gradients naturally develop, driving diffusion processes in accordance with Fick's law, which results in particle fluxes

$$\Gamma = -D\nabla_r n + nV, \tag{2.66}$$

where D is the diffusion coefficient and V the convective transport due to the directed motion. Heat flux is calculated as

$$Q = -\chi n\nabla T, \tag{2.67}$$

where χ is the heat diffusivity. To determine the diffusion coefficient D and the thermal diffusivity χ, we must identify the transport mechanisms responsible for these fluxes.

Classical Transport

Classical transport arises because the ions and electrons collide in their gyro motion, which can be treated as the random walk due to Coulomb collisions between particles. To describe this motion, we use the characteristic spatial and temporal quantities: Larmor radius r_L, representing the spatial scale of the motion, and the collision frequency ν, which is the inverse of the characteristic time between collisions τ. Using these scales, the classical diffusion coefficient can be expressed as

$$D_{class} = \frac{r^2_{L(e,i)}}{\tau_{ei,ie}} = r^2_{L(e,i)}\nu_{ei,ie}, \tag{2.68}$$

and in the presence of a density gradient, a particle flux is driven by this diffusion. Note that because the particles are gyrating on the magnetic flux surfaces, they can only escape the magnetic field line if they experience a collision. Because of the conservation of momentum, a collision between two particles of the same species would only lead to them switching places and there would be no effective particle flux. Because of this, the collisional diffusion of electrons with the Larmor radius $r_{L,e}$ happens with the

frequency that electrons collide with ions ν_{ei} and vice versa. If only two particle species are considered, the diffusion is ambipolar for the electrons and ions because $r_i^2 = (m_i/m_e)r_e^2$ and $\nu_{ie} = (m_e/m_i)\nu_{ei}$ so the mass dependent factor cancels out. Similarly, the transport of energy uses the same random walk argument as

$$\chi = r_{L,a}^2 \nu, \tag{2.69}$$

with the species *a* Larmor radius $r_{L,a}^2$ and the collision frequency between species *a* and species *b* proportional to

$$\nu_{a,b} \propto Z_a^2 Z_b^2 \sqrt{m_{ab}}/m_a \tag{2.70}$$

where $m_{ab} = (m_a m_b)/(m_a + m_b)$ is the reduced mass and Z the particle charge. From this follows that

$$\chi_{ee} \approx \chi_{ei} \approx \chi_{ie} \approx \sqrt{\frac{m_e}{m_i}}\chi_{ii}, \tag{2.71}$$

therefore, the classical collisional heat conductivity is significantly higher for ion/ion collisions.

In the toroidal geometry of a tokamak, the collision frequency resulting solely from Coulomb collisions is inadequate to fully describe the amount of actual transport. The radial transport is significantly higher, requiring the inclusion of additional effects.

Neoclassical Transport

When the toroidal geometry of the magnetic field lines is included in the calculation of the collisional transport, several adaptations to the diffusion coefficients need to be made. This type of transport is called neoclassical transport [54, 55]. The most significant effect comes due to formation of magnetic mirrors in the typical tokamak geometry. This is illustrated in figure 2.11.

To understand this effect, we must first consider that the conservation of energy $E=1/2(v_\parallel^2 + v_\perp^2)$ and the invariance of the magnetic moment $\mu = mv_\perp^2/2B$ which is constant in plasmas with slow variations of $\vec{B}$.

Here it should be noted again, that the magnetic field strength B, decreases with the major radius R, following a 1/R dependence. As a particle travels from the low-field side (LFS) to the high-field side (HFS), B increases. Due to the invariance of the magnetic moment, μ, the perpendicular velocity component $v_\perp$ increases, while the conservation of total energy causes the parallel velocity $v_\parallel$ component to decrease. If $v_\parallel = 0$, the particle cannot follow the magnetic field line, and this results in the particle being reflected before completing a full poloidal orbit, as illustrated in figure 2.11. Such particles are called trapped particles. Because of the poloidal projection of these trapped particles, (2.11 right panel) the characteristic paths of trapped particles are called banana orbits. The trapped particles significantly increase radial transport. On the other hand, the particles that have enough parallel velocity to overcome the mirror effect are called passing particles. The characteristic length needed to determine the diffusion coefficient is then given by the banana orbit width

$$r_b \approx r_{L,pol}\sqrt{\varepsilon}q \tag{2.72}$$

Here, $r_{L,pol}$ represents the poloidal component of the Larmor radius, and ε denotes the inverse aspect ratio of the tokamak, defined as $\varepsilon = \frac{a}{R}$, where a is the minor radius and R is the major radius. Since $\varepsilon < 1$ and $q>1$, the banana orbit width is significantly larger than the Larmor radius.

The trapped particle fraction is approxi-

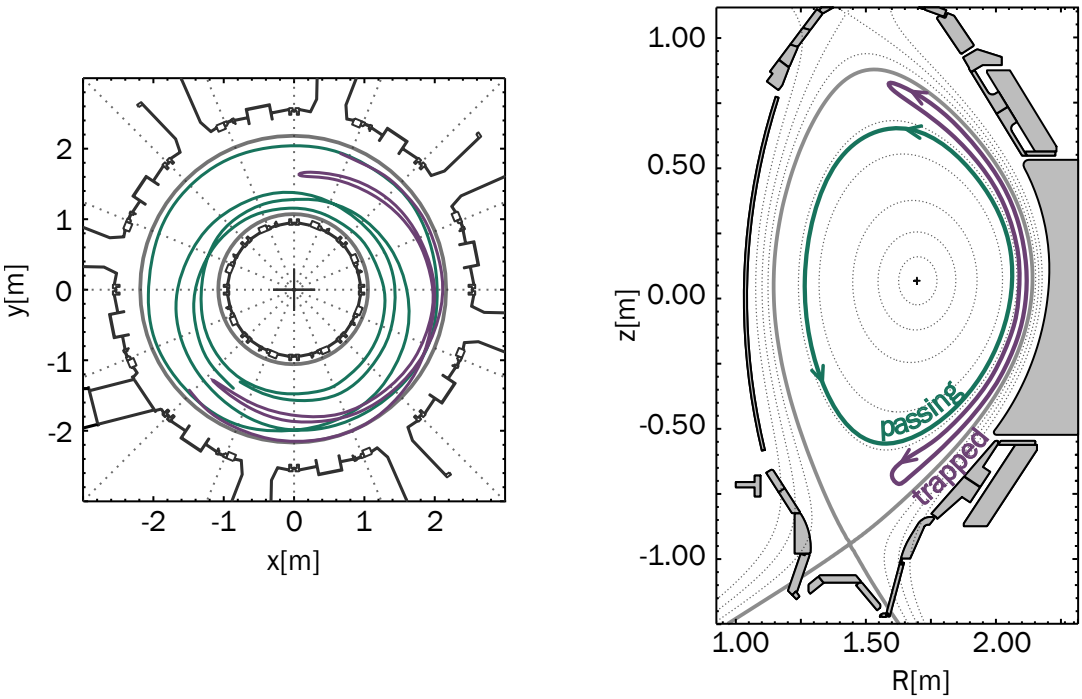

Figure 2.11: Toroidal (left) and poloidal (right) projection of trapped particles in purple and passing particles in green.

mated as

$$f_t = \sqrt{\frac{2r}{(R_0 + r)}} \tag{2.73}$$

where R_0 is the major radius at the magnetic axis for a cylindrical plasma.

Bootstrap Current

The bootstrap current[6] has been mentioned several times, especially in the context of MHD and peeling-ballooning stability. The actual mechanism behind it can be formulated as follows:

Consider a density gradient pointing toward the plasma core and two neighbouring banana orbits, shown in figure 2.12c. Examining the surface between these orbits reveals that more ions move in the upward direction than downward. This distribution is shown in 2.12a. The electrons have an opposite drift because of the mirror effect, and they will, contrary to ions, be more populated in the downward direction. Due to collisions, the distribution at the critical parallel velocity is continuous, as can be seen in figure 2.12b. This phenomenon is known as the banana current.

Passing particles then gain extra momentum in the same direction, generating an additional secondary current, which is called the bootstrap current j_{bs} [56–58]. The bootstrap current can be approximated

[6] The name of the bootstrap current already hints at its function, since it comes from the phrase from 19th century physics text books that ask why someone can not "pull themselves up by their bootstraps". The name is used to illustrate how plasma creates its own current. And a bonus fact: the phrase "booting" a computer has the same origin.

as [57]:

$$j_{bs} \approx -\sqrt{b}\frac{F(\psi)}{B_0}\left[2.44(T_e + T_i)\frac{dn}{d\psi} + \right.$$
$$\left. +0.69n\frac{dT_e}{d\psi} - 0.42n\frac{dTi}{d\psi}\right] \quad (2.74)$$

with $b=(B_{max} - B_{min})/(B_{max} + B_{min})$. More complex and accurate descriptions of j_{bs} can be found in [56] and [58].

This current has many significant roles in a tokamak, and it was previously mentioned in the context of MHD. It will also play a crucial role in the analysis presented in the following chapters, as it strongly influences plasma stability and confinement.

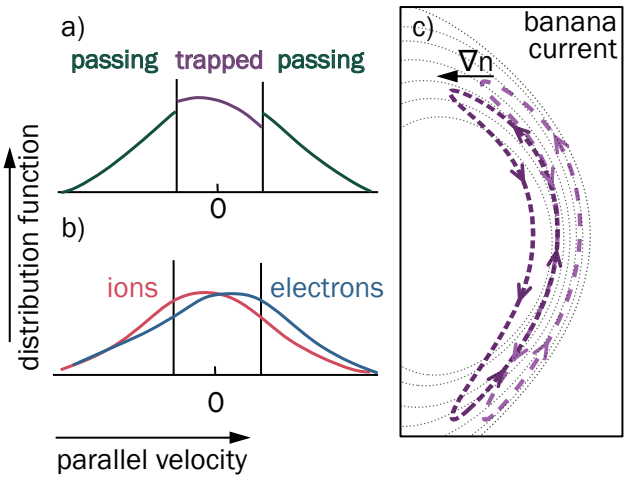

Figure 2.12: Mechanism of the bootstrap current: a) shows the distribution function depending on the parallel velocity and the trapping of ions, without including the effect of collisions, in b) different distributions of ions and electrons, also considering collisions are shown. In c) two neighbouring banana orbits illustrate the banana current mechanism.

Collisionality regimes

Depending on the frequency of collisions, plasma exhibits different regimes regarding its diffusion coefficient. The collisionality (ν_a^*) of species *a* is a dimensionless parameter that quantifies the impact of collisions on transport. It normalises the collision frequency to some characteristic time. There can be different normalisations depending on the plasma region or the effect that is described with ν^*. In the pedestal it is often defined as as the ratio of the effective collision frequency (ν_a) to the trapped particle bounce frequency (ω_{bounce}):

$$\nu_a^* = \frac{\nu_a}{\varepsilon\omega_{bounce}} = \frac{qR}{\varepsilon^{3/2}v_{th,a}}\nu_a, \quad (2.75)$$

where $v_{th,a}$ is the thermal velocity of the species, ε is the inverse aspect ratio, q is the safety factor, and R is the major radius of the tokamak. The effective collision frequency ν_a accounts for collisions of species a with itself and with other species. It is given by:

$$\nu_a = \sum_b \nu_{ab}, \quad (2.76)$$

where ν_{ab} represents the binary collision frequency between species *a* and *b*:

$$\nu_{ab} = \frac{4\sqrt{2\pi}e^4}{3}\sqrt{\frac{m_a m_b}{m_a + m_b}}\frac{Z_a^2 Z_b^2}{m_a}\frac{n_b}{T^{3/2}}\Lambda_{ab}. \quad (2.77)$$

Here, m is the mass, Z is the atomic number, n is the density, T is the temperature, and Λ_{ab} is the Coulomb logarithm. The Coulomb logarithm is expressed as:

$$\Lambda_{ab} = 23.46 - \ln\left(Z_a Z_b T_a^{3/2}\sqrt{n_a Z_a^2 + n_b Z_b^2}\right). \quad (2.78)$$

Collisionality is directly proportional to the density and inversely proportional to the square of the temperature. As collisions are the primary mechanism for de-trapping particles, the transport behaviour is influenced

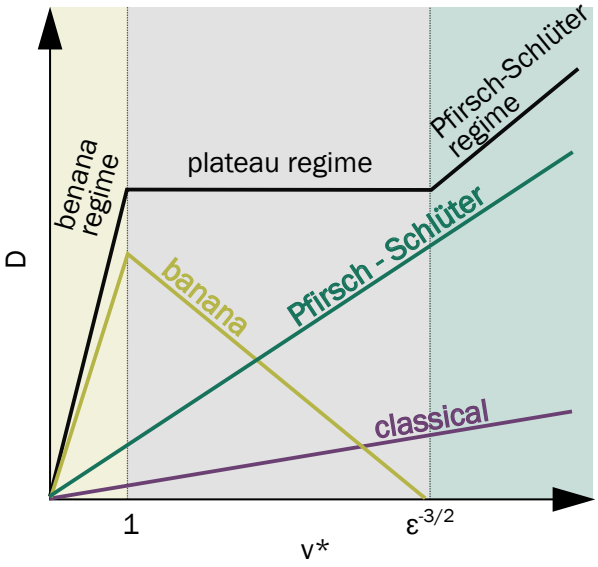

Figure 2.13: Diffusion coefficient in dependence on collisionality shown as the black line. Collisionality regimes marked as yellow, gray and green area. Its individual components, banana diffusion, Pfirsch Schlüter diffusion and classical diffusion are shown as yellow, green and purple lines on the plot.

by the collisionality regime. Depending on whether trapped or passing particles dominate, three distinct collisionality regimes can be identified, each affecting the diffusion coefficient differently.

Banana regime

For low collisionality ($\nu^* \ll 1$), the trapped particles complete multiple banana orbits before undergoing collisions. This regime, known as the banana regime, is characterized by a neoclassical diffusion coefficient $D_{neo,B}$, which can be expressed as

$$D_{neo,B} = \omega_B^2 \nu_{eff} f_t \frac{q^2}{\varepsilon^{3/2}} D_{class}, \qquad (2.79)$$

In the banana regime, the diffusion coefficient is significantly larger than the classical diffusion coefficient and depends linearly on the collision frequency.

Plateau Regime

For medium collisionality ($1 \ll \nu^* \ll \varepsilon^{-3/2}$), the bounce frequency of trapped particles is approximately equal to the collision frequency. This regime is referred to as the plateau regime, as the diffusion coefficient becomes independent of the collision frequency. The neoclassical diffusion coefficient in this regime, $D_{neo,P}$, is given by

$$D_{neo,P} = \nu_{th} r_L^2 \frac{q}{R}, \qquad (2.80)$$

where ν_{th} is the thermal velocity.

Pfirsch-Schlüter Regime

For high collisionality ($\nu^* \gg \varepsilon^{-3/2}$), collisions occur frequently enough that particles are scattered before completing their banana orbits. This regime is known as the Pfirsch-Schlüter regime, and the diffusion coefficient, $D_{neo,PS}$, is given by

$$D_{neo,PS} = q^2 r_L^2 \nu = q^2 D_{class}, \qquad (2.81)$$

The neoclassical diffusion coefficient is calculated as the sum of the three contributions, shown in figure 2.13.

Despite the neoclassical diffusion being significantly larger than the classical transport, it mostly remains largely insufficient to account for the observed profiles, indicating the presence of additional transport mechanisms, such as turbulence. Turbulence is typically the primary contributor to the outward particle and heat transport. However, in the regions where turbulence is suppressed, like for example in the pedestal - the main focus of this thesis - collisional transport is still significant or even dominant, especially for the ion heat transport (see equation (2.71)). Additionally, because of the Z^2 dependence of the collision frequency, neoclassical transport is crucial

for the transport of heavier impurities that also strongly influence the development of plasma [59–61].

2.2.2 Turbulent Transport

Turbulent structures in a tokamak account for a significant amount of radial transport. As already mentioned, turbulence is suppressed in the pedestal region to a various extent. Interestingly, exactly because of this suppression, the gradients in density and temperature reach their maximum and drive the turbulence. Yet, the additional mechanisms suppressing turbulence are even more dominant - a topic explored in the next section.

The turbulent motion is very challenging to model because it spans a large range of scales, from small structures in the range of electron gyro radius, to eddies comparable to the system size. Its highly complex structures strongly influence particle and heat transport in the plasma, which in turn changes the turbulence drive, creating a non-linear system. Turbulence, in a plasma or in a neutral fluid, is also fundamentally unpredictable on an individual particle level, due to the chaotic and complex motion. Previously derived equations of motion for individual particles are therefore insufficient to describe the system, and a statistical approach that relies on various distributions is once again crucial for successful interpretation and prediction of plasma behaviour. Despite impressive work done on understanding turbulence physics, because of its immense complexity, in both modelling and diagnosing, we sometimes have to settle for educated estimates in our analysis. Unlike in a standard fluid, modelling turbulence in a plasma has many additional obstacles due to the electro - magnetic interactions between particles and waves. The interactions can serve as a sink of free energy such as for example Landau damping [62, 63], or be resonant and enable the turbulence. Depending on the resonance conditions, the turbulence is classified as slab mode (parallel motion of passing particles), toroidal mode (magnetic drift of passing particles) or trapped particle mode (toroidal precession of trapped particles) [64].

If we trust MHD to handle all the large structures, and it declares everything MHD stable, the density and temperature gradients can still drive microscopic turbulence. When analysing microturbulence, we apply the same principles as we did in section 2.2.1: we are asking what happens if we introduce a small perturbation to the equilibrium? Does it get damped and die out, does it keep oscillating around the equilibrium, or does it exponentially grow? Unlike in the previous section, we are not applying the MHD equations, but using the more scale-appropriate approach - gyrokinetics. Microturbulence is characterised by the small length and time scales relative to the overall system dynamics, yet their scale remains large enough to average out the gyromotion effects, making the gyrokinetics particularly suitable for studying them. This framework is used in chapter 7, and it will be introduced in section 2.2.2.

Another similarity with the ideal MHD stability analysis emerges: even though linear analysis is strongly simplified, it is valuable. Not only for faster computation, but also because the stability of a perturbation can be assessed by solving a system of linear equations with the wave ansatz, which is not applicable in non-linear dynamics. From such analysis, we derive a complex dispersion relation, which provides valuable insights into the stability behaviour of various modes. The dispersion relation is defined with its characteristic quantities,

such as the wave number k and the complex frequency ω, which comprises a real frequency component and a growth rate γ. The unstable mode shows exponential growth. While linear differential equations combined with a wave ansatz provide a numerically straightforward way to analyse linear stability, they cannot completely capture their suppression and the saturation processes [65].

This limitation means that linear methods, though useful, miss some key dynamics, underscoring the need to complement them with nonlinear approaches. This thesis focuses exclusively on the local linear treatment of microturbulence, leaving the nonlinear aspects for separate, more comprehensive studies. Fortunately, through close collaboration, insights into the global nonlinear processes are being actively pursued, and answers will soon be available elsewhere [66].

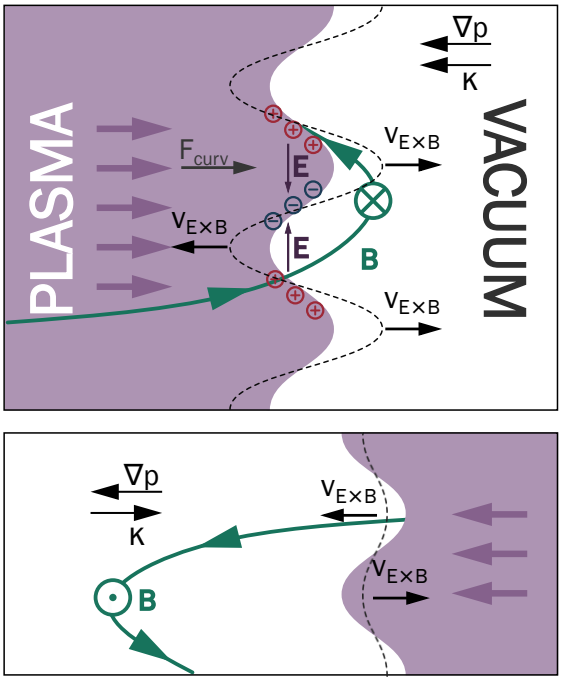

Figure 2.14: Kinetic description of an interchange instability. Upper panel shows the region of bad curvature and lower panel the region of good curvature. The effect of the interchange on the perturbation is illustrated with dashed lines.

Instability Mechanisms

Before delving further into the numerical techniques of studying microturbulent activity of the plasma, let us go through an overview of the key instability types relevant to our discussion and summarise the physics that drives them, to set the stage for the analysis in the following chapters.

- **Interchange instability**

Not many pages ago, we discussed the interchange instability from an MHD perspective (figure 2.7). The same instability can also be examined using a kinetic description, which, while differing in framework, captures the same underlying physical phenomenon.

In this simplified scenario, illustrated in figure 2.14, we assume a pressure gradient between plasma and vacuum (though, it can be between any two regions of high/low pressure) and a perturbation between them. For this instability, it suffices that the perturbation lies within the plane and requires no parallel component. When magnetic field lines bend inward toward the plasma, the resulting centrifugal acceleration, shown by the purple arrows in figure 2.14, acts outward. The outward centrifugal force induces a curvature drift, causing charge separation within the perturbation, marked as red and blue charges. This charge separation generates an electric field, which, combined with the magnetic field, drives an E × B drift.

The E × B drift can either dampen or amplify the perturbation, depending on the curvature direction, bad curvature shown in the top panel in figure 2.14 and good curvature, shown in the bottom panel. In regions of good curvature (HFS), the drift

smoothens the pressure perturbation, stabilising the system. In regions of bad curvature (LFS), the drift enhances the perturbation, destabilising the plasma. Consequently, magnetic field lines interchange between the plasma and vacuum regions, effectively swapping two flux tubes and lowering the system's potential energy. As a reminder, the characteristic of the interchange modes to be localised at the LFS is called ballooning.

- **Drift wave instability**

To understand the drift wave instability, let us first consider a stable drift wave in figure 2.15. A density perturbation occurs with a parallel dimension along the magnetic field lines, illustrated as two planes along the magnetic field lines that are out of phase. This perturbation creates a density gradient along B between two planes. Due to their lower mass and therefore lower inertia, electrons respond much more quickly to this gradient compared to ions, and follow the magnetic field line faster to the region of less density. Consequently, a charge separation temporarily forms.

This charge separation establishes an electric field $\vec{E}$, which in turn generates an $E \times B$ drift. Since the $E \times B$ drift is charge-independent, it causes the entire plasma to move. Oppositely directed electric fields along the wave result in varying small displacements, effectively shifting the density perturbation. The resulting shift in the density perturbation is depicted as dashed lines in figure 2.15.

If the plasma potential and density perturbation remain in phase, characteristic of adiabatic electrons, this setup leads to a marginally stable wave that neither dissipates nor grows. However, when there is a phase delay in the electron response to the plasma potential perturbation, the density and potential become misaligned. This phase difference drives the instability, as the shifted density enhances the original perturbation rather than damping it. The instability arises due to the delayed electron response, transforming a stable wave into a growing perturbation.

- **Tearing modes**

The tearing instability results from deformations in the magnetic field configuration. A perturbation in the parallel current alters the local magnetic topology, resulting in the formation of a magnetic island (see figure 2.16). The magnetic island introduces its own X-points and flux surfaces. Due to the rapid transport along flux surfaces, the island creates a radial shortcut, connecting regions that would otherwise remain separated by multiple flux surfaces. This process flattens the pressure gradient within the island. The reduced pressure gradient diminishes the parallel current via MHD force balance, further amplifying the island and enabling its growth. This instability is most

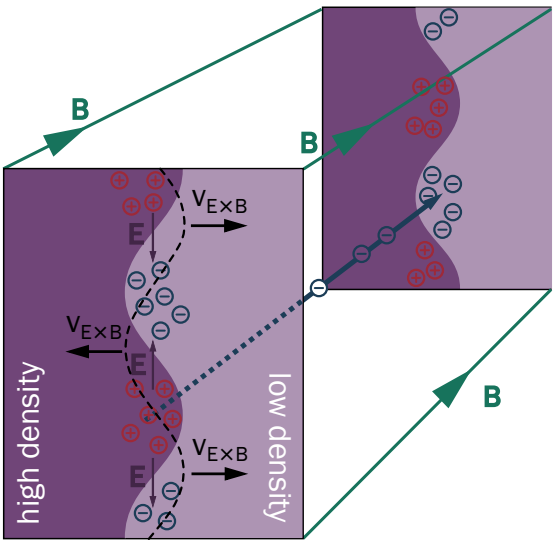

Figure 2.15: Drift wave illustration. Two panels represent two wave cross-sections along the magnetic field line B. the effect of the drift wave on the perturbation is indicated with the dashed line. Figure reinterpreted from [46].

likely to occur at low-order rational surfaces, meaning magnetic field lines close on themselves after a few toroidal rotations.

They however also appear both in microscopic and macroscopic scale. In the case of large islands, particularly in Neoclassical Tearing Modes (NTMs), this mechanism can significantly impact plasma stability and transport. Such instabilities may escalate to major disruptions, posing challenges to maintaining confinement.

Classification of Microturbulence

When analysing the microturbulent transport, one looks into several characteristic quantities:

1. frequency - depending on its sign, we can conclude if the instability is propagating in the electron or the ion diamagnetic drift direction (figure 2.2)

2. size - the size of the mode is usually estimated with its $k_y\rho^*$ component, where k_y is the wave number in the binormal direction (normal to the radial direction and to the magnetic field lines) and $\rho* = \rho_i/a$ is the ratio of the ion gyroradius ρ_i and the minor radius of the plasma a. This characteristic length varies from sizes comparable to the ion gyro-radius, to the scale of electron gyro-radius

3. diffusion ratio [67] - using only quasi-linear models (discussed in the section 2.2.3) we can not make conclusions on the absolute values of electron and ion heat fluxes and particle fluxes, however we can estimate their ratios, which can help us in identifying the type of microinstability.

4. ballooning angle - the radial wave number at the outboard midplane defines the tilt of the mode in the poloidal cross-section and connects to the ballooning angle, which tracks how fluctuations wrap around the torus.

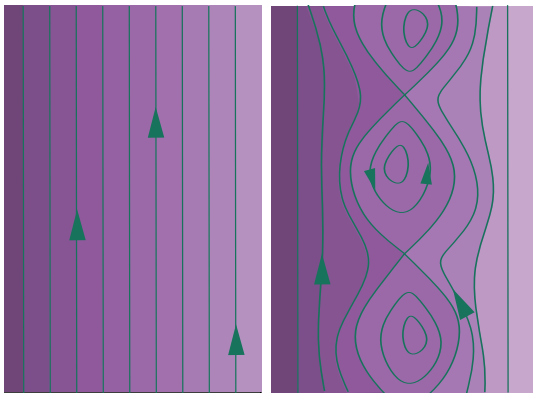

Figure 2.16: Illustration of a tearing mode. On the left, ordinary magnetic field lines with a gradient in pressure are shown. On the right, a chain of magnetic islands with their magnetic topology, building a tearing instability, is sketched. Regions of the plasma between high and low pressure that would be separated by several magnetic field lines are now closer together and are mixing inside the magnetic island.

These are only some of the criteria used to identify different types of instabilities. Additionally, one can numerically test the sensitivity of different instabilities by doing different parameter scans, for example by scaling local β or collisionality. The main types of instability, usually found in the pedestal, are listed in the following, and the summarised explanations in large follow reference [48].

Ion Temperature Gradient mode (ITG): The microturbulent modes that are driven by the ion temperature gradient are thought to strongly contribute to the anomalous transport of ion heat at lower values of local $\beta = p/(B^2/8\pi)$. If the electrons are adiabatic, ITG modes do not contribute to particle and electron heat transport. The perpendicular phase velocity of ITGs is in the

ion-diamagnetic direction. They are considered to be relatively large modes, comparable to the ion gyroradii with $k_y\rho^* \approx 0.1 - 1$. This microturbulence can have both an interchange drive in the toroidal branch and a drift wave drive in the slab branch. For more information, see [68–70].

Electron Temperature Gradient mode (ETG): In the idealised conditions, ETGs [71, 72] are the analogue to ITGs, but with reversed roles of ions and electrons due to their different charge sign. They are destabilised by the electron temperature gradient, and stabilised by the density gradient. ETGs propagate in the electron diamagnetic direction, and their size corresponds to the size of the electron gyro radius, so significantly smaller than the ITGs, with $k_y\rho^* \approx 10 - 200$. They are thought to be responsible for a significant amount of electron heat transport [73, 74]. ETGs can also have an interchange or a drift wave drive, depending on the characteristic of the particle-wave interaction resonance.

Trapped Electron Mode (TEM): TEMs arise if the electron response is not adiabatic and the wave numbers that destabilise it are in the medium range with $k_y\rho \approx 0.5 - 1.5$, meaning that they can overlap with ITG characteristic wave numbers. They are destabilised by both electron temperature and density gradient. Its growth rates can be decreased by increasing the collision frequency due to de-trapping of particles [75, 76].

Kinetic Ballooning Bode (KBM): Kinetic ballooning modes [77–79] are of particular interest for this thesis. Their size is comparable with the ion gyroradius, with the wave number ranging from $k_y\rho_i \approx 0.1$ to $k_y\rho_i \approx 1$. The propagation of KBMs is also in the ion diamagnetic direction. They are destabilised by pressure gradient and are therefore very sensitive to local β. By increasing β, one goes from ITG to KBM dominated transport. Since they are driven by an interchange instability, they have a strong dependence on curvature, giving them a very pronounced ballooning structure, giving them their designation.

Micro Tearing Mode (MTM): The micro tearing modes are usually larger than the ion gyroradius, however they propagate in the electron diamagnetic direction. The MTM is driven by the tearing mechanism and destabilised by the temperature gradient and parallel current perturbations. They are similar to the KBMs, but have a different drive and direction of propagation.

Of course, this categorisation has a limited applicability, and the situation is more intricate, as modes can couple and influence one another. Typically, our analysis focuses solely on the most dominant instability — the one with the fastest growth rate — while other, less prominent modes can be overlooked.

Nevertheless, we can deepen our understanding of microturbulence and the resulting transport by analysing these phenomena through the lens of gyrokinetics.

2.2.3 Gyrokinetics

As previously outlined, a straightforward Newton-Maxwell system of equations would suffice if we could compute a system of 10^{20} equations while knowing the initial conditions for each individual particle. Since this is impossible, statistical methods are employed and instead of calculating the motion of each individual particle, we consider a distribution f_a of species *a*. If we assume that the phenomena of interest occur on timescales much shorter than those of collisions, we can initially neglect collisions and use the Vlasov equation (2.11). Because the flow of energy in the system

becomes essential in this framework, the equations are formulated in terms of Hamiltonian mechanics as

$$\frac{\partial f_a}{\partial t} + \{f_a, H_a\} = 0 \tag{2.82}$$

with the Poisson bracket $\{\cdot,\cdot\}$ in coordinates (x,y) defined as

$$\{A, B\} = \frac{\partial A}{\partial x}\frac{\partial B}{\partial y} - \frac{\partial A}{\partial y}\frac{\partial B}{\partial x} \tag{2.83}$$

and the Hamiltonian of collisionless motion

$$H_a = \frac{1}{2m_a}\left|m_a\vec{v} - \frac{q_a}{c}\vec{A}\right|^2 + q_a\varphi \tag{2.84}$$

where m_a and q_a are the charge and mass of the particle species *a*, the light speed is noted as c, φ is the electrostatic potential and $\vec{A}$ is the vector potential for the magnetic field $\vec{B} = \nabla \times \vec{A}$. In the same way as in the MHD, the moments of f_a give the particle density and the current density and Maxwell equations are used to relate $\vec{E}$ and $\vec{B}$.

This leads to a kinetic model that, while still six-dimensional (three spatial and three velocity components), involves one equation per species rather than per particle, which is a relief. To further simplify, we adopt a gyrokinetic model. This reduction requires several assumptions:

$$\mathcal{O}(\varepsilon) \sim \frac{\omega_{turb.}}{\omega_c} \sim \frac{k_\parallel}{k_\perp} \sim \frac{v_{E\times B}}{v_{th}} \sim \sim \frac{n_1}{n_0} \sim \frac{B_1}{B_0} \sim \frac{\rho_L}{L_{ref}} \tag{2.85}$$

$\omega_{turb.}$ is the characteristic turbulence frequency, ω_c is the gyrofrequency, $k_\parallel$ and $k_\perp$ are the parallel and the perpendicular components of the wave vector $\vec{k}$, $E \times B$ drift velocity must be much smaller than thermal velocity, the perturbed density (n_1) and magnetic field (B_1) must be much smaller than their equilibrium values noted with subscripted 0 and the Larmor radius ρ_L is much larger than the reference length, usually minor machine radius. For microturbulence, as described earlier, these conditions usually hold, making the GK model well-suited for its description. In GK, the particle trajectory is separated into guiding centre motion and the gyroradius, forming the basis of the model.

The transition from a kinetic to a gyrokinetic model involves a change of coordinate system. In Cartesian coordinates, the gyrating motion around the magnetic field line is represented across all three axes, making the system more complex to analyse. By changing the coordinate system, it becomes easier to evolve the system while effectively simplifying the description by "averaging out" one of the axes. This is achieved by aligning the velocity coordinate system with the magnetic field.

In the new coordinate system, one coordinate, $\vec{v}_\parallel$, represents the velocity component along the magnetic field line. The second coordinate corresponds to the size of the gyroradius, which reflects the perpendicular velocity, $v_\perp$. Alternatively, the perpendicular velocity can also be represented using the magnetic moment $\mu = mv^2/2B$ as the second axis. This approach has the advantage of conserving the magnetic moment in slowly varying magnetic fields, which can further simplify the model. Finally, the third coordinate is the gyrophase θ, which describes the angle within the circular motion in the gyroradius. Since the motion of the particle in the gyrophase is very rapid, it is averaged out and θ is effectively ignored. This transformation is effectively a cylindrical coordinate system that follows the magnetic field line. It enables a more efficient and focused study of plasma

behaviour by filtering out fast gyration effects. By neglecting the gyrophase and assuming the magnetic moment remains constant, we derive a simplified form of the Vlasov equation in this new coordinate system, which is:

$$\frac{dF}{dt} + \frac{d\vec{x}}{dt} \cdot \nabla F + \frac{dv_{\parallel}}{dt} \frac{\partial F}{\partial v_{\parallel}} = 0 \qquad (2.86)$$

where F is the new distribution function, and $\vec{x}$ represents the position in three spatial coordinates. This formulation leverages the new coordinates aligned with the magnetic field and incorporates the reduced complexity due to the ignored gyrophase, reducing the problem from 6 to 5 dimensions.

The gyrokinetic approach reaches its limits of validity if the electric and magnetic fields are changing rapidly and disturbing the gyromotion. Special care is also required when incorporating Maxwell's equations, as electromagnetic effects challenge this guiding centre approximation.

To discuss the limitations of gyrokinetics in the pedestal, we focus on the last term in equation 2.85, and consider the reference length L_{ref} to be the gradient length for parameters like T_e, T_i, or n, where the gradient length of x is defined as $x/\nabla x$. Since the gradients in the pedestal are typically steeper, this reference length becomes smaller. In this context, we are primarily concerned with ions because, due to the mass difference, the ion gyroradius (ρ_i) is larger than the electron gyroradius (ρ_e), which remains quite small. For ions, ρ_i/L_{T_i} can reach higher values. While this is still small, there is some debate about whether it is sufficiently small for the assumptions to hold in the presence of large structures. In this thesis, particularly in chapter 7, where we present results from gyrokinetic simulations, we assume that ρ_i/L_{T_i} is sufficiently small to justify the validity of the mode, and allows us to make qualitative comparisons between different shapes within a single discharge.

Another important element to the discussion is that, so far, collisions were not included. Their re-introduction is especially important in the pedestal, where the temperature sinks and the collisions are much more frequent. The collisions are also important for several reasons. Firstly, they provide a mechanism for dissipation so that the finite turbulence can reach a steady state where their exploration is meaningful. Another reason is including any kind of neoclassical effect, which rely on existence of collisions. To address these issues, there is usually a collision operator that is introduced to the right side of the equation (2.11).

2.2.4 Codes

GENE

To perform the gyrokinetic simulations presented in this thesis, the GENE code (Gyrokinetic Electromagnetic Numerical Experiment) [71] was used. Specifically, the local linear version of GENE was employed, as advanced non-linear and global simulations are beyond my expertise. While a detailed theoretical exploration is outside the scope of this work, some brief context is provided.

GENE is primarily used to simulate microturbulence in plasmas and has been continuously developed since around 2000, incorporating many features over time. The linear version of GENE, is typically applied to identify the fastest-growing instabilities. In this work, simulations were performed in a local flux-tube geometry. In this setup, the temperature, density, and their gradients are constant along the radial direction within the tube. Although this approach has its limitations, it is significantly less compu-

tationally intensive than global or non-linear simulations, which require much more computational time, and definitely more expertise.

GENE can simulate either electrostatic turbulence, where only the electric potential fluctuates, or electromagnetic turbulence, where both electric and magnetic potentials fluctuate. It operates in straight-field line coordinates, where the radial coordinate is defined based on toroidal flux, the modified poloidal angle represents a straight field line angle, and the toroidal angle is the standard angular coordinate. More practical coordinates used in GENE include the radial coordinate, typically identified with the toroidal flux, the parallel coordinate corresponding to the modified poloidal angle, and the binormal coordinate.

Important equilibrium parameters include the safety factor, which represents the ratio of toroidal to poloidal magnetic field line rotations, and the magnetic shear, which characterises the variation of the safety factor. GENE incorporates magnetic shear locally, since it is following the magnetic field lines. To account for collisions, GENE can incorporate various collision operators. The standard choice is the Landau operator, but more refined options are available, including those that account for finite Larmor radius effects.

The workflow in this thesis involved preparing ion and electron temperatures and densities, as well as the total equilibrium configuration. Simulations were configured to scan over the binormal wave number k_y to calculate growth rates. Two species, ions and electrons, were included, with most other parameters set to their default values. Simulations were then executed to determine growth rates, followed by the application of quasilinear models to estimate fluxes based on the simulation results.

ASTRA

To calculate plasma transport and compare it with the gyrokinetic simulations, the ASTRA code is used (Automated System for TRansport Analysis).

ASTRA is a flexible and modular 1.5D transport code, in which equilibrium is treated in 2D, while the plasma profiles are given as 1D functions of poloidal flux surfaces.

In this thesis, the following profiles were used as inputs for ASTRA: electron density (n_e), electron temperature (T_e), ion temperature (T_i), and ion density (n_i), which was calculated from the effective charge (Z_{eff}). Additionally, equilibrium quantities and information were provided. The input power profiles represent the heating power deposited into the plasma.

The heating systems will be discussed in detail in section 3.1.1. As will be demonstrated in chapters 4 and 7, for the discharges where ASTRA was applied, neutral beam heating was employed, with the RABBIT code [80] used to interpret the power input from the neutral beam. Similarly, TORIC [81] was used to calculate the profile of the ion cyclotron heating power deposition.

With these inputs, ASTRA computes the profiles of heat transport coefficients for ions (χ_i) and electrons (χ_e) as well as the effective particle diffusivity (D_{eff}), which will be explored further in this work.

2.3 Multifaceted understanding of the pedestal

Here is our current understanding of the pedestal in the context of the theoretical background discussed in this chapter. When sufficient power is introduced into the plasma, it transitions from low confinement mode (L-mode) to high confinement mode (H-mode), as sketched in figure 1.7. The exact mechanisms behind this transition have been a subject of study for over three decades due to the intricate processes occurring within the pedestal region.

One widely accepted model proposes that a radial electric field (E_r) forms in the pedestal, generating an $E \times B$ shear. This shear distorts and elongates turbulent eddies (figure 1.6), significantly reducing their transport and allowing the pressure gradient in the pedestal to steepen. Importantly, E_r itself depends on the pressure gradient — an increased ∇p leads to a stronger E_r, which enhances the shear, further reducing transport, and allowing ∇p to grow even more. Additionally, E_r is influenced by plasma rotation, which can modify it and, consequently, impact the pedestal structure.

Despite this reduction in turbulent transport, some losses of energy and particles remain. There is still neoclassical transport, microturbulence, and larger MHD instabilities. Plasma inherently always resists confinement to some degree. Eventually, when the gradients become too steep and store excessive energy, MHD instabilities trigger a collapse, resulting in an edge-localized mode (ELM). However, there are ELM-free regimes where mechanisms exist to prevent gradient growth from reaching the point of collapse. These regimes either actively limit the gradients or extend the tolerance of the plasma to higher gradients through stabilising effects.

Understanding the pedestal remains a key area of research, as many questions remain unanswered, and current models, while reasonably effective, are not completely precise. The pedestal is critical for future fusion devices, as it plays a central role in determining overall confinement and performance. To optimise and control it, we need to refine our models and reduce uncertainties. As it stands, our understanding is still broad and lacks the fine detail necessary for accurate predictions.

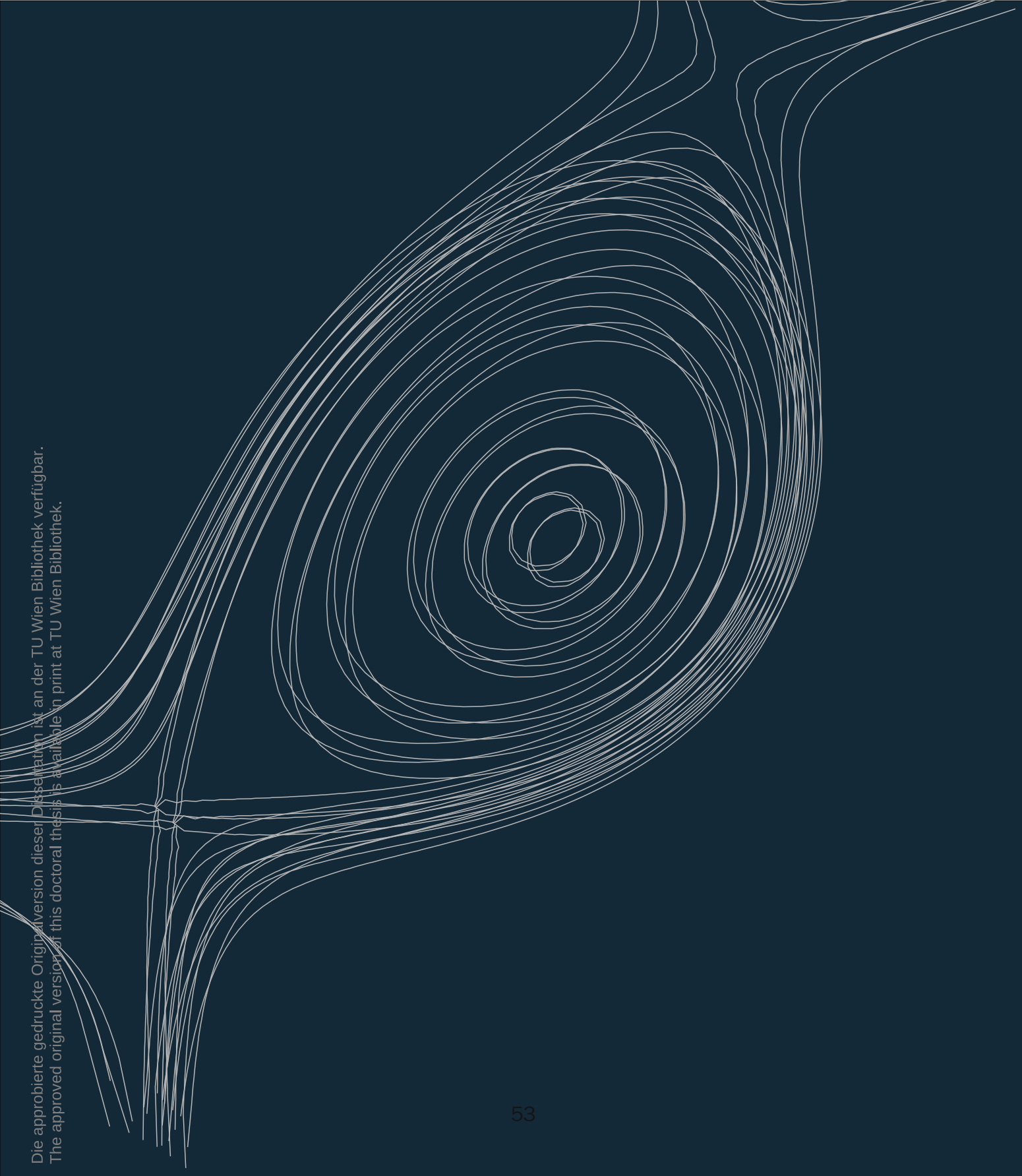

53

EXPERIMENTAL FRAMEWORK

3 Experimental Framework

The experiments in this thesis were performed on ASDEX Upgrade. This section gives a summary of the reactor properties, its available diagnostics and heating systems, and finally, a detailed overview of the experiment design will be presented.

3.1 ASDEX Upgrade

Overview

As previously summarised in the introduction, ASDEX Upgrade is a tokamak-type research fusion reactor that is operated at the Max Planck Institute for Plasma Physics in Garching, Germany since 1991 [82, 83]. An overview of typical plasma parameters is given in table 3.1.

ASDEX Upgrade (AUG) is equipped with multiple heating systems, exceptional plasma control capabilities, and numerous complementary advanced diagnostics, making it a great facility for plasma research. The heating systems provide a total of 27 MW of power, including 1 MW of ohmic heating, 20 MW of neutral beam injection, and about 10 MW of wave heating. Plasma fuelling is achieved through two primary methods: gas puffing, which predominantly fuels the plasma edge, and the injection of frozen pellets, effectively delivering fuel to the plasma core. A wide range of plasma scenarios are studied at AUG.

Property	Value
Total height	9 m
Total radius over all	5 m
Weight of the experiment	800 t
Material of the first wall	tungsten
No. of toroidal field coils	16
No. of poloidal field coils	12
Max. magnetic field	3.1 T
Max. plasma current	1.6 MA
Pulse duration	<10 s
Time between pulses	15 - 20 min
Amount of data / pulse	≈40 GByte
Max. Plasma heating	27 MW
Major plasma radius R_0	1.65 m
Minor plasma radius a	0.5 m
Plasma fuels	D, H, He
Plasma volume	14 m^3
Plasma mass	3 mg
Electron density	10^{20} m^{-3}
Max. plasma temperature	10^8 degrees

Table 3.1: Technical details of the experiment and typical parameters. Information summarised from ASDEX Upgrade internal website.

3.1.1 Heating systems

The plasma is heated using several systems that together can deliver up to 27 MW of power. The most fundamental of these is ohmic heating, which is intrinsic to the

plasma because of its finite conductivity. Beyond this, additional active heating methods are employed in the experiments, which are outlined and briefly explained below.

Electron Cyclotron Resonance Heating (ECRH):

Electron wave heating with ECRH [84–86] delivers power into the plasma via electromagnetic waves tuned to frequencies equal to harmonics of the electron cyclotron frequency, $\omega_e = \frac{eB}{m_e}$ (see section 2). At the resonant frequency, the wave energy is absorbed by electrons, and through collisions, this energy is transferred to ions. The efficiency of this transfer depends on different plasma conditions.

On ASDEX Upgrade, these microwaves are generated by eight gyrotrons, each capable of producing beams with a heating power of up to 1 MW. Since the resonant frequency depends on the magnetic field, which varies spatially, ECRH enables precise, localized energy deposition rather than uniform heating throughout the plasma. The gyrotrons are located outside the tokamak, and the waves are transmitted to the plasma using a system of waveguides and mirrors, which offers flexible control, allowing targeted heating. The microwaves operate at either 105 GHz or 130 GHz and have a beam diameter of several centimetres.

Ion Cyclotron Resonance Heating (ICRH):

ICRH [87–89] operates similarly to ECRH, using electromagnetic waves, but at the ion cyclotron frequency, $\omega_c = \frac{ZeB}{m_i}$. These waves are slower, with frequencies in the MHz range, and larger, with wavelengths around 1 m. Unlike ECRH, the antennas of ICRH must be placed inside the tokamak vessel. Four antennas are installed, collectively capable of delivering up to 6 MW of heating power. However, placing the antennas close to the plasma introduces challenges. Electric fields generated near the antennas can lead to tungsten deposition in the plasma, which can negatively impact performance [90]. Optimizing the antenna design and placement is crucial to mitigate these effects.

Neutral Beam Injection (NBI):

NBI [91, 92] works as follows: First, positive deuterium ions (D^+) are accelerated to high speeds using a strong electric field. These high-energy ions are then passed through a chamber filled with neutral deuterium gas. As the D^+ ions travel through this chamber, they undergo charge exchange, picking up electrons and becoming neutral deuterium atoms. This process creates a neutral beam of fast deuterium atoms, which is then injected into the tokamak vessel and directed toward the plasma.

Inside the tokamak, the strong magnetic field confines only charged particles, which means that neutral atoms in the beam can penetrate the plasma. Once in the plasma, the fast neutral atoms collide with plasma ions, undergoing a second charge exchange. During this interaction, the neutral atoms lose an electron to a slower plasma ion, which itself becomes neutral and is subsequently lost from the plasma as it is no longer confined by the magnetic field. The energetic ions from the neutral beam then thermalise through collisions, effectively transferring their energy to the plasma and heating it.

On ASDEX Upgrade, NBI delivers the main amount of heating. It has 8 beams, each delivering 2.5 MW of heating power. They are oriented in different ways, where 2 are aligned radially and referred to as on-axis and 4 are aligned tangentially, and therefore called off-axis, which can be used to vary the amount of external torque added

to the plasma.

The NBI system offers highly flexible beams that can be switched on and off within milliseconds, enabling two critical functions for this thesis. Firstly, it plays a pivotal role in fine-tuning β_{pol} feedback control. This is achieved by rapidly adapting the total plasma pressure in response to changes in confinement and magnetic pressure, using the flexibility of the NBI to adjust the integrated ion temperature, and consequently the total pressure.

Secondly, NBI is needed for charge exchange diagnostics, which will be discussed in detail in the following pages. In cases where heating from the NBI is not desired, short "blips" or brief NBI pulses on the order of 10 ms can be used solely to generate the signals required for charge exchange recombination spectroscopy (CXRS). Thus, NBI not only serves as a strong heating tool but also proves to be highly versatile in its applications in experiment design.

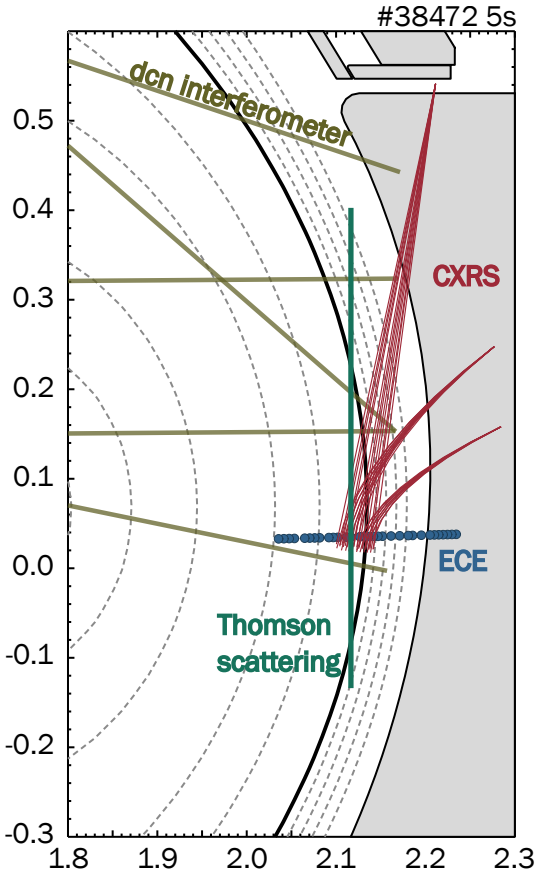

Figure 3.1: Diagnostic systems used to measure ion and electron temperature and density. Deuterium Cyanide Laser Interferometry (DCN) interferometer is shown in green, Charge Exchange Recombination Spectroscopy (CXRS) in red, Electron Cyclotron Emission (ECE) is depicted as blue circles and the edge Thomson Scattering (TS) laser as the brown line.

3.1.2 Utilised Diagnostics

The plasma edge diagnostics that were used in this work are shown in figure 3.1, and more physical principles and technical details are given in the following.

Thomson Scattering (TS) (n_e, T_e)

When a laser beam passes through the plasma, the electromagnetic field of the light accelerates charged particles, causing them to emit electromagnetic waves of the same frequency at different angles — a process known as Thomson Scattering (TS). The thermal motion of electrons induces Doppler[1] broadening in the scattered light spectrum, which provides a measure of the electron temperature, while the radiation intensity is proportional to the electron density.

At ASDEX Upgrade, two TS systems are employed [93, 94], one in the core and one at the edge. The core system has four and the edge system 6 Nd-YAG lasers with a wavelength of 1064 nm and a repetition rate of 20 Hz, so that time-resolution is 80 Hz and 120 Hz for core and edge respectively. The spatial resolution of TS is

[1] Christian Doppler is one of the most famous alumni of TU Wien. More random information I discovered while fact-checking this: so is Josef Strauss (composer, also son of Johann Strauss), Rudolf Steiner (occultist) and Fritz Lang (director of the 1927 film *Metropolis*). What an eccentric company to be in.

25mm in the core and 3mm in the edge. The scattered light is captured by an optical system and directed to polychromators, where the electron density and temperature are resolved.

Electron Cyclotron Emission (ECE) (T_e)

When electrons gyrate around magnetic field lines in the plasma, they emit microwave radiation. The frequency of this gyration depends on the magnetic field strength, which varies inversely with the radial distance R. This relationship allows for radial determination of the electron temperature. In high-density regions where the plasma is optically thick, the emitted radiation is fully reabsorbed, behaving like blackbody radiation. The electron temperature in these regions can be calculated using the Rayleigh-Jeans law:

$$T_e = \frac{8\pi^2 c^2}{k_B \omega_c^2} I \qquad (3.1)$$

where c is the speed of light, ω_c is the angular frequency of the electron gyration, and I is the intensity of the blackbody radiation.

Near the plasma edge, however, the density is lower, and the plasma becomes optically thin. Here, the relationship between radiation intensity and electron temperature becomes more complex. In such cases, forward modelling of electron cyclotron radiation is used. This approach relies on modelling radiation transport and having an accurate knowledge of the plasma density profile [95, 96]. The ECE system on AUG consists of 60 channels, that sample at a very fast rate of 1 MHz, with a spatial resolution of 5 mm.

Deuterium Cyanide Laser Interferometry (DCN) (n_e)

Interferometry measures the refractive effects of plasma on light, causing a phase shift described by:

$$\varphi = \lambda_0 r_e \int_0^L n_e(x)\, dx \qquad (3.2)$$

where λ_0 is the laser wavelength in vacuum, r_e is the classical electron radius, and $n_e(x)$ is the electron density along the beam path L. The phase shift is determined by comparing the beam passing through the plasma with a reference beam in vacuum. Since absolute phase differences cannot be directly measured, multiples of 2π must be tracked and accounted for. Sudden changes in local density can disrupt this count, leading to fringe jumps, which are corrected by cross-referencing with other diagnostics.

On ASDEX Upgrade, a DCN laser with a wavelength of 195 µm is used, sending five beams through the plasma at different radial positions.

Charge Exchange Recombination Spectroscopy (CXRS) (T_i, Z_{eff})

CXRS is a diagnostic technique used to measure ion temperature (T_i), rotation velocity (v_{rot}), and ion density (n_i). A neutral beam, most commonly consisting of D^0 atoms, is injected into the plasma from the NBI heating source. These neutral atoms undergo charge exchange with ions already present in the plasma. During this process, the D^0 atoms lose an electron, while the plasma ions become (partially) neutralized and initially in an excited state, subsequently emitting light.

From the Doppler broadening of spectral lines, the random motion of ions can be deduced, providing a measurement of ion temperature. The Doppler shift of these lines gives the rotation velocity, while the intensity of the emitted light is used to estimate the ion density.

The light emitted from the main ions could provide key data for analysis of the

plasma. However, due to the NBI beam halo and significant radiation from the main ions, the noise coming from the charge exchange reaction with D^+ is too high and the post-processing of the data very complex. Because of this, the focus is placed on light emitted by impurity ions instead.

Temperature equalisation between impurity and main ions occurs rapidly through collisions, so we can assume that both species have the same temperature. Impurity ions are also assumed to be generally carried along with the main ions, resulting in comparable velocities. However, due to their higher charge Z, impurity ions experience greater friction, requiring additional calculations and corrections to accurately derive the main ion velocity.

In contrast, the densities of impurity and main ions differ significantly and cannot be assumed to be similar. Nevertheless, the principle of quasi-neutrality ensures that if the composition and concentration of impurities are known, the main ion density can be determined indirectly by calculating the effective charge Z_{eff} as

$$Z_{eff} = \frac{\sum_a n_a Z_a^2}{n_e} \tag{3.3}$$

where *a* represents an impurity species. If we assume that there is only one impurity species that is present in a considerable amount in a hydrogen isotope plasma, we can calculate the main ion density as:

$$n_i = \frac{Z_{eff} - Z_a}{1 - Z_a}. \tag{3.4}$$

Acquiring high-quality CXRS data sometimes requires the deliberate introduction of impurity species into the plasma, depending on the machine conditions and plasma discharge settings. This is not needed if the discharges are performed shortly after boronisation, such was the case for the experiments in this thesis. In boronisation, a plasma vapour deposition of a thin boron film on the first wall suppresses impurities (oxygen, carbon, and metals) and reduces hydrogen recycling, enhancing tokamak discharge performance. This also means that the main impurity species is boron, so no additional impurity puffs are needed.

Different NBI beams are used in the CXRS systems. There are three core and one edge system. The core systems, with a radial resolution of 2.5 cm, typically operate with a 10 ms integration time, though values as low as 3.5 ms are achievable [97]. The edge system measures with faster integration times, down to 1.9 ms and higher radial resolution, of about 5 mm [98]. To enhance the radial coverage of edge measurements, a radial sweep of the plasma edge through the line of sight, known as a R_{aus} scan, is employed.

It has now become clear that CXRS delivers us information about impurity temperature, density, and both poloidal and toroidal rotation. These measurements are significant because together, they provide all the inputs needed to self-consistently calculate the radial electric field E_r, using equation 2.41[99]. This calculation, performed as part of this thesis, is an important step in studying the plasma edge physics.

Profile Alignment and Integrated Data Analysis (IDA)

The analysis of pedestal measurements involves multiple diagnostics, each measuring different quantities. While this provides a lot of information, the edge region of the pedestal is an extremely narrow zone, requiring careful alignment of the profiles obtained from different diagnostics to ensure physical consistency. Combining complementary data enhances confidence in the measurements and increases both temporal and spatial resolution, which is

particularly critical in the pedestal, since in real space, it is only 1-2 cm wide. Additionally, since different diagnostics measure at varying locations, it is necessary to map all measurements onto a common radial coordinate ρ_{pol} before proceeding. This mapping, however, introduces uncertainties that must be corrected.

The first step in this process is determining the position of the separatrix. This is based on power balance and parallel heat transport, using a one-dimensional heat conduction model and the maximum parallel heat flux in the divertor [100, 101]. In ELMy H-Mode discharges, the separatrix is identified as the location where $T_e \approx 100\,eV$. With this definition, the edge Thomson scattering system, which measures both T_e and n_e, is aligned to this value.

Next, ECE measurements are matched to the same separatrix position, although this alignment is typically satisfactory by default. Other diagnostics measuring n_e are subsequently aligned to the edge Thomson system. For ions and electrons, alignment is achieved by shifting CXRS data so that the locations of the maximum temperature gradients of T_i and T_e coincide. Finally, the alignment process concludes with ensuring consistency among different CXRS systems.

A key tool used to combine the measurements is Integrated Data Analysis IDA [102], which operates based on Bayesian probability theory. This approach is applied to the diagnostics of electron-related measurements, including Lithium Beam Emission Spectroscopy (not used in this thesis, due to temporary unavailability), DCN, TS, ECE. By simultaneously incorporating all four diagnostics, IDA estimates T_e and n_e while accounting for interdependencies that correlate density and temperature. This comprehensive integration significantly enhances the quality and reliability of the analysis, providing a unified and robust dataset. Similarly, Gaussian process regression is applied to estimate ion temperature and angular velocity from the measured data using Integrated Data Analysis Ions (IDI).

3.1.3 Equilibrium Reconstruction and Plasma Shape

Equilibrium reconstruction is fundamentally based on magnetohydrodynamics (MHD). By balancing the forces arising from the plasma pressure gradient, ∇p, and the $\vec{j} \times \vec{B}$ force, the Grad-Shafranov equation (equation 2.34) is derived. This partial differential equation describes the equilibrium and must be solved in two dimensions to resolve the poloidal cross-section of plasma flux surfaces. While analytic solutions to the Grad-Shafranov equation exist for only a few specific cases, numerical methods are required for general scenarios.

At ASDEX Upgrade, the interpretive equilibrium solver CLISTE is commonly employed [103, 104]. It utilizes inputs such as control coil currents, magnetic flux loop measurements, and poloidal magnetic field data. Additional constraints, including the safety factor q, pressure profiles, can also be incorporated into the reconstruction process in a post-processing routine. Performing equilibrium reconstructions independently for each time point can sometimes introduce discontinuities in physical quantities, leading to non-physical behaviour.

To address this issue, smoothing terms can be applied, or alternatively, the Grad-Shafranov solver can be coupled with a current diffusion solver, as implemented in the Integrated Data Analysis Equilibrium (IDE) framework [105]. IDE combines recon-

structed pressure profiles, magnetic measurements, and calculated current densities to refine the equilibrium reconstruction. By leveraging this coupling, IDE mitigates discontinuities and ensures more physically consistent equilibrium profiles.

The equilibrium is not only significant when it is reconstructed, but also plays a crucial role in plasma control. At ASDEX Upgrade, 12 vertical field coils are employed to regulate the plasma position and guide its shape. These coils enable precise adjustments, effectively allowing the plasma to be shaped according to specific requirements. A summary of the different plasma shape parameters is provided in figure 3.2. We roughly characterise plasma shape using the geometric and magnetic axis, as well as its height and width to construct useful parameters such as elongation $\kappa = b/a$, and upper and lower triangularity ($\delta_u = d^u/a$ and $\delta_l = d^l/a$) as sketched in figure 3.2. When the plasma has high values of κ and δ we say that it has *strong shaping*.

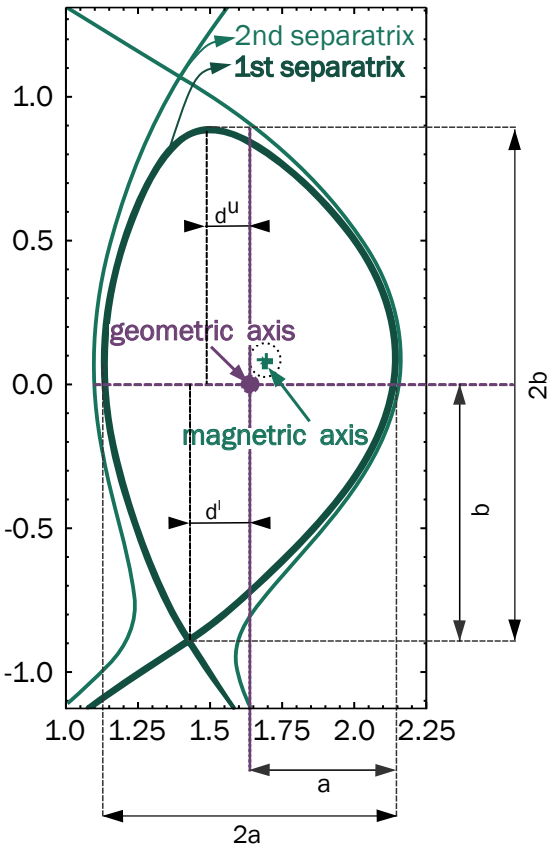

Figure 3.2: Geometric specifications of 2D plasma cross-section. Plasma elongation is calculated as $\kappa = b/a$, and upper and lower triangularity as $\delta_u = d^u/a$ and $\delta_l = d^l/a$

3.2 Experiment Design

The experimental results shown in this chapter are in the revision process in the Nuclear Fusion journal.

In this thesis, the aim is to use versatile lenses to analyse several physical parameters that determine the pedestal structure. Initially, the focus was on the pedestal width; however, it became evident that additional questions regarding the overall structure needed to be addressed. One key factor influencing the pedestal structure is the interplay between β_{pol} and plasma shape. To investigate this, we designed three dedicated experiments. Each experiment was conducted at a different constant β_{pol}, and for each discharge, two distinct plasma shapes—kept consistent across all discharges—were implemented.

Three AUG discharges are compared in the studies: #38472, #38474, and #38819, and their overall properties are listed in table 3.2. All three discharges have a plasma current I_p of 800 kA in type-I ELMy H-mode. The magnetic field varies slightly, being -2.5 T for #38472 and #38474, and -2.7 T for #38819. The heating changes are due to the β_{pol} feedback, with NBI ranging from 2 to 10 MW; #38472 and #38819 are additionally heated with 2 MW ion cyclotron resonance heating, while #38474 is heated with 3.7 MW electron cyclotron resonance heating. The safety factor at 95% of the

Table 3.2: Plasma properties overview

discharge #	β_{pol}	β_N	I_P	B_T	NBI	ICRH	ECRH	q_{95}
#38472	1.35	1.95	800kA	-2.5T	4-10MW	2MW	/	5.1-5.6
#38474	1.1–1.15	1.6	800kA	-2.5T	2.4-5MW	/	3.7MW	5.1-5.6
#38819	1	1.3	800kA	-2.7T	2-7MW	2MW	/	5.5-6

normalised flux ψ_N, q_{95}, has relatively similar values, ranging from 5.1 in the low triangularity phase to 6 in the high triangularity phase. All discharges are fuelled with $8 \cdot 10^{21} s^{-1}$ of deuterium gas puff.

The plasma shape is known to substantially affect the pedestal structure [106–109]. It is commonly observed that increasing plasma shaping enhances its global peeling-ballooning MHD stability limit toward higher pressure gradients, thus allowing for higher pedestal top values. This effect is further explored, also analysing the impact of the plasma shape on the local ideal ballooning modes (IBMs). By varying the upper triangularity δ_{up} and elongation κ, the local magnetic shear changes, and therefore the stabilisation of the local IBMs is influenced. The implications for the pedestal width are studied by conducting discharges in which two time-windows with different plasma shapes are analysed. In each of the three discharges, at 4 s, a shape transition occurs from lower shaping ($\delta_{up} = 0.1$, $\kappa = 1.6$) to higher shaping ($\delta_{up} = 0.25$, $\kappa = 1.7$), as illustrated in figure 3.3a.

The normalised plasma pressure, β_{pol}, is thought to be a key factor influencing the width of the pedestal [30, 110–112]. To investigate this property, each discharge is configured to maintain a distinct fixed value of β_{pol}. This is accomplished through the use of β_{pol} feedback, which utilises the flexible neutral beam injection (NBI) heating system to dynamically adjust the total plasma pressure in response to changes in magnetic pressure and confinement, thereby ensuring a constant β_{pol}. Even though the total plasma pressure remains stable, the pedestal characteristics can exhibit considerable variability, as will be illustrated in the subsequent analysis.

The values of β_{pol} across the discharges are established as follows: #38472 features a high β_{pol} of 1.35, #38474 has a medium β_{pol} of 1.15, and #38819 corresponds to a low β_{pol} of 1.0, with the measured results depicted in figure 3.3b. While the feedback mechanism functioned effectively in both the low and high β scenarios, discharge #38474 presents slight variations in β_{pol} between the two phases; nonetheless, both values remain within the medium range.

3.3 Workflow

In chapter 4, the experimental results of this thesis will be shown, including kinetic plasma profiles, some equilibrium quantities and the radial electric field. The workflow begins with the measurement of plasma parameters, including electron density n_e obtained through deuterium cyanide laser interferometry (DCN), and Thomson scattering (TS), electron temperature (T_e) measured via Thomson scattering and electron cyclotron emission spectroscopy (ECE),

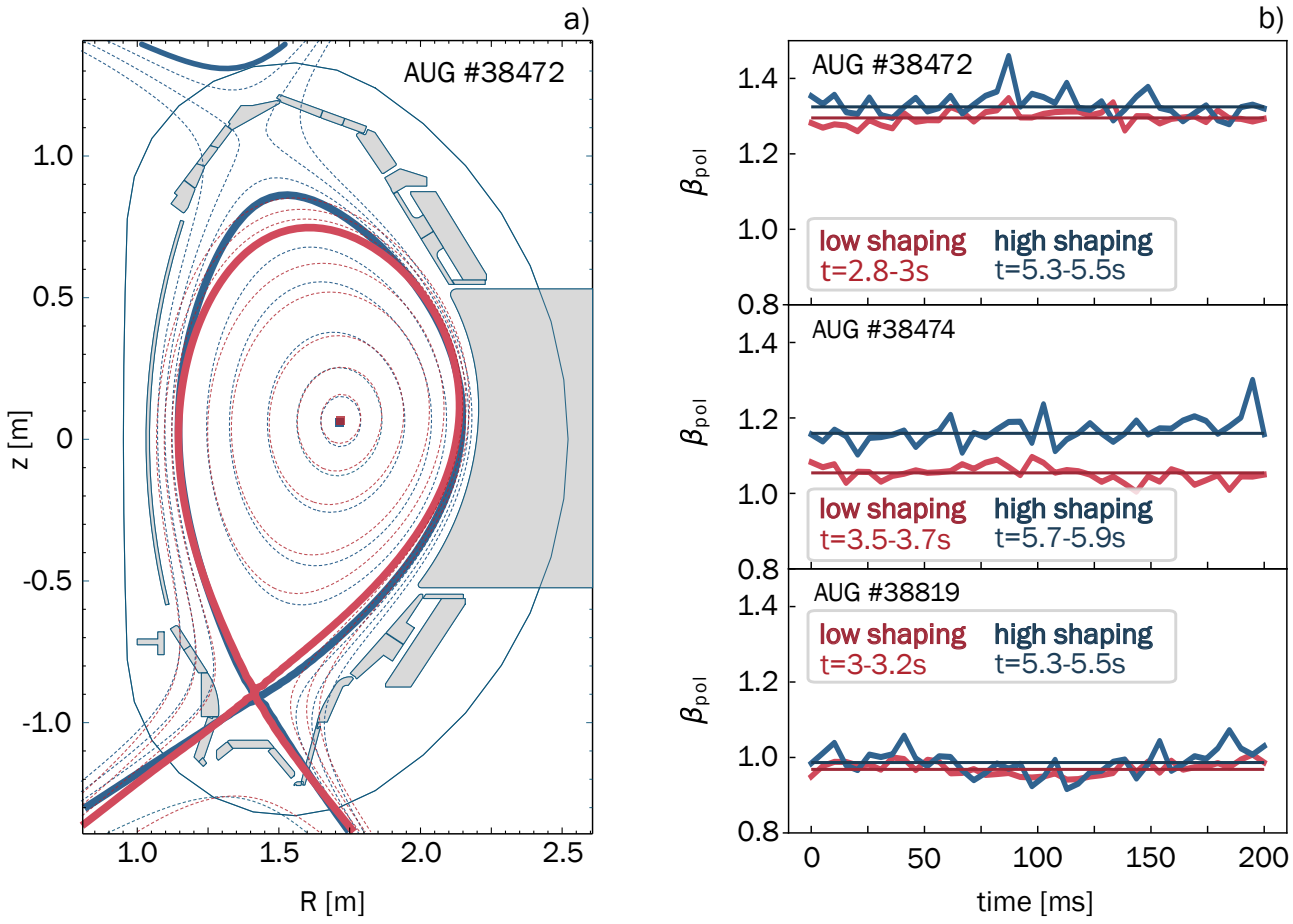

Figure 3.3: Experimental setup for the three analysed ASDEX Upgrade discharges: a) Cross-section of the plasma illustrating the shape variation for each discharge, where red lines correspond to the low shaping phases and blue lines to the high shaping phases. b) Variation of β_{pol} across the 200 ms time windows, displayed in descending order, with the horizontal line indicating the median value for each window.

and ion temperature (T_i) determined using charge exchange recombination spectroscopy (CXRS). The ion density is derived from n_e and the effective charge number (Z_{eff}). The quantities are mapped on the available real-time CLISTE equilibrium.

These physical parameters are then incorporated into a forward model using Bayesian probability theory within the framework of IDA/IDI. Next, in IDE the equilibrium is reconstructed, coupled with the flux diffusion equation and using the previously fitted profiles. Additionally, the value of local magnetic shear s_{loc}, that will be important in the 5th, the 6th and the 7th chapter, is evaluated in 2D using the results from IDE. The profiles and equilibria are estimated with a temporal resolution of 5 ms. Each analysed time window lasts 200 ms and the time windows of the discharge are chosen so that all diagnostics deliver optimal quality data. The discharges performed in this thesis are all type-I ELMy H-Mode, with ELM frequency ranging from 100Hz to 200Hz. Because of this, the profiles and equilibria that are strongly affected by an ELM - 1 ms before 3 ms after the ELM onset - are filtered out. After ELM filtering, the

median of the profiles is taken, and in the results presented in the following analyses, if not stated differently, the full line represents the median and the shaded area the 90% quantile.

In this analysis, the focus lies on the pedestal and for this purpose we distinguish between several distinct regions: the last closed flux surface *separatrix*; the *pedestal foot*, located just inside the separatrix, typically within the range $0.99 < \rho_{pol} < 1$; the *pedestal middle*, representing the steep gradient region, typically in the range $0.975 < \rho_{pol} < 0.99$; the *pedestal top*, identified as the radial position of the "knee" of the pedestal, generally around $0.965 < \rho_{pol} < 0.975$; and the *outer core*, which refers to the flat gradient region, typically at $\rho_{pol} < 0.96$.

From the CXRS measurements, the radial electric field E_r is self-consistently calculated and mapped on the IDE equilibrium. The reconstructed E_r profiles are binned according to the selected time windows, excluding the phases immediately following an ELM crash. The remaining data is then fitted using a Gaussian process fit.

In chapter 5, the MHD analysis of the discharges will be presented. IDE provides input for the HELENA code [50], including the pressure gradient along the normalised flux, $dp/d\psi_N$, the diamagnetic profile, $F\,dF/d\psi_N$, where $F = RB_T$, and the last closed flux surface, taken at $\psi_N = 0.997$, defining the plasma boundary. Using this input, HELENA solves the Grad-Shafranov equation to reconstruct the equilibrium with high resolution. It also solves the $n \rightarrow \infty$ ideal ballooning stability of the plasma. Next, the MISHKA code [113] is used to calculate the global peeling - ballooning stability.

In chapter 6 a large part of this MHD analysis is repeated, but this time with input data that has been ELM-synchronised so that instead of taking an inter-ELM average, such, as done in chapter 5, the whole inter-ELM dynamics is captured.

Chapter 7 focuses on gyrokinetic simulations and transport analysis. Here, IDA profiles and IDE equilibrium were used as input for GENE [71]. Kinetic profiles, reconstructed with IDA and Z_{eff} from CXRS are used as inputs for ASTRA [114], which delivers information about transport coefficients for electron and ion heat and particle diffusion and anomalous transport.

The workflow is schematically illustrated in figure 3.4. I marked each step I performed myself with a green filled rectangle to give an overview but also reflect my sense of accomplishment in the numerous skills I have acquired while working on this thesis, ranging from diagnostics shifts to MHD and gyrokinetic simulations. Of course, this knowledge and expertise did not come out of nowhere — next to each green rectangle, I have noted the names of people who generously provided me the codes and scripts, guided me through the process, gave input and clarified many questions that arose[2].

[2] It's not about the data, it's about the friends we made along the way.

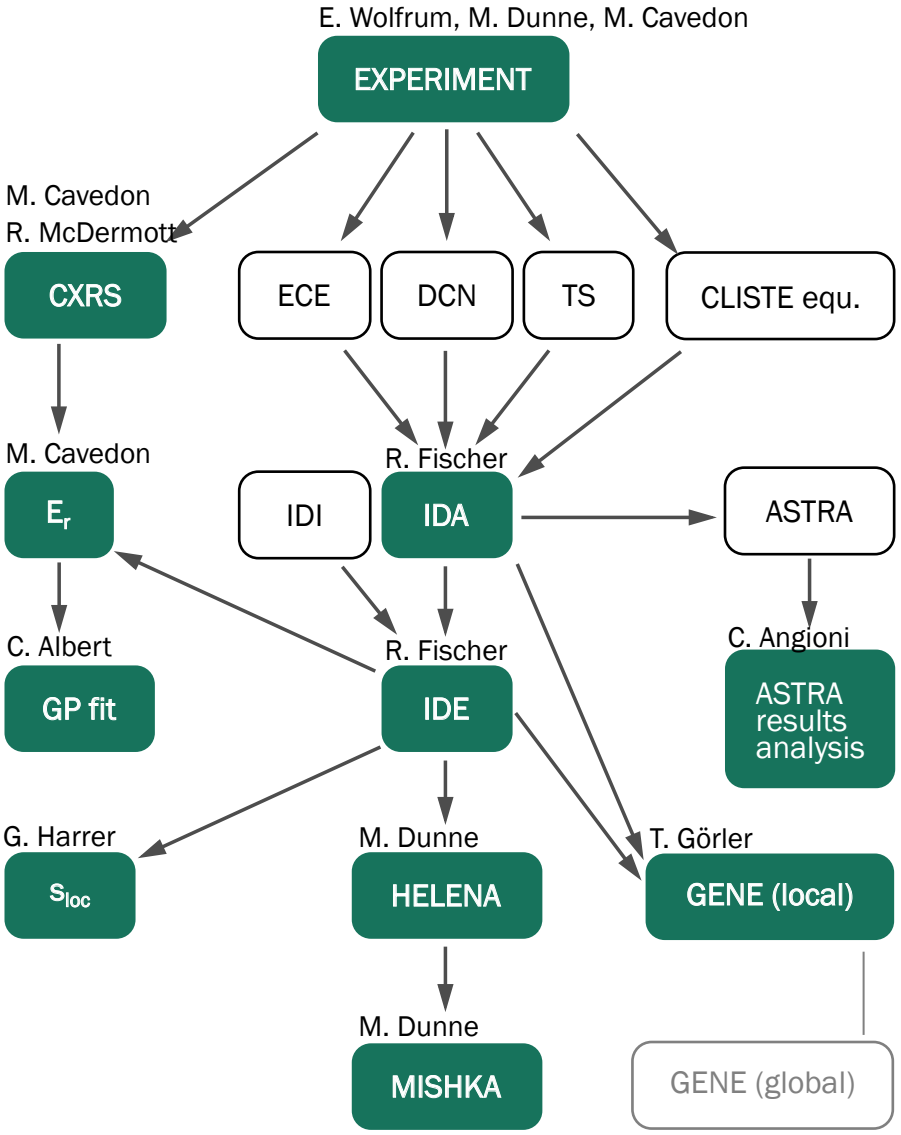

Figure 3.4: Workflow overview. Green rectangles show the steps of the analysis I performed in the framework of this thesis, and white rectangles some (however incomplete) additional steps carried out by the ASDEX Upgrade team, whose kind support made this work possible.

EXPERIMENTAL RESULTS

4 Experimental Results

The experimental results shown in this chapter are in the revision process in the Nuclear Fusion journal.

4.1 Discharge Overview

The first step after the experiment is to examine the time traces of various quantities, as shown in figures 4.1-4.3. In panel a), the plasma current I_p (purple, left scale) and the toroidal magnetic field B_t (green, right scale) are plotted. These traces show a ramp-up phase in I_p until 1.5 s, while B_t remains constant across all discharges. Panel b) shows heating power contributions, including NBI power P_{NBI} (green), ohmic heating P_{OH} (yellow), and figures 4.1 and 4.3 include ICRH power P_{ICRH} (purple), while figure 4.2 includes ECRH power P_{ECRH} (purple), all in MW. Additionally, radiative power P_{rad} is plotted in gray. In each figure, panel c) shows density measurements from DCN diagnostics, with core density in green and edge density in purple. In panel d), β_N (green), β_p (purple), and the confined MHD energy W_{MHD} (yellow) are depicted. Finally, panel (e) includes elongation k (green), the safety factor q at $\psi_n = 0.95$ (purple, scaled by -10 for better visualization), and the upper triangularity δ_{up} (yellow), the primary quantity intentionally varied. The scale for δ_{up} is shown on the right y-axis.

For discharge #38472 in figure 4.1, we select the time intervals 2.8–3.0 s and 5.3–5.5 s for further analysis, marked by grey stripes in the figure. At approximately 6 s, a large instability occurs, significantly perturbing the plasma. Aside from this, panel b) highlights the neutral beam injection (NBI) power in green. There is a baseline level of NBI power, while the flexible beam appears as a comb-like pattern, switching on and off to maintain a constant β_p of 1.3. This regulation is effective, as seen in panel d) where β_{pol} is shown in purple. However, the overall NBI heating in the second high-shaping phase is lower than in the first phase.

In panel (e), the yellow curve shows δ_{up} increasing between 4 and 5 s, reflecting the deliberate change in plasma shape. This shape change has an immediate and pronounced effect on n_e, with both core and edge densities increasing significantly. Additionally, there is a slight increase in elongation k, indicating a change in the plasma's overall structure.

In discharge #38474 (figure 4.2) time windows 3.5-3.7s for the low shaping phase and 5.7-5.9 for the high shaping phase were chosen, as marked with the gray stripes. The conditions are largely similar to the previous case, with the main difference being a β_{pol} of 1.1, which results in reduced NBI heating. In this instance, β_{pol} is not matched as well as in #38472, likely because the flexible NBI beam was

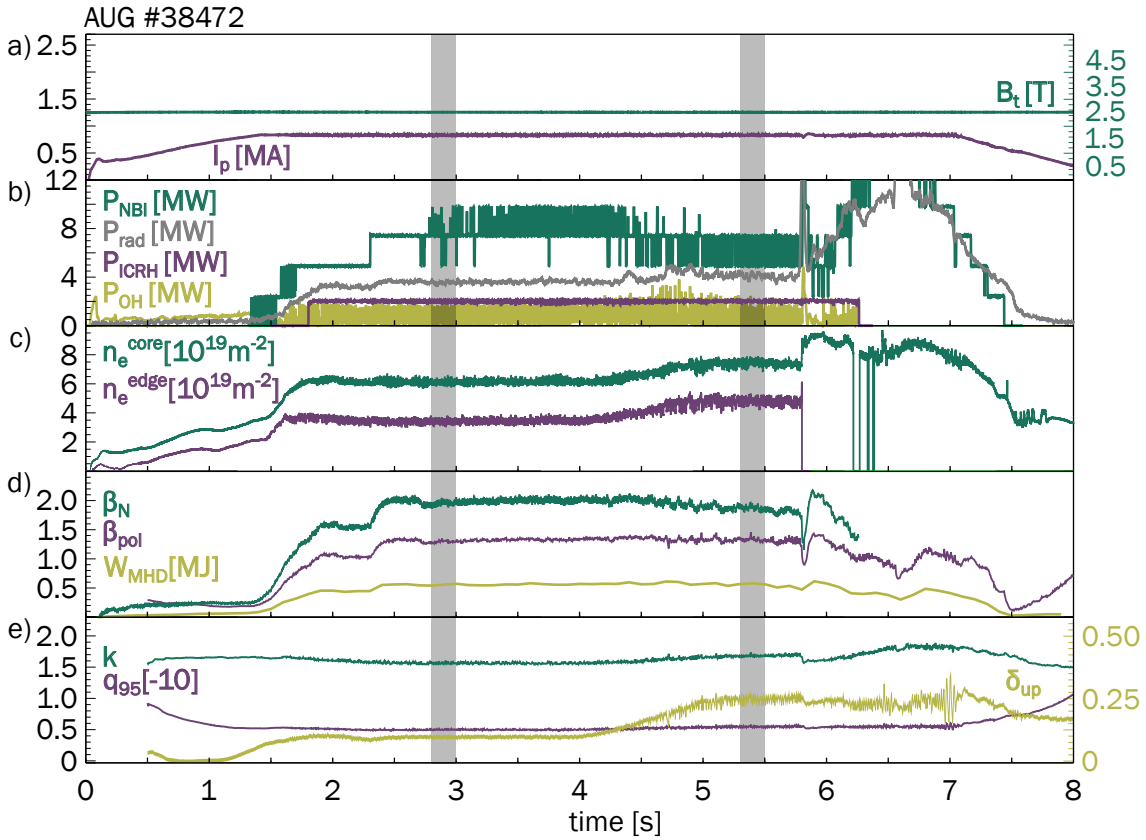

Figure 4.1: Panel a) shows the plasma current I_p (purple, left axis) and toroidal magnetic field B_t (green, right axis), with I_p ramping up until 1.5 s, while B_t remains constant across discharges. Panel b) depicts heating power contributions: NBI power P_{NBI} (green), ohmic heating P_{OH} (yellow), and ICRH power P_{ICRH} (purple), alongside radiative power P_{rad} (gray). Panel c) presents density from DCN diagnostics, with core (green) and edge (purple) line integrated densities. Panel d) displays β_N (green), β_p (purple), and W_{MHD} (yellow). Panel e) illustrates elongation k (green), the safety factor q at $\psi_n = 0.95$ (purple, scaled by -10), and upper triangularity δ_{up} (yellow, right axis).

already turned off, leaving only the baseline contribution. Consequently, β_{pol} remains slightly higher in the high shaping phase than in the low shaping phase, though the discrepancy is not very large.

In the final discharge #38819 in figure 4.3, we used a slightly higher B_t of 2.7 T compared to 2.5 T in the previous cases. The shape remained the same, but even lower β_{pol} was aimed for, targeting a value of 1.0 throughout the discharge, which was achieved quite consistently. There was a slight increase in radiative power just before our time window, but it was not significant; for instance, W_{MHD} remained unchanged. While there was some variation in the core density, the edge density stayed constant, ensuring stable conditions. For this discharge, we selected time windows from 3.0–3.2s for the low and 5.7–5.9 s for the high shaping phase.

4.2 Kinetic Profiles

The next step in the analysis involves comparing the ion temperature (T_i), electron temperature (T_e), electron density (n_e) at

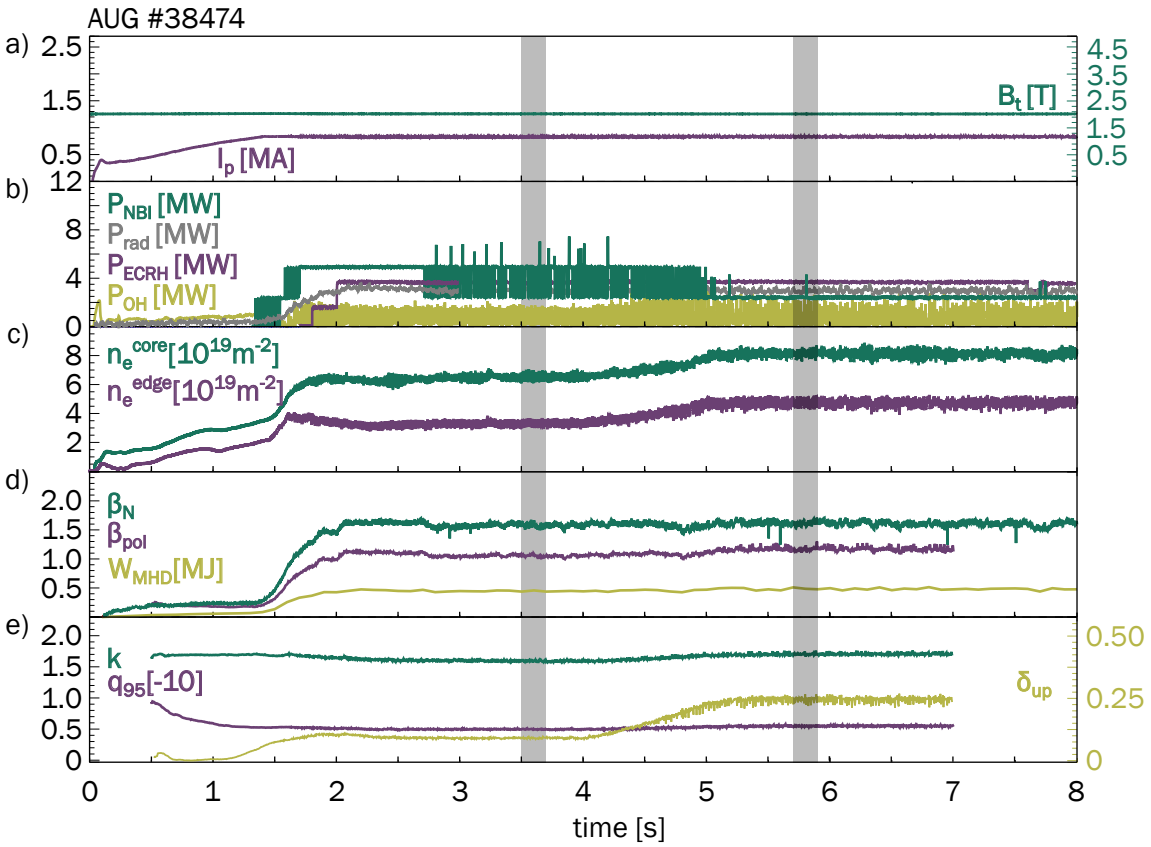

Figure 4.2: Panel a) shows the plasma current I_p (purple, left axis) and toroidal magnetic field B_t (green, right axis), with I_p ramping up until 1.5 s, while B_t remains constant across discharges. Panel b) depicts heating power contributions: NBI power P_{NBI} (green), ohmic heating P_{OH} (yellow), and ECRH power P_{ECRH}, alongside radiative power P_{rad} (gray). Panel c) presents density from DCN diagnostics, with core (green) and edge (purple) line integrated densities. Panel d) displays β_N (green), β_p (purple), and W_{MHD} (yellow). Panel e) illustrates elongation k (green), the safety factor q at $\psi_n = 0.95$ (purple, scaled by -10), and upper triangularity δ_{up} (yellow, right axis).

the plasma edge as a function of the normalised pressure, β_{pol}, as shown in figure 4.4. For this purpose, the low triangularity phase in three selected discharges is examined: #38819 ($\beta_{pol} = 1.0$) shown in green, #38474 ($\beta_{pol} = 1.1$) shown in orange, and #38472 ($\beta_{pol} = 1.3$) shown in black. Time windows of 200 ms are considered, with ELM phases filtered out. The median values are presented as solid lines, while shaded areas represent 95% quantiles.

Figure 4.4a demonstrates that T_i increases with rising β_{pol}, with higher T_i values observed both at the separatrix and in the core. Additionally, the discharge with the highest β_{pol} shows a slight increase in the T_i gradient. This trend aligns with expectations, as increasing β_{pol} experimentally involves heating ions with NBI beams, thereby raising the total plasma pressure. However, the scenario is complex since β_{pol}, being a global parameter, influences both core and edge physics. The associated Shafranov shift increases with β_{pol}, altering both local and global MHD stability and enabling a higher pressure pedestal. The experimental setup realises this increased total pressure

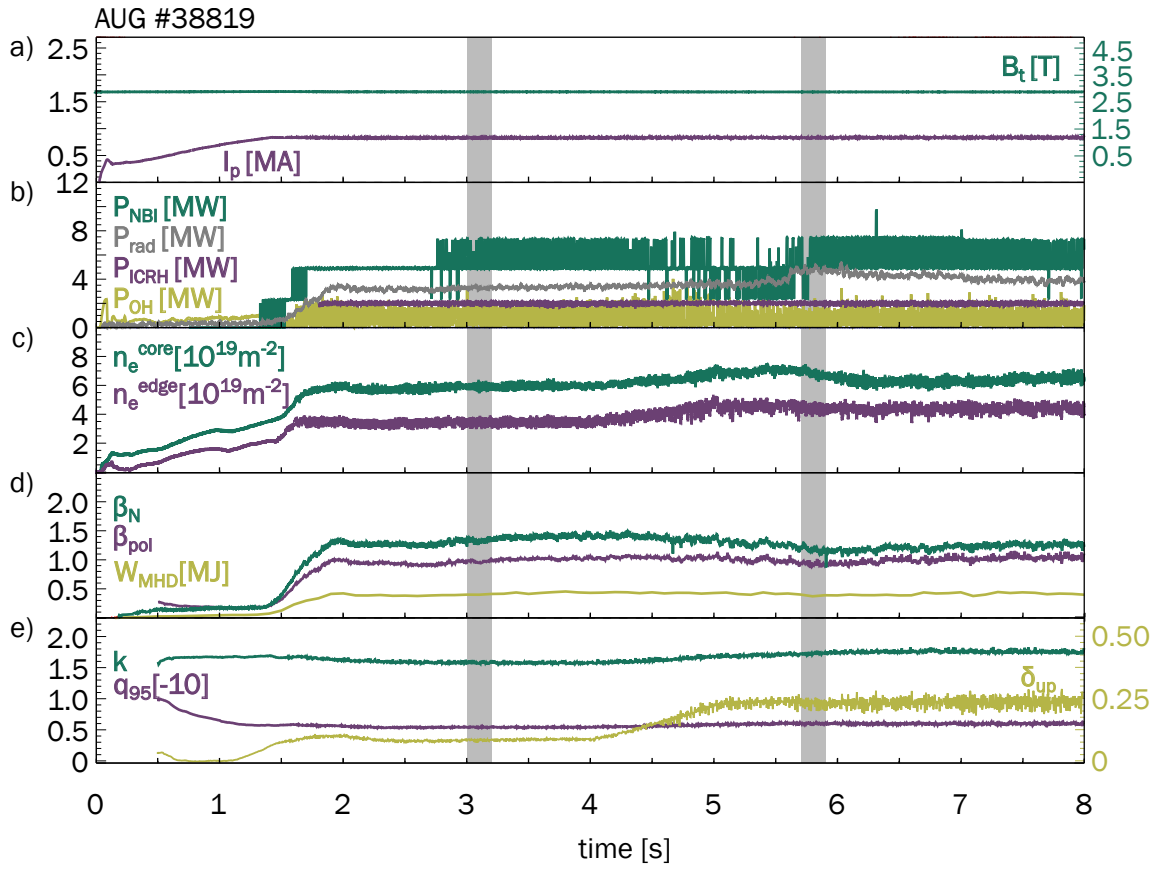

Figure 4.3: Panel a) shows the plasma current I_p (purple, left axis) and toroidal magnetic field B_t (green, right axis), with I_p ramping up until 1.5 s, while B_t remains constant across discharges. Panel b) depicts heating power contributions: NBI power P_{NBI} (green), ohmic heating P_{OH} (yellow), and ICRH power P_{ICRH} (purple), alongside radiative power P_{rad} (gray). Panel c) presents density from DCN diagnostics, with core (green) and edge (purple) line integrated densities. Panel d) displays β_N (green), β_p (purple), and W_{MHD} (yellow). Panel e) illustrates elongation k (green), the safety factor q at $\psi_n = 0.95$ (purple, scaled by -10), and upper triangularity δ_{up} (yellow, right axis).

pedestal primarily through higher T_i.

The electron temperature (T_e), as shown in Figure 4.4b, exhibits notable changes only in the outer core region ($0.94 < \rho_{pol} < 0.97$) for the low β_{pol} discharge. The n_e profile (figure 4.4c) remains largely unchanged within the uncertainty.

To investigate the influence of shaping, the analysis focuses on the kinetic profiles for the high β_{pol} case, as the profiles for all three β_{pol} values exhibit qualitatively the same behaviour. The complete set of resulting profiles will be shown in the appendix A. Figure 4.4d-f compares the low shaping phase (red) and high shaping phase (blue).

In this comparison, T_i (figure 4.4d) shows minimal variation, except for a slight deviation at the pedestal foot near the separatrix, which is mostly within the uncertainty. In figure 4.4a, the T_i profile changes, supposedly because of the increase in NBI heating due to the β_{pol} feedback loop mechanism. However, one should note that the NBI heating also decreases in the high shaping phase, because of the increase in confinement. Yet, the ion temperature does not

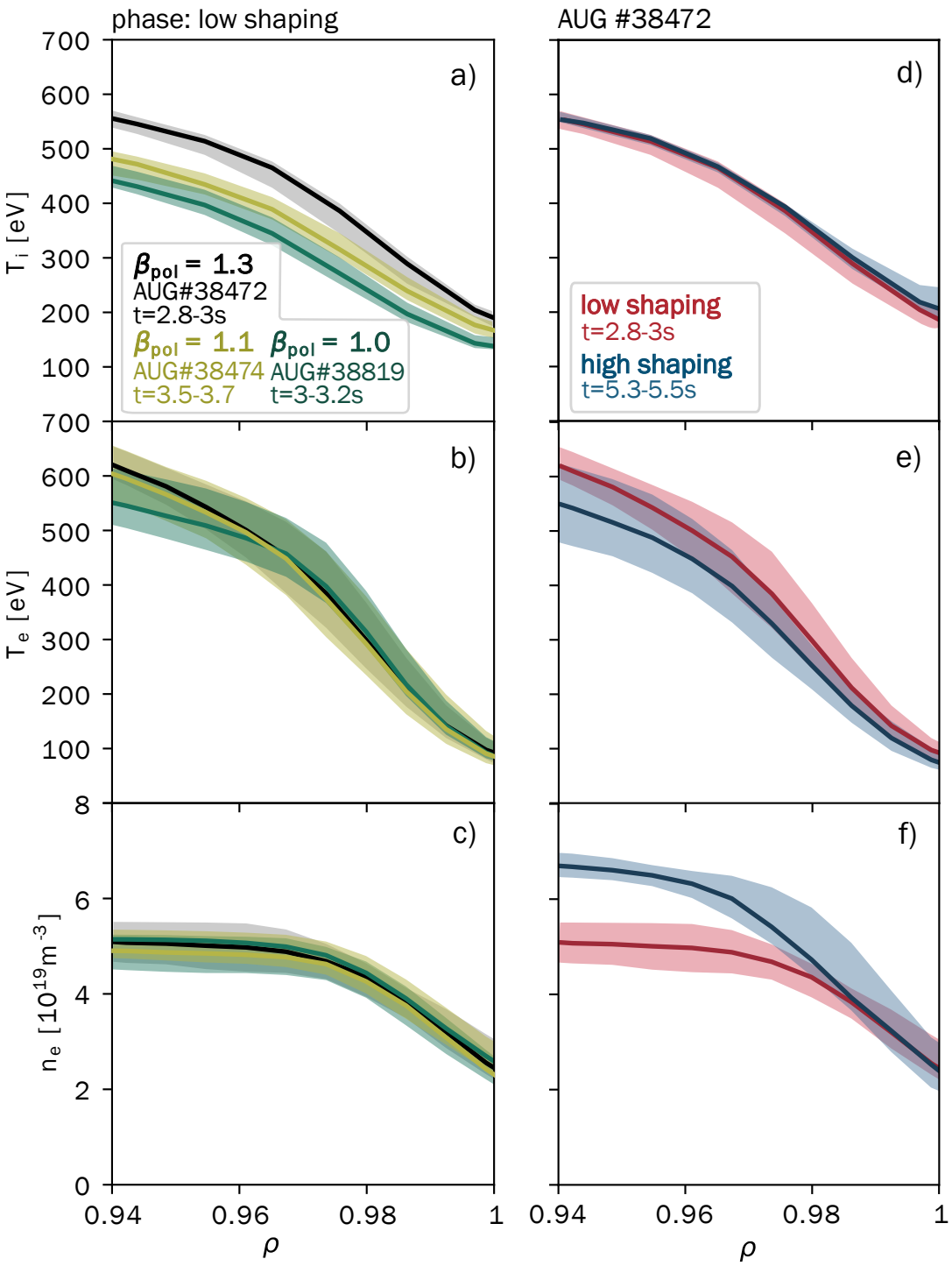

Figure 4.4: Reconstructed kinetic profiles at the plasma edge for two cases: a)–c) Profiles at different β_{pol} values during the low shaping phase, including ion temperature (a), electron temperature (b), and electron density (c). Black lines represent high β_{pol}, orange lines medium β_{pol}, and green lines low β_{pol}. d)–f) Profiles at different shapes for the high β_{pol}, with ion temperature (d), electron temperature (e), and electron density (f). Red lines correspond to low shaping and blue lines to high shaping. In all cases, the lines depict median values, while shaded regions indicate 95% of the temporal variation over the 200 ms time windows.

change, suggesting reduced ion heat flux at constant T_i.

Higher shaping leads to an increased width and gradient of the n_e pedestal (figure 4.4f) at the same separatrix density, indicating reduced particle transport, additional sources, or a particle pinch. The electron temperature (T_e), shown in figure 4.4e, decreases slightly, which may result from longer inter-ELM recovery times for ∇T_e [115, 116] and higher n_e in the high shaping phase. During the ELM cycle, n_e and T_i pedestals recover faster than T_e, potentially reaching a peeling-ballooning MHD limit before full recovery of the T_e pedestal, which will be discussed in the chapter 6. The high shaping phase, characterised by an increased n_e pedestal, limits the T_e pedestal contribution in later phases of the ELM cycle. While the extended ∇T_e recovery explains this partially, additional factors may be at play. Analysis shown in chapter 7 explores the interplay of ion and electron heat transport, particle transport, and potential source changes.

Both figures reveal that β_{pol} and shaping have distinct effects on ion and electron density and temperature. While total plasma pressure significantly impacts global MHD stability, and is at the same time limited by it, the results underscore the importance of analysing pedestals separately, as elaborated in the following chapters.

4.3 Equilibrium Quantities

Having analysed the profiles of electron and ion temperatures and densities, we now analyse the equilibrium, starting with the total pressure, p. The total pressure is expressed as

$$p = p_i + p_e,$$

where following equation 2.16, $p_i = k_B T_i n_i$ and $p_e = k_B T_e n_e$.

Additionally, we can also examine the current density, j, and the safety factor, q, since both of these parameters play critical roles in determining the equilibrium properties. Figure 4.5 shows the β_{pol} influence on these three quantities in the left and the shape influence in the right column.

Total pressure p shown in 4.5a shows that the pedestal top pressure increases with β_{pol}, partially due to the slight gradient increase in the pedestal middle, and partially due to pedestal width increase. The middle β_{pol} value, shown in yellow, does not follow the step-wise widening trend and shows a wider pedestal than the maximum β_{pol} case, shown in black. Still, these values are in the 90% quantile region, so it is difficult to make a conclusive comment on this outlying from the expected behaviour.

Interestingly, the q profile (in 4.5b) shows no differences between high and medium β_{pol}, depicted in yellow and black, however there is an obvious increase for lowest β_{pol}, shown in green.

The current density profile j_{tor}, shown in 4.5c generally has larger deviations in the selected phases. The maximum value is similar in all three cases, ranging between 0.4 MA and 0.43 MA, which is somewhat expected since the change in the pressure gradient, which drives the bootstrap current, is not very large, as shown in figure 4.5a.

When analysing the effect of shape change at constant β_{pol} it is observed that the pedestal width of total pressure p (in figure 4.5d) also increases. Here, the increase in gradient with the increase in shaping is much more significant than in the previous comparison of β_{pol} influence.

Also, the q profile (figure 4.5e) increases significantly, which reflects that not only

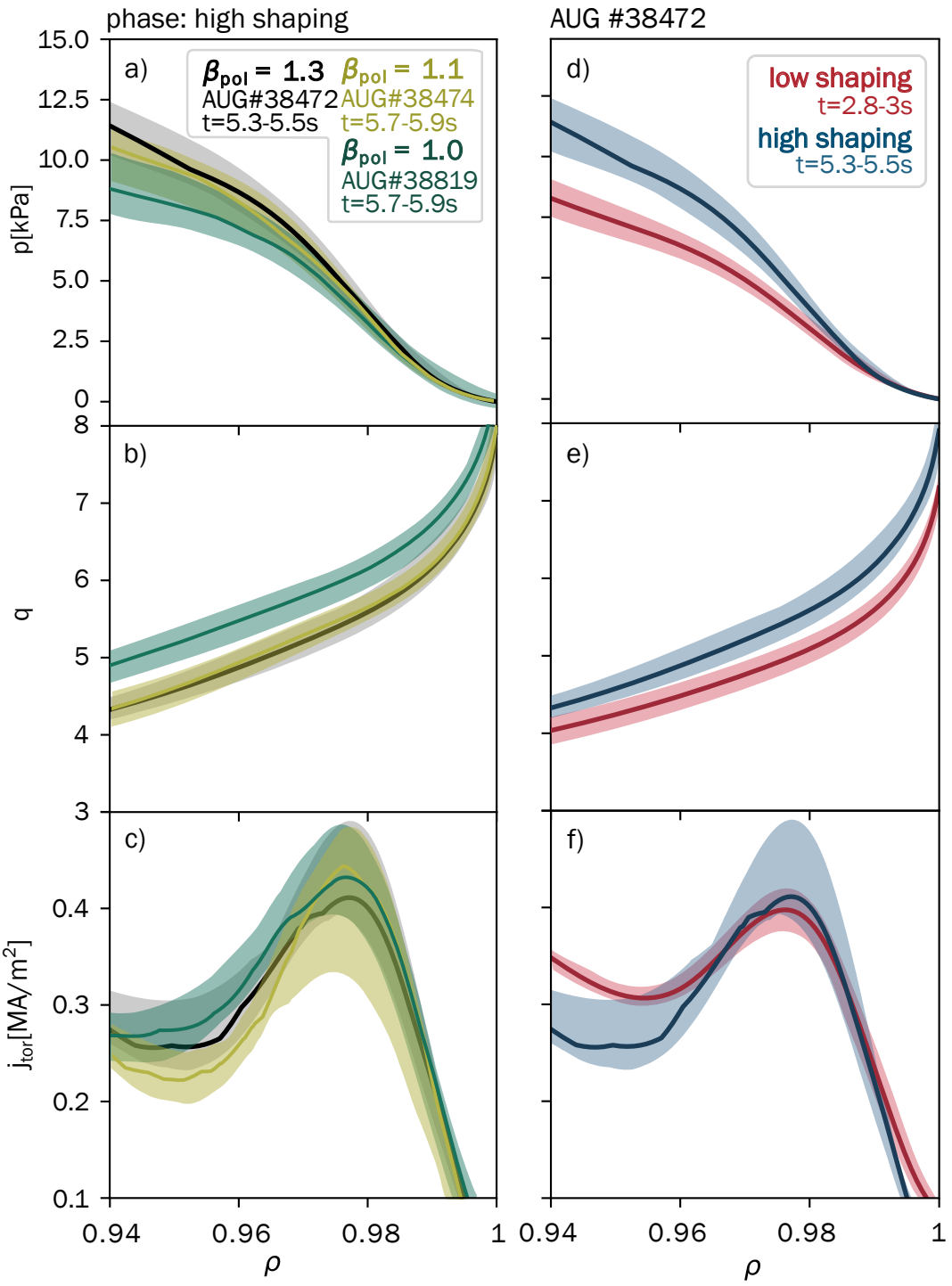

Figure 4.5: Reconstructed profiles of equilibrium profiles at the plasma edge for two cases: a)–c) Profiles at different β_{pol} values during the high shaping phase, including total pressure (a), safety factor q (b), and toroidal current density j_{tor} (c). Black lines represent high β_{pol}, orange lines medium β_{pol}, and green lines low β_{pol}. d)–f) Profiles at different shapes for the high β_{pol}, with total pressure p (d), safety factor q (e), and toroidal current density j_{tor} (f). Red lines correspond to low shaping and blue lines to high shaping. In all cases, the lines depict median values, while shaded regions indicate 95% of the temporal variation over the 200 ms time windows.

does the plasma pressure change because of the increased confinement, but the shape change also influences the magnetic pressure.

The current density (figure 4.5f) in this case shows a somewhat unexpected behaviour. The maximum current density in the pedestal middle, which corresponds to the bootstrap current contribution, does not change very much. One would expect it to increase with shaping, since there is a significant increase in pressure gradient, which drives the bootstrap current. Here, once again, the differentiation between the particle density and temperature should be underlined. When the shaping is increased, particle density increases, and electron temperature decreases. Both these phenomena increase the plasma collisionality which leads to the reduction in current density.

4.4 Radial Electric Field

The E × B shear is widely regarded as the most significant factor in suppressing turbulence in the pedestal region. Therefore, in this section, the behaviour of E_r is examined.

On ASDEX Upgrade, E_r can be calculated self-consistently. The calculation follows the previously given equation (2.41):

$$E_r = \frac{\nabla_r p_a}{n_a q_a} + v_{\perp,a} \cdot \vec{B} = \\ = \frac{\nabla_r p_a}{n_a Z_a e} - v_{\varphi,a} B_\theta + v_{\theta,a} B_\varphi. \quad (4.1)$$

The required inputs are all derived from different CXRS measurements, for the dominant species, in this case, boron. The ion density, n_i, is determined from the intensity of the CXRS spectral line, while the ion temperature T_i, is measured from Doppler broadening of the spectral line. Poloidal and toroidal velocities are obtained from Doppler shift measurements using dedicated poloidal and toroidal CXRS systems. The magnetic field, $\vec{B}$, is taken from equilibrium reconstructions.

After calculating E_r for each time window, as indicated in figures 4.1-4.3, the ELM phases are filtered out. The data is subsequently binned, and a Gaussian process fit is applied to smooth the results and evaluate uncertainties. Figure 4.6 shows the resulting E_r profile of discharge #38472 in a), the $v_{tor}B_{pol}$ term in b), the diamagnetic term $\nabla p/q_a n_a$ in c) and $-v_{pol}B_{tor}$ in d). Red scatter marks the low and blue scatter the high shaping phase of each discharge. The same analysis of E_r profiles with its individual components was also performed for other discharges, and because the results are all qualitatively and quantitatively similar, therefore difficult to directly compare when shown in different figures, they are shown in the appendix.

Discharge #38472, depicted in this section, shows the most pronounced differences. When examining the resulting E_r, we observe that for low shaping, the E_r minimum shifts slightly inward, is somewhat lower at the pedestal top, and slightly higher in the pedestal middle/foot region. Regarding the toroidal velocity term, shown in b), it is overall positive, the low shaping case exhibits a lower toroidal velocity, while the high shaping case has a higher toroidal velocity. This is intriguing because the low shaping configuration involves more NBI input (see figure 4.1), which should, in principle, provide more torque to the plasma. Yet, the toroidal velocity remains lower, suggesting that additional effects, additional effects, such as a change in momentum transport, might play a significant role.

The diamagnetic term shown in panel c)

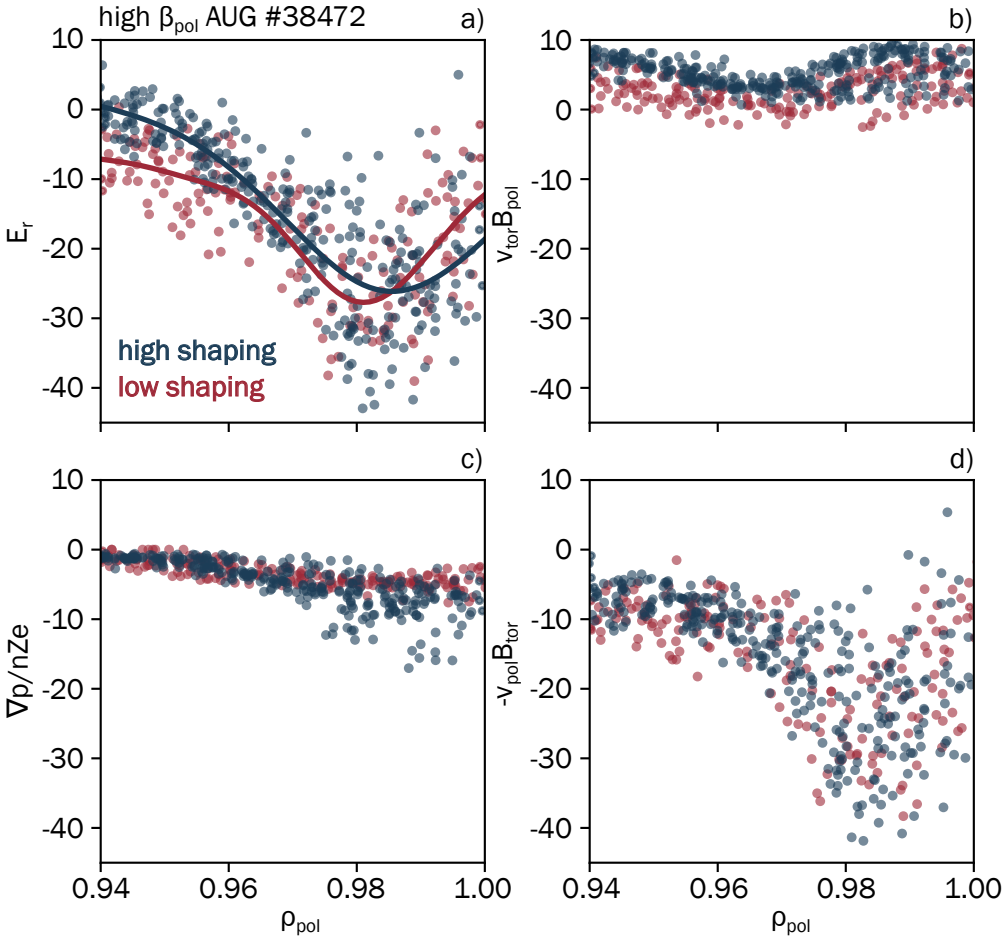

Figure 4.6: a) Total E_r, b) the component $v_{tor}B_{pol}$, c) the diamagnetic component $\nabla(p)/nZe$, and d) the component $-v_{pol}B_{tor}$. Scatter points represent measurements derived from CXRS, while the solid line in a) shows the Gaussian process fit for E_r. Red indicates low shaping and blue indicates high shaping.

behaves as expected, and its contribution in the high shaping case is stronger in the pedestal middle/foot region due to its ∇p dependence. The distinction in the poloidal velocity contribution (in d) between high and low shaping is less pronounced, leaving its role in E_r dependence on shape uncertain.

Looking again at E_r in a), the largest contribution appears to arise from the $-v_{pol}B_{tor}$ contribution (noting that this applies to the impurity velocity). The toroidal velocity contribution pushes the E_r profile downward in the pedestal top for low shaping, while the diamagnetic contribution lifts it upward in the pedestal foot region.

Our primary focus is on the $E \times B$ shearing rate, which is calculated as [22, 117]:

$$\omega_{E\times B} = \left| \frac{(RB_{pol})^2}{B} \frac{\partial}{\partial \psi} \left(\frac{E_r}{RB_{pol}} \right) \right| \tag{4.2}$$

so the radial gradient of E_r provides an estimate for turbulence suppression. Although the shearing rate impacts different mode sizes in various regions of the pedestal differently, this approach is sufficient for the qualitative analysis. In figure 4.7 the gradient of E_r is shown for the three discharges,

low β_{pol} discharge #38819 in a), medium β_{pol} discharge #38474 in b) and high β_{pol} discharge #38472 in c). The red and blue lines show the low and high shaping phase, respectively.

In the gradients, it can be observed that during the low β_{pol} phase, there is barely any noticeable change. In the medium β_{pol} case (figure 4.7b), differences become apparent in the pedestal middle and foot regions, where higher shaping reduces the gradients in these areas. A similar trend occurs in the high β_{pol} case, shown in c), although to a lesser extent, and with an additional reduction in the outer core/pedestal top region for the high shaping phase.

Moreover, the minimum of ∇E_r shifts inward as β_{pol} increases, a pattern that aligns with the behaviour seen in figure 4.5, where the gradient, a key term in E_r, exhibits a similar inward shift. Another notable difference is the depth of the ∇E_r well: at low β_{pol}, it reaches approximately -1.6, while this depth decreases with increasing β_{pol}, reaching around -1.2 for medium β_{pol} and about -1 for high β_{pol}.

4.5 Conclusions

In this chapter, the initial measurements obtained from the experiment are presented, marking the first step in our analysis. The experiment focuses on six cases, consisting of three discharges at different values of β_{pol}, each analysed for two configurations: low shaping and high shaping.

Examining the kinetic profiles: T_i, T_e, and n_e, as shown in figure 4.4, yields several intriguing observations. Notably, T_i exhibits a clear dependence on β_{pol}, while n_e remains unaffected by it. T_e, on the other hand, shows sensitivity to β_{pol} only in the outer core, with the pedestal region remaining unchanged. Additionally, T_i appears indifferent to the shaping, whereas T_e demonstrates a lower gradient under high shaping conditions. In contrast, n_e responds

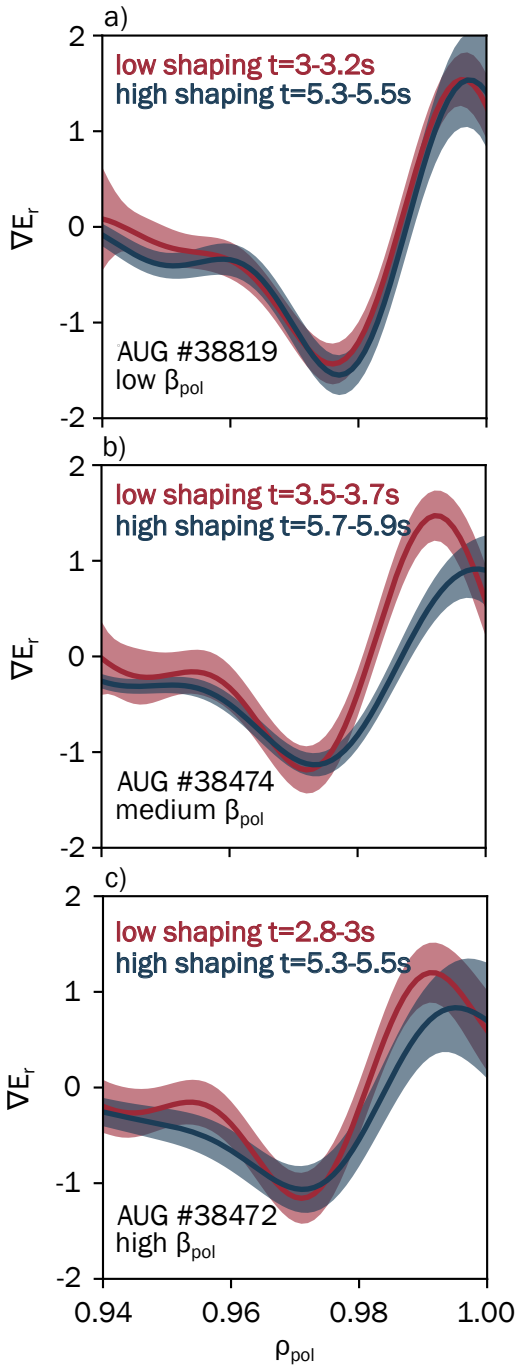

Figure 4.7: The E_r gradients are shown for low shaping (red) and high shaping (blue). Panel (a) presents the results for low β, panel (b) for medium β, and panel (c) for high β discharge.

strongly to shaping, showing a significant increase with higher shaping.

These preliminary findings strongly suggest the presence of multiple mechanisms that respond differently to β_{pol} and shaping, influencing the kinetic profiles in distinct ways. This highlights the need to move beyond treating the pedestal solely as a pressure profile. Instead, the densities and temperatures that constitute the pedestal must be recognised as individual components with unique behaviours. This nuanced perspective will be further explored and developed throughout this thesis.

The differing behaviours of temperature and density have a pronounced impact on the bootstrap current through two main mechanisms. First, they contribute differently to the bootstrap current directly. Second, their variations alter the plasma collisionality, which, in turn, further affects the bootstrap current. This interconnected behaviour introduces considerable complexity. However, we have obtained measurements of several equilibrium quantities to compare and analyse some of these effects.

The pressure gradient decreases with increasing β_{pol} and is consistently higher in the high shaping configuration. The q-profile also increases with high shaping, particularly for the lowest value of β_{pol}, where the difference is significant. Interestingly, the toroidal current density does not vary much, neither with shape nor with β_{pol}, despite the substantial changes in other parameters. Its maximum remains at the same radial position and retains a very similar value. What does change, however, is the bootstrap current near the outer core at the pedestal top, which could influence both the q-profile and its trends. Together, these observations underscore the substantial impact of temperature, density, and their associated mechanisms on the overall equilibrium.

We also examined our calculations of E_r derived from the CXRS measurements, with particular attention to its gradients. In the low β_{pol} case, the gradients remain largely unchanged in the pedestal region, and ∇E_r exhibits the deepest minimum. At medium β_{pol}, the middle and foot of the pedestal show reduced values. The most significant differences appear at high β_{pol}, where the ∇E_r peak broadens, affecting both the pedestal top and foot.

These findings regarding ∇E_r could prove useful later, as they allow us to test how consistently different phenomena influence the pedestal structure. Since E_r is often considered a key driver of pedestal formation, these results provide an opportunity to evaluate that assumption further.

81

ELM-FILTERED MHD ANALYSIS

5 ELM-filtered MHD Analysis

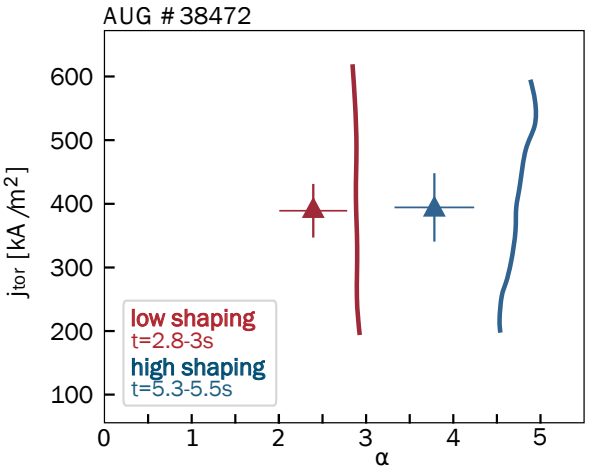

Figure 5.1: The peeling-ballooning stability diagram for the ELM-filtered time window of the high β_{pol} case is presented as a plot of the toroidal current density (j_{tor}) versus the normalised pressure gradient (α). Red markers correspond to low shaping, while blue markers represent high shaping phases. Stability limits, defined by $\gamma = 0.04\omega_A$, are shown as lines. The operational points are marked with triangles.

The experimental results shown in this chapter are in the revision process in the Nuclear Fusion journal.

5.1 Global Peeling-Ballooning Stability

To evaluate global peeling-ballooning stability, the stability boundary is determined using the MISHKA code, which takes as input the reconstructed equilibria, along with the pressure and current profiles. Figure 4.5d illustrates the total pressure profile for the high β_{pol} discharge #38472. As shaping increases, the pressure pedestal becomes broader and steeper. Normally, this would result in an increased bootstrap current. However, as shown in figure 4.5f, this is not observed. Higher density and lower temperature contribute to increased collisionality, suppressing the build-up of the bootstrap current.

Figure 5.1 presents the global peeling-ballooning stability analysis as a j–α diagram, where j_{tor} represents the flux surface-averaged current density and α the normalised pressure gradient. The stability limit is defined as the growth rate $\gamma = 0.04\omega_A$ (4% of the Alfvén frequency) for the most unstable mode and is shown as a solid line. Operational points are represented by triangles using the same colour scheme as previous figures. Consistent with common observations, the analysis shows that increased shaping shifts the stability boundary to higher α values, permitting the total pressure gradient to increase. However, the toroidal current density does not rise for the reasons outlined earlier.

This suggests that, in this scenario, the mode structure predominantly exhibits ballooning rather than peeling characteristics, as ballooning modes are primarily driven by α. To further explore this, we examine the

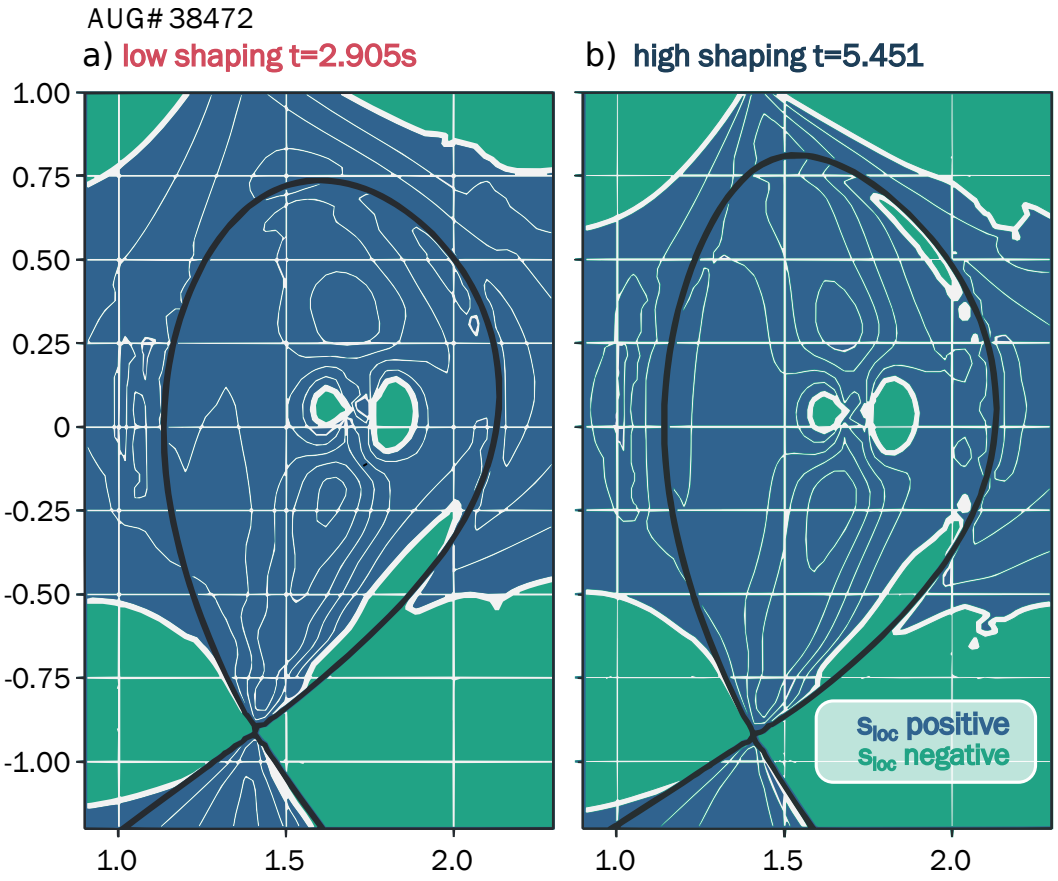

Figure 5.2: A two-dimensional map of the local magnetic shear (s_{loc}) is provided, where regions with $s_{loc} > 0$ are depicted in blue, and those with $s_{loc} < 0$ are shown in green. The separatrix is indicated by the black line, while thin white contours represent surfaces of constant s_{loc}. The thick white contour highlights the surfaces where $s_{loc} = 0$, signifying regions without ballooning mode stabilisation.

development of local features of ideal $n \to \infty$ ballooning stability in different pedestal regions. The local ideal ballooning modes (IBMs) are stabilised by the square of the magnetic shear. The two-dimensional distribution of the local magnetic shear s_{loc}, as defined in [118], is shown in figure 5.2. Positive s_{loc} regions are indicated in blue, and negative regions are shown in green. Thin white contours represent areas with equal s_{loc} values, while thicker white lines mark locations where s_{loc} crosses zero, indicating no ballooning mode stabilisation.

5.2 Local Ideal Ballooning Modes

Transitioning from low shaping (figure 5.2a) to high shaping (figure 5.2b) introduces a small region of negative s_{loc} on the upper low-field side (LFS), creating an additional zero-shear contour. Although negative shear stabilises modes through s^2_{loc}, even as the global surface-averaged shear decreases, this change can significantly impact the distribution of IBM instabilities due to the localisation of ballooning modes on the LFS.

The driving force for ballooning modes is the normalised pressure gradient α. Using experimental data, HELENA computes both the experimental α_{exp} and the critical α_{crit}, where the plasma becomes ballooning unstable. Figure 5.3a depicts α_{exp} as solid lines and α_{crit} as dashed lines, with red indicating low shaping and blue indicating high shaping.

For higher shaping, the critical pressure gradient becomes larger and broader, with the experimental profile following suit. Dashed circles highlight pedestal regions closest to the ideal ballooning stability limit. During the low shaping phase, the maximum gradient region at $\rho \approx 0.975$ is closest to the stability boundary. With increased shaping, two unstable regions appear on either side of the α_{exp} profile. This behaviour is also visible in figure 5.3b, which shows the marginal ballooning stability factor $F_{marg} = \alpha_{crit}/\alpha_{exp}$. Higher triangularity shifts the stable region in the outer core inward, towards lower ρ_{pol} values. The location of this F_{marg} minimum is compared to changes in the electron pressure pedestal width for three different β_{pol} values.

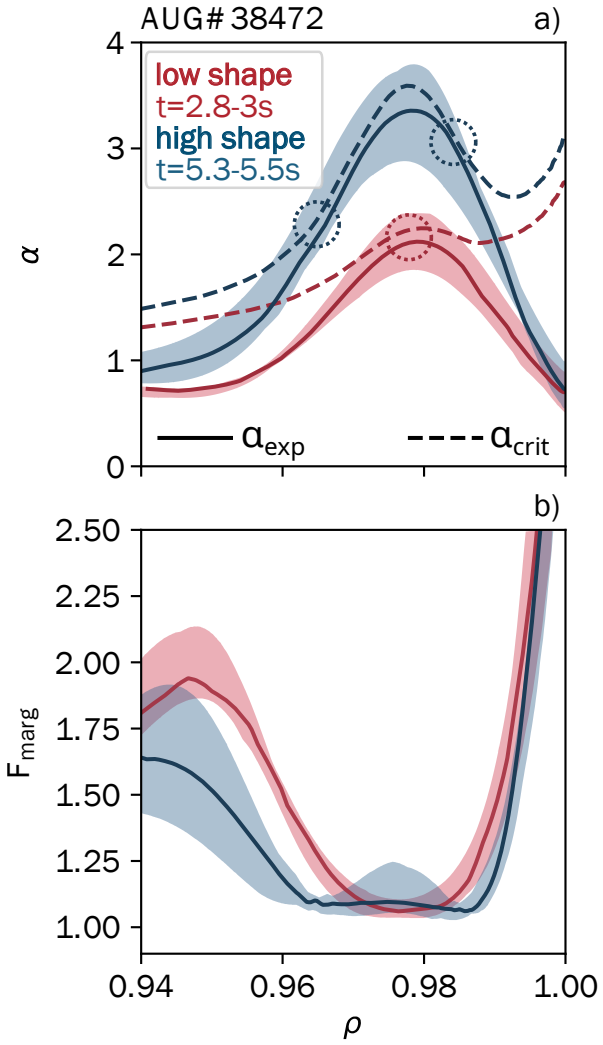

Figure 5.3: Radial profiles of the critical α (dashed lines) and experimental α (solid lines) are shown in panel a), alongside the ballooning stability factor F_{marg} in panel b). Red lines correspond to low shaping phases, and blue lines to high shaping phases. The solid lines represent temporal medians, with the shaded areas indicating 95% of the temporal variation over the analysed 200 ms window.

5.3 Effect of Plasma Boundary and Profiles

To better understand the separate influences of plasma shaping and the pressure and current profiles on local IBMs, we perform a series of analyses by integrating low (high) shape profiles into high (low) shape plasma boundaries. Figure 5.4 presents the first column, which displays the actual cases for (a) α_{exp} and α_{crit}, along with (d) F_{marg}, comparing high and low shaping conditions.

In the second column, the dark blue

lines illustrate the actual scenario for high shaping, while the light blue lines represent the results from a HELENA run using high shaping profiles with a low shaping plasma boundary. The third column shows the opposite configuration: the dark red lines indicate the original low shaping case, and the pink lines combine low triangularity (δ) profiles with a high shaping plasma boundary.

From this examination, we conclude that the choice of plasma boundary influences local IBM stability linearly, as demonstrated in figures 5.4e) and 5.4f). Meanwhile, the profiles primarily dictate the structure of the F_{marg} profile, determining the presence of a local stability maximum in the pedestal's middle region. It is essential to recognize that this analysis does not completely disentangle the effects of profiles from those of equilibrium, since the input consists solely of the plasma boundary. The equilibrium reconstruction incorporates the profiles, meaning the resulting structure of F_{marg} is largely influenced by effects of the profiles on the magnetic equilibrium.

Notably, in the middle column, both high and low triangularity plasma boundaries yield characteristic F_{marg} profiles featuring two minima and a local maximum within the pedestal. This suggests that the impact of profiles on the equilibrium facilitates access to a second stability region, which will be further examined in the subsequent section.

5.4 Access to the Second Stability Regime

As previously noted, the stabilizing factor in the ballooning equation is dependent on the square of the magnetic shear. Therefore, even in regions with locally negative magnetic shear, its squared value retains a stabilizing effect. In typical ASDEX Upgrade configurations, this phenomenon primarily occurs on the low field side (LFS), where ballooning modes become destabilized due to adverse curvature, as illustrated in figure 5.2b. When the local shear s_{loc} changes sign, its square value reaches zero, eliminating any stabilizing effect. This condition contributes to a local minimum in F_{marg} observed at both the top and the foot of the pedestal. Additionally, pressure influences the magnetic shear by enhancing its poloidal variation, mainly due to an increased Shafranov shift, which further reinforces the stabilizing effect.

The impact of poloidally varying magnetic shear is also reflected in the $s - \alpha$ diagram, as detailed in section 2.1.3 and schematically shown in figure 2.8. In summary, at the plasma edge, heightened pressure gradients induce a bootstrap current that modifies the q profile, leading to a local reversal of the shear, particularly at the LFS where ballooning modes are concentrated. As α increases, the negative local shear at the LFS increases further, resulting in an increased square of the local magnetic shear. Consequently, ideal ballooning modes experience further stabilization, transitioning the operational point into the second stability region. If the middle of the pedestal lies within this second stable region, it facilitates higher pressure gradients and enhances plasma confinement. In such scenarios, the pressure gradient is constrained not by local IBMs but by global finite-n effects or another type of micro turbulence.

The relationship between the first and second stability regions is illustrated in figure 5.5, which presents diagrams for the high β_{pol} discharge #38472. In figure 5.5a), the unstable region, along with the

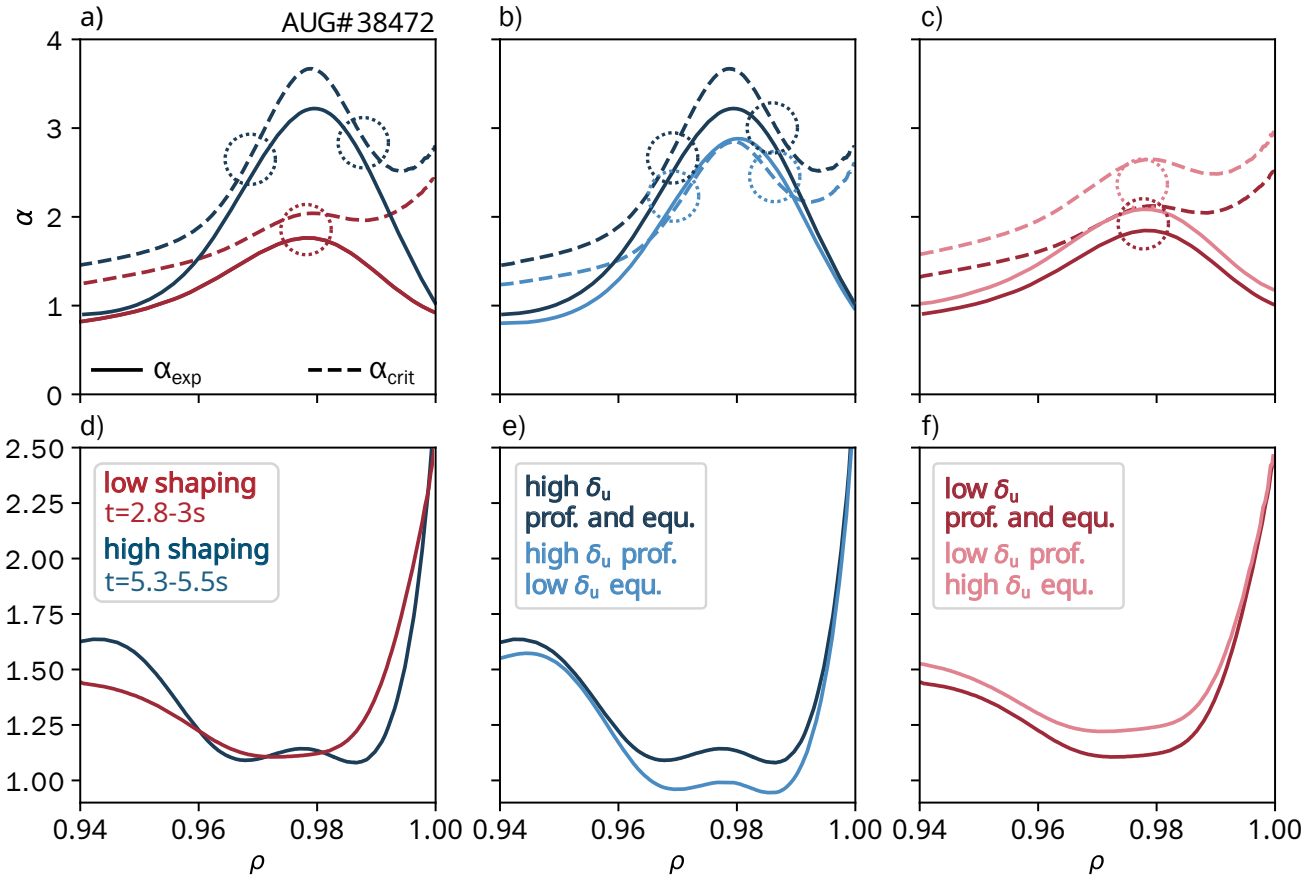

Figure 5.4: Radial profiles of the critical α (dashed lines) and experimental α (solid lines) are presented for two distinct time points in panels a), b), and c), with the corresponding ballooning stability factor $F_{marg} = \alpha_{crit}/\alpha_{exp}$ in panels d), e), and f). Panel a) and d) depict actual high and low shaping values, with red representing low shaping and blue representing high shaping phases. Panels b) and e) show high shaping profiles (dark blue) combined with low shaping plasma boundaries (light blue). Conversely, panels c) and f) show low shaping profiles (dark red) mixed with high shaping plasma boundaries (pink). Regions where α_{exp} and α_{crit} are closest are highlighted with dashed circles.

first and second stable regions, is marked in red and extended with the dashed gray line. The three columns correspond to different radial positions in the pedestal: the left column at $\rho_{pol} = 0.965$ (the F_{marg} minimum at the top of the high triangularity pedestal), the middle column at $\rho_{pol} = 0.975$ (the F_{marg} minimum in the middle of the low triangularity pedestal), and the right column at $\rho_{pol} = 0.985$ (the F_{marg} minimum at the foot of the high triangularity pedestal). The first row depicts the low triangularity phase, while the second row illustrates the high triangularity phase.

Each panel indicates the position of the operational point, marked as a triangle, within the s – α space. The current and pressure gradient profiles utilized as input for HELENA are scaled from 80% to 120% of their initial values. The resulting grid is represented as dots in figure 5.5. Using the original plasma boundary, the equilibrium is reconstructed for each point, allowing for the evaluation of local IBM stabil-

ity. Each grid point is assigned a value of F_{marg}, depicted as a colour map, where blue indicates stable and red unstable regions. The proximity of the operational point to the stability limit, represented by a black contour line, indicates the degree of ballooning instability present in the configuration. It is important to note that while local IBMs serve as a proxy for KBMs, which exhibit qualitatively similar behaviour, KBMs are typically less stable. Therefore, points within the white shaded areas may already be susceptible to KBM instabilities.

In the first row, which presents the low triangularity case, the stability limit remains relatively low for both s and α across all three locations. At $\rho_{pol} = 0.965$ (figure 5.5a), the operational point resides well within the first stability region, excluding the possibility of achieving higher pressure gradients. Further down in the pedestal region, at $\rho_{pol} = 0.975$ (figure 5.5b), the operational point shifts slightly toward the transition region. However, at $\rho_{pol} = 0.985$ (figure 5.5c), it returns to the first stability region, again at low pressure gradient values.

The second row illustrates the high triangularity case. Already at $\rho_{pol} = 0.965$ (figure 5.5d), at the top of the p_e pedestal, the operational point is positioned closer to the transition into the second stability region. Panel e) clearly shows that the operational point gains access to second stability, attributed in part to the higher α. Additionally, the stability boundary is positioned at significantly higher values of magnetic shear due to the altered plasma shape compared to the first phase. At the foot of the pedestal, in panel f), the stability limit is even higher, placing the operational point within the transition region.

The interpretation of the F_{marg} profiles in figure 5.3 is as follows: for the high shaping scenario, in the region of increased stability (i.e., $0.965 < \rho_{pol} < 0.985$), F_{marg} approaches 1. However, since this region is second stable, the pressure gradient is not actually restricted by the ideal ballooning modes, as increasing α_{exp} only serves to stabilise the IBMs, as depicted in figure 5.5e). Moreover, if α_{exp} were to rise in figure 5.3a), the values of α_{crit} would increase at a faster rate. This insight is impossible to derive solely from profile examination, and it can only be gained through the analysis of the $s - \alpha$ diagram, underlying the importance of such detailed analysis.

5.5 Comparison of the Electron, Ion and Total Pressure Profiles with F_{marg} and E_r

The radial positions of the electron (p_e) and ion (p_i) pedestal tops are compared with the marginal stability factor F_{marg} and the gradient of E_r, normalised to c_s/R, where c_s is the sound speed defined as

$$c_s = \sqrt{T_e + T_i/m_i}$$

serving as a proxy for the $E \times B$ shear. The pedestal top position is determined by fitting lines through the region of maximal gradient and the outer core, identifying their intersection point, as described in [119].

Figure 5.6 illustrates a strong correlation between the p_e pedestal (first row) and F_{marg} (second row), with F_{marg} values between 1.2 and 1.25 at the radial position of the respective p_e pedestal top. Similarly, p_i (third row) correlates with ∇E_r (fourth row). The analysis is presented across a range of β_{pol} values—high in the first column, medium in the second, and low in the third.

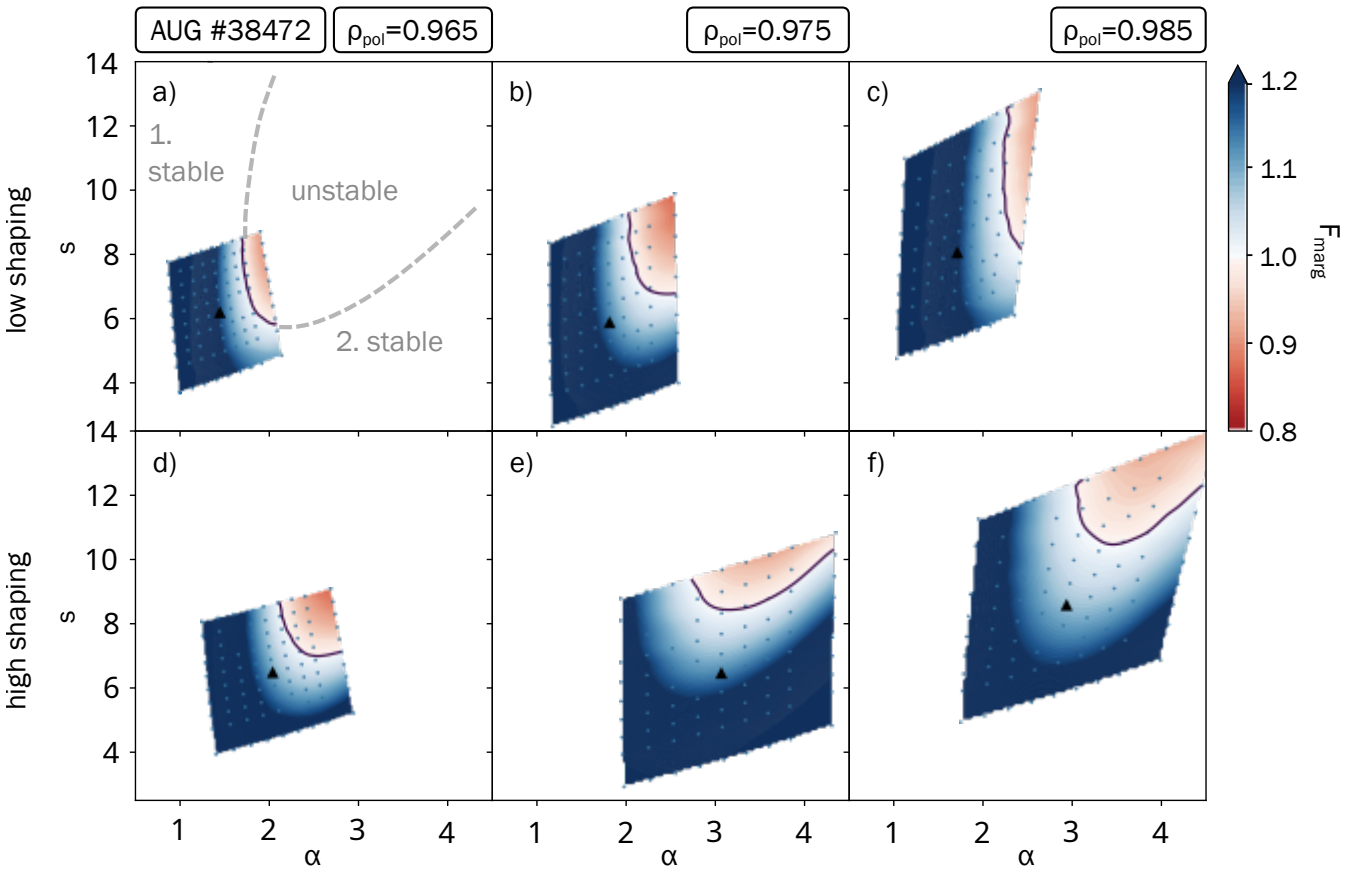

Figure 5.5: s-α diagrams are shown for three distinct positions within the pedestal for discharge #38472. The first row (a-c) represents the low shaping phase, while the second row (d-f) corresponds to the high shaping phase. Blue contours indicate marginally ballooning-stable regions, and red contours denote marginally ballooning-unstable regions. The solid line marks the ballooning stability limit where $F_{marg} = 1$. Operational points are highlighted with black triangles.

The positions of the pedestal tops for p_e and p_i are marked with dashed red and blue lines for high and low triangularity, respectively, and projected to the rows below, indicating F_{marg} and ∇E_r.

In examining the electron pressure profiles (figures 5.6 a)-c)), only discharge #38474 shows a slight increase in pressure gradient during the high shaping phase, while the others maintain a constant gradient as the pedestal widens and rises. The widening of the pedestal, attributed mainly to expanding density profiles, results in a constant p_e gradient, as shown in figure 5.6. The standard deviation of F_{marg} in this region is just 0.02, around a median value of $F_{marg} = 1.21$, highlighted with a gray stripe in figures 5.6 d)-f). It is crucial to note that HELENA, the code used to calculate F_{marg}, lacks information on E_r, making it difficult to estimate any E×B shearing stabilisation effect in the local IBMs.

Comparing F_{marg} profiles in figure 5.6 d-f reveals that the profile shifts to higher values with increasing β_{pol}. Additionally, the peak in the pedestal centre during high shaping phases becomes more prominent as the stability boundary shifts towards higher values of s and α, as detailed in section 4.4.

The strong correlation between p_i (figure 5.6 g-i) and ∇E_r (figure 5.6 j-l) arises because E_r, calculated as defined in equation equation, is dominated by the diamagnetic term of main ions, directly proportional to ∇p_i. However, turbulent processes affecting radial transport of particles and ion heat are suppressed by ∇E_r. So the whole mechanism can be seen as an interplay between neoclassical transport and MHD effects.

To further analyse these correlations, we determine the radial positions of the pedestal tops for each pressure profile (p_e, p_i, and total pressure p). We evaluate F_{marg} and ∇E_r at these positions and calculate the median values ($\overline{F_{marg}}$ and $\overline{\nabla E_r}$) for six points (three β_{pol} values and two shapes each). The median values and their respective standard deviations are listed in add table. Figure 5.7 plots the radial positions of the pedestal tops on the x-axes and the radial positions of $\overline{F_{marg}}$ and $\overline{\nabla E_r}$ on the y-axes, with error bars indicating the standard deviation range and a diagonal x = y gray line in each panel. The correlation strength is quantified as the R^2 value, as shown in table add table.

Figures 5.6 a-f) show a strong correlation between the p_e pedestal top position and F_{marg} value of 1.21, reflected in figure 5.7 a), which also shows correlations with $\overline{F_{marg}}$ positions. Small error bars indicate low standard deviations around the median, except for discharge #38474 in the low triangularity phase, which has a notably flat profile in the region of the expected F_{marg} value.

The ion pressure pedestal top, shown in figure 5.7 b), has larger error bars due to the greater scatter of F_{marg} values at the pedestal top positions. In figure 5.7 c), total pressure positions still reflect the general trend, albeit with larger variations.

Figure 5.7 d) shows the correlation between the p_e pedestal top and the median position of $\overline{\nabla E_r}$, indicating that all triangles (high-shaped phases) are wider than the median, while all circles (low-shaped phases) are narrower. The p_e pedestal tops for low and high triangularity occur at distinctly different values of $\overline{\nabla E_r}$, suggesting additional stabilisation in the high triangularity cases.

The strongest correlation with E_r is observed in p_i (figure 5.7 e), where, despite smaller changes in pedestal width, the pedestal top positions align well with $\overline{\nabla E_r}$, and the error bars are small. Figure 5.7 f) also reflects these correlations, although with slightly larger deviations from $\overline{\nabla E_r}$.

5.6 Conclusions

In this study, the impact of various physical mechanisms on the pedestal width is studied, with a particular focus on the relation of shaping and normalised poloidal pressure and MHD. Specifically, it was investigated how these factors influence temperature and density, as well as their separate effects on electrons and ions.

All analysed discharges are in ELMy H-mode, where the overall limit on the total pressure pedestal is determined by global MHD peeling-ballooning modes. Changes in shape shift the peeling-ballooning stability limit towards higher values of the normalised pressure gradient, α, and current density, j. It was found that α plays a more significant role, as temperature and density respond differently to increased shaping: both increase collisionality, which lowers the bootstrap current, while the enhanced total pressure gradient increases it, resulting in the maximal j_{tor} remaining approximately constant.

Notable differences in the influence of

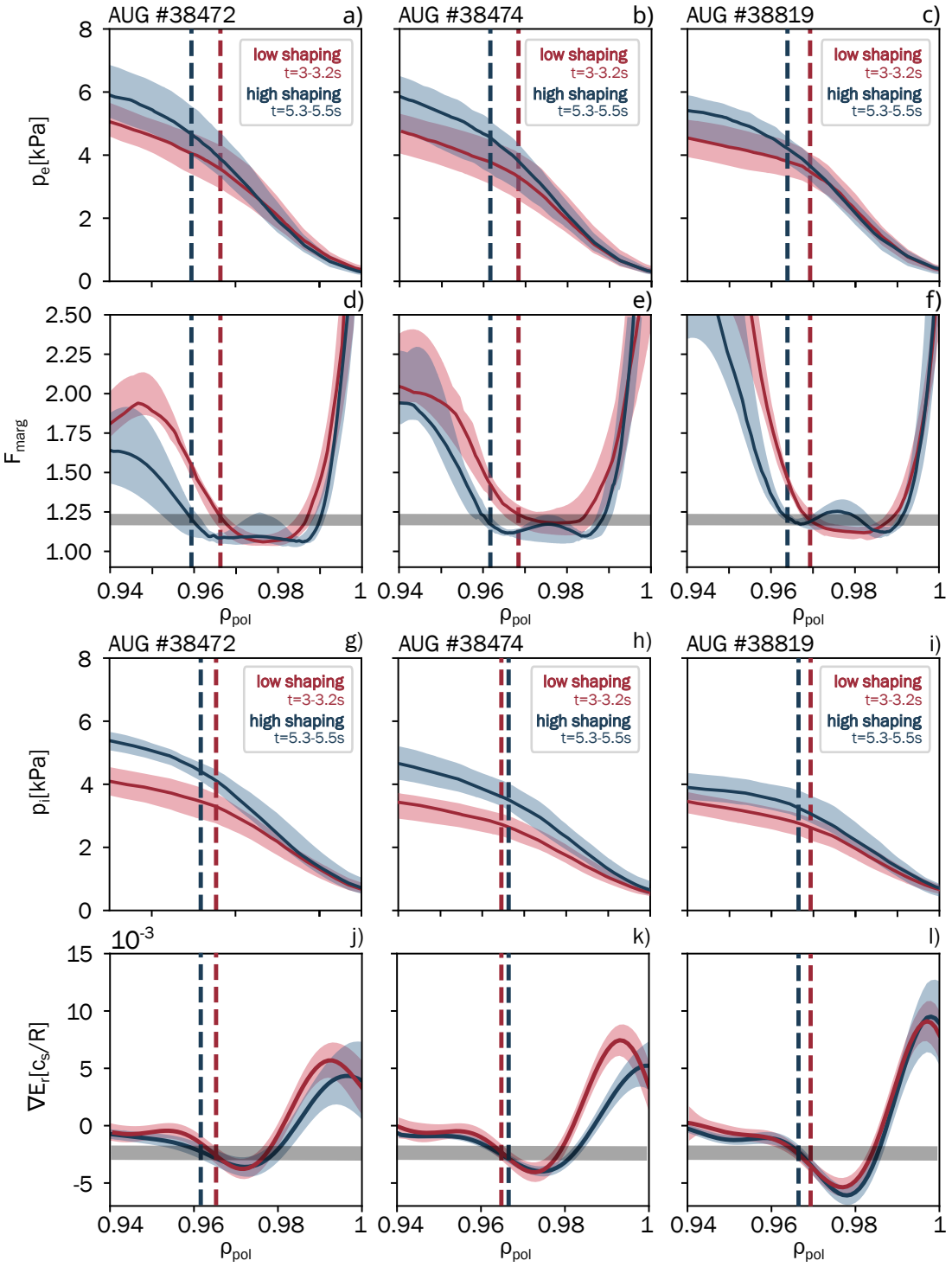

Figure 5.6: The first row (a-c) displays profiles of electron pressure (p_e), the second row (d-f) shows the ballooning stability factor (F_{marg}), the third row (g-i) represents ion pressure (p_i), and the fourth row (j-l) presents the gradient of the radial electric field (∇E_r), normalised to the sound speed (c_s) and major radius (R). Solid lines represent the median, and shaded areas indicate the 95% temporal variation over the analysed 200 ms. Low shaping phases are shown in red, while high shaping phases are in blue. The pedestal tops, determined using a two-line fit through the maximum gradient and outer core, are marked with vertical dashed lines. In panels d-f and j-l, the horizontal grey bands depict the standard deviation around the median values of F_{marg} and ∇E_r at the pedestal tops of p_e and p_i, respectively.

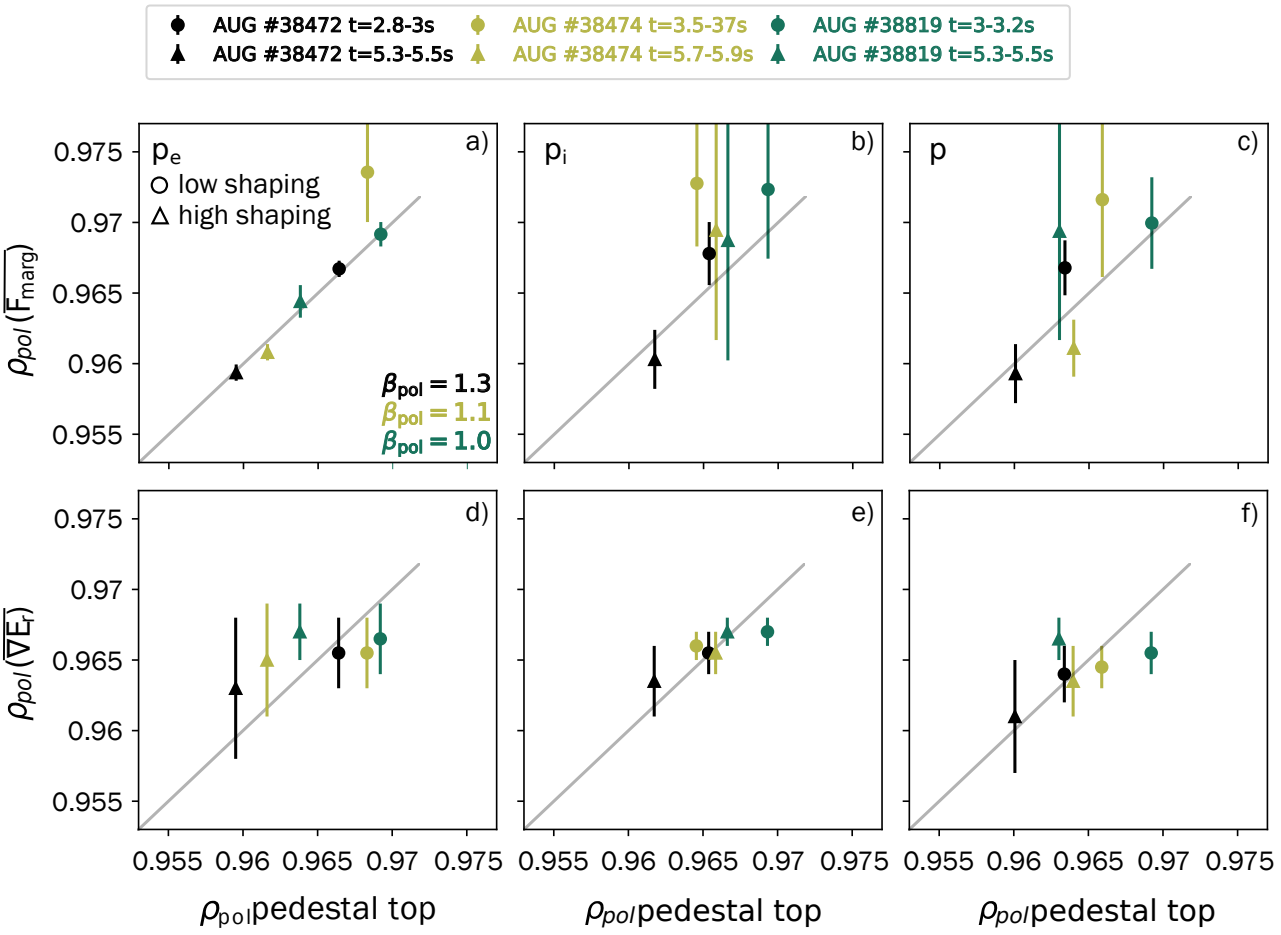

Figure 5.7: The radial positions of the pedestal tops for electron (p_e), ion (p_i), and total pressure (p) are correlated with the radial positions of the median values of F_{marg} (first row: a-c) and ∇E_r (second row: d-f). Circles indicate low shaping phases, while triangles represent high shaping phases. The colour of the markers indicates the value of β_{pol}: black for $\beta_{pol} = 1.3$, orange for $\beta_{pol} = 1.1$, and green for $\beta_{pol} = 1.0$. Error bars represent the range of ρ_{pol} corresponding to the standard deviation.

shaping and β_{pol} were observed. It was shown that β_{pol} had no effect on density, a small effect on electron temperature, and a significant effect on ion temperature, partially due to the functionality of the β_{pol} feedback loop. In contrast, shaping primarily influences the density profile, increasing both its width and gradient. While shaping slightly affects electron temperature, the latter is lower in higher density phases. Given that electron temperature recovers more slowly during the inter-ELM cycle [115], this can be interpreted as a rise in temperature during the ELM cycle, but only until the electron pressure gradient reaches a constant value. Ion temperature does not significantly change with shaping; however, in high shaping phases, β_{pol} feedback reduces NBI heating and increases plasma volume, both of which contribute to a reduction in heat flux.

The explanation for these changes lies in the modification of local magnetic shear, s_{loc}, which creates a region with strong but negative magnetic shear, stabilising local ideal ballooning modes (IBMs). This

leads to transitions from having one unstable region spanning most of the pedestal to scenarios where the pedestal top and foot are unstable, while the middle enters the second stability region, free of ballooning modes, enabling pedestal widening.

This behaviour is reflected in the substantial correlation between the pedestal top position of the electron pressure, p_e, and a specific value of the ballooning stability factor, F_{marg}. Similarly, a correlation exists between the pedestal top position of ion pressure, p_i, and the gradient of the radial electric field, ∇E_r. The resulting total pressure widths also show a weaker but observable correlation with both the median of F_{marg} and ∇E_r. A potential model emerges from analysing this correlation starting in the plasma core.

In the core, turbulence dominates transport. Approaching the pedestal, ∇E_r strongly suppresses turbulence, but the suppression varies across the pedestal region. At a threshold of ideal ballooning stability, local E_r stabilisation weakens, allowing IBMs (or alternative modes such as KBMs or resistive ballooning modes) to emerge and enhance transport. Beyond this region, E_r stabilisation strengthens, and together with other stabilising mechanisms, suppresses IBMs again. For high triangularity, even though F_{marg} approaches ballooning stability in the pedestal middle, the second stability region permits higher pressure gradients without triggering instability.

The total pressure is primarily constrained by global MHD phenomena, setting the overall limit on the pedestal structure. Within this constraint, local transport, turbulence, and its suppression further shape the pedestal. The interplay between shaping and β_{pol} significantly affects the pedestal structure: shaping predominantly impacts density and electron temperature, whereas β_{pol} determines the position of MHD stability limits and influences the overall pedestal width. The identified mechanisms enhancing the pedestal and reducing radial transport are $E \times B$ shear and magnetic shear, which are counteracted by global MHD stability limits. Once these limits are exceeded, ELMs occur, leading to pedestal crashes. Additionally, local IBMs in different pedestal regions contribute to transport.

These findings underscore the limitations of scaling laws and empirical models in predicting pedestal behaviour for future machines. A separate treatment of ion and electron pedestals, for both temperature and particles, is essential to understand the pedestal structure. Our results suggest that magnetic shear strongly influences the electron pressure profile, while ion temperature remains unaffected by shear but correlates with E_r. Distinct mechanisms must therefore be considered for different pedestal components when designing models for predictive calculations in future machines, such as ITER. Further testing and integration of these mechanisms into predictive models are required.

Several open questions remain, such as the behaviour of ion and electron heat diffusivities and the role of other microturbulent modes in the pedestal, which will be further discussed in chapter 7. Additionally, the role of resistivity requires further investigation, either through resistive codes or by examining ballooning mode responses under varying collisionalities. While this study highlights the importance of magnetic shear in pedestal formation, the interaction of these modes with $E \times B$ shear remains an unresolved question, as this effect is not captured in HELENA.

It is important to recognise that stabilisation and drives of different modes

vary across the pedestal, necessitating a well-resolved radial analysis of pedestal physics. This presents challenges both experimentally and in modelling, particularly when considering distinct electron and ion transport channels for particles and heat. Nonetheless, such detailed analysis is crucial for understanding and explaining diverse pedestal behaviours.

ELM-SYNCHRONISED MHD ANALYSIS

6 ELM-Synchronised MHD analysis

A part of the analysis presented in this chapter was conducted by Vanessa Schweidler [120] in her project thesis that I supervised in 2023. The analysed discharges are performed by Florian Laggner in his PhD thesis and are published in [115].

The temporal resolution of our measurements is limited, which poses challenges when analysing the dynamics of an ELM due to the typically high ELM frequency, often in the range of 100–200 Hz. This makes it difficult to resolve one whole ELM cycle with the available diagnostics. To address this limitation, we employ ELM synchronisation.

ELM synchronisation works as follows: we first detect the precise timing of an ELM. After identifying an ELM, we capture all available measurements until the occurrence of the next ELM. These measurements are then aligned and layered on top of one another. By repeating this process over multiple cycles, we construct ELM-synchronised profiles that reveal the average behaviour of the system during the ELM cycle.

Figure 6.1 illustrates the evolution of electron density (in a and c) and temperature (in b and d) during an ELM cycle for two distinct discharges - low shaping discharge #33207 with the triangularity $\delta = 0.24$ (figure 6.1 a and b) and high shaping discharge #33194 with $\delta = 0.4$ (figure 6.1 c and d). These discharges are described in detail in [115] but a brief overview is shown in figure 6.1. From the observations in [115] and additional findings in [116], we characterise the progression of the ELM cycle in three phases. During an ELM crash, the entire pedestal, including density and temperature profiles, flattens—this is referred to as phase I. Following this, the ion temperature and particle density recover relatively quickly, whereas the electron temperature lags behind, marking phase II. In phase III, the electron temperature also recovers, bringing the pedestal back to a pre-ELM state.

6.1 Analysis of the ballooning stability profiles

Because we are interested in the stability, we examine how the pressure and toroidal current density evolve during the ELM cycle. Due to the higher ELM frequency in the low shaping case, the average ELM cycle is shorter. As a result, the analysis for the low shaping discharge focuses on a 5 ms window following the ELM crash and a 0.5 ms period before the next ELM. In contrast, the high shaping case, which features a lower ELM frequency, allows for a longer ELM cycle analysis, covering 9 ms.

Figure 6.2 presents the corresponding plots, where radial positions are indicated in

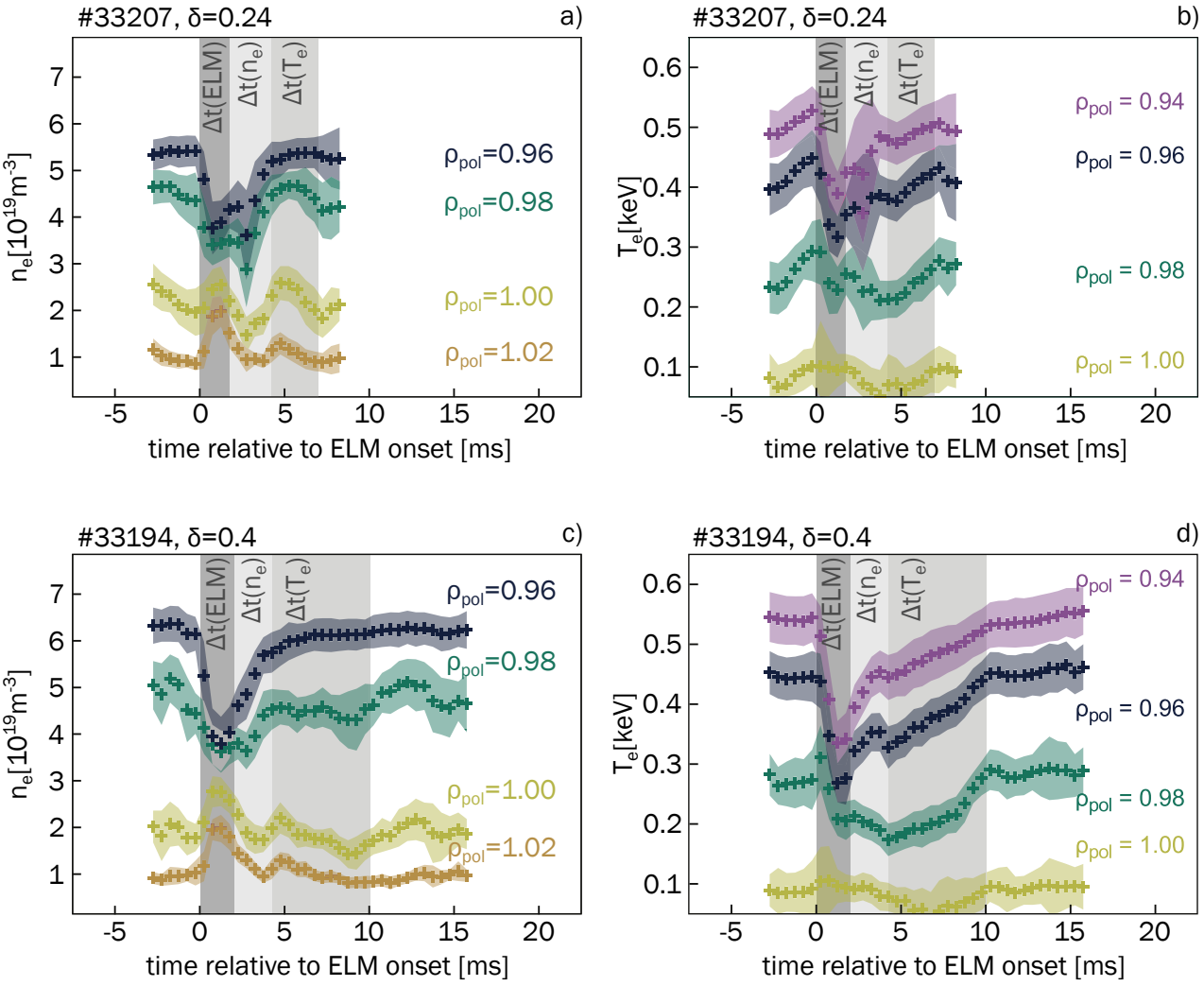

Figure 6.1: Figures adapted from [115]. Inter-ELM pedestal evolution is illustrated for electron density (n_e) in panels (a) and (c) and for electron temperature (T_e) in panels (b) and (d), at various radial positions across the pedestal (ρ_{pol}). Panels (a) and (b) correspond to the low-δ case, while panels (c) and (d) represent the high-δ case. In all scenarios, the n_e pedestal is re-established before the T_e pedestal, and the sequence of recovery phases remains consistent. Notably, the duration of the T_e pedestal recovery phase (Δt_{T_e}) and the pre-ELM phase increases with higher δ, correlating with a reduction in f_{ELM}.

different colours, ranging from yellow for the outermost region to dark blue for the outer core/pedestal top. The x-axis represents time relative to the ELM onset, while the y-axis shows various quantities of interest, mapped to illustrate their evolution over the ELM cycle.

Panels (a) and (b) in figure 6.2 illustrate the evolution of pressure throughout the ELM cycle for the two shaping cases. The behaviour is largely comparable and consistent with expectations. Following an ELM crash, pressure values drop significantly across all radial positions. In the low shaping case, the pressure begins to recover, particularly deeper in the pedestal, at $\rho = 0.98$ and inward. This recovery continues until a collapse occurs.

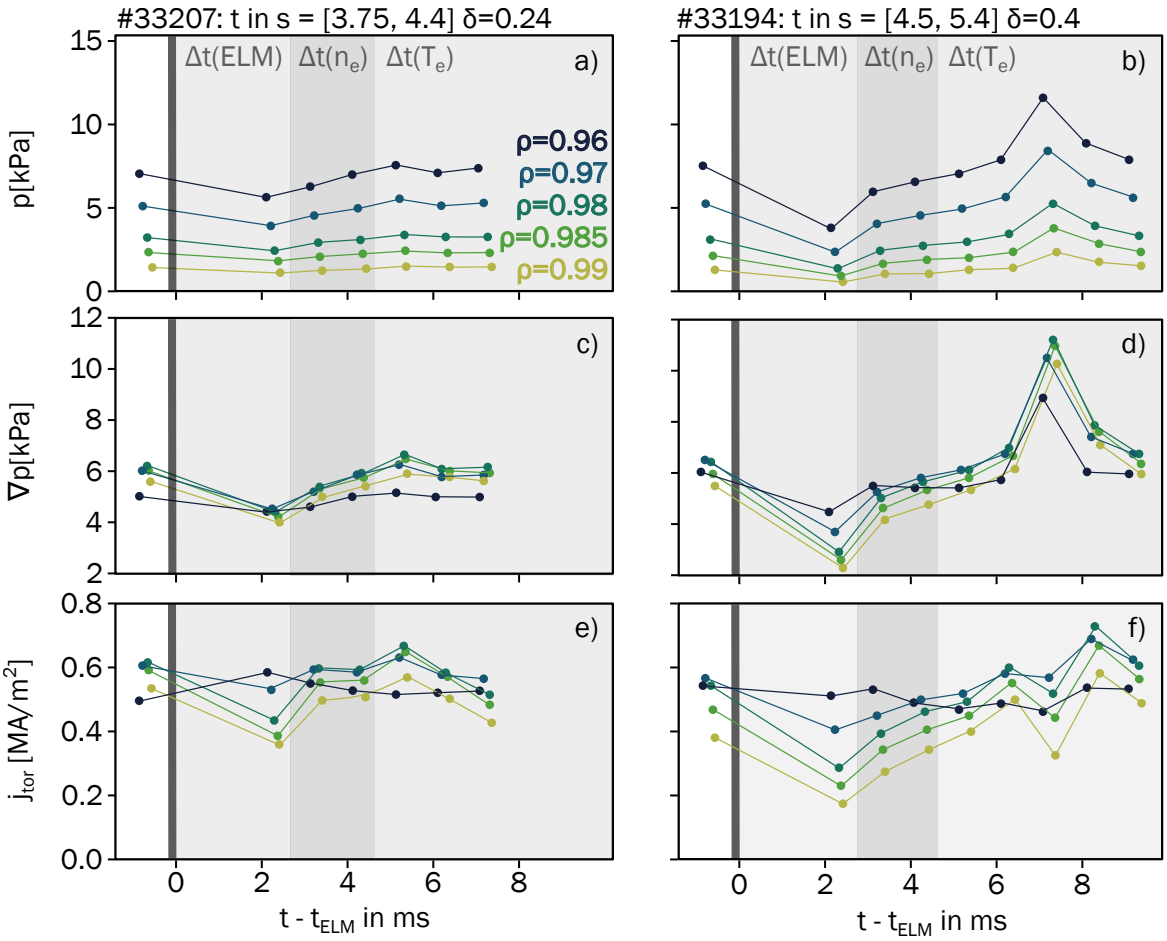

Figure 6.2: Inter-ELM evolution of pressure p (in a and b), pressure gradient ∇p (in c and d) and toroidal current density j_{tor}. In the left column, an ELM-cycle from the low shaping discharge, and in the right column, an ELM-cycle from the high shaping discharge is depicted. Different colours mark different radial positions. The x-axis is marking the time relative to ELM onset, with gray areas marking different pedestal recovering phases.

In the high shaping case, the pressure values initially exhibit a similar trend to the low shaping case, with comparable growth up to the point just before the low shaping case experiences its collapse. However, in the high shaping case, the pressure continues to grow further, reaching a secondary peak. This additional phase of growth in the high shaping case is a notable distinction and underscores the differences in pressure dynamics between the two configurations. In figure 6.2a and 6.2b, the gradients appear to decrease just before an ELM. However, this is likely due to the fact that ELMs are not perfectly periodic. The evolution of ∇p, which represents the pressure gradient taken as a derivative along the normalized dimensionless coordinate ψ_N, also mirrors these trends. Following an ELM crash, the pressure gradient collapses significantly in both shaping cases. However, in the high shaping case, the gradient experiences a much more pronounced collapse. In the low shaping case, the recovery of ∇p is limited by the shorter ELM cycle, as another ELM crash occurs before the gradient can

fully develop. In contrast, the high shaping case demonstrates continued growth of the gradient, reflecting the extended ELM cycle and the differences in the pedestal dynamics between the two shaping configurations. In figure 6.2a and 6.2b, the gradients appear to decrease just before an ELM. However, this is possibly due to the fact that ELMs are not perfectly periodic and some points are caught from the already collapsed pedestal. It is also possible that at that point, modes in the pedestal appear that increase transport and flatten the pressure gradient again.

Panels (e) and (f) show the toroidal current density, j_{tor}, for the low and high shaping discharges, respectively. In both cases, the dark blue curve, corresponding to $\rho = 0.96$, remains relatively flat and shows minimal variation throughout the ELM cycle. This behaviour aligns with expectations, as the bootstrap current is located primarily in the steepest pedestal region.

At other radial positions, we observe significant growth in j_{tor} during the ELM cycle for both plasma shapes. Comparing the behaviour in the second phase at $t = 4$ ms, we note that j_{tor} is slightly lower in the highly shaped discharge (panel f). In the low shaping discharge, this point marks the maximum j_{tor}, as it decreases afterwards, despite relatively constant ∇p. In the high shaping case, on the other hand, both j_{tor} and ∇p keep increasing.

From these observations, we can draw several important conclusions that will be useful for the subsequent analysis of ideal ballooning stability. In the low shaping case, after an ELM crash, quantities such as p, ∇p, and j_{tor} all increase during phase two, marked as $\Delta t(n_e)$, where the electron density is recovering. However, from the radial profiles, we know that during this phase, the electron temperature does not yet reach its full value. In the third phase, marked as $\Delta t(T_e)$, although T_e continues to increase, the total pressure p remains constant, ∇p stabilizes, and j_{tor} even starts to decrease. Additionally, in figure 6.1a it can be noted that in the steepest gradient region, at $\rho_{pol} = 0.98$, the electron density is even slightly decreasing, which is not the case at the pedestal top position $\rho_{pol} = 0.96$.

In contrast, for the high shaping case, the behaviour is notably different. Here, p increases during both the second and third phases, ∇p continues to grow in the third phase, and j_{tor} also shows an increase during this final phase. These distinctions between the two shaping configurations are intriguing and will play a key role as we move forward with our analysis.

Now, we continue to analyse the local IBMs and the stabilising and destabilising factors influencing them, following a similar approach as in the previous chapter. Figure 6.4 illustrates key quantities: the first row (panels a and b) depicts the global, magnetic surface-averaged shear s; the second row (panels c and d) presents both the experimental (α_{exp}, shown as connected dots) and critical (α_{crit}, represented by dashed lines) normalised pressure gradients; and the final row shows the ideal ballooning stability factor $F_{marg} = \alpha_{exp}/\alpha_{crit}$.

Examining the magnetic shear s in 6.3a and 6.3b, we observe very distinct behaviours in the two shaping cases. In the low shaping case, at $\rho_{pol} > 0.97$, s initially decreases during phase II $\Delta t(n_e)$ before increasing again during phase III $\Delta t(T_e)$. This trend aligns with the evolution of the toroidal current density j_{tor} shown in figure 6.2e, where j_{tor} decreases during phase III, thereby driving an increase in s. Conversely, in the high shaping case, s behaves differently: it increases sharply following an ELM

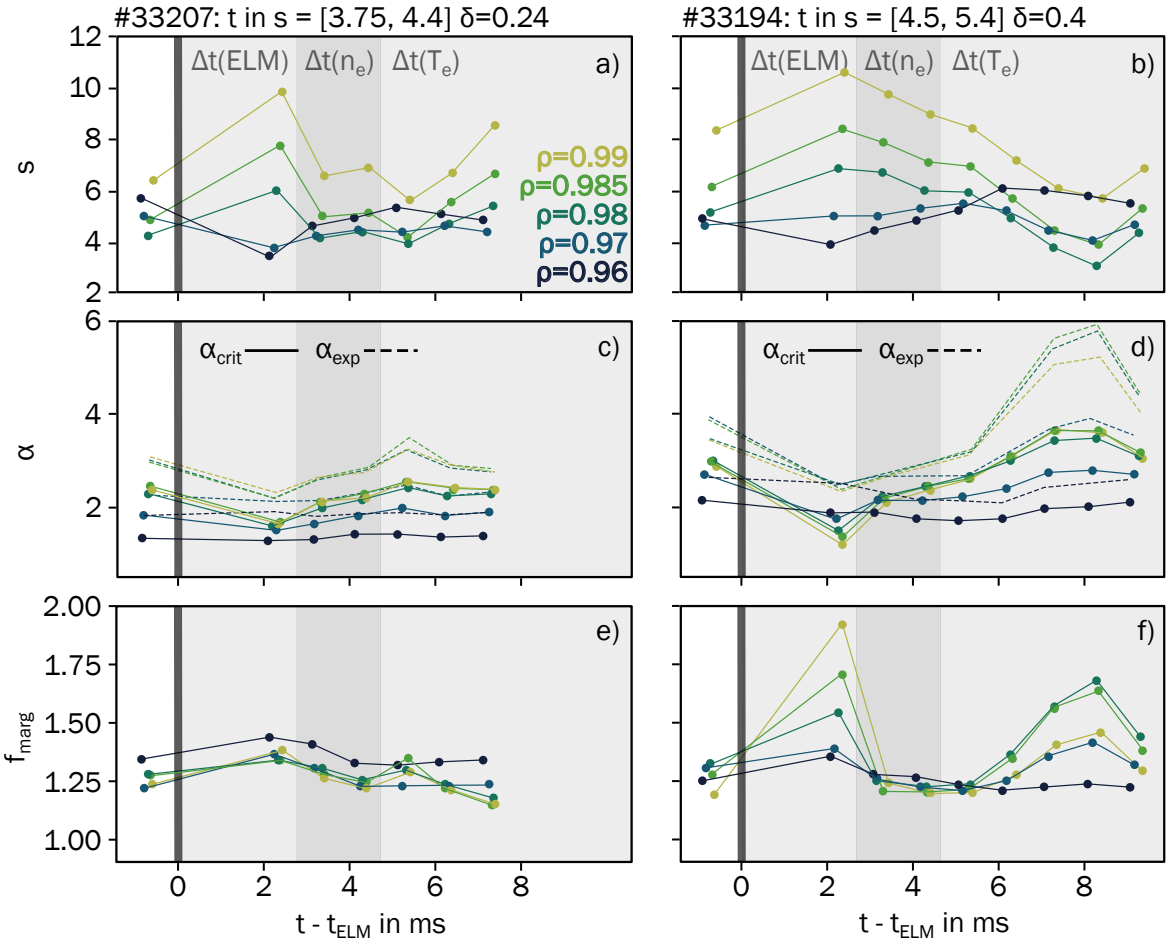

Figure 6.3: Inter-ELM evolution of surface averaged magnetic shear s (in a and b), experimental (solid lines) and critical (dashed lines) α (in c and d) and marginal stability factor $F_{marg}=\alpha_{crit}/\alpha_{exp}$. In the left column, an ELM-cycle from the low shaping discharge, and in the right column, an ELM-cycle from the high shaping discharge is depicted. Different colours mark different radial positions. The x-axis is marking the time relative to ELM onset, with gray areas marking different pedestal recovering phases.

crash and subsequently decreases throughout the whole ELM cycle. This behaviour can be attributed to the increase in j_{tor} seen in figure 6.2g, which modifies the safety factor q in a manner that continuously reduces s over time.

If we take into account the behaviour of s, as well as ∇p and j_{tor}, we can see some interesting trends. In the low shaping case, shown in figure 6.3c, the normalised pressure gradient α increases during phase II, where n_e is recovering, but it remains constant in phase III. Specifically, α_{exp} stays constant during this phase, while α_{crit} first increases and then slightly decreases. In contrast, this pattern does not occur in the high shaping (6.3d). After phase II is completed—when n_e has fully recovered and T_e is still recovering—the critical values α_{crit} increase significantly (despite s decreasing), and α_{exp} also continues to rise. This suggests that during phase III, the high shaping case may enter the second stability region. Supporting this, we observe

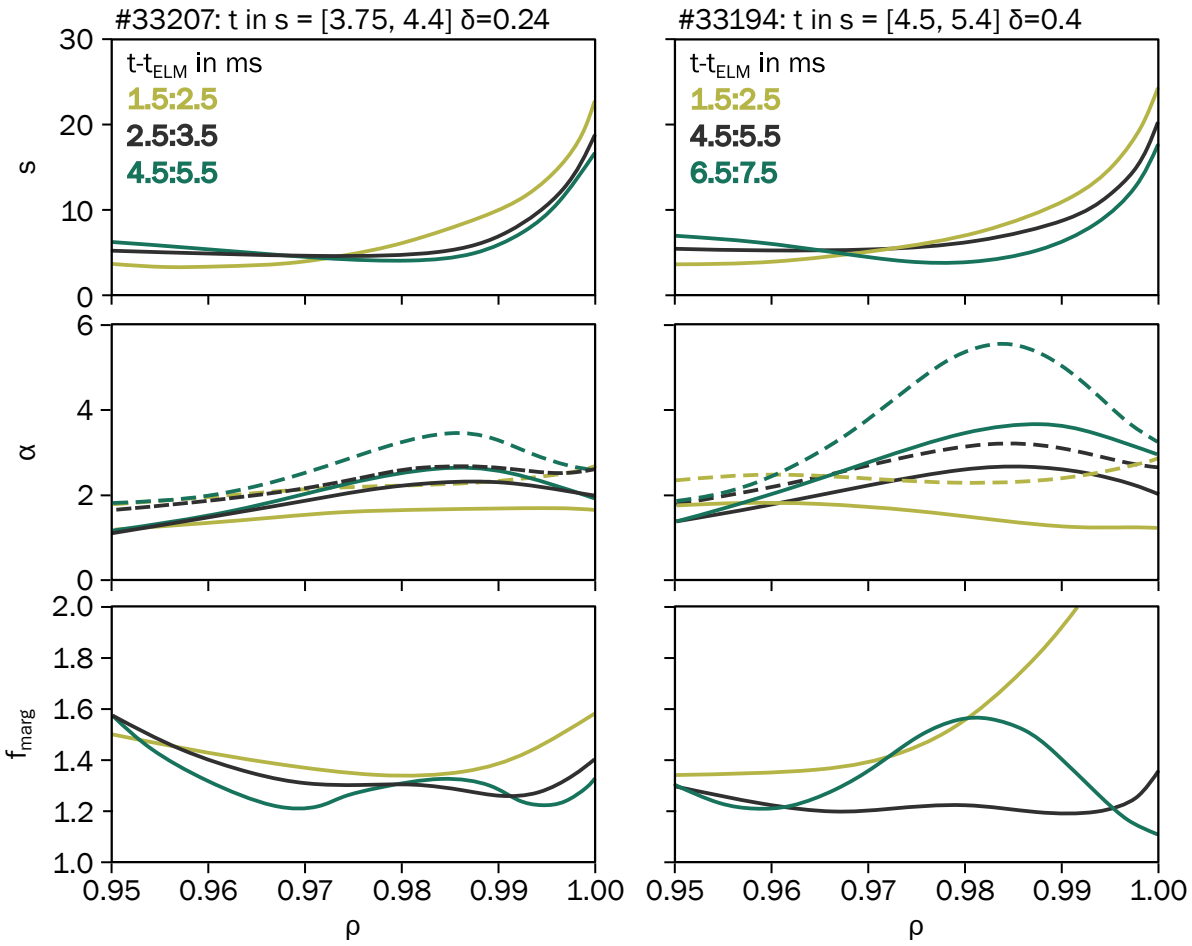

Figure 6.4: Radial profiles of the local IBM relevant quantities: surface averaged magnetic shear s (in a and b), experimental and critical α (in c and d) and marginal stability factor $F_{marg}=\alpha_{crit}/\alpha_{exp}$. In the left column, an ELM-cycle from the low shaping discharge, and in the right column, an ELM-cycle from the high shaping discharge is depicted. Three phases of the ELM-cycle are taken for each discharge, relevant to the ELM onset, these are: phase I (flat gradient) - 1.5–2.5 ms; phase II (n_e recovered) - 2.5 – 3.5 ms in low shaping and 4.5 – 5.5 ms in high shaping; and phase III - 4.5 – 5.5 ms in low shaping and 6.5 – 7.5 ms in high shaping.

that the steepest parts of the pedestal, at $\rho = 0.98$ and $\rho = 0.97$, α_{crit} show the largest increases, while s decreases most significantly at these radial positions.

In the same figure 6.3, panels e and f highlight this phenomenon more clearly by showing F_{marg}. In the low triangularity case, F_{marg} at the pedestal top remains fairly constant during phase III, but in the middle and foot regions ($\rho = 0.99$, 0.985, and 0.98), it briefly increases (corresponding to the decrease in s around 5 ms) before continuing to decrease. In contrast, for the high shaping case, F_{marg} remains fixed at a low value for $\rho = 0.96$, while all other radial positions show a significant jump during phase III as T_e recovers.

Based on the previously analysed plots, the following hypothesis regarding the behaviour during one ELM cycle emerges: The cycle begins with an ELM crash, which disrupts the edge pedestal. The density, n_e,

and the ion temperature T_i are the first to recover. In the low shaping, the n_e recovery drives the normalised pressure gradient α, to a maximum value. At this point, due to the lack of access to the second stability region, the total ∇p is clamped. After that, the electron temperature, T_e, begins to recover, likely driven by transport processes [116].

The first time point of $\Delta t(T_e)$ lies within the second stability region. This conclusion arises from the observation that f_{marg} is higher in the middle of the pedestal compared to the top, as shown in figure 6.3e, at t = 5.5 s. At this stage, α shows a brief increase, suggesting the system is temporarily accessing the second stability region. However, at the subsequent time point, the pressure gradient, ∇p, becomes clamped in the 1st stability. This clamping prevents α from increasing further, forcing the system deeper back into the first stability region. As a result, n_e slightly decreases in the steepest gradient region of the pedestal (but not at the top), as shown in figure 6.1a. This decrease is likely caused by ballooning modes that limit ∇p. Meanwhile, T_e continues to rise, potentially due to transport effects becoming more pronounced.

Subsequently, a series of interconnected processes occur: n_e decreases further, T_e increases, and the bootstrap current lowers. The reduction in the bootstrap current causes the magnetic shear, s, to increase, which pushes the system further into the first stability region.

Finally, around t = 7.5 s, another ELM is triggered, which is caused by the global peeling-ballooning stability mechanism, which governs the overall stability of the edge pedestal.

To visualise this phenomenon differently while conveying the same point, we examine individual profiles at different phases of the ELM recovery. In figure 6.4, the first row shows the magnetic shear, s, the second row presents the normalised pressure gradient, α, and the third row depicts f_{marg}. In this case, the x-axis represents the normalised radius ρ_{pol}, allowing us to analyse the entire profile.

The left-hand panels correspond to the low shaping case, while the right-hand panels represent the high shaping case. For the low shaping case, we again selected time points to represent three phases: phase I no pedestal: 1.5-2.5 ms; phase II a phase with a developed n_e 2.5:3.5 ms; and phase III a phase with both developed n_e and T_e: 4.5-5.5 ms. Notably, the third phase corresponds to a brief time window where the low triangularity configuration allows access to the second stability region. In the high shaping case the chosen phases are the same, however the time points are different due to the longer ELM-cycle. That is phase I again corresponds to 1.5-2.5 ms after the ELM crash; phase II is now 4.5-5.5 ms; and finally phase III corresponds to 6.5-7.5 ms.

First, let us compare the evolution of s between the low and high shaping cases. In both cases, the trend is qualitatively similar: s decreases in the steep region of the pedestal as the recovery progresses. This behaviour is attributed to the growing edge current, which flattens the q-profile, however it is significantly more pronounced in the high shaping case since the bootstrap current grows throughout all three phases, unlike the low shaping discharge, where the growth is suspended in the third phase.

Next, consider α, shown in panels (c) and (d). Once again, the qualitative behaviour is comparable between the two cases; however, significant quantitative differences are again evident. In the high shaping case, there is much deeper access to the second

stability region, as indicated by the very high α_{crit} in panel (d), and the broad f_{marg} profile with two local minima in (f), which signals access to second stability. In contrast, the low shaping case exhibits narrower and less stable access to the second stability region, as seen in panel (e). Furthermore, as previously noted in figure 6.3, this access is quickly lost as the edge current decreases over time.

6.2 Analysis in the s - α space

To confirm the hypothesis regarding access to the second stability region, we again utilise s-α diagrams, as in the previous chapter. To illustrate how access to second stability is lost, we analyse the same three specific time points for the low and high shaping case. The first phase corresponds to the state immediately following the ELM crash, when the pedestal is fully collapsed. The second phase, from 4.5 to 5.5 ms, occurs when n_e has fully recovered, and T_e is just beginning to recover. The final phase, from 6.5 to 7.5 ms, represents the later stage of pedestal recovery, and in the low shaping discharge, this is the time point where we expect it to briefly have access to 2nd stability.

In the s-α diagrams, we first focus on a specific radial position that corresponds to the maximum ∇p region, taken as $\rho_{pol} = 0.9825$ for both discharges. Figure 6.5 illustrates the results, with the low shaping case displayed in the first row and the high shaping case in the second row, while the phases progress from left to right.

In the first phase, both the low shaping and high shaping cases remain entirely within the first stability region, reflecting the fully collapsed state of the pedestal. By the second phase (4.5–5.5 ms), in both shapes plasma accesses the second stability region, but it remains in a transitional state, somewhere between the first and second stability. The most significant difference arises in the third phase (6.5–7.5 ms), where the low shaping case is pushed back into the first stability region, constrained by the passage boundaries. In contrast, the high shaping case firmly resides in the second stability region. In this state, α is no longer limited by the local ideal ballooning modes (IBMs), highlighting the better stability achieved in the high shaping configuration.

If we compare figure 6.5c and 6.5f we can notice that several effects play a role for this development: the stability boundary shifts upwards in the high shaping, the global s is lower in high shaping and the high shape has higher values of α.

For the pedestal top, it is crucial to note that two different radial positions are used due to the differing pedestal widths between the low and high shaping cases. In the low shaping discharge, the radial position is taken at $\rho_{pol} = 0.97$, reflecting the narrower pedestal. In the high shaping case, the radial position is set at $\rho_{pol} = 0.96$, corresponding to the wider pedestal.

A particularly striking observation emerges from this analysis. Regardless of the phase and despite the fact that α increases as the phases progress, the relative position between the operational point and the stability limit remains remarkably consistent. In fact, it appears to be almost identical across the phases — a surprising result that underscores the robustness of this behaviour. Note that also in chapter 5 figure 5.5b and 5.5d - where the pedestal top for the non-synchronised pre ELM case is shown - shows the same relative position of

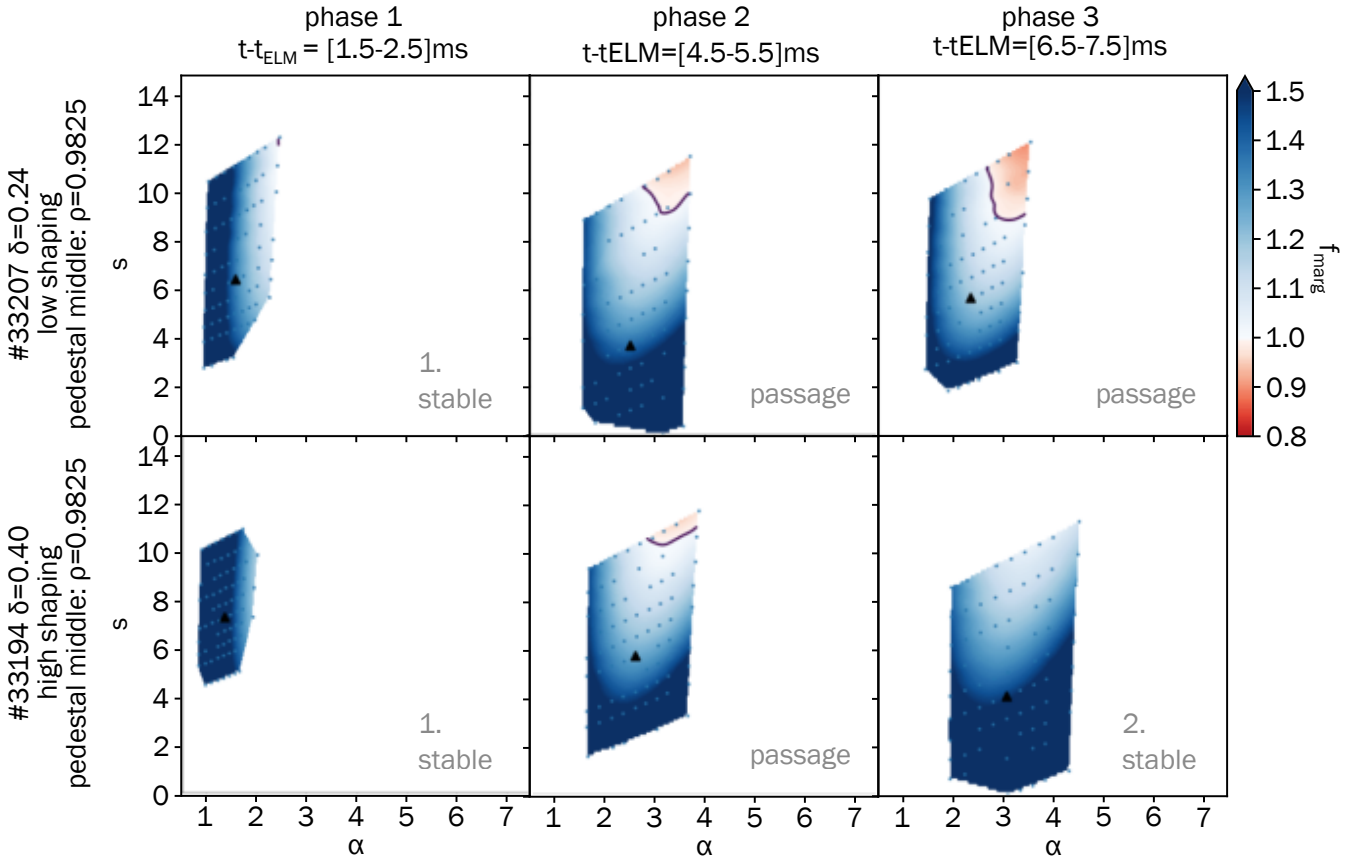

Figure 6.5: s-α diagrams are shown for three distinct phases within the ELM cycle for low shaping discharge #33207 (first row) and high shaping discharge #33194 (second row) in the pedestal middle. Blue contours indicate marginally ballooning-stable regions, and red contours denote marginally ballooning-unstable regions. The solid line marks the ballooning stability limit, where $F_{marg} = 1$. Operational points are highlighted with black triangles.

boundary and operational point.

6.3 Conclusions

Building on our previous understanding, we know that ion temperature T_i and electron density n_e recover very quickly following an ELM crash, and the electron temperature T_e takes more time. However, to deepen our perspective on the ELM cycle, we analysed local ideal ballooning modes (IBMs), which serve as proxy for both the resistive ballooning modes and the kinetic ballooning modes. The analysis does not take into account the stabilising behaviour of the E × B shear and also not the destabilising effects of collisions or resistivity.

The emerging picture from this analysis is as follows. In the second phase of the ELM cycle, for both high and low shaping cases, the density begins to build up first. In the low shaping configuration, there is a brief window where conditions seem favourable for accessing the second stability region, and the bootstrap current starts to grow. However, this time window is short-lived, as the maximum pressure gradient becomes rapidly constrained by local IBMs in the first stable region, effectively clamping the progression of the pedestal build up.

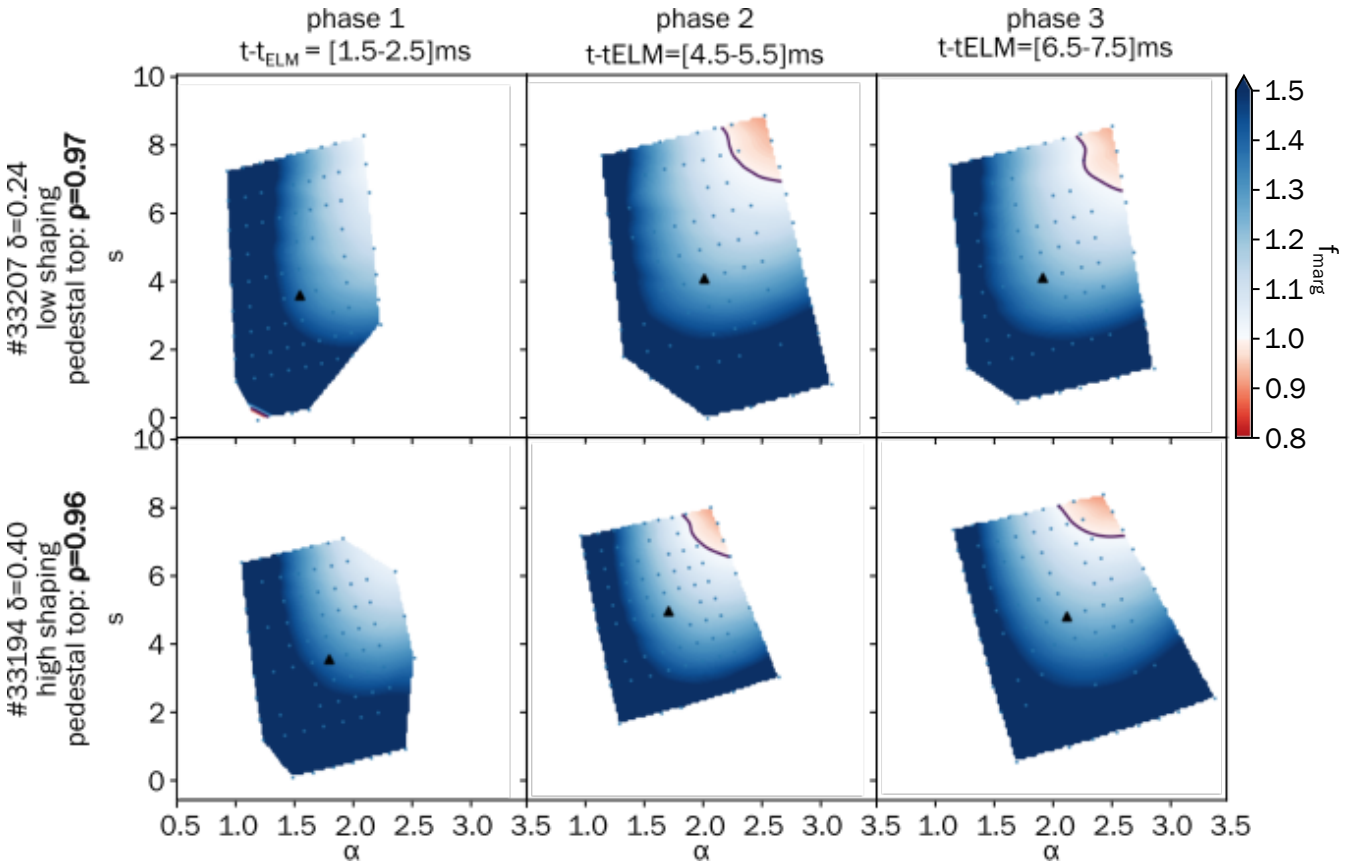

Figure 6.6: For the pedestal top, s-α diagrams are shown for three distinct phases within the ELM cycle for low shaping discharge #33207 (first row) at ρ = 0.97 and high shaping discharge #33194 (second row) at ρ = 0.96. Blue contours indicate marginally ballooning-stable regions, and red contours denote marginally ballooning-unstable regions. The solid line marks the ballooning stability limit where F_{marg} = 1. Operational points are highlighted with black triangles.

In contrast, the high shaping case provides more robust access to the second stability region due to the favourable geometry of the plasma. This enables the pressure gradient to continue increasing without significant constraints. This difference also leads to distinct behaviours in the toroidal current density. In the high shaping case, the current density continues to grow alongside the increasing pressure gradient. Conversely, in the low shaping case, we observe stagnation in the pressure gradient, likely caused by the influence of IBMs.

These contrasting behaviours may partially stem from the observed decrease in pedestal density as the electron temperature rises, observed in the low shaping case. Since density plays a significant role in the bootstrap current, this interplay becomes critical. However, collisionality may also contribute to these differences, and further work is needed to disentangle these effects.

In the high shaping case, the current, gradient, and other related parameters increase largely unhindered by ideal ballooning modes, showing no signs of the stagnation observed in the low shaping scenario. This is due to the stabilising effect of locally negative magnetic shear, which

becomes particularly evident during phase III. As shown in figure 6.3b, magnetic shear (s) decreases significantly in the high shaping case, whereas it increases in the low shaping case, as seen in figure 6.3a. This difference appears to be a key factor in the observed behaviours.

Further insights were gained from the s-α diagrams, which confirm the enhanced access to second stability in the high shaping case. Perhaps even more striking is the observation that, regardless of the chosen radial positions, the pedestal top exhibits qualitatively similar behaviour in terms of the relative positions of operational points and stability limits.

Despite these findings, several open questions remain. For instance, what drives the toroidal current to first increase and then decrease? This dynamic warrants further investigation to fully understand the underlying mechanisms at play. It is worth noting that these results are based on only two cases; however, they align with and confirm many of the trends explored in the previous chapter.

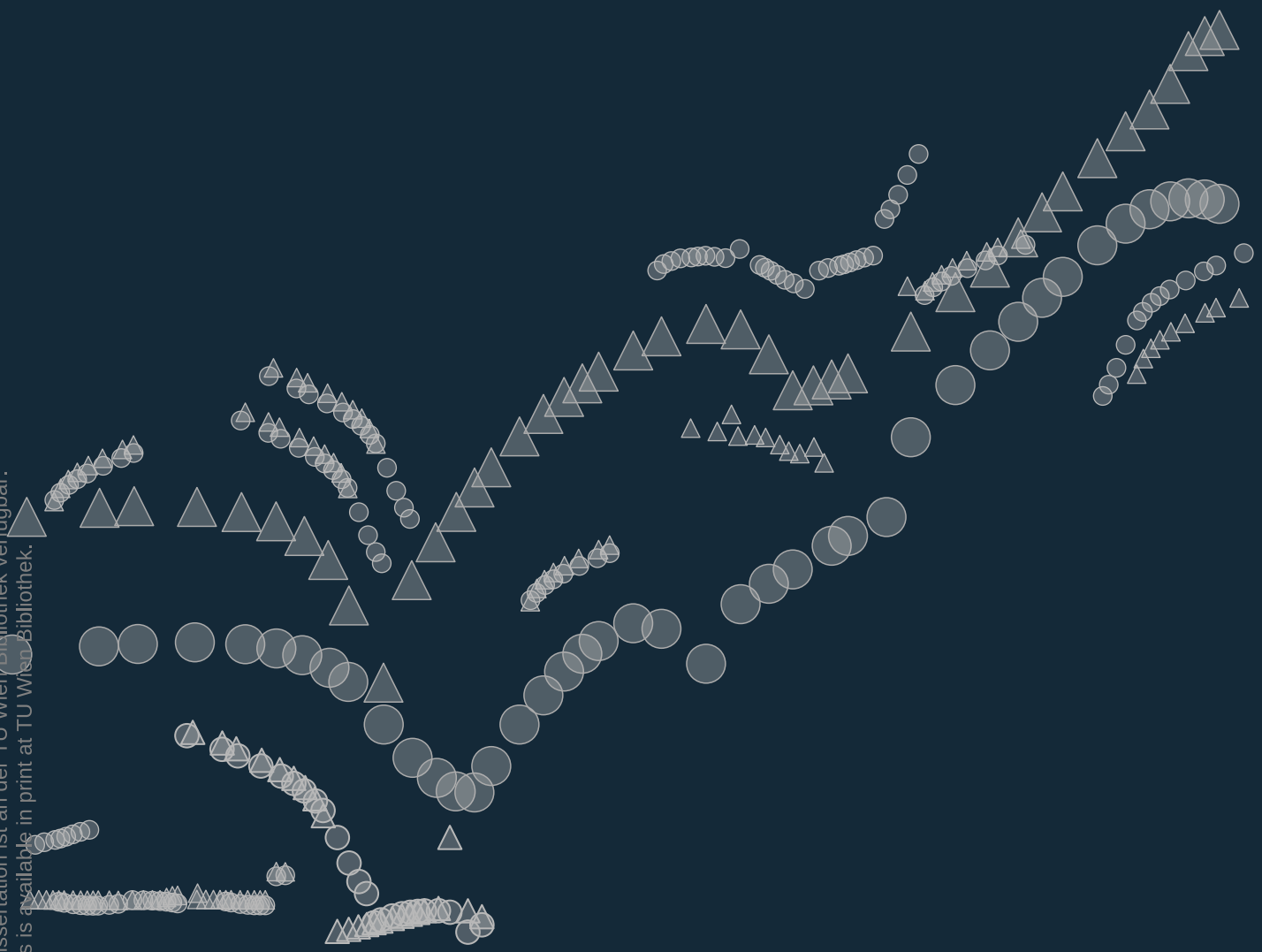

TRANSPORT ANALYSIS AND GYROKINETIC SIMULATIONS

7 Transport Analysis and Gyrokinetic Simulations

Having examined the MHD in considerable detail, using both ELM-filtering and ELM-synchronising techniques, it is important to highlight that the MHD analysis focuses on total pressure, and it incorporates information about ion and electron temperatures and densities only thought the effects they have on the bootstrap current. As discussed in chapters 5 and 6 this dependency is not completely straightforward, since it varies depending on the influence of density vs. temperature contributions and collisionality. Most importantly, the differences observed in the behaviour of density and temperature profiles of ions and electrons, indicate that it is necessary to expand the analytical tools applied.

Therefore, in this chapter, we explore how the heat and particle transport coefficients change as we vary β_{pol} and the plasma shape, using two new approaches. Firstly, with ASTRA, the transport analysis is performed to learn how particles and energy are distributed and evolve within the plasma. Gyrokinetics, on the other hand, delves into the detailed behaviour of charged particles in the presence of magnetic fields, capturing micro instabilities and turbulence, which are crucial for understanding the intricate dynamics observed in the experiments. Both tools were introduced earlier, in section 2.2.4, but their application here provides deeper insights into the specific differences noted in density and temperature evolution for ions and electrons.

In this chapter, we return to the dedicated discharges of this thesis #38472 and #38819. In this section, the medium β_{pol} discharge #38474 is omitted, partially to prevent overcrowding the analysis and partially because that experiment is heated with ECRH, whereas the chosen two discharges both have ICRH heating which enhances consistency of the results. Additionally, the medium β_{pol} discharge had some mismatch in the feedback, so that β_{pol} was not constant over the two different shapes. Here we also step away from the ELM-synchronisation and employ the filtering of the ELMs and take the median of selected time windows. The time windows are the same as described in section 4, namely for both discharges the low shaping phase is $t_1 = 2.8-3\,s$ and the high shaping phase is $t_2 = 5.3-5.5\,s$.

7.1 ASTRA Transport Simulations

7.1.1 Transport Coefficients

The experimental details for the analysed discharges are outlined in chapters ?? and 4, but they are summarised here again for clarity and completeness. Figure 7.1 shows again an overview of the kinetic profiles of: n_e, T_e and T_i. These serve as inputs for the simulations with the ASTRA code [121], which is employed in this section. Additionally, n_i is calculated using Z_{eff}, obtained via CXRS, as described in equation 3.3, with the same colours as in chapter 5: medians of the selected 200 ms are shown in red for the low shaping phases and blue for the high shaping phases. Here, the dotted lines represent the low β_{pol} discharge #38819 and the dash-dot lines the high β_{pol} discharge #38472.

To summarise the overview provided in chapter 4, the density n_e in figure 7.1a is found to vary significantly with shaping but shows less dependence on β_{pol}. In contrast, the electron temperature T_e in 7.1b exhibits notable differences primarily in the outer core region, while the pedestal width and height remain relatively consistent across the cases. The ion temperature shown in figure 7.1c, however, is strongly dependent on β_{pol}, with little to no influence from shaping. Notably, the entire T_i pedestal increases uniformly with increase in β_{pol}, affecting both the top and foot. As a result, changes in pedestal width are not particularly pronounced, though some variations are observed.

The profiles obtained are input into ASTRA, which then calculates the heat and particle transport coefficients. The results of these computations are compared. First, it is important to note that the scales used

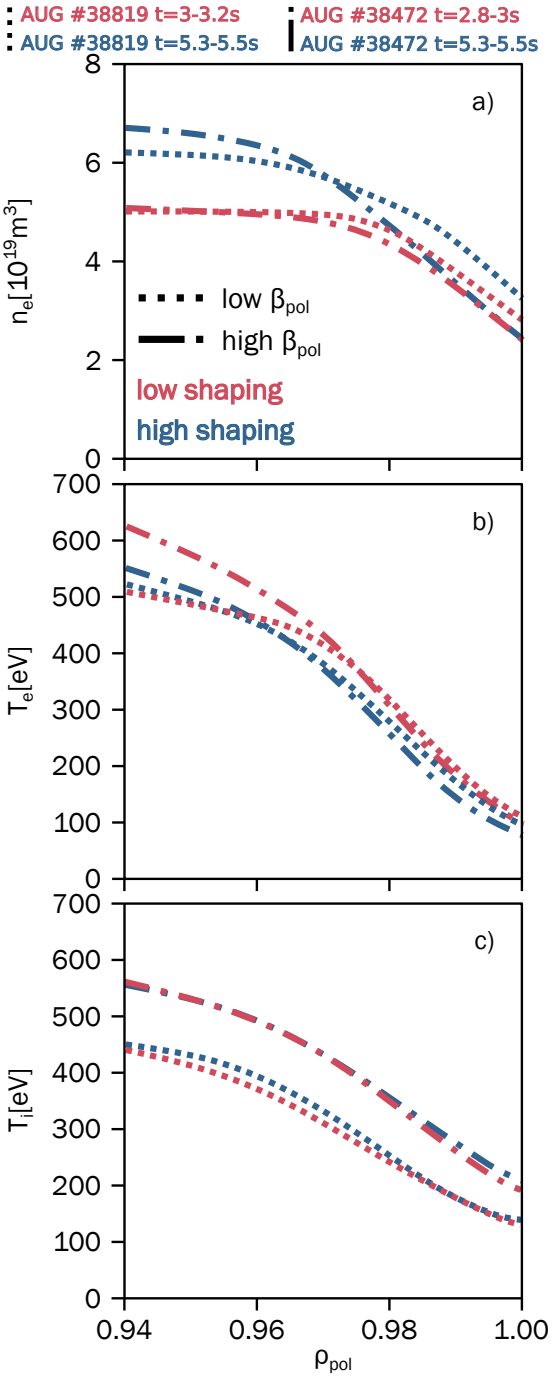

Figure 7.1: Kinetic profiles used as an input for ASTRA simulations: n_e shown in a), T_e in b), and T_i in c). The dotted lines mark the low β_{pol} discharge #38819 and the dash-dot lines show the high β_{pol} discharge #38472. The low shaping phases are shown in red and high shaping phases in blue.

in figures 7.2 and 7.3 are logarithmic. This choice is necessary to capture the wide range of scales at which different components of the ion heat diffusivity operate, providing a comprehensive view of both the neoclassical and turbulent contributions. The colour scheme stays the same (red shows the low shaping and blue the high shaping phases), circles show the low β_{pol} discharge #38819 and crosses the high β_{pol} discharge #38472. We begin the interpretation of results with particle transport, shown in figure 7.2a.

The analysis of particle transport presents certain challenges due to the uncertainty regarding the neutral density at the separatrix, which is proportional to the source term for D_{eff}, the effective diffusivity for electrons and ions. A scan of neutral densities and some further analysis was performed, as detailed later in this chapter, but the results were inconclusive to what the exact neutral density is. However, the qualitative trends remain consistent despite this uncertainty, although the quantitative values are not definitively known.

In figure 7.2a the particle diffusivity is shown. From a qualitative perspective, in the outer core — particularly between $\rho = 0.92$ and $\rho = 0.94$ — there is evidence of a mechanism driving particle transport that is strongly dependent on β_{pol}. Beyond $\rho = 0.94$ and approaching the separatrix, the observed differences are predominantly influenced by shaping effects. Interestingly, the transport shows a substantial drop-off at the pedestal top, with values decreasing to approximately 10^{-2}, leaving minimal transport activity. Although an increase in neutral density at the separatrix would elevate these values, the overall transport reduction in the pedestal remains significant.

The separation between the red and blue trends, representing different shapes,

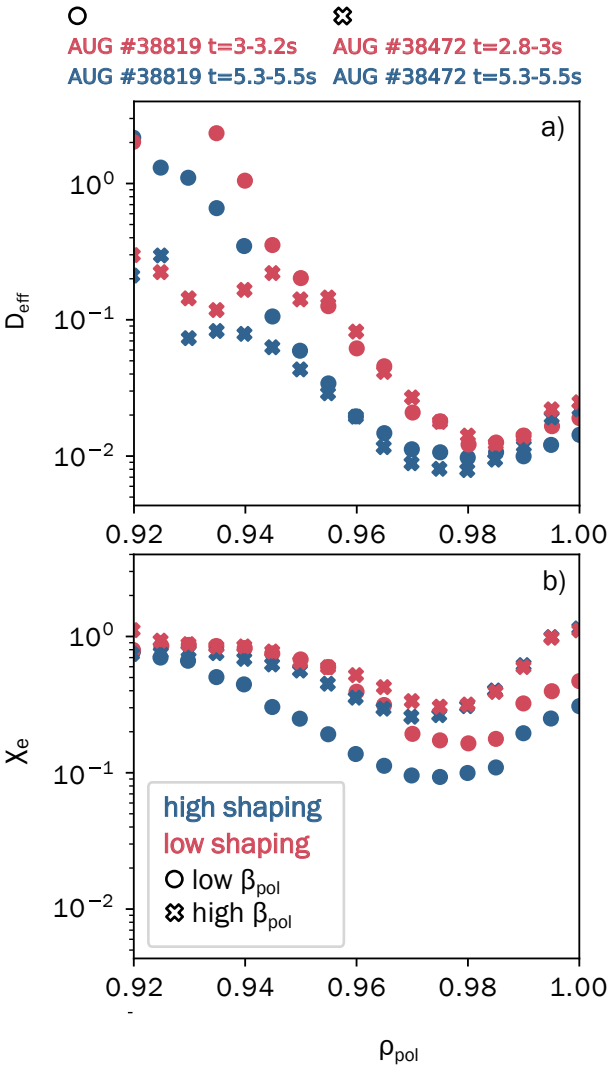

Figure 7.2: ASTRA results for effective particle diffusivity D_{eff} in a) and electron heat diffusivity χ_e in b). The circles mark the low β_{pol} discharge #38819 and the crosses mark the high β_{pol} discharge #38472. The low shaping phases are shown in red and high shaping phases in blue.

aligns with the differences in the pedestal width of n_e. Since ASTRA matches the profiles, this is not too surprising, however it becomes evident that particle transport predominantly occurs at the pedestal top, and it is reduced in the pedestal itself.

With particle transport discussed, the focus now shifts to the electron heat trans-

port, as shown in figure 7.2b. As anticipated, the results for electron heat transport exhibit smaller differences. The largest difference is observed in the low-β_{pol}, high-shaping case, which demonstrates lower values of χ_e in the whole pedestal. In the pedestal middle and foot regions, a stronger β_{pol} dependence is apparent, while the dependence on shaping is less pronounced. High-β_{pol} cases show negligible changes with shaping, whereas low-β cases exhibit a decrease in χ_e with higher shaping. Overall, these results align with expectations that higher shaping has higher electron heat diffusivity, and that there is only weak beta dependence. One should note that χ_e reflects mostly turbulent transport, and the neoclassical contribution is negligible due to the much smaller particle mass, as shown in equation (2.71).

The next analysis focuses on the ion heat diffusivity χ_i, as depicted in 7.3. The ion heat diffusivity is particularly interesting because ASTRA provides both χ_i (total ion heat diffusivity) and $\chi_{i,neo}$ (the neoclassical component of ion heat diffusivity). Consequently, the ion heat diffusivity can be conveniently decomposed into its neoclassical component, $\chi_{i,neo}$, and the turbulent component, $\chi_{i,turb} = \chi_i - \chi_{i,neo}$. This allows for a detailed observation of how the neoclassical and turbulent contributions to the ion heat diffusivity differ.

When observing the total χ_i in figure 7.3a, there is a noticeable reduction in transport within the pedestal region, compared to the core plasma, which aligns with expectations. The transport then increases again at the pedestal foot. In the outer core, it is less clear which mechanism dominates the transport, but in the pedestal foot region, a separation between crosses and circles indicates that β_{pol} has a stronger influence than shaping.

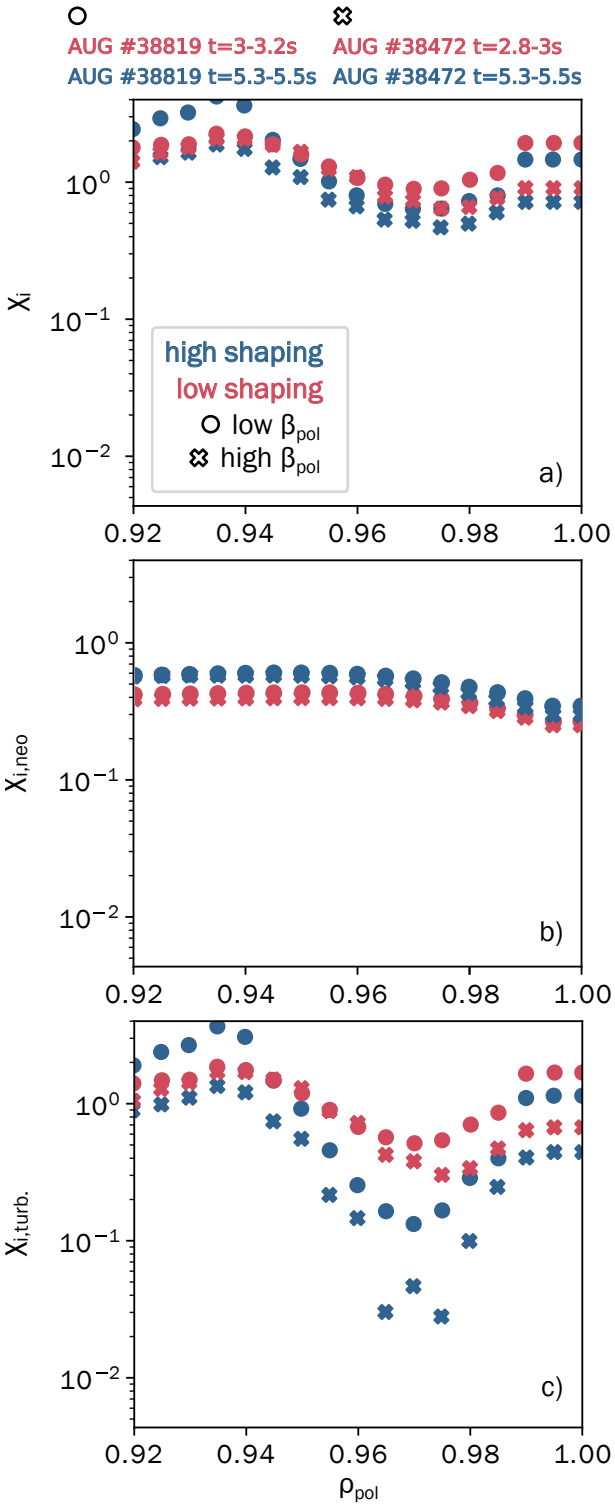

Figure 7.3: ASTRA results for total ion heat diffusivity χ_i in a), its neoclassical contribution in b) and the turbulent contribution in c). The circles mark the low β_{pol} discharge #38819 and the crosses mark the high β_{pol} discharge #38472. The low shaping phases are shown in red and high shaping phases in blue.

It should be noted that χ_i decreases with increased shaping. However, because constant β_{pol} is achieved with the use of the flexible NBI system, the amount of heating power also decreases with shaping. These effects balance out, resulting in a temperature profile that varies exclusively with β, showing no dependence on shaping. It is worth emphasising that, despite these β_{pol} and shaping variations, the values of χ_i remain relatively high overall.

Turning now to the neoclassical contribution, shown in figure 7.3b, we observe that $\chi_{i,neo}$ remains relatively constant and high, however slightly decreases in the pedestal region due to its dependence on n_i. While there is a slight increase with shaping and a minor decrease with β, these changes are not substantial.

Lastly, figure 7.3c shows a clear trend for the turbulent part of heat transport: turbulence suppression is more pronounced for high β and high shaping, particularly in the middle of the pedestal. This aligns with the observation from the MHD analysis, where access to the second stability region was achieved in this area. Turbulence intensifies again at the pedestal foot, which is a noteworthy detail.

Another observation is that in the pedestal foot region, ranging from 0.99 to 1, increasing shaping causes $\chi_{i,neo}$ to increase while $\chi_{i,turb}$ decreases. As a result, the total χ_i experiences minimal change. On the other hand, both $\chi_{i,neo}$ and $\chi_{i,turb.}$ decrease with the increase in β_{pol} which enhances the difference in total χ_i.

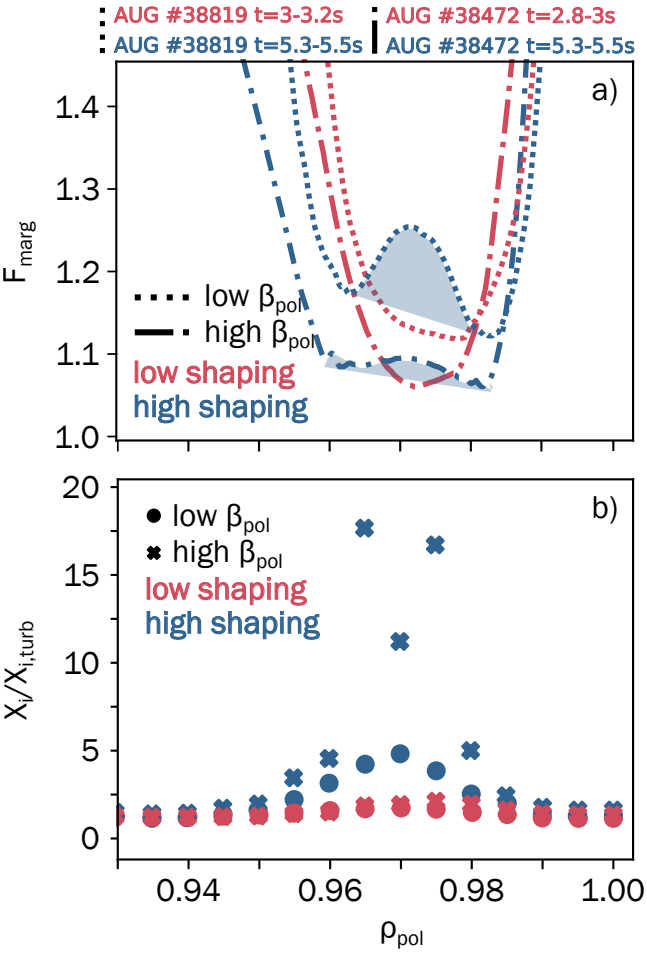

Figure 7.4: Comparison of local IBMs marginal stability factor $f_{marg} = \alpha_{crit}/\alpha_{exp}$ shown in a) and the ratio of total ion heat diffusivity χ_i and turbulent ion heat diffusivity $\chi_{i,turb}$ depicted in b). In a) the dotted lines mark the low β_{pol} discharge,#38819, and the dash-dot lines show the high β_{pol} discharge, #38472. The low shaping phases are shown in red and high shaping phases in blue. In b) the circles mark the low β_{pol} and the crosses the high β_{pol} discharge. Low shaping phases are shown in red and high shaping phases in blue.

7.1.2 Comparison with local IBMs

To delve deeper into these findings, figure 7.4 presents two key plots for further investigation. In 7.4a the f_{marg} profiles discussed in chapter 5 are revisited, while 7.4b shows the ratio $\frac{\chi_i}{\chi_{i,turb}}$.

A short disclaimer: the f_{marg} profiles in 7.4a have been shifted to the left by $\rho = 0.003$ due to a misalignment identified during the analysis. Specifically, the input

pressure gradient and the output pressure gradient from HELENA equilibrium reconstruction exhibited this offset, therefore all HELENA outputs in this step were adapted to ensure alignment of the pressure gradients. This issue likely stems from how HELENA handles the total plasma current, which is integrated across the entire plasma up to the separatrix. Since HELENA requires a last closed flux surface—assumed here to be at $\rho = 0.997$—it redistributes the current differently than expected. Ideally, the plasma current density should be integrated from $\rho = 0$ to $\rho = 0.997$, but due to time constraints, this correction was not implemented in the frame of this thesis. It will, however, be addressed in future work.

The dotted lines in figure 7.4 represent low β_{pol}, while the dot-dash lines correspond to high β_{pol}. Similarly, low shaping is shown in red, and high shaping in blue. As previously discussed in chapters 5 and 6, high shaping cases grant the plasma access to the second stability region, allowing steeper gradients that are not limited by local IBMs. The two dips in the f_{marg} profile, shown in 7.4a, along with a small hill in the middle, indicate regions within the second stability. These areas, i.e. the small hills in the middle, although close to the stability limit, are devoid of ballooning modes. To highlight these local IBM-free regions, shaded blue areas are included in figure 7.4a.

We now look at the ratio of total ion heat diffusivity, χ_i, to its turbulent component, $\chi_{i,turb}$. A lower value of this ratio indicates that turbulent transport is comparable to the total transport. Typically, it is assumed (as supported by previous studies [122, 123]) that turbulent transport in the pedestal is suppressed, making it valid to approximate the pedestal heat diffusivity as purely neoclassical. However, the data in figure 7.4b demonstrate this assumption does not always hold.

For both high and low β_{pol}, the low shaping phases shown in red maintain a ratio of approximately 1.5–2 throughout the pedestal. This signifies that turbulent transport accounts for roughly half of the total transport, and is therefore far from negligible. In contrast, in high shaping cases, particularly in the pedestal top to pedestal middle region, this ratio significantly increases. For low β_{pol}, the ratio peaks around 5, while for high β_{pol}, it reaches a maximum of approximately 17.

This indicates that in conditions of high shaping and high β_{pol}, turbulent transport is greatly suppressed and becomes negligible compared to total χ_i. Furthermore, the radial extent of this suppression coincides with the regions of f_{marg}, reinforcing the relationship between shaping, transport dynamics, and local IBMs stability characteristics, which reflects the stability of KBMs.

An important insight arises from this observation: the suppression of turbulent transport in the pedestal is strongly linked to the shaping of the plasma and the access to second stability regions, particularly in high shaping and high β_{pol} cases. In these cases, the significant reduction in turbulent transport relative to the total χ_i aligns spatially with the regions where f_{marg} indicates second stability. Because the turbulent transport makes such a small contribution if KBMs have access to second stability, it is suggested that a large part of the turbulent transport in the pedestal top could be carried by the KBMs. Conversely, in low shaping cases, turbulent transport remains a substantial contributor across the entire pedestal, indicating that second stability access is a critical factor in determining whether turbulence can be effectively suppressed. This underscores

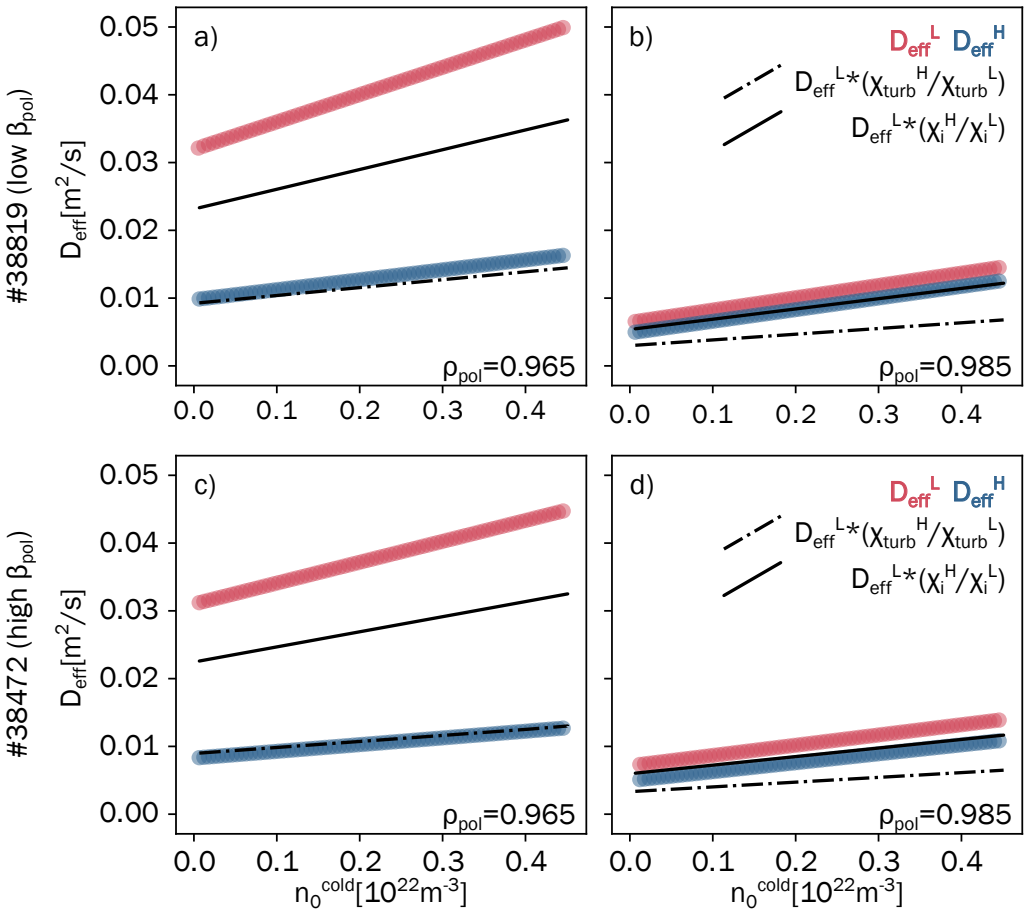

Figure 7.5: The separatrix neutral density is plotted on the x-axis, while the y-axis shows the effective particle diffusivity (D_{eff}). The left column corresponds to the outer core/pedestal top at $\rho_{pol} = 0.965$, and the right column represents the pedestal middle at $\rho_{pol} = 0.985$. The first row displays results for the low β_{pol} discharge (#38819), and the second row for the high β_{pol} discharge (#38472). Red and blue dots indicate the effective diffusivity in low and high shaping (D^L_{eff} and D^H_{eff}, respectively). Black lines represent different predictions for D^H_{eff}: the solid line assumes particle transport is proportional to ion heat diffusivity ($D^L_{eff} \cdot \chi^H_i/\chi^L_i$), while the dashed line assumes proportionality to turbulent diffusivity ($D^L_{eff} \cdot \chi^H_{turb}/\chi^L_{turb}$).

the importance of shaping in tailoring the transport dynamics within the pedestal and achieving optimal performance.

7.1.3 Scaling of Particle Diffusivity

The final aspect of the ASTRA results to be discussed involves performing a scan over the neutral density at the separatrix. The motivation for this analysis stems from recent studies on ASDEX Upgrade, which suggest that particle diffusivity exhibits behaviour proportional to ion diffusivity. This was indicated in [124], however, regarding the amount of gas puff, which influenced both channels, particle and heat transport, with the same factor. Specifically, the relationship $D^L_{eff}/D^H_{eff} = \chi^L_i/\chi^H_i$ has been observed, where superscripted L and H represent low and high shaping cases, respectively.

Figure 7.5 illustrates this analysis. The first row corresponds to the low-β_{pol} case, while the second row represents the high-β_{pol} case. The left panels depict results at $\rho_{pol} = 0.965$ (pedestal top), and the right panels focus on $\rho_{pol} = 0.985$ (pedestal middle).

The y-axis represents D_{eff}, while the x-axis denotes the neutral particle density at the separatrix. Red lines indicate ASTRA results for low shaping as the separatrix neutral density increases, whereas blue lines show the corresponding results for high shaping. These values are computed by ASTRA using the input density profile and separatrix neutral density.

Black lines represent the expected values of D_{eff} for high shaping, calculated under two assumptions: proportionality of D_{eff} with χ_i (solid line) and proportionality of D_{eff} with χ_{turb} (dash-dot line). Essentially, the red line, corresponding to D^L_{eff}, is fixed, and the blue lines (D^H_{eff}) are compared to the expected values, either $D^L_{eff}(\chi^H_i/\chi^L_i)$ or $D^L_{eff}(\chi^H_{turb}/\chi^L_{turb})$, as indicated by the respective black lines.

As shown in figures 7.5a and 7.5c, the blue line aligns almost perfectly with the assumption that D_{eff} is proportional to turbulent ion heat transport across the entire range of neutral densities at the pedestal top. This scaling indicates that the reduction in turbulent transport with increased shaping is the dominant factor driving particle transport. This further supports the notion that a dominant turbulent mode in this region influences the pedestal width of D_{eff}, while the neoclassical contribution remains largely unchanged.

However, at the pedestal middle, where effective particle diffusion is remarkably suppressed to almost negligible levels, the blue line instead matches χ_i, as shown in figures 7.5b and 7.5d, suggesting proportionality to total ion heat diffusivity, including the neoclassical component. This result is less conclusive compared to the pedestal top because D_{eff} at the pedestal foot changes minimally and is very small overall. Nevertheless, a more detailed analysis involving the separation of neoclassical and turbulent contributions to D_{eff} is necessary. This calculation is planned for future work.

7.2 Gyrokinetic Simulations with GENE

To delve deeper into the turbulence discussed so far, gyrokinetic simulations are conducted. This approach is particularly advantageous because gyrokinetic theory operates at the scale of microturbulence, enabling it to capture phenomena smaller than those analysed in the scope of MHD. At this stage of the analysis, only local linear simulations are performed. This means the calculations are restricted to a single flux tube (local approach) and rely on linearised equations. This methodology comes with notable limitations. For instance, it struggles to account for $E \times B$ effects comprehensively, mode coupling is not accounted for and saturation levels of different instabilities are not captured.

Despite its limitations, this approach offers several advantages. The simulations are relatively fast, allowing for the exploration of different cases and parameter variations with ease. This flexibility makes it particularly suitable for the scope of this thesis, serving as a preliminary investigation to test the waters. Additionally, there is another PhD thesis that specialises in GENE, where global nonlinear simulations for these cases are run, providing a complementary and more comprehensive analysis beyond the linear approach presented here

[66].

Another key motivation for performing these gyrokinetic simulations is the opportunity to address a significant aspect of the analysis: while local IBMs have been discussed extensively, they have consistently been used as a proxy for KBMs. With the GENE simulations [66], it becomes possible to directly test this assumption by comparing the behaviour of KBMs with that of local IBMs, offering valuable insight into the relationship between these modes.

In this section, we focus on analysing discharge #38472, which features high β_{pol}. The same kinetic profiles and equilibrium data previously employed in the MHD and ASTRA analyses are used as input for GENE. The primary scan is over the wave number k_y (in the y-direction - binormal to the magnetic field and plasma radius), covering a range spanning several orders of magnitude, from approximately 0.005 to $100m^{-1}$.

The output of this scan provides the growth rate (the imaginary part of the frequency), normalised to the sound speed $c_s = \sqrt{T_e/m_i}$ and reference length, $L_{ref} = 0.65m$ which we plot on the y-axis. In figures 7.6-??, the colours of the markers in indicate the real part of the frequency: violet represents a mode that propagates in the ion diamagnetic direction, while green corresponds to the electron diamagnetic direction. Low-shaping results are shown as circles, and high-shaping results as triangles [1].

The large panels in a) show the growth rate results, while the smaller panels on the right display quasi-linear transport estimates for effective particle transport (D_{eff}^{QL}), and ion and electron heat transport (Q_i^{QL} and Q_e^{QL}), as discussed in chapter 2. This model accounts for the impact of specific modes on transport, balancing high-growth-rate modes that are small and contribute little, against larger modes with lower growth rates but significant transport impact. The quasilinear model also factors in some additional shaping effects, since the modes located at different poloidal positions contribute differently to the particle and heat transport.

In the panels showing the quasi-linear estimates, the panel a) shows particle transport estimates, the panel b) focuses on ion heat transport, and the panel c) highlights electron heat transport. All quasi-linear transport values are presented in arbitrary units (a.u.), as they derive from the growth rates and represent approximate transport contributions based on linear code outputs.

The growth rate vs. k_y plots are particularly useful as they distil complex turbulent behaviour into a more interpretable form by highlighting the fastest-growing mode for each specific wave number. This creates distinct peaks in the structure of the plots. The identification of these modes is based on several factors, as explained in greater detail in section 2.2.2.

The key factors include: *the size of the mode*, determined by its k_y value (low k_y corresponds to larger structures, while high k_y corresponds to smaller ones); *the propagation direction*, whether in the ion diamagnetic or electron diamagnetic direction; *the level of transport* associated with the mode, as estimated by the quasi-linear model.

This analysis is divided into two sections, each focusing on the growth rates at different radial positions. In gyrokinetics, it is common to use ρ_{tor}, while the rest of the analysis employs ρ_{pol}. Therefore, the radial positions at which the data were collected correspond to $\rho_{tor} = 0.92, 0.94, 0.96,$

[1] What a visual mnemonic: high triangularity - triangles; low triangularity - circles. So witty.

0.98, which in these discharges translates to $\rho_{pol} = 0.966, 0.976, 0.984, 0.992$, respectively.

In the first section, we will compare the low and high shaping cases, examining the insights gained from GENE regarding microturbulence using input profiles and equilibria from different cases. The second section parallels the exercise conducted with MHD in section 5.3. Here, we compare the standard low shaping case with a mixed case, wherein we utilise profiles from the low shaping phase alongside the equilibrium from the high shaping phase. This approach differs from that used in HELENA, as we incorporate the entire equilibrium in our analysis. In HELENA, only a different boundary was provided, which is then used to reconstruct the equilibrium with the given profiles. In contrast, the method used with GENE can take the whole artificial equilibrium, which offers a more comprehensive and comparison.

7.2.1 Comparison of Turbulence Growth Rates in Low and High Shaping

We now compare low and high shaping at different radial positions, starting with the outer core at $\rho_{pol} = 0.966$ as shown in figure 7.6. For the low shaping case, represented by circles, in 7.6a we observe two dominant instabilities. The first is identified as ion temperature gradient (ITG) modes, occurring on the ion scale, at low k_y), and propagating in the ion diamagnetic direction, as indicated by the purple-coloured circles. The second dominant instability is depicted as green circles, as it is propagating in the electron diamagnetic direction, and it is in the electron scale, that is, it has high k_y numbers. This instability is therefore identified to be electron temperature gradient ETG mode.

As the shaping increases, represented by triangles, we observe the emergence of an additional mode between the ITG and ETG modes. This new mode is hypothesised to be either a trapped electron mode (TEM) or another branch[2] of the ETG mode [66]. The growth rates are relatively similar for all k_y values.

To understand the implications of these modes, we turn to the quasi-linear model, shown in panels a)-c) to assess the expected transport contributions, which is ultimately of primary interest. Regarding particle transport, the low-k_y mode (the ITG mode) contributes less in the low shaping case. For heat transport, the trend reverses: high shaping reduces ITG heat transport but increases it for the ETG mode.

Interestingly, the intermediate mode, interpreted as either a TEM or a secondary ETG branch, contributes neither to particle transport nor significantly to heat transport, showing its minimal role in overall transport.

Moving radially outward to $\rho_{pol} = 0.976$ in figure 7.7, which corresponds to the transition between the pedestal middle and pedestal top, we observe more pronounced differences in the growth rates shown in a). The ETG mode has little variation between low and high shaping cases, but the mid-range k_y mode (interpreted as either a TEM or ETG) displays a significantly higher growth rate for the high shaping case.

The most notable change occurs in the low-k_y mode, which is higher for the high shaping phase. Its structure now exhibits a fall-off behaviour toward $k_y = 1$, a charac-

[2] Two types of ETG modes exist, each with distinct characteristics. The slab branch produces modes with ($k_x \approx k_y$) and a high $k_\parallel$, whereas the toroidal branch generates radially elongated streamers and has a low $k_\parallel$. These branches dominate in different regions of $k_y\rho_i$: toroidal ETGs at lower $k_y\rho_i \approx 1-10$, whereas slab ETGs are more prevalent at higher $k_y\rho_i \approx 50-150$.

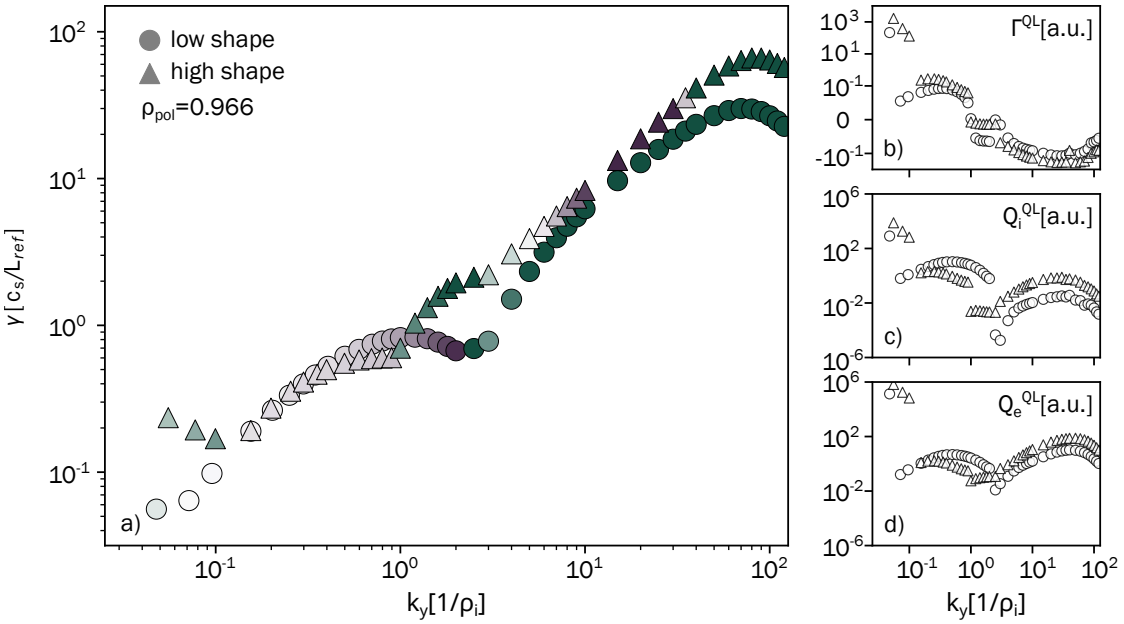

Figure 7.6: In a), growth rate spectra of the dominant mode at the radial position $\rho_{pol} = 0.966$ of discharge #38472 are shown for low shaping phase in circles, and high shaping phase marked as triangles, at zero ballooning angle, scanned over the wave number k_y. In b), c) and d) the quasi-linear estimate of particle flux, ion heat flux and electron heat flux, respectively, are shown.

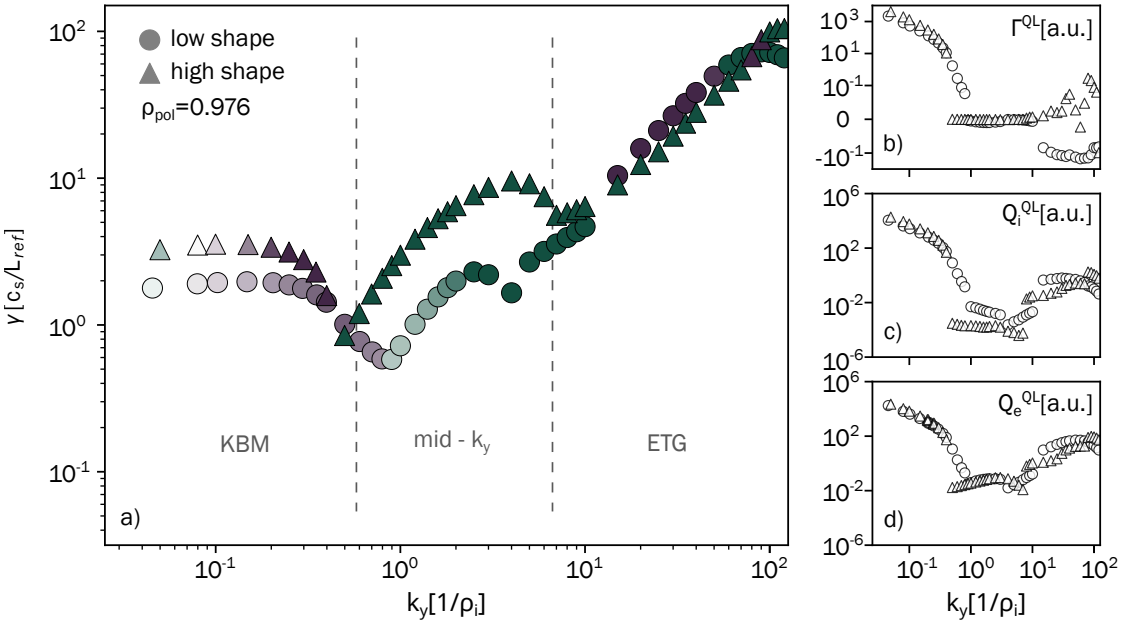

Figure 7.7: In a), growth rate spectra of the dominant mode at the radial position $\rho_{pol} = 0.976$ of discharge #38472 are shown for low shaping phase in circles, and high shaping phase marked as triangles, at zero ballooning angle, scanned over the wave number k_y. In b), c) and d) the quasi-linear estimate of particle flux, ion heat flux and electron heat flux, respectively, are shown.

teristic feature of KBMs. A further indication of its KBM nature comes from the quasi-linear analysis: particle transport attributed to this mode increases dramatically, rising from around 0.1 to over 1000, suggesting a strong contribution to particle transport in this region.

Despite the differences in growth rate, the quasi-linear analysis reveals that the particle and heat transport contributions from the KBM are remarkably similar when compared between low and high shaping cases. Interestingly, the mid-range k_y mode, which exhibits higher growth rates in high shaping, contributes no particle transport (figure 7.7b). However, in high shaping, this mode spans a broader k_y range. This suggests that the KBM, which is causing a significant amount of particle transport, gets narrower in the k_y space, and it is replaced by the more dominant middle mode that does no particle transport. Particle transport could then be reduced due to this expanded coverage. This, however, remains speculative.

As for heat transport, the ion heat transport in panel c), associated with the mid-k_y, is lower for high shaping, while the electron heat transport remains nearly unchanged. Thus, despite the elevated growth rates of the mid-k_y mode in high shaping, the primary difference lies in the increased k_y range of the KBM.

Moving further outward in the analysis, in figure 7.8 we reach $\rho_{pol} = 0.984$, which corresponds to the steepest pedestal region for all profiles (T_e, T_i, and n_e) across both shaping cases. At this location, the differences in growth rates are smaller (panel a). Specifically, the KBM region is slightly narrower in the high shaping case, the TEM growth rate is marginally higher, and the ETG growth rate is slightly lower, but none of these variations are particularly pronounced.

In the quasi-linear analysis presented in panels b), c), and d), the mid-k_y mode again shows no particle transport (panel b). Ion heat transport is slightly higher for high shaping (panel c), and similarly, electron heat transport is also slightly elevated for high shaping (panel d). However, these differences are also minimal. The ETG contribution remains largely unchanged, and the narrower k_y width of the KBM in high shaping is consistently reflected in both particle and heat transport trends.

Lastly, we analyse the pedestal foot at $\rho_{pol} = 0.992$, shown in figure 7.9. At this position, some k_y cases in the lower k_y region of the ETG part did not converge in the simulations. Nevertheless, we can identify some trends in panel a).

Starting with the KBM region, we observe that the k_y range is significantly narrower than at other radial positions. High shaping also has much lower growth rates compared to low shaping. This narrowing and reduction are also reflected in the transport results in panels b)-d): KBM contributes significantly more to transport in the low shaping case across all categories. Next, for the mid-k_y mode (interpreted as TEM/ETG), the growth rates are identical for both low and high shaping. Consistently, the transport contributions from this mode remain minimal and show no discernible difference between the two shaping cases. Finally, in the ETG region, the growth rates are consistently lower for high shaping compared to low shaping. This trend is mirrored in the transport results, where ETG-related transport is always reduced for high shaping.

In summary, the most notable differences at $\rho_{pol} = 0.992$ are found in the KBM region, with high shaping resulting in significantly reduced growth rates and transport contributions, while the mid-k_y

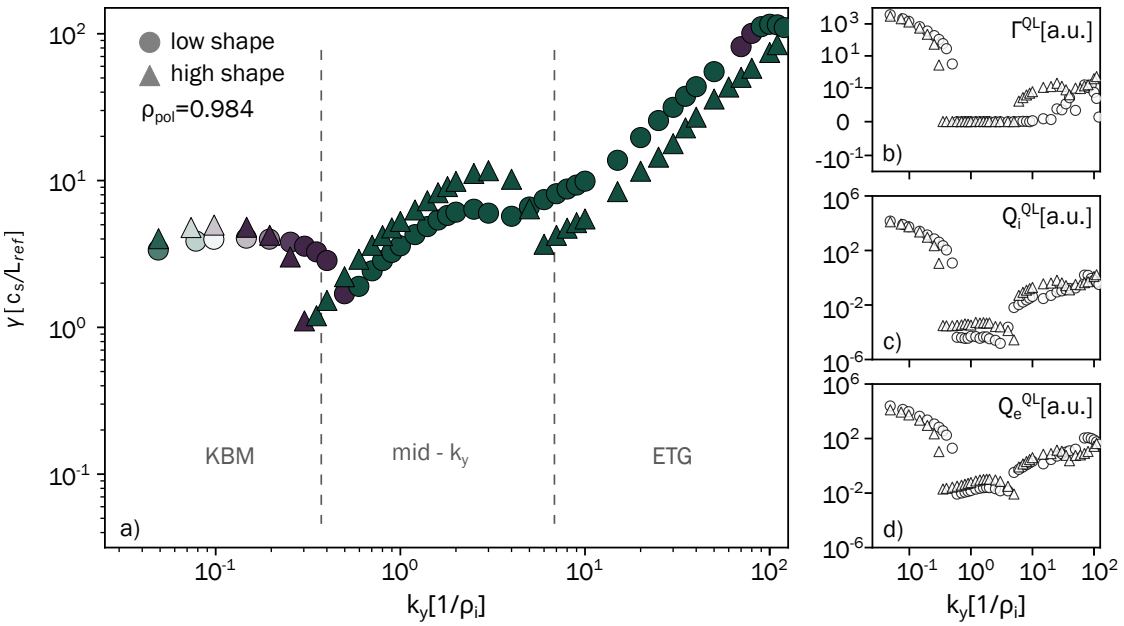

Figure 7.8: In a), growth rate spectra of the dominant mode at the radial position $\rho_{pol} = 0.984$ of discharge #38472 are shown for low shaping phase in circles, and high shaping phase marked as triangles, at zero ballooning angle, scanned over the wave number k_y. In b), c) and d) the quasi-linear estimate of particle flux, ion heat flux and electron heat flux, respectively, are shown.

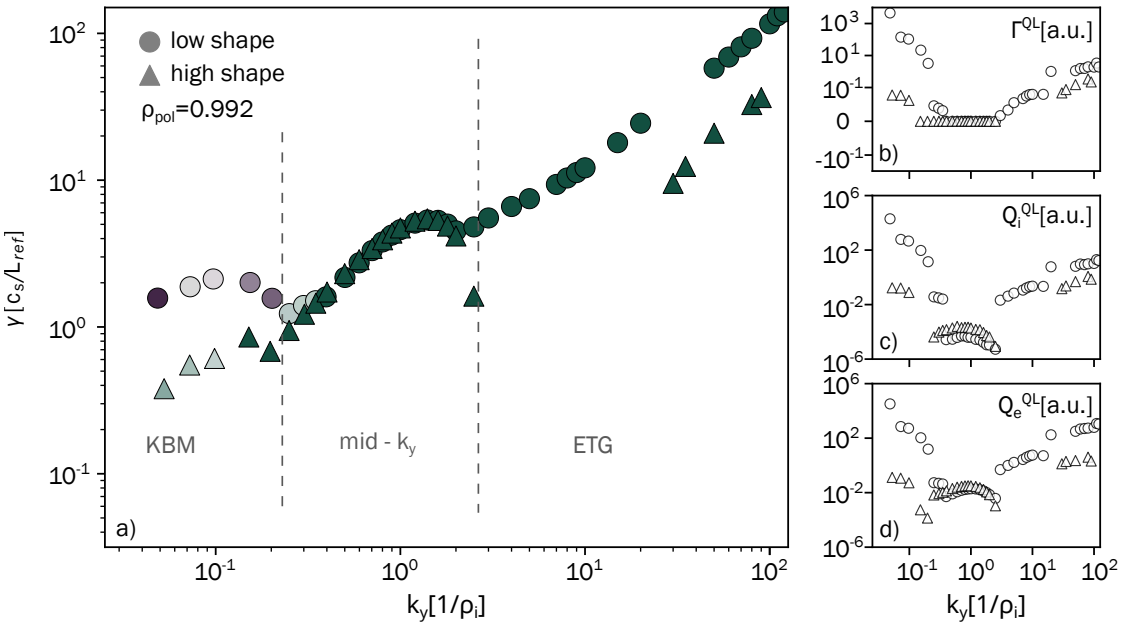

Figure 7.9: In a), growth rate spectra of the dominant mode at the radial position $\rho_{pol} = 0.992$ of discharge #38472 are shown for low shaping phase in circles, and high shaping phase marked as triangles, at zero ballooning angle, scanned over the wave number k_y. In b), c) and d) the quasi-linear estimate of particle flux, ion heat flux and electron heat flux, respectively, are shown.

mode remains unchanged and ETG transport is consistently lower for high shaping.

In this section, it is important to note that E × B stabilisation is not included in the analysis, so no conclusions can be drawn regarding its effects. Despite this, some interesting observations can be made: as we move from the outer core to the pedestal top, the dominant instability on the ion scale shifts from ITGs to KBMs. While ITGs could still be present, they become less influential in regions dominated by KBMs. This transition is significant because KBMs contribute substantially more to particle transport compared to ITGs, emphasising their role in the structure of the density pedestal.

The strong correlation between KBMs and particle transport underscores their critical role in shaping the pedestal structure. This aligns with trends hypothesised in HELENA simulations, where changes in particle density are closely tied to shape-induced modifications in KBMs.

Closer to the plasma edge, mid-range k_y modes become more prominent. However, these modes have minimal impact on both particle and heat transport, which limits their direct significance despite their increased presence.

7.2.2 Decoupling Effects of Kinetic Profiles and Equilibrium

Here, we again analyse four radial locations, just as in the previous discussion. The original low-shaping case, which has already been shown, is still marked with circles. However, instead of comparing it to the high-shaping scenario, we compare it to a mixed case. In this mixed case, we use the same low-shaping profiles but apply the high-shaping equilibrium to disentangle the effects of gradients versus equilibrium. The results from this mixed case are marked as pentagons.

In the first figure 7.10 ($\rho_{pol} = 0.966$), we observe that altering the plasma equilibrium does not significantly impact the growth rate, as shown in panel a). Both the ITG and ETG modes remain largely unaffected. Similarly, the heat and particle transport are nearly identical between cases, with one exception: the ITG contribution to particle transport in panel b). Interestingly, when we introduce the high-shaping equilibrium, the transport flips its sign. However, the D_{eff}^{QL} is not particularly strong to begin with, so it should not have a substantial impact overall.

Moving outward to $\rho_{pol} = 0.976$ in figure 7.11, the KBM becomes more dominant than the ITG in the ion-scale modes. In this region, we observe a significant decrease in the growth rate of the KBM in panel (a), which is also reflected in the heat and particle transport shown in panels (b) and (d). The ETG remains unaffected, and the mid-k_y mode is mostly unchanged. According to the quasi-linear model, the mid-k_y mode exhibits slightly reduced transport for both ion and electron heat, but given its already small contribution, this reduction is not particularly important.

In summary, altering the shape has a pronounced effect on the KBM in this region, where it is most prominent. This is particularly noteworthy as this is the region in high-shaping cases where second-stability access is achieved (see figure 7.4a).

In the next figure 7.12, at $\rho_{pol} = 0.984$, we observe a very similar trend to the previous radial point. The mid-k_y mode remains unaffected, maintaining a low contribution for both low and high shaping. However, the KBM shows a smaller difference in this region compared to figure 7.11, further to-

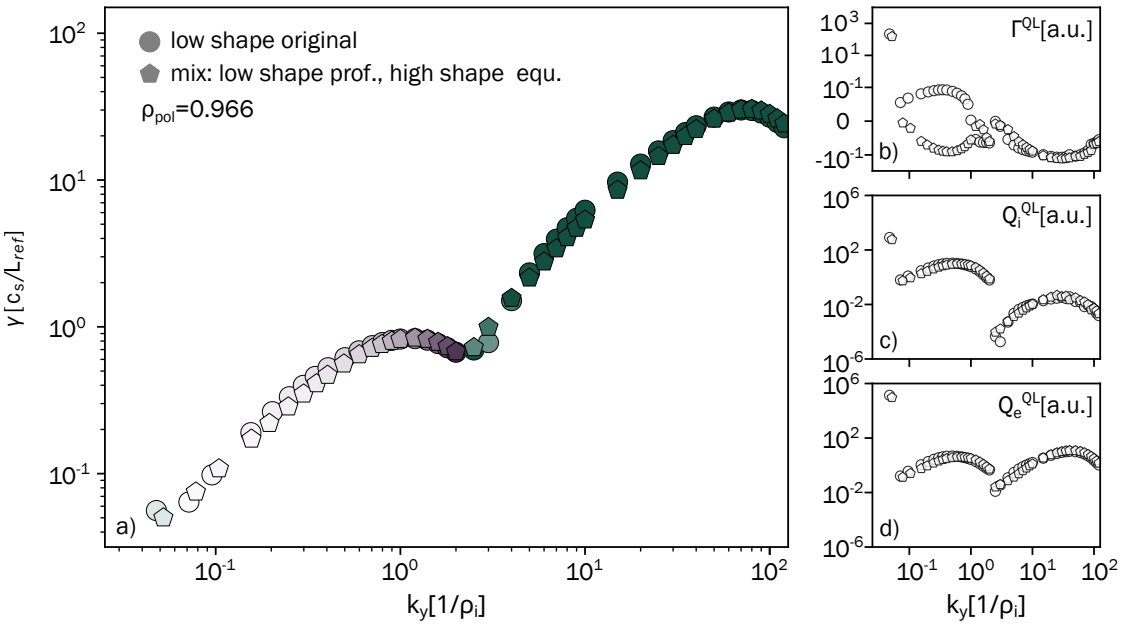

Figure 7.10: In a), growth rate spectra of the dominant mode at the radial position $\rho_{pol} = 0.966$ of discharge #38472 are shown. Circles show the low shaping phase and the pentagons the mixed case where the low shaping phase profiles are used with the high shaping profile equilibrium. The simulations are at zero ballooning angle, scanned over the wave number k_y. In b), c) and d) the quasi-linear estimate of particle flux, ion heat flux and electron heat flux, respectively, are shown.

wards the core. This aligns with the findings from HELENA, which indicated that the operational point in this region is not as deep in the second stability regime.

At the last radial position, shown in figure 7.13, apart from three points around $k_y = 10^{-1}$ where the growth rate is slightly reduced, there are no significant changes observed.

In the previous four plots, we observed that the results from HELENA and GENE align regarding shape stabilisation of KBMs, and the regions where this may have the most effect. This further confirms that shaping has a substantial impact on KBMs. Also, as reflected in the quasi-linear models, the KBMs significantly affects particle transport. These findings are also consistent with the results from ASTRA in figure 7.4, which demonstrate turbulence suppression with the shape change.

7.3 Conclusions

In this chapter, we examined how transport and microturbulence complement and align with the MHD analysis. The ASTRA simulations provided a quantitative estimate of transport in different channels, helping us assess the extent of the suppression, whereas the GENE simulations offered some insight in how microturbulence changes in the pedestal as β_{pol} and plasma shape are varied.

Before drawing conclusions, it is important to acknowledge some limitations in the scope of this analysis. One key factor that has not been included in the gyrokinetic analysis is E × B shearing, which could significantly influence stability and transport mechanisms. Additionally, all gyrokinetic simulations were conducted in a local and linear framework, which may not fully cap-

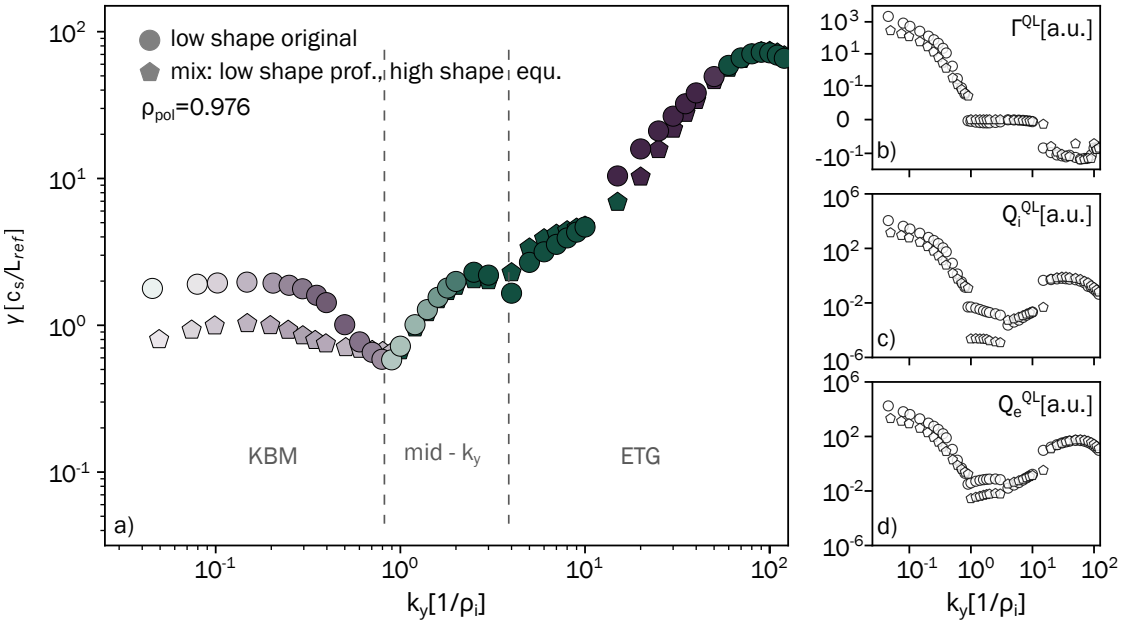

Figure 7.11: In a), growth rate spectra of the dominant mode at the radial position $\rho_{pol} = 0.976$ of discharge #38472 are shown. Circles show the low shaped phase and the pentagons the mixed case where the low shaping phase profiles are used with the high shaping profile equilibrium. The simulations are at zero ballooning angle, scanned over the wave number k_y. In b), c) and d) the quasi-linear estimate of particle flux, ion heat flux and electron heat flux, respectively, are shown.

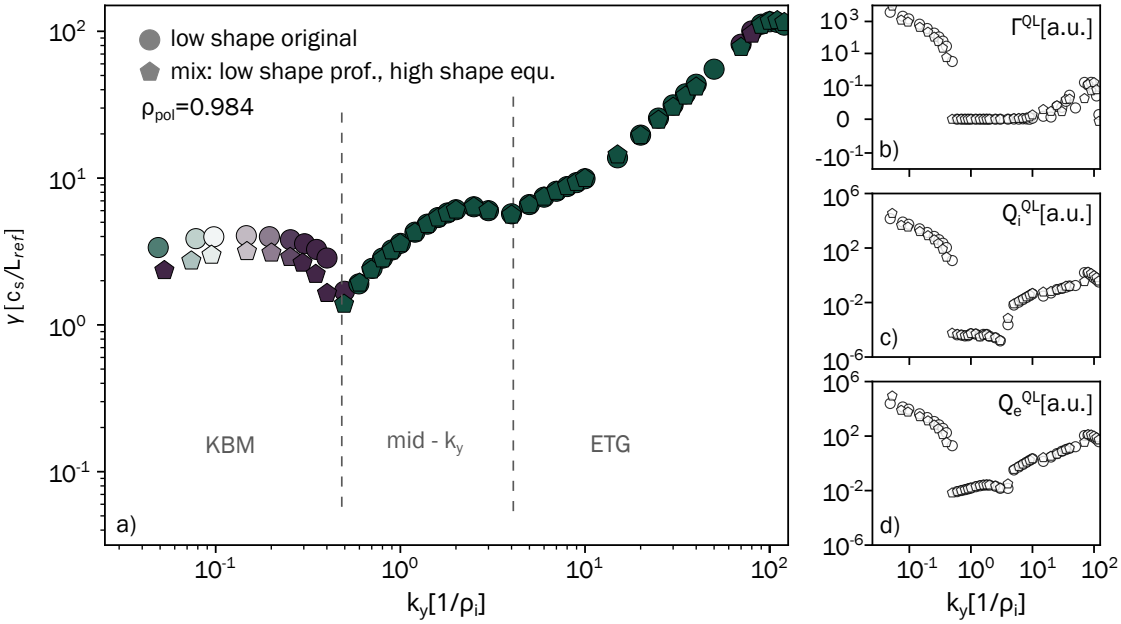

Figure 7.12: In a), growth rate spectra of the dominant mode at the radial position $\rho_{pol} = 0.984$ of discharge #38472 are shown. Circles show the low shaped phase and the pentagons the mixed case where the low shaping phase profiles are used with the high shaping profile equilibrium. The simulations are at zero ballooning angle, scanned over the wave number k_y. In b), c) and d) the quasi-linear estimate of particle flux, ion heat flux and electron heat flux, respectively, are shown.

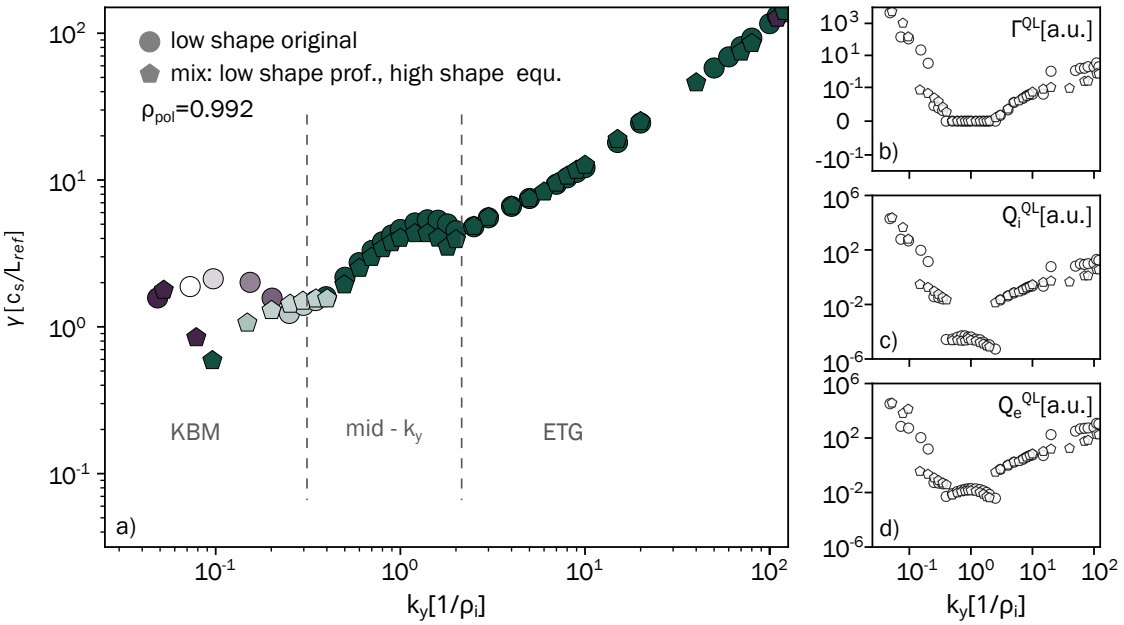

Figure 7.13: In a), growth rate spectra of the dominant mode at the radial position $\rho_{pol} = 0.966$ of discharge #38472 are shown. Circles show the low shaped phase and the pentagons the mixed case where the low shaping phase profiles are used with the high shaping profile equilibrium. The simulations are at zero ballooning angle, scanned over the wave number k_y. In b), c) and d) the quasi-linear estimate of particle flux, ion heat flux and electron heat flux, respectively, are shown.

ture the global and nonlinear dynamics of the system.

Even with these limitations, certain observations can still be made. First, it is clear that changes to the equilibrium, as achieved through shaping in these discharges, most significantly impact kinetic ballooning modes (KBMs), particularly at the pedestal top, as it is shown in section 7.2.2. This analysis confirms that the role of local magnetic shear is especially important, as it stabilises these modes, as discussed in the recent work in [125].

The results also highlight the strong influence of KBMs on particle transport, suggesting that these modes play a critical role in shaping the density pedestal structure, as it was also suspected in the MHD analysis. From the f_{marg} analysis in chapter 5 and figure 7.4, we see that when there is no access to second stability at the pedestal top, KBMs emerge in the region where f_{marg} reaches its minimum. In high shaping scenarios, two distinct minima are observed: one located deeper inside the plasma, likely associated with KBMs, and another closer to the separatrix, which may be suppressed by E×B shearing.

Another indication of this turbulent characteristic of D_{eff} is observed at the pedestal top, where its suppression mirrors the behaviour of χ_{turb}, as shown in figure 7.5. This suggests a potential connection in the pedestal top region: the density pedestal width is naturally tied to D_{eff}, which in turn is coupled with χ_{turb} at the pedestal top. This link extends to the HELENA f_{marg}, indicating KBM activity, which is further supported by GENE results. It seems evident that the KBMs play a particularly significant role in shaping the density pedestal width.

At the pedestal foot, the f_{marg} results (figure 7.4a) show that there should theoretically be no KBMs. GENE simulations show

the presence of KBMs in the pedestal top, potentially extending to the middle region. As we move outward in the pedestal, these KBMs become narrower in the k_y space. Furthermore, in the far edge, increased E×B shear likely exerts additional influence.

The behaviour of χ_{turb} (figure 7.3) extends this picture. Even when significantly suppressed at the pedestal top, it starts rising again at the middle and gets to outer-core values near the pedestal foot. This could suggest the presence of another mode, possibly ITG, which might not dominate growth rates in GENE scans but could still contribute substantially to the ion heat transport. Importantly, this mode appears to have no impact on particle transport, as evidenced by the minimal values of D_{eff} at the pedestal foot. As shown in figure 7.10, ITG modes seem largely unaffected by changes in the equilibrium. A key question is whether such a mode would be suppressed by E × B shear and, if so, to what extent. Further analysis is required to clarify this. Additionally, the neoclassical component of ion heat transport plays a considerable role, sometimes even dominating, and its dependence on density again connects back to D_{eff}.

Finally, the electron heat diffusivity (χ_e) interpretation presents its own challenges. Due to the low electron mass, the neoclassical component of χ_e is negligible, leaving it predominantly turbulent. GENE simulations have so far been inconclusive for Q_e^{QL}. ASTRA simulations shown in 7.2b reveal an unusual trend: higher beta leads to increase electron heat transport χ_e, unlike χ_i. Moreover, higher beta also correlates with higher ELM rates. Since T_e has significantly slower recovery in an ELM cycle [115, 116], it could be that the shorter ELM-cycle in high β_{pol} regime causes the operational point to cross the PB boundary before the T_e profile has fully developed. This may cause ASTRA to interpret χ_e as higher in the high β_{pol} discharge. A possible way to explore T_e further is investigating its pedestal formation in detail in an ELM-free regime.

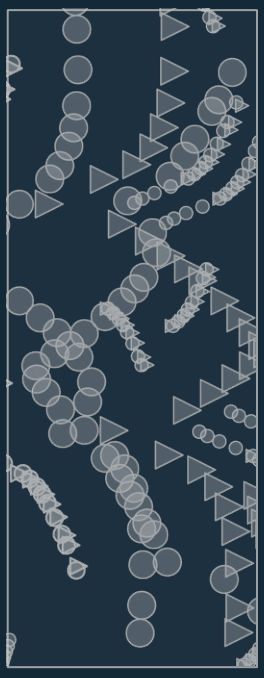

SUMMARY, DISCUSSION AND OUTLOOK

8 Summary, Discussion and Outlook

In this final chapter, I summarise the key aspects of this thesis and present the conclusions drawn from the conducted study.

The primary focus of this work was to investigate the behaviour of the pedestal in experiments conducted at ASDEX Upgrade. Initially, the study aimed to address the fundamental question of what physical phenomenon determines the pedestal width. For this reason, two control parameters were selected; because the EPED model [30] assumes KBMs as the dominant mode in the transport barrier, it models the pedestal width using β_{pol}, which was taken as the first control parameter; the second control parameter is plasma shape, which directly influences the local magnetic shear s_{loc}, which stabilises ballooning modes. With these two quantities in focus, our goal was to determine how the pedestal width is fundamentally set and to clarify the role of KBMs with more precision. However, as the analysis progressed, it became evident that a broader perspective was necessary, requiring the systematic consideration of how the whole pedestal structure changes under these varying factors.

The analysis centred on three discharges with a different β_{pol}, designed to each include two phases: one with low and one with high shaping, resulting in 6 time windows to be studied. The discharges were subjected to an extensive analysis, employing a large variety of diagnostic and computational tools.

The findings encompass several key areas. Experimental observations included an analysis of time traces, kinetic profiles, and equilibrium behaviour, providing a solid foundation for understanding the discharges and how the plasma reacts to changing conditions.

Building on this, the study delved into the MHD stability of the pedestal, going beyond the traditional focus on global peeling-ballooning stability to include a detailed examination of local ideal ballooning stability. The local IBMs are here used as a proxy for KBMs. A crucial aspect of this analysis was the exploration of the role of access to the second stability regime, which emerged as a significant factor influencing the pedestal behaviour, particularly its width. Such analysis is then also performed beyond the dedicated experiments, by studying the ELM-synchronised development of local ideal MHD stability.

The thesis also presents an analysis of transport coefficients under these varying plasma conditions, offering insights into the heat and particle transport processes within the pedestal, and specifically how they relate to the previously explored local IBMs. Additionally, gyrokinetic simulations were conducted to complement and validate the findings. These simulations, which focus on the microturbulence and its im-

pact on the pedestal structure, align well with the results of the MHD analysis. This integration of gyrokinetic simulations with transport analysis and MHD underscores the robustness of the findings and highlights the interconnected nature of the processes governing the pedestal behaviour.

Two overarching conclusions emerge as the most important takeaways from this thesis.

Firstly, it is not sufficient to treat the pedestal as a simple pressure pedestal. The distinct components of the pedestal, the temperature and density of ions and electrons, not only affect the bootstrap current and, consequently, the equilibrium differently, but they are also governed by fundamentally different mechanisms. These components exhibit different responses to variations in plasma shape and β_{pol}.

Secondly, in different regions of the pedestal, there are different instabilities driving the transport, and also, the stabilising effect of both E × B shear, and importantly magnetic shear have varying effects in different pedestal regions. Because of this it is differentiated between different pedestal regions: top, middle and foot.

The local magnetic shear has been shown to have a far greater influence on the pedestal than previously acknowledged. While a number of works emphasised its importance [69, 126–130], the focus on magnetic shear turbulence stabilisation has waned, perhaps due to the community's concentrated efforts on measuring E_r. These efforts have been valuable — E × B shear is undoubtedly important and plays a key role in pedestal formation. However, the susceptibility to kinetic ballooning modes (KBMs), stabilised by the magnetic shear, should not be overlooked.

In the local MHD analysis using HELENA, described in chapters 5 and 6, we confirmed the presence of local IBMs at the pedestal top, which suggests the existence of KBMs. The radial position of the most ballooning-unstable region depends on whether the pedestal has access to second stability, which is a crucial factor. Furthermore, the ELM-synchronised analysis showed that access to second stability enables the total pedestal pressure gradient to increase significantly in the final pedestal phase compared to cases without access, highlighting its importance. Additionally, this study demonstrated a strong correlation between the radial location of the electron pressure pedestal top and the region where ballooning modes are expected, primarily reflecting changes in the density pedestal top.

In chapter 7, ASTRA simulations further support the KBM hypothesis. First, at the pedestal top, where the MHD analysis with HELENA indicates the presence of KBMs, we observe that both χ_i^{turb} and D_{eff} exhibit proportional decrease with the increase in shape for both β_{pol} discharges. While χ_i^{turb} could be linked to ITGs, the fact that it also contributes significantly to particle transport suggests a KBM-driven mechanism. Additionally, turbulence reduction is significantly stronger when the plasma has access to the second stability, occurring in the same radial region, as the steepest gradient region, further reinforcing the KBM interpretation at the pedestal top.

In contrast, at the pedestal foot, other modes may be active; since they do not contribute to particle transport, ITGs are the most likely candidate in this region. However, this has not been confirmed by local linear GENE studies. It remains to be seen whether global nonlinear simulations will provide further insight.

Nevertheless, GENE does confirm that while ITGs dominate in the outer core,

KBMs are prevalent at the pedestal top. Moreover, the analysis shows that KBMs are the primary modes stabilised by shaping, with the strongest effect occurring in the second stability region where the pressure gradient is steepest. Additionally, GENE confirms the presence of ETGs across the entire pedestal region, which served as a basis for setting the electron heat diffusivity in the IMEP model (see [31, 32, 35]).

To summarise, what began as a study of the pedestal width evolved into a broad investigation of the detailed pedestal structure. However, several open questions remain.

The stabilisation of E_r has not been thoroughly incorporated into this analysis. We know that E_r naturally relates to ∇p_i and particle density, given that its diamagnetic term is proportional to $\nabla p_i/n_i$. Moreover, we understand that E_r shear likely sets the initial conditions for pedestal formation through a feedback loop: $E \times B$ shear reduces turbulence, allowing ∇p to form, which means that ∇p_i grows, reinforcing E_r and further increasing $E \times B$. This simple picture however does not consider what further instabilities are driven due to the gradients, nor how they are stabilised. The stabilising effect of $E \times B$ shear is not explicitly accounted for in either HELENA or GENE in this study.

Second, the source term for density, which determines the fluxes, remains uncertain. Although we attempted to investigate this, the results were inconclusive. While it is valuable to confirm that our findings on particle diffusivity hold across a range of cold neutral influx conditions, we still lack a precise method to determine these fluxes and must rely on approximations.

Finally, an important question is how reliable the findings are and how they can be implemented in general. Understanding whether these results hold across different operational scenarios and how they extrapolate to larger devices remains crucial for their application to future machines.

To address the question of reliability, the experimental conditions were well-controlled, and the study benefited from an excellent team working across multiple diagnostics, leading to advanced fits and high-quality data. However, the analysis is based on six experimental datasets, primarily because great care was taken in data collection, making the process time-intensive. Now that clear conclusions have been drawn, these findings could be tested and solidified on a larger dataset to assess their validity across different plasma currents, a wider range of collisionalities, and possibly larger variations in β_{pol} and shaping.

Applying these findings essentially means developing a predictive model or improving existing ones. A possible approach would start with an equilibrium calculation, providing F_{marg} from HELENA, which helps determine the density pedestal structure and the level of turbulence reduction for ion heat transport at the pedestal top, represented by χ_{turb}. Using the particle density, one can then compute χ_{neo} and obtain T_i. For the electron temperature, the IMEP approach could be used, where T_e is determined based on the fixed $T_e/\nabla T_e = 2$ cm [35], which has shown promising results [31, 32, 131]. This process then feeds back into generating a new equilibrium until a peeling-ballooning boundary is reached.

Since this model requires iterative calculations, implementing it would not be straightforward, as multiple contributions need to be carefully balanced. However, with further effort, it could be developed in the future.

In summary, this hypothetical model

combines s_{loc} with ∇p from the equilibrium to determine the onset of KBMs. KBMs then set the density pedestal. At the pedestal top, KBMs and neoclassical ion heat transport dominate, while in the pedestal foot, ITG or KBM modes could play a role, depending on the separatrix conditions, shaping the ion temperature profile. The electron temperature is governed by ETGs, which impose a fixed gradient length. The entire system is iterated towards the peeling-ballooning boundary, ultimately leading to an ELM.

These results highlight that while scaling laws and empirical models provide valuable insights they should be complemented for fully predicting pedestal behaviour in future fusion devices. A separate treatment of ion and electron pedestals for temperature and particle transport is crucial for understanding the pedestal structure. Importantly, in different pedestal regions, the stabilisation and drive mechanisms of various modes exhibit different strengths. This implies that a simple, global model for the entire pedestal cannot accurately capture its complexity. Instead, a well radially-resolved approach is required to capture the detailed physics governing pedestal dynamics. Achieving this is challenging both experimentally and in modelling, particularly when considering the distinct roles of ion and electron channels in particle and heat transport. However, such an approach is essential for explaining the observed variations in pedestal behaviour. Further testing of this hypothesis is necessary, along with integrating these mechanisms into models capable of predictive calculations.

Bibliography

[1] J. D. Jenkins, M. Luke, and S. Thernstrom, "Getting to Zero Carbon Emissions in the Electric Power Sector", Joule, vol. 2, no. 12, pp. 2498–2510, Dec. 2018, ISSN: 2542-4351. DOI: 10.1016/j.joule.2018.11.013 (cit. on p. 3).

[2] E. R. Sadik-Zada, A. Gatto, and Y. Weißnicht, "Back to the future: Revisiting the perspectives on nuclear fusion and juxtaposition to existing energy sources", Energy, vol. 290, p. 129 150, Mar. 2024, ISSN: 0360-5442. DOI: 10.1016/j.energy.2023.129150 (cit. on p. 4).

[3] I. Palermo et al., "Radiological impact mitigation of waste coming from the European fusion reactor DEMO with DCLL breeding blanket", Fusion Engineering and Design, Proceedings of the 29th Symposium on Fusion Technology (SOFT-29) Prague, Czech Republic, September 5-9, 2016, vol. 124, pp. 1257–1262, Nov. 2017, ISSN: 0920-3796. DOI: 10.1016/j.fusengdes.2017.02.080 (cit. on p. 4).

[4] J. Knaster, A. Moeslang, and T. Muroga, "Materials research for fusion", Nature Physics, vol. 12, no. 5, pp. 424–434, May 2016, ISSN: 1745-2481. DOI: 10.1038/nphys3735 (cit. on p. 4).

[5] A. Glaser and R. J. Goldston, "Proliferation risks of magnetic fusion energy: Clandestine production, covert production and breakout", Nuclear Fusion, vol. 52, no. 4, p. 043 004, Mar. 2012, ISSN: 0029-5515. DOI: 10.1088/0029-5515/52/4/043004 (cit. on p. 4).

[6] The Indirect Drive ICF Collaboration et al., "Achievement of Target Gain Larger than Unity in an Inertial Fusion Experiment", Physical Review Letters, vol. 132, no. 6, p. 065 102, Feb. 2024. DOI: 10.1103/PhysRevLett.132.065102 (cit. on p. 5).

[7] P. H. Rebut and B. E. Keen, "The JET Experiment: Evolution, Present Status, and Prospects", Fusion Technology, vol. 11, no. 1, pp. 13–42, Jan. 1987, ISSN: 0748-1896. DOI: 10.13182/FST87-A24999 (cit. on p. 5).

[8] M. Maslov et al., "JET D-T scenario with optimized non-thermal fusion", Nuclear Fusion, vol. 63, no. 11, p. 112 002, Oct. 2023, ISSN: 0029-5515. DOI: 10.1088/1741-4326/ace2d8 (cit. on p. 5).

[9] C. F. Maggi et al., "Overview of T and D–T results in JET with ITER-like wall", Nuclear Fusion, vol. 64, no. 11, p. 112 012, Aug. 2024, ISSN: 0029-5515. DOI: 10.1088/1741-4326/ad3e16 (cit. on p. 5).

[10] S. Ishida et al., "Overview of the JT-60SA project", Nuclear Fusion, vol. 51, no. 9, p. 094 018, Aug. 2011, ISSN: 0029-5515. DOI: 10.1088/0029-5515/51/9/094018 (cit. on p. 5).

[11] P. Barabaschi et al., "Progress of the JT-60SA project", Nuclear Fusion, vol. 59, no. 11, p. 112 005, Jun. 2019, ISSN: 0029-5515. DOI: 10.1088/1741-4326/ab03f6 (cit. on p. 5).

[12] Y. Shimomura et al., "ITER overview", Nuclear Fusion, vol. 39, no. 9Y, p. 1295, Sep. 1999, ISSN: 0029-5515. DOI: 10.1088/0029-5515/39/9Y/307 (cit. on p. 5).

[13] N. Holtkamp, "An overview of the ITER project", Fusion Engineering and Design, Proceedings of the 24th Symposium on Fusion Technology, vol. 82, no. 5, pp. 427–434, Oct. 2007, ISSN: 0920-3796. DOI: 10.1016/j.fusengdes.2007.03.029 (cit. on p. 5).

[14] S. Geng, "An Overview of the ITER Project", Journal of Physics: Conference Series, vol. 2386, no. 1, p. 012 012, Dec. 2022, ISSN: 1742-6596. DOI: 10.1088/1742-6596/2386/1/012012 (cit. on p. 5).

[15] V. Mukhovatov et al., "Overview of physics basis for ITER", Plasma Physics and Controlled Fusion, vol. 45, no. 12A, A235, Nov. 2003, ISSN: 0741-3335. DOI: 10.1088/0741-3335/45/12A/016 (cit. on p. 5).

[16] A. J. Creely et al., "Overview of the SPARC tokamak", Journal of Plasma Physics, vol. 86, no. 5, p. 865 860 502, Oct. 2020, ISSN: 0022-3778, 1469-7807. DOI: 10.1017/S0022377820001257 (cit. on p. 5).

[17] P. Rodriguez-Fernandez et al., "Predictions of core plasma performance for the SPARC tokamak", Journal of Plasma Physics, vol. 86, no. 5, p. 865 860 503, Oct. 2020, ISSN: 0022-3778, 1469-7807. DOI: 10.1017/S0022377820001075 (cit. on p. 5).

[18] Fusion Industry Reports https://www.fusionindustryassociation.org/fusion-industry-reports/ (cit. on p. 5).

[19] Max Planck Institute for Plasma Physics, ASDEX Upgrade Machine Vessel https://www.aug.ipp.mpg.de/ (cit. on p. 8).

[20] F. Wagner et al., "Regime of Improved Confinement and High Beta in Neutral-Beam-Heated Divertor Discharges of the ASDEX Tokamak", Physical Review Letters, vol. 49, no. 19, pp. 1408–1412, Nov. 1982. DOI: 10.1103/PhysRevLett.49.1408 (cit. on p. 9).

[21] H. Biglari, P. H. Diamond, and P. W. Terry, "Influence of sheared poloidal rotation on edge turbulence", Physics of Fluids B: Plasma Physics, vol. 2, no. 1, pp. 1–4, Jan. 1990, ISSN: 0899-8221. DOI: 10.1063/1.859529 (cit. on p. 9).

[22] T. S. Hahm and K. H. Burrell, “Flow shear induced fluctuation suppression in finite aspect ratio shaped tokamak plasma”, Physics of Plasmas, vol. 2, no. 5, pp. 1648–1651, May 1995, ISSN: 1070-664X. DOI: 10.1063/1.871313 (cit. on pp. 9, 77).

[23] E. J. Synakowski, “Formation and structure of internal and edge transport barriers”, Plasma Physics and Controlled Fusion, vol. 40, no. 5, p. 581, May 1998, ISSN: 0741-3335. DOI: 10.1088/0741-3335/40/5/006 (cit. on p. 9).

[24] M. Cavedon et al., “Interplay between turbulence, neoclassical and zonal flows during the transition from low to high confinement mode at ASDEX Upgrade”, Nuclear Fusion, vol. 57, no. 1, p. 014 002, Oct. 2016, ISSN: 0029-5515. DOI: 10.1088/0029-5515/57/1/014002 (cit. on p. 9).

[25] P. Manz, M. Ramisch, and U. Stroth, “Physical Mechanism behind Zonal-Flow Generation in Drift-Wave Turbulence”, Physical Review Letters, vol. 103, no. 16, p. 165 004, Oct. 2009. DOI: 10.1103/PhysRevLett.103.165004 (cit. on p. 10).

[26] H. Zohm, “Edge localized modes (ELMs)”, Plasma Physics and Controlled Fusion, vol. 38, no. 2, p. 105, Feb. 1996, ISSN: 0741-3335. DOI: 10.1088/0741-3335/38/2/001 (cit. on p. 10).

[27] Y. Igitkhanov, R. Fetzer, and B. Bazylev, “Effect of heat loads on the plasma facing components of demo”, Fusion Engineering and Design, Proceedings of the 12th International Symposium on Fusion Nuclear Technology-12 (ISFNT-12), vol. 109–111, pp. 768–772, Nov. 2016, ISSN: 0920-3796. DOI: 10.1016/j.fusengdes.2016.02.002 (cit. on p. 10).

[28] T. Eich et al., “ELM divertor peak energy fluence scaling to ITER with data from JET, MAST and ASDEX upgrade”, Nuclear Materials and Energy, Proceedings of the 22nd International Conference on Plasma Surface Interactions 2016, 22nd PSI, vol. 12, pp. 84–90, Aug. 2017, ISSN: 2352-1791. DOI: 10.1016/j.nme.2017.04.014 (cit. on p. 10).

[29] E. Viezzer, “Access and sustainment of naturally ELM-free and small-ELM regimes”, Nuclear Fusion, vol. 58, no. 11, p. 115 002, Sep. 2018, ISSN: 0029-5515. DOI: 10.1088/1741-4326/aac222 (cit. on p. 10).

[30] P. B. Snyder et al., “Development and validation of a predictive model for the pedestal heighta)”, Physics of Plasmas, vol. 16, no. 5, p. 056 118, May 2009, ISSN: 1070-664X. DOI: 10.1063/1.3122146 (cit. on pp. 10, 62, 131).

[31] T. Luda et al., “Integrated modeling of ASDEX Upgrade plasmas combining core, pedestal and scrape-off layer physics”, Nucl. Fusion, 2020 (cit. on pp. 10, 11, 133).

[32] T. Luda et al., “Validation of a full-plasma integrated modeling approach on ASDEX Upgrade”, Nuclear Fusion, vol. 61, no. 12, p. 126 048, Nov. 2021, ISSN: 0029-5515. DOI: 10.1088/1741-4326/ac3293 (cit. on pp. 10, 133).

[33] J. W. Connor, "A review of models for ELMs", Plasma Physics and Controlled Fusion, vol. 40, no. 2, p. 191, Feb. 1998, ISSN: 0741-3335. DOI: 10.1088/0741-3335/40/2/003 (cit. on pp. 11, 36).

[34] C. C. Hegna, "Nonlinear tearing mode interactions and mode locking in reversed-field pinches", Physics of Plasmas, vol. 3, no. 12, pp. 4646–4657, Dec. 1996, ISSN: 1070-664X. DOI: 10.1063/1.872033 (cit. on pp. 11, 36).

[35] P. A. Schneider et al., "Analysis of temperature and density pedestal gradients in AUG, DIII-D and JET", Nuclear Fusion, vol. 53, no. 7, p. 073 039, Jun. 2013, ISSN: 0029-5515. DOI: 10.1088/0029-5515/53/7/073039 (cit. on pp. 11, 133).

[36] P. B. Snyder et al., "A first-principles predictive model of the pedestal height and width: Development, testing and ITER optimization with the EPED model", Nuclear Fusion, vol. 51, no. 10, p. 103 016, Aug. 2011, ISSN: 0029-5515. DOI: 10.1088/0029-5515/51/10/103016 (cit. on p. 12).

[37] D. Dickinson et al., "Towards the construction of a model to describe the inter-ELM evolution of the pedestal on MAST", Plasma Physics and Controlled Fusion, vol. 53, no. 11, p. 115 010, Oct. 2011, ISSN: 0741-3335. DOI: 10.1088/0741-3335/53/11/115010 (cit. on p. 12).

[38] L. Radovanovic et al., "Developing a physics understanding of the quasi-continuous exhaust regime: Pedestal profile and ballooning stability analysis", Nuclear Fusion, vol. 62, no. 8, p. 086 004, May 2022, ISSN: 0029-5515. DOI: 10.1088/1741-4326/ac6d6a (cit. on p. 12).

[39] G. F. Harrer et al., "Quasicontinuous Exhaust Scenario for a Fusion Reactor: The Renaissance of Small Edge Localized Modes", Physical Review Letters, vol. 129, no. 16, p. 165 001, Oct. 2022. DOI: 10.1103/PhysRevLett.129.165001 (cit. on p. 12).

[40] H. Zohm, Magnetohydrodynamic Stability of Tokamaks. John Wiley & Sons, Dec. 2014, ISBN: 978-3-527-67734-4 (cit. on p. 17).

[41] J. P. Freidberg, Ideal MHD. Cambridge: Cambridge University Press, 2014, ISBN: 978-1-107-00625-6. DOI: 10.1017/CBO9780511795046 (cit. on pp. 17, 35).

[42] J. P. Freidberg, Plasma Physics and Fusion Energy. Cambridge University Press, Jul. 2008, ISBN: 978-1-139-46215-0 (cit. on p. 17).

[43] F. F. Chen, Introduction to Plasma Physics. Springer Science & Business Media, Dec. 2012, ISBN: 978-1-4757-0459-4 (cit. on p. 17).

[44] P. Helander and D. J. Sigmar, Collisional Transport in Magnetized Plasmas. Cambridge University Press, Oct. 2005, ISBN: 978-0-521-02098-5 (cit. on p. 17).

[45] J. Wesson and J. Wesson, Tokamaks (International Series of Monographs on Physics), Fourth Edition, Fourth Edition. Oxford, New York: Oxford University Press, Oct. 2011, ISBN: 978-0-19-959223-4 (cit. on p. 17).

[46] U. Stroth, Plasmaphysik. Springer, 2011 (cit. on pp. 17, 46).

[47] G. G. Howes et al., "Astrophysical Gyrokinetics: Basic Equations and Linear Theory", The Astrophysical Journal, vol. 651, no. 1, p. 590, Nov. 2006, ISSN: 0004-637X. DOI: 10.1086/506172 (cit. on p. 18).

[48] X. Garbet et al., "Gyrokinetic simulations of turbulent transport", Nuclear Fusion, vol. 50, no. 4, p. 043 002, Mar. 2010, ISSN: 0029-5515. DOI: 10.1088/0029-5515/50/4/043002 (cit. on pp. 20, 47).

[49] W. A. Newcomb, "Ballooning transformation", Physics of Fluids B; (USA), vol. 2:1, Jan. 1990, ISSN: 0899-8221. DOI: 10.1063/1.859491 (cit. on p. 33).

[50] Huysmans, GTA, "Computational Physics (Proc. Int. Conf. Amsterdam, 1991)", Goedbloed, JP, vol. Kerner, WOK, 1991 (cit. on pp. 36, 64).

[51] R. Zille and C. Konz, "HELENA Fixed Boundary Equilibrium Solver - Manual", 2007 (cit. on p. 36).

[52] A. B. Mikhailovskii et al., "Optimization of computational MHD normal-mode analysis for tokamaks", Plasma Physics Reports, vol. 23, Oct. 1997. DOI: 10.1134/1.952514 (cit. on pp. 36, 38).

[53] R. M. O. Galvão and J. Rem, "Application of the suydam method to the balloonings stability problem", Computer Physics Communications, vol. 22, no. 4, pp. 399–402, May 1981, ISSN: 0010-4655. DOI: 10.1016/0010-4655(81)90136-3 (cit. on p. 37).

[54] X. Garbet et al., "Physics of transport in tokamaks", Plasma Physics and Controlled Fusion, vol. 46, no. 12B, B557, Nov. 2004, ISSN: 0741-3335. DOI: 10.1088/0741-3335/46/12B/045 (cit. on p. 40).

[55] S. P. Hirshman and D. J. Sigmar, "Neoclassical transport of impurities in tokamak plasmas", Nuclear Fusion, vol. 21, no. 9, p. 1079, Sep. 1981, ISSN: 0029-5515. DOI: 10.1088/0029-5515/21/9/003 (cit. on p. 40).

[56] O. Sauter, C. Angioni, and Y. R. Lin-Liu, "Neoclassical conductivity and bootstrap current formulas for general axisymmetric equilibria and arbitrary collisionality regime", Physics of Plasmas, vol. 6, no. 7, pp. 2834–2839, Jul. 1999, ISSN: 1070-664X, 1089-7674. DOI: 10.1063/1.873240 (cit. on pp. 41, 42).

[57] A. G. Peeters, "The bootstrap current and its consequences", Plasma Physics and Controlled Fusion, vol. 42, no. 12B, B231–B242, Dec. 2000, ISSN: 0741-3335. DOI: 10.1088/0741-3335/42/12B/318 (cit. on pp. 41, 42).

[58] A. Redl et al., "A new set of analytical formulae for the computation of the bootstrap current and the neoclassical conductivity in tokamaks", Physics of Plasmas, vol. 28, no. 2, p. 022 502, Feb. 2021, ISSN: 1070-664X. DOI: 10.1063/5.0012664 (cit. on pp. 41, 42).

[59] F. J. Casson et al., "Theoretical description of heavy impurity transport and its application to the modelling of tungsten in JET and ASDEX upgrade", Plasma Physics and Controlled Fusion, vol. 57, no. 1, p. 014 031, Nov. 2014, ISSN: 0741-3335. DOI: 10.1088/0741-3335/57/1/014031 (cit. on p. 44).

[60] C. Angioni and O. Sauter, "Neoclassical transport coefficients for general axisymmetric equilibria in the banana regime", Physics of Plasmas, vol. 7, no. 4, pp. 1224–1234, Apr. 2000, ISSN: 1070-664X. DOI: 10.1063/1.873933 (cit. on p. 44).

[61] W. M. Stacey, "Neoclassical theory for rotation and impurity transport in tokamaks with neutral beam injection", Physics of Plasmas, vol. 8, no. 1, pp. 158–166, Jan. 2001, ISSN: 1070-664X. DOI: 10.1063/1.1324664 (cit. on p. 44).

[62] J. Dawson, "On Landau Damping", The Physics of Fluids, vol. 4, no. 7, pp. 869–874, Jul. 1961, ISSN: 0031-9171. DOI: 10.1063/1.1706419 (cit. on p. 44).

[63] J. Wesson, "Landau damping", Physics of Plasmas, vol. 22, no. 2, p. 022 519, Feb. 2015, ISSN: 1070-664X. DOI: 10.1063/1.4913426 (cit. on p. 44).

[64] J.-Y. Kim and W. Horton, "Transition from toroidal to slab temperature gradient driven modes", Physics of Fluids B: Plasma Physics, vol. 3, no. 5, pp. 1167–1170, May 1991, ISSN: 0899-8221. DOI: 10.1063/1.859808 (cit. on p. 44).

[65] P. W. Terry, "Suppression of turbulence and transport by sheared flow", Reviews of Modern Physics, vol. 72, no. 1, pp. 109–165, Jan. 2000. DOI: 10.1103/RevModPhys.72.109 (cit. on p. 45).

[66] F. Sheffield, T. Görler, Private Communication, 2024 (cit. on pp. 45, 119, 120).

[67] M. Kotschenreuther et al., "Gyrokinetic analysis and simulation of pedestals to identify the culprits for energy losses using 'fingerprints'", Nuclear Fusion, vol. 59, no. 9, p. 096 001, Jul. 2019, ISSN: 0029-5515. DOI: 10.1088/1741-4326/ab1fa2 (cit. on p. 47).

[68] W. Horton, "Drift waves and transport", Reviews of Modern Physics, vol. 71, no. 3, pp. 735–778, Apr. 1999. DOI: 10.1103/RevModPhys.71.735 (cit. on p. 48).

[69] B. N. Rogers, W. Dorland, and M. Kotschenreuther, "Generation and Stability of Zonal Flows in Ion-Temperature-Gradient Mode Turbulence", Physical Review Letters, vol. 85, no. 25, pp. 5336–5339, Dec. 2000. DOI: 10.1103/PhysRevLett.85.5336 (cit. on pp. 48, 132).

[70] F. Romanelli, "Ion temperature-gradient-driven modes and anomalous ion transport in tokamaks", Physics of Fluids B: Plasma Physics, vol. 1, no. 5, pp. 1018–1025, May 1989, ISSN: 0899-8221. DOI: 10.1063/1.859023 (cit. on p. 48).

[71] F. Jenko et al., "Electron temperature gradient driven turbulence", Physics of Plasmas, vol. 7, no. 5, pp. 1904–1910, May 2000, ISSN: 1070-664X. DOI: 10.1063/1.874014 (cit. on pp. 48, 50, 64).

[72] F. Jenko and W. Dorland, "Prediction of Significant Tokamak Turbulence at Electron Gyroradius Scales", Physical Review Letters, vol. 89, no. 22, p. 225 001, Nov. 2002. DOI: 10.1103/PhysRevLett.89.225001 (cit. on p. 48).

[73] B. Chapman-Oplopoiou et al., "The role of ETG modes in JET–ILW pedestals with varying levels of power and fuelling", Nuclear Fusion, vol. 62, no. 8, p. 086 028, Jun. 2022, ISSN: 0029-5515. DOI: 10.1088/1741-4326/ac7476 (cit. on p. 48).

[74] E. Hassan et al., "Gyrokinetic benchmark of the electron temperature-gradient instability in the pedestal region", Physics of Plasmas, vol. 28, no. 6, p. 062 505, Jun. 2021, ISSN: 1070-664X. DOI: 10.1063/5.0043006 (cit. on p. 48).

[75] T. Dannert and F. Jenko, "Gyrokinetic simulation of collisionless trapped-electron mode turbulence", Physics of Plasmas, vol. 12, no. 7, p. 072 309, Jul. 2005, ISSN: 1070-664X. DOI: 10.1063/1.1947447 (cit. on p. 48).

[76] J. Lang, S. E. Parker, and Y. Chen, "Nonlinear saturation of collisionless trapped electron mode turbulence: Zonal flows and zonal densitya)", Physics of Plasmas, vol. 15, no. 5, p. 055 907, Mar. 2008, ISSN: 1070-664X. DOI: 10.1063/1.2884036 (cit. on p. 48).

[77] W. M. Tang, J. W. Connor, and R. J. Hastie, "Kinetic-ballooning-mode theory in general geometry", Nuclear Fusion, vol. 20, no. 11, p. 1439, Nov. 1980, ISSN: 0029-5515. DOI: 10.1088/0029-5515/20/11/011 (cit. on p. 48).

[78] A. Ishizawa et al., "Global gyrokinetic simulation of turbulence driven by kinetic ballooning mode", Physics of Plasmas, vol. 26, no. 8, p. 082 301, Aug. 2019, ISSN: 1070-664X. DOI: 10.1063/1.5100308 (cit. on p. 48).

[79] M. J. Pueschel, M. Kammerer, and F. Jenko, "Gyrokinetic turbulence simulations at high plasma beta", Physics of Plasmas, vol. 15, no. 10, p. 102 310, Oct. 2008, ISSN: 1070-664X. DOI: 10.1063/1.3005380 (cit. on p. 48).

[80] M. Weiland et al., "RABBIT: Real-time simulation of the NBI fast-ion distribution", Nuclear Fusion, vol. 58, no. 8, p. 082 032, Jul. 2018, ISSN: 0029-5515. DOI: 10.1088/1741-4326/aabf0f (cit. on p. 51).

[81] R. Bilato et al., "Simulations of combined neutral beam injection and ion cyclotron heating with the TORIC-SSFPQL package", Nuclear Fusion, vol. 51, no. 10, p. 103 034, Sep. 2011, ISSN: 0029-5515. DOI: 10.1088/0029-5515/51/10/103034 (cit. on p. 51).

[82] ASDEX Upgrade Team, "ASDEX Upgrade Special Edition", Fusion Science and Technology, vol. 44, no. 3, 2003 (cit. on p. 55).

[83] O. Gruber et al., "Physics background of the ASDEX upgrade project", Journal of Nuclear Materials, vol. 121, pp. 407–414, May 1984, ISSN: 0022-3115. DOI: 10.1016/0022-3115(84)90153-3 (cit. on p. 55).

[84] F. Leuterer et al., "Recent ECRH results in ASDEX Upgrade", Nuclear Fusion, vol. 43, no. 11, p. 1329, Nov. 2003, ISSN: 0029-5515. DOI: 10.1088/0029-5515/43/11/005 (cit. on p. 56).

[85] D. Wagner et al., "Status of the new multi-frequency ECRH system for ASDEX Upgrade", Nuclear Fusion, vol. 48, no. 5, p. 054 006, Apr. 2008, ISSN: 0029-5515. DOI: 10.1088/0029-5515/48/5/054006 (cit. on p. 56).

[86] J. Stober et al., "Exploring fusion-reactor physics with high-power electron cyclotron resonance heating on ASDEX Upgrade", Plasma Physics and Controlled Fusion, vol. 62, no. 2, p. 024 012, Jan. 2020, ISSN: 0741-3335. DOI: 10.1088/1361-6587/ab512b (cit. on p. 56).

[87] J. .-. Noterdaeme et al., “The ASDEX upgrade ICRH antenna”, Fusion Engineering and Design, vol. 24, no. 1, pp. 65–74, Feb. 1994, ISSN: 0920-3796. DOI: 10.1016/0920-3796(94)90037-X (cit. on p. 56).

[88] V. Bobkov et al., “ICRF operation with improved antennas in ASDEX Upgrade with W wall”, Nuclear Fusion, vol. 53, no. 9, p. 093 018, Aug. 2013, ISSN: 0029-5515. DOI: 10.1088/0029-5515/53/9/093018 (cit. on p. 56).

[89] V. Bobkov et al., “Improved operating space of the ICRF system in ASDEX upgrade”, AIP Conference Proceedings, vol. 2254, no. 1, p. 040 005, Sep. 2020, ISSN: 0094-243X. DOI: 10.1063/5.0014238 (cit. on p. 56).

[90] R. Dux et al., “Tungsten erosion at the ICRH limiters in ASDEX Upgrade”, Journal of Nuclear Materials, Plasma-Surface Interactions-17, vol. 363–365, pp. 112–116, Jun. 2007, ISSN: 0022-3115. DOI: 10.1016/j.jnucmat.2007.01.014 (cit. on p. 56).

[91] O. Vollmer et al., “Commissioning and first operation of the ASDEX Upgrade neutral beam system”, in 15th IEEE/NPSS Symposium. Fusion Engineering, vol. 1, Oct. 1993, 451–454 vol.1. DOI: 10.1109/FUSION.1993.518370 (cit. on p. 56).

[92] B. Streibl et al., “Chapter 2: Machine Design, Fueling, and Heating in ASDEX Upgrade”, Fusion Science and Technology, vol. 44, no. 3, pp. 578–592, Nov. 2003, ISSN: 1536-1055. DOI: 10.13182/FST03-A400 (cit. on p. 56).

[93] B. Kurzan and H. D. Murmann, “Edge and core Thomson scattering systems and their calibration on the ASDEX Upgrade tokamak”, Review of Scientific Instruments, vol. 82, no. 10, p. 103 501, Oct. 2011, ISSN: 0034-6748. DOI: 10.1063/1.3643771 (cit. on p. 57).

[94] B. Kurzan et al., “Improvements in the evaluation of Thomson scattering data on ASDEX upgrade”, Review of Scientific Instruments, vol. 72, no. 1, pp. 1111–1114, Jan. 2001, ISSN: 0034-6748. DOI: 10.1063/1.1321747 (cit. on p. 57).

[95] S. K. Rathgeber et al., “Estimation of edge electron temperature profiles via forward modelling of the electron cyclotron radiation transport at ASDEX Upgrade”, Plasma Physics and Controlled Fusion, vol. 55, no. 2, p. 025 004, Dec. 2012, ISSN: 0741-3335. DOI: 10.1088/0741-3335/55/2/025004 (cit. on p. 58).

[96] S. S. Denk et al., “Analysis of electron cyclotron emission with extended electron cyclotron forward modeling”, Plasma Physics and Controlled Fusion, vol. 60, no. 10, p. 105 010, Sep. 2018, ISSN: 0741-3335. DOI: 10.1088/1361-6587/aadb2f (cit. on p. 58).

[97] R. M. McDermott et al., “Extensions to the charge exchange recombination spectroscopy diagnostic suite at ASDEX Upgrade”, Review of Scientific Instruments, vol. 88, no. 7, p. 073 508, Jul. 2017, ISSN: 0034-6748. DOI: 10.1063/1.4993131 (cit. on p. 59).

[98] E. Viezzer et al., “High-resolution charge exchange measurements at ASDEX Upgrade”, Review of Scientific Instruments, vol. 83, no. 10, p. 103 501, Oct. 2012, ISSN: 0034-6748. DOI: 10.1063/1.4755810 (cit. on p. 59).

[99] E. Viezzer et al., “High-accuracy characterization of the edge radial electric field at ASDEX Upgrade”, Nuclear Fusion, vol. 53, no. 5, p. 053 005, Apr. 2013, ISSN: 0029-5515. DOI: 10.1088/0029-5515/53/5/053005 (cit. on p. 59).

[100] J. Neuhauser et al., “Transport into and across the scrape-off layer in the ASDEX Upgrade divertor tokamak”, Plasma Physics and Controlled Fusion, vol. 44, no. 6, p. 855, May 2002, ISSN: 0741-3335. DOI: 10.1088/0741-3335/44/6/316 (cit. on p. 60).

[101] A. Kallenbach et al., “Multi-machine comparisons of H-mode separatrix densities and edge profile behaviour in the ITPA SOL and Divertor Physics Topical Group”, Journal of Nuclear Materials, PSI-16, vol. 337–339, pp. 381–385, Mar. 2005, ISSN: 0022-3115. DOI: 10.1016/j.jnucmat.2004.10.099 (cit. on p. 60).

[102] R. Fischer et al., “Integrated Data Analysis of Profile Diagnostics at ASDEX Upgrade”, Fusion Science and Technology, vol. 58, no. 2, pp. 675–684, Oct. 2010, ISSN: 1536-1055. DOI: 10.13182/FST10-110 (cit. on p. 60).

[103] P. J. Mc Carthy, “Analytical solutions to the Grad–Shafranov equation for tokamak equilibrium with dissimilar source functions”, Physics of Plasmas, vol. 6, no. 9, pp. 3554–3560, Sep. 1999, ISSN: 1070-664X. DOI: 10.1063/1.873630 (cit. on p. 60).

[104] P. J. M. Carthy and A. U. Team, “Identification of edge-localized moments of the current density profile in a tokamak equilibrium from external magnetic measurements”, Plasma Physics and Controlled Fusion, vol. 54, no. 1, p. 015 010, Dec. 2011, ISSN: 0741-3335. DOI: 10.1088/0741-3335/54/1/015010 (cit. on p. 60).

[105] R. Fischer et al., “Coupling of the Flux Diffusion Equation with the Equilibrium Reconstruction at ASDEX Upgrade”, Fusion Science and Technology, vol. 69, no. 2, pp. 526–536, Apr. 2016, ISSN: 1536-1055. DOI: 10.13182/FST15-185 (cit. on p. 60).

[106] M. G. Dunne et al., “Global performance enhancements via pedestal optimisation on ASDEX Upgrade”, Plasma Physics and Controlled Fusion, vol. 59, no. 2, p. 025 010, Dec. 2016, ISSN: 0741-3335. DOI: 10.1088/1361-6587/59/2/025010 (cit. on p. 62).

[107] W. Suttrop et al., “Effect of plasma shape variation on ELMs and H-mode pedestal properties in ASDEX Upgrade”, Plasma Physics and Controlled Fusion, vol. 42, no. 5A, A97, May 2000, ISSN: 0741-3335. DOI: 10.1088/0741-3335/42/5A/308 (cit. on p. 62).

[108] S. K. Kim et al., “Dependence of pedestal properties on plasma parameters”, Nuclear Fusion, vol. 58, no. 1, p. 016 036, Nov. 2017, ISSN: 0029-5515. DOI: 10.1088/1741-4326/aa96bb (cit. on p. 62).

[109] T. H. Osborne et al., “The effect of plasma shape on H-mode pedestal characteristics on DIII-D”, Plasma Physics and Controlled Fusion, vol. 42, no. 5A, A175, May 2000, ISSN: 0741-3335. DOI: 10.1088/0741-3335/42/5A/319 (cit. on p. 62).

[110] C. F. Maggi et al., "Characteristics of the H-mode pedestal in improved confinement scenarios in ASDEX Upgrade, DIII-D, JET and JT-60U", Nuclear Fusion, vol. 47, no. 7, p. 535, Jun. 2007, ISSN: 0029-5515. DOI: 10.1088/0029-5515/47/7/005 (cit. on p. 62).

[111] M. N. A. Beurskens et al., "H-mode pedestal scaling in DIII-D, ASDEX Upgrade, and JET a)", Physics of Plasmas, vol. 18, no. 5, p. 056 120, May 2011, ISSN: 1070-664X. DOI: 10.1063/1.3593008 (cit. on p. 62).

[112] A. W. Leonard et al., "Influence of global beta, shape, and rotation on the H-mode pedestal structure in DIII-Da)", Physics of Plasmas, vol. 15, no. 5, p. 056 114, Apr. 2008, ISSN: 1070-664X. DOI: 10.1063/1.2894214 (cit. on p. 62).

[113] G. T. A. Huysmans et al., "Modeling of diamagnetic stabilization of ideal magnetohydrodynamic instabilities associated with the transport barrier", Physics of Plasmas, vol. 8, no. 10, pp. 4292–4305, Oct. 2001, ISSN: 1070-664X. DOI: 10.1063/1.1398573 (cit. on p. 64).

[114] G. V. Pereverzew et al., "ASTRA. An Automatic System for Transport Analysis in a Tokamak.", 1991 (cit. on p. 64).

[115] F. M. Laggner et al., "Plasma shaping and its impact on the pedestal of ASDEX Upgrade: Edge stability and inter-ELM dynamics at varied triangularity", Nuclear Fusion, vol. 58, no. 4, p. 046 008, Feb. 2018, ISSN: 0029-5515. DOI: 10.1088/1741-4326/aaaa43 (cit. on pp. 74, 92, 97, 98, 128).

[116] M. Cavedon et al., "On the ion and electron temperature recovery after the ELM-crash at ASDEX upgrade", Nuclear Materials and Energy, vol. 18, pp. 275–280, Jan. 2019, ISSN: 2352-1791. DOI: 10.1016/j.nme.2018.12.034 (cit. on pp. 74, 97, 103, 128).

[117] K. H. Burrell, "Effects of E×B velocity shear and magnetic shear on turbulence and transport in magnetic confinement devices", Physics of Plasmas, vol. 4, no. 5, pp. 1499–1518, May 1997, ISSN: 1070-664X. DOI: 10.1063/1.872367 (cit. on p. 77).

[118] P. J. M. Carthy and T. A. U. Team, "Practical expressions for local magnetic shear, normal and geodesic curvatures in an axisymmetric plasma equilibrium of arbitrary cross-section", Plasma Physics and Controlled Fusion, vol. 55, no. 8, p. 085 011, Jun. 2013, ISSN: 0741-3335. DOI: 10.1088/0741-3335/55/8/085011 (cit. on p. 84).

[119] P. A. Schneider et al., "Differences in the H-mode pedestal width of temperature and density", Plasma Physics and Controlled Fusion, vol. 54, no. 10, p. 105 009, Aug. 2012, ISSN: 0741-3335. DOI: 10.1088/0741-3335/54/10/105009 (cit. on p. 88).

[120] V. Schweidler, Project Thesis: Investigation of ELM–synchronized local ballooning stability in H-mode plasmas, 2023 (cit. on p. 97).

[121] G. Pereverzev and P. N. Yushmanov, ASTRA Automated System for TRansport Analysis in a Tokamak, 2002 (cit. on p. 112).

[122] E. Viezzer et al., "Ion heat and momentum transport in the edge pedestal of ASDEX Upgrade", 42nd EPS Conference on Plasma Physics, 2015 (cit. on p. 116).

[123] E. Viezzer et al., "Investigation of inter-ELM ion heat transport in the H-mode pedestal of ASDEX Upgrade plasmas", Nuclear Fusion, vol. 57, no. 2, p. 022 020, Oct. 2016, ISSN: 0029-5515. DOI: 10.1088/0029-5515/57/2/022020 (cit. on p. 116).

[124] C. U. Schuster et al., "Edge transport and fuelling studies via gas puff modulation in ASDEX Upgrade L-mode plasmas", Nuclear Fusion, vol. 62, no. 6, p. 066 035, Apr. 2022, ISSN: 0029-5515. DOI: 10.1088/1741-4326/ac6072 (cit. on p. 117).

[125] L. A. Leppin et al., "Complex structure of turbulence across the ASDEX Upgrade pedestal", Journal of Plasma Physics, vol. 89, no. 6, p. 905 890 605, Dec. 2023, ISSN: 0022-3778, 1469-7807. DOI: 10.1017/S0022377823001101 (cit. on p. 127).

[126] G. Saibene et al., "The influence of isotope mass, edge magnetic shear and input power on high density ELMy H modes in JET", Nuclear Fusion, vol. 39, no. 9, p. 1133, Sep. 1999, ISSN: 0029-5515. DOI: 10.1088/0029-5515/39/9/307 (cit. on p. 132).

[127] G. Bateman et al., "Simulations of pedestal formation and ELM cycles", Plasma Physics and Controlled Fusion, vol. 48, no. 5A, A93, Apr. 2006, ISSN: 0741-3335. DOI: 10.1088/0741-3335/48/5A/S08 (cit. on p. 132).

[128] T. Onjun, T. Siriburanon, and O. Onjun, "A pedestal temperature model with self-consistent calculation of safety factor and magnetic shear", Journal of Physics: Conference Series, vol. 123, no. 1, p. 012 013, Jul. 2008, ISSN: 1742-6596. DOI: 10.1088/1742-6596/123/1/012013 (cit. on p. 132).

[129] Y. Pianroj, J. Techakunchaiyanunt, and T. Onjun, "Model for Pedestal Transport Based on Suppression of Anomalous Transport Using ωE ×B Flow Shear and Magnetic Shear", Journal of the Physical Society of Japan, vol. 81, no. 4, p. 044 502, Apr. 2012, ISSN: 0031-9015. DOI: 10.1143/JPSJ.81.044502 (cit. on p. 132).

[130] M. Sugihara et al., "A model for H mode pedestal width scaling using the International Pedestal Database", Nuclear Fusion, vol. 40, no. 10, p. 1743, Oct. 2000, ISSN: 0029-5515. DOI: 10.1088/0029-5515/40/10/306 (cit. on p. 132).

[131] T. Luda et al., "Validation of IMEP on Alcator C-Mod and JET-ILW ELMy H-mode plasmas", Plasma Physics and Controlled Fusion, vol. 65, no. 3, p. 034 001, Jan. 2023, ISSN: 0741-3335. DOI: 10.1088/1361-6587/acb011 (cit. on p. 133).

[132] S. Bilgen, "Structure and environmental impact of global energy consumption", Renewable and Sustainable Energy Reviews, vol. 38, pp. 890–902, Oct. 2014, ISSN: 1364-0321. DOI: 10.1016/j.rser.2014.07.004.

[133] Y. Camenen et al., "Transport of Parallel Momentum Induced by Current-Symmetry Breaking in Toroidal Plasmas", Physical Review Letters, vol. 102, no. 12, p. 125 001, Mar. 2009. DOI: 10.1103/PhysRevLett.102.125001.

[134] M. Cavedon et al., "A fast edge charge exchange recombination spectroscopy system at the ASDEX Upgrade tokamak", Review of Scientific Instruments, vol. 88, no. 4, p. 043 103, Apr. 2017, ISSN: 0034-6748. DOI: 10.1063/1.4979801.

[135] C. S. Chang and F. L. Hinton, "Effect of finite aspect ratio on the neoclassical ion thermal conductivity in the banana regime", The Physics of Fluids, vol. 25, no. 9, pp. 1493–1494, Sep. 1982, ISSN: 0031-9171. DOI: 10.1063/1.863934.

[136] J. W. Connor et al., "Magnetohydrodynamic stability of tokamak edge plasmas", Physics of Plasmas, vol. 5, no. 7, pp. 2687–2700, Jul. 1998, ISSN: 1070-664X. DOI: 10.1063/1.872956.

[137] M. Coronado and H. Wobig, "On the definition of Pfirsch–Schlüter and bootstrap currents in toroidal systems", Physics of Fluids B: Plasma Physics, vol. 4, no. 5, pp. 1294–1300, May 1992, ISSN: 0899-8221. DOI: 10.1063/1.860085.

[138] J. M. Dawson, "Particle simulation of plasmas", Reviews of Modern Physics, vol. 55, no. 2, pp. 403–447, Apr. 1983. DOI: 10.1103/RevModPhys.55.403.

[139] R. Dux, "Chapter 11: Impurity Transport in ASDEX Upgrade", Fusion Science and Technology, vol. 44, no. 3, pp. 708–715, Nov. 2003, ISSN: 1536-1055. DOI: 10.13182/FST03-A409.

[140] I. P. B. Editors et al., "Chapter 1: Overview and summary", Nuclear Fusion, vol. 39, no. 12, pp. 2137–2174, Dec. 1999, ISSN: 0029-5515. DOI: 10.1088/0029-5515/39/12/301.

[141] E. Fable et al., "Novel free-boundary equilibrium and transport solver with theory-based models and its validation against ASDEX Upgrade current ramp scenarios", Plasma Physics and Controlled Fusion, vol. 55, no. 12, p. 124 028, Nov. 2013, ISSN: 0741-3335. DOI: 10.1088/0741-3335/55/12/124028.

[142] R. Fischer et al., "Estimation and Uncertainties of Profiles and Equilibria for Fusion Modeling Codes", Fusion Science and Technology, vol. 76, no. 8, pp. 879–893, Nov. 2020, ISSN: 1536-1055. DOI: 10.1080/15361055.2020.1820794.

[143] G. Fussmann et al., "Impurity transport and neoclassical predictions", Plasma Physics and Controlled Fusion, vol. 33, no. 13, p. 1677, Nov. 1991, ISSN: 0741-3335. DOI: 10.1088/0741-3335/33/13/013.

[144] S. Günter and H. Zohm, "Chapter 9: Performance-Limiting MHD Activity and Possibilities for Its Stabilization in ASDEX Upgrade", Fusion Science and Technology, vol. 44, no. 3, pp. 682–691, Nov. 2003, ISSN: 1536-1055. DOI: 10.13182/FST03-A407.

[145] H. J. Hartfuss, T. Geist, and M. Hirsch, "Heterodyne methods in millimetre wave plasma diagnostics with applications to ECE, interferometry and reflectometry", Plasma Physics and Controlled Fusion, vol. 39, no. 11, p. 1693, Nov. 1997, ISSN: 0741-3335. DOI: 10.1088/0741-3335/39/11/001.

[146] S. R. Haskey et al., "Ion thermal transport in the H-mode edge transport barrier on DIII-D", Physics of Plasmas, vol. 29, no. 1, p. 012 506, Jan. 2022, ISSN: 1070-664X. DOI: 10.1063/5.0072155.

[147] A. Herrmann and O. Gruber, "Chapter 1: ASDEX Upgrade - Introduction and Overview", Fusion Science and Technology, vol. 44, no. 3, pp. 569–577, Nov. 2003, ISSN: 1536-1055. DOI: 10.13182/FST03-A399.

[148] F. L. Hinton and R. D. Hazeltine, "Theory of plasma transport in toroidal confinement systems", Reviews of Modern Physics, vol. 48, no. 2, pp. 239–308, Apr. 1976. DOI: 10.1103/RevModPhys.48.239.

[149] G. Laval, R. Pellat, and J. S. Soule, "Hydromagnetic stability of a current-carrying pinch with noncircular cross section", Physics of Fluids, vol. 17, pp. 835–845, Apr. 1974, ISSN: 0899-82131070-6631. DOI: 10.1063/1.1694796.

[150] V. Mertens, G. Raupp, and W. Treutterer, "Chapter 3: Plasma Control in ASDEX Upgrade", Fusion Science and Technology, vol. 44, no. 3, pp. 593–604, Nov. 2003, ISSN: 1536-1055. DOI: 10.13182/FST03-A401.

[151] V. Mertens et al., "Plasma Performance Optimization in ASDEX Upgrade", Fusion Technology, vol. 32, no. 3, pp. 459–467, Nov. 1997, ISSN: 0748-1896. DOI: 10.13182/FST97-A8.

[152] K. Miyamoto, Plasma Physics and Controlled Nuclear Fusion (Springer Series on Atomic, Optical, and Plasma Physics 38). Berlin ; New York: Springer, 2005, ISBN: 978-3-540-24217-8.

[153] A. Mlynek et al., "Design of a digital multiradian phase detector and its application in fusion plasma interferometry", Review of Scientific Instruments, vol. 81, no. 3, p. 033 507, Mar. 2010, ISSN: 0034-6748. DOI: 10.1063/1.3340944.

[154] A. O. Nelson, C. Paz-Soldan, and S. Saarelma, "H-mode inhibition in negative triangularity tokamak reactor plasmas", arXiv:2204.12625 [physics], Apr. 2022. arXiv: 2204.12625 [physics].

[155] R. Neu et al., "Chapter 10: Plasma-Wall Interaction and First-Wall Materials in ASDEX Upgrade", Fusion Science and Technology, vol. 44, no. 3, pp. 692–707, Nov. 2003, ISSN: 1536-1055. DOI: 10.13182/FST03-A408.

[156] J. Neuhauser et al., "Chapter 8: Edge and Divertor Physics in ASDEX Upgrade", Fusion Science and Technology, vol. 44, no. 3, pp. 659–681, Nov. 2003, ISSN: 1536-1055. DOI: 10.13182/FST03-A406.

[157] T. E. G. Nicholas et al., "Re-examining the role of nuclear fusion in a renewables-based energy mix", Energy Policy, vol. 149, p. 112 043, Feb. 2021, ISSN: 0301-4215. DOI: 10.1016/j.enpol.2020.112043.

[158] "Optimization of computational MHD normal-mode analysis for tokamaks",

[159] G. Pautasso and O. Gruber, "Chapter 12: Study of Disruptions in ASDEX Upgrade", Fusion Science and Technology, vol. 44, no. 3, pp. 716–729, Nov. 2003, ISSN: 1536-1055. DOI: 10.13182/FST03-A410.

[160] "(PDF) TOPICAL REVIEW: Gyrokinetic simulations of turbulent transport", ResearchGate, Oct. 2024, ISSN: 0029-5515.

[161] A. G. Peeters et al., “Overview of toroidal momentum transport”, Nucl. Fusion, 2011.

[162] S. Potzel et al., “Formation of the high density front in the inner far SOL at ASDEX Upgrade and JET”, Journal of Nuclear Materials, PLASMA-SURFACE INTERACTIONS 21, vol. 463, pp. 541–545, Aug. 2015, ISSN: 0022-3115. DOI: 10.1016/j.jnucmat.2014.12.008.

[163] T. Puetterich, “Fast CXRS-Measurements in the Edge Barrier of ASDEX Upgrade”,

[164] S. K. Rathgeber et al., “Estimation of profiles of the effective ion charge at ASDEX Upgrade with Integrated Data Analysis”, Plasma Physics and Controlled Fusion, vol. 52, no. 9, p. 095 008, Aug. 2010, ISSN: 0741-3335. DOI: 10.1088/0741-3335/52/9/095008.

[165] F. Reimold et al., “The high field side high density region in SOLPS-modeling of nitrogen-seeded H-modes in ASDEX Upgrade”, Nuclear Materials and Energy, Proceedings of the 22nd International Conference on Plasma Surface Interactions 2016, 22nd PSI, vol. 12, pp. 193–199, Aug. 2017, ISSN: 2352-1791. DOI: 10.1016/j.nme.2017.01.010.

[166] G. Rewoldt and W. Tang, “Toroidal microinstability studies of high temperature tokamaks”, United States, Tech. Rep., 1989, p. 19.

[167] B. N. Rogers, J. F. Drake, and A. Zeiler, “Phase Space of Tokamak Edge Turbulence, the $\mathit{L}\ensuremath{-}\mathit{H}$ Transition, and the Formation of the Edge Pedestal”, Physical Review Letters, vol. 81, no. 20, pp. 4396–4399, Nov. 1998. DOI: 10.1103/PhysRevLett.81.4396.

[168] F. Ryter, A. Stäbler, and G. Tardini, “Chapter 5: Core Energy Transport in Conventional Scenarios in ASDEX Upgrade”, Fusion Science and Technology, vol. 44, no. 3, pp. 618–635, Nov. 2003, ISSN: 1536-1055. DOI: 10.13182/FST03-A403.

[169] S. Saarelma et al., “Non-local effects on pedestal kinetic ballooning mode stability”, Plasma Physics and Controlled Fusion, vol. 59, no. 6, p. 064 001, Apr. 2017, ISSN: 0741-3335. DOI: 10.1088/1361-6587/aa66ab.

[170] V. D. Shafranov, “Equilibrium of a toroidal pinch in a magnetic field”, Soviet Atomic Energy, vol. 13, no. 6, pp. 1149–1158, Nov. 1963, ISSN: 1573-8205. DOI: 10.1007/BF01312317.

[171] A. Sips, J. Hobirk, and A. G. Peeters, “Chapter 4: Advanced Tokamak Studies in ASDEX Upgrade”, Fusion Science and Technology, vol. 44, no. 3, pp. 605–617, Nov. 2003, ISSN: 1536-1055. DOI: 10.13182/FST03-A402.

[172] P. B. Snyder et al., “Pedestal stability comparison and ITER pedestal prediction”, Nuclear Fusion, vol. 49, no. 8, p. 085 035, Jul. 2009, ISSN: 0029-5515. DOI: 10.1088/0029-5515/49/8/085035.

[173] A. Stäbler et al., “Chapter 13: Current Drive in ASDEX Upgrade”, Fusion Science and Technology, vol. 44, no. 3, pp. 730–742, Nov. 2003, ISSN: 1536-1055. DOI: 10.13182/FST03-A411.

[174] A. Stagni et al., "The effect of plasma shaping on high density H-mode SOL profiles and fluctuations in TCV", Nuclear Fusion, vol. 64, no. 2, p. 026 016, Jan. 2024, ISSN: 0029-5515. DOI: 10.1088/1741-4326/ad1a56.

[175] J. K. Stober, P. T. Lang, and V. Mertens, "Chapter 7: High-Density H-Mode Operation in ASDEX Upgrade", Fusion Science and Technology, vol. 44, no. 3, pp. 650–658, Nov. 2003, ISSN: 1536-1055. DOI: 10.13182/FST03-A405.

[176] U. Stroth, P. Manz, and M. Ramisch, "On the interaction of turbulence and flows in toroidal plasmas", Plasma Physics and Controlled Fusion, vol. 53, p. 024 006, Jan. 2011. DOI: 10.1088/0741-3335/53/2/024006.

[177] W. Suttrop et al., "Chapter 6: H-Mode and Pedestal Physics in ASDEX Upgrade", Fusion Science and Technology, vol. 44, no. 3, pp. 636–649, Nov. 2003, ISSN: 1536-1055. DOI: 10.13182/FST03-A404.

[178] A. G. Tenner, Computational Physics: Proceedings Of The Cp90 International Conference. #N/A, Apr. 1991, ISBN: 978-981-4569-39-2.

[179] D. Told et al., "Gyrokinetic microinstabilities in ASDEX Upgrade edge plasmas", Phys. Plasmas, 2008.

[180] H. Urano, "Pedestal structure in H-mode plasmas", Nuclear Fusion, vol. 54, no. 11, p. 116 001, Nov. 2014, ISSN: 0029-5515. DOI: 10.1088/0029-5515/54/11/116001.

[181] E. Viezzer et al., "Dynamics of the pedestal transport during edge localized mode cycles at ASDEX Upgrade", Plasma Physics and Controlled Fusion, vol. 62, no. 2, p. 024 009, Jan. 2020, ISSN: 0741-3335. DOI: 10.1088/1361-6587/ab5b1d.

[182] E. Viezzer, "Radial electric field studies in the plasma edge of ASDEX Upgrade", PhD thesis, p. 123, 2012.

[183] D. Wagner et al., "Status, Operation, and Extension of the ECRH System at ASDEX Upgrade", Journal of Infrared, Millimeter, and Terahertz Waves, vol. 37, no. 1, pp. 45–54, Jan. 2016, ISSN: 1866-6906. DOI: 10.1007/s10762-015-0187-z.

[184] C. Windsor, "Can the development of fusion energy be accelerated? An introduction to the proceedings", Philosophical Transactions of the Royal Society A: Mathematical, Physical and Engineering Sciences, vol. 377, no. 2141, p. 20 170 446, Feb. 2019. DOI: 10.1098/rsta.2017.0446.

[185] K. X. Ye et al., "Parameter dependence of density pedestal width and correlation with pedestal turbulence in EAST type-I ELMy H-mode plasma", Physics Letters A, vol. 481, p. 128 983, Sep. 2023, ISSN: 0375-9601. DOI: 10.1016/j.physleta.2023.128983.

[186] H. Zohm et al., "Overview of ASDEX upgrade results in view of ITER and DEMO", Nuclear Fusion, vol. 64, no. 11, p. 112 001, Aug. 2024, ISSN: 0029-5515. DOI: 10.1088/1741-4326/ad249d.

List of Abbreviations

ASDEX Upgrade Axially Symmetric Divertor Experiment Upgrade. 8–10, 12, 55, 56

AUG ASDEX Upgrade. 55, 61

CXRS Charge Exchange Recombination Spectroscopy. 57–60, 63, 64, 76, 112

DCN Deuterium Cyanide Laser Interferometry. 57, 58, 60, 62, 69–72

ECE Electron Cyclotron Emission. 57, 58, 60, 62

ECRH Electron Cyclotron Resonance Heating. 56, 61, 62, 69, 71, 111

ELM Edge Localized Mode. 10, 11, 35, 36, 74, 103, 131

ETG Electron Temperature Gradient mode. 48, 120, 122, 124

GS Grad Shafranov. 26, 36, 37

H-mode High confinement mode. 9, 10

IBM Ideal Ballooning Mode. 37, 85, 89, 100, 115, 116, 119, 131

ICRH Ion Cyclotron Resonance Heating. 56, 61, 62, 69, 70, 72, 111

IDA Integrated Data Analysis. 59, 60, 63, 64

IDE Integrated Data Analysis Equilibrium. 60, 63, 64

IDI Integrated Data Analysis Ions. 60, 63

ITG Ion Temperature Gradient mode. 47, 48, 120, 124

KBM Kinetic Ballooning Mode. 12, 48, 116, 119, 122, 124, 125, 127, 131

L-mode Low confinement mode. 9

MHD Magnetohydrodynamics. 10, 37, 127

MTM Micro Tearing Mode. 48

NBI Neutral Beam Injection. 56–59, 61, 69–72, 76

QCE Quasi Contiuous Exhaust Regime. 12

SOL Scrape Off Layer. 9

TEM Trapped Electron Mode. 48, 120, 122

TS Thomson Scattering. 57, 60, 62

List of Symbols

E_r radial electric field. 9, 19, 27

$F(\psi)$ diamagnetic profile $F(\psi) = RB_{\square}$. 26, 37, 42, 64

T_e electron temperature. 62, 105, 112

T_i ion temperature. 58, 63, 105

Z_{eff} effective charge. 59, 63, 64

α_{crit} critical value of normalised pressure gradient, at which the plasma is ideal $n\rightarrow\infty$ unstable. 101, 102, 104

α_{exp} experimental value of normalised pressure gradient. 101, 102, 104

β_N ratio of plasma pressure to magnetic pressure. 61

β_{pol} ratio of plasma pressure to poloidal magnetic pressure. 11, 12, 27, 57, 61, 62, 79, 111, 112

μ_0 vacuum magnetic permeability. 26, 27, 30–33

ω_c gyration frequency. 17, 20, 56, 58

$\square$ toroidal direction. 24, 26–28

ψ magnetic flux. 26

ρ_L Larmor radius. 17, 20

ρ_{pol} normalised radial component $\rho_{pol} = \sqrt{(\psi - \psi_0)/(\psi_{sep} - \psi_0)}$. 11, 60, 64

θ poloidal direction. 27, 28, 31

j_{tor} toroidal current density. 37, 75

n_e electron density. 105, 112

q safety factor $q=m/n$. 8, 31, 42, 61, 62, 75

s_{loc} local magnetic shear. 63

v_d drift velocity. 18, 19

v_{rot} rotation velocity. 58, 59

$\mathbf{F}_{marg}$ marginal ideal $n\rightarrow\infty$ stability $F_{marg} = \alpha_{crit}/\alpha_{exp}$. 89, 101, 102, 104

A Complete Kinetic Profiles

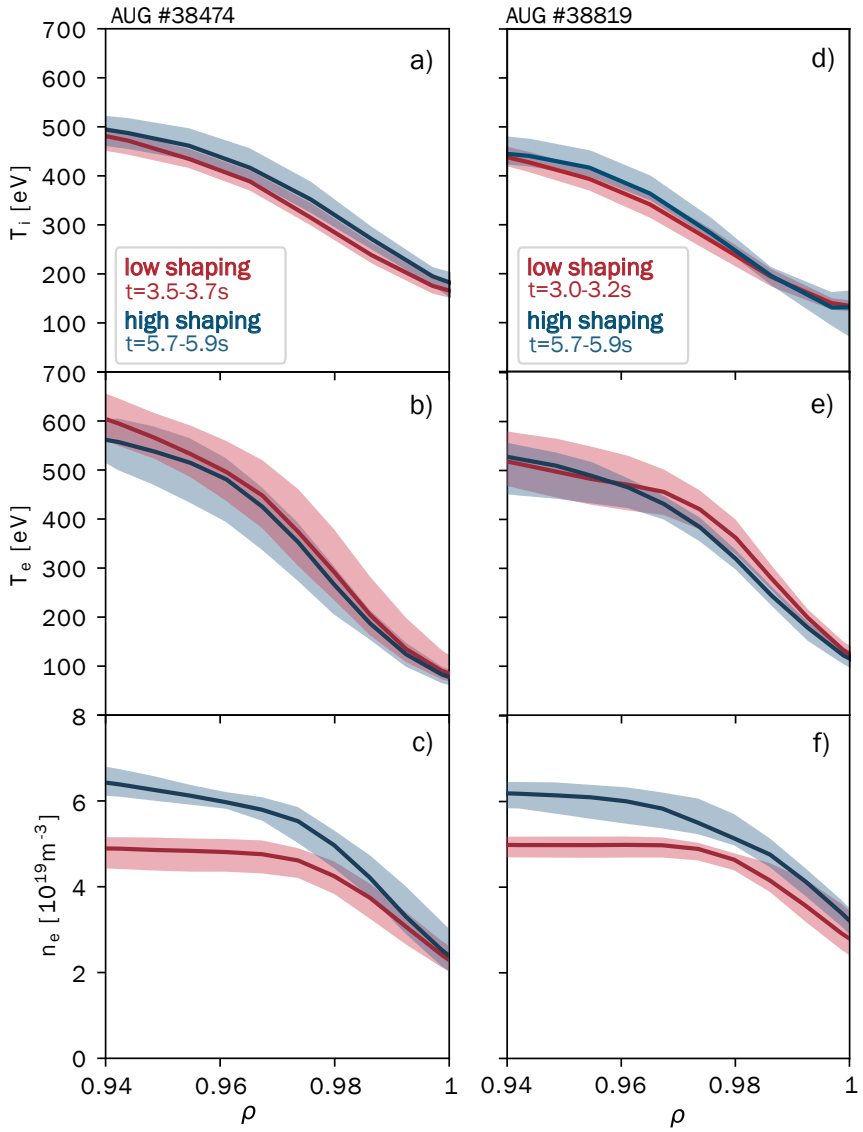

Figure A.1: Reconstructed kinetic profiles at the plasma edge. Profiles at different shapes for discharges #38474 (a-c), and #38819 (d-f), with ion temperature (a, d), electron temperature (b, e), and electron density (c, f). Red lines correspond to low shaping and blue lines to high shaping. In all cases, the lines depict median values, while shaded regions indicate 95% of the temporal variation over the 200 ms time windows.

B Complete E_r profiles

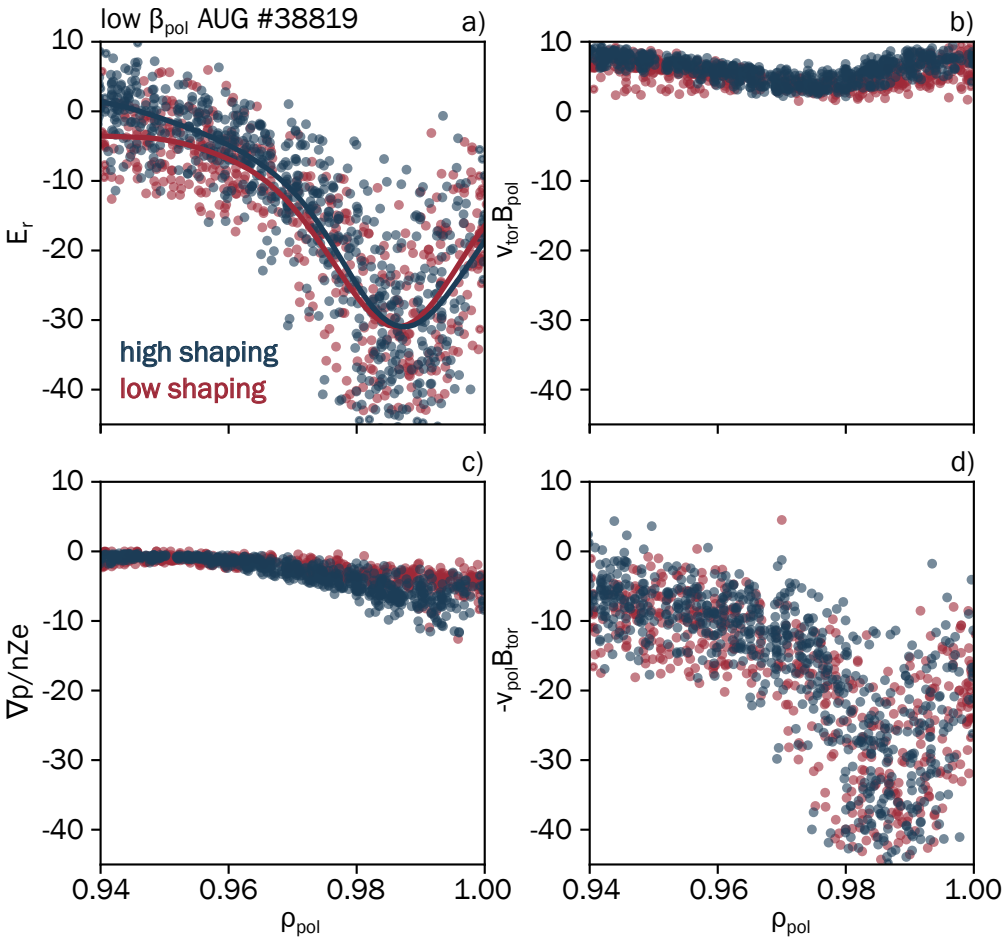

Figure B.1: a) Total E_r, b) the component $v_{tor}B_{pol}$, c) the diamagnetic component $\nabla(p)/nZe$, and d) the component $-v_{pol}B_{tor}$. Scatter points represent measurements derived from CXRS, while the solid line in a) shows the Gaussian process fit for E_r. Red indicates low shaping and blue indicates high shaping.

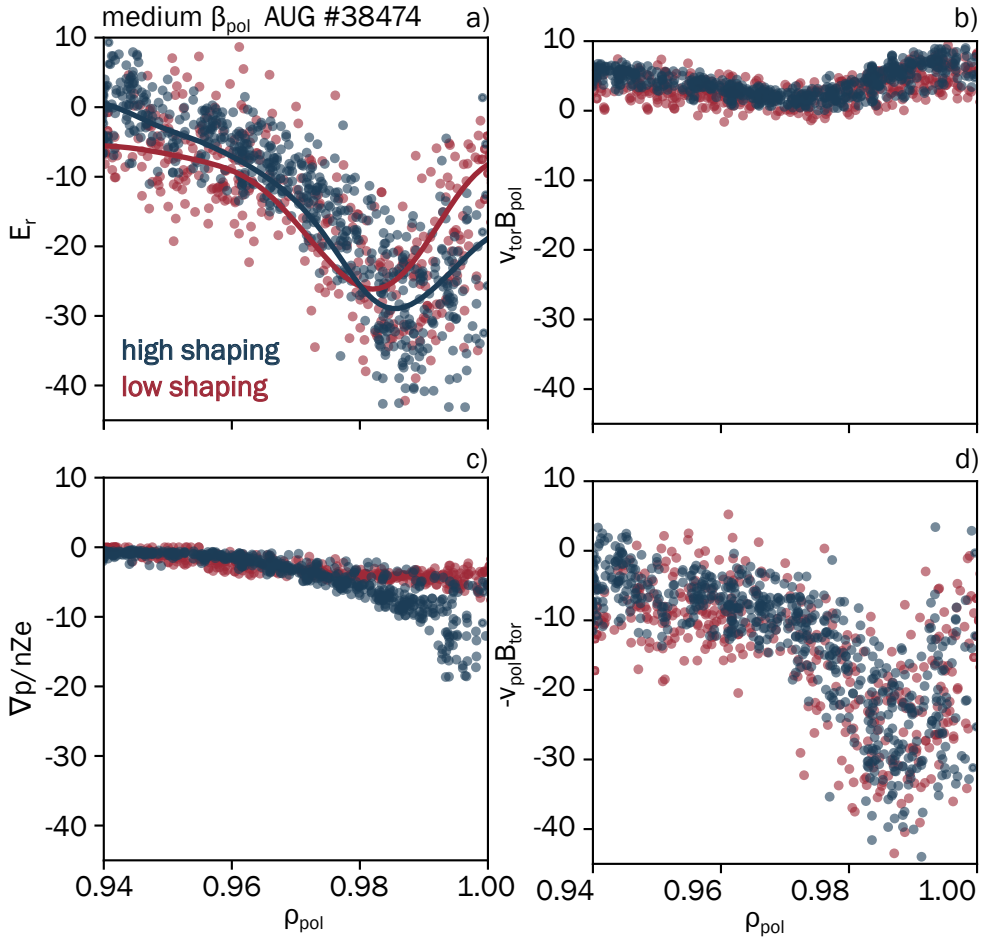

Figure B.2: a) Total E_r, b) the component $v_{tor}B_{pol}$, c) the diamagnetic component $\nabla(p)/nZe$, and d) the component $-v_{pol}B_{tor}$. Scatter points represent measurements derived from CXRS, while the solid line in a) shows the Gaussian process fit for E_r. Red indicates low shaping and blue indicates high shaping.

Acknowledgements

You made it to the end! Or you just scrolled to the end to see if I mentioned you in the Danksagung, which is okay, we all do it. I am very fortunate to be in the situation where I have so many people to thank! I will for sure however forget somebody, and I am very sorry about that, I am very tired at this point. Tired and happy.

First, I would like to thank the Universe, you know, the exact amount of entropy going on around, pure luck, bigger forces? Being randomly lucky is the most important requirement for any kind of success. But working hard is also necessary, so I would like to thank myself. In the hindsight, doing the PhD was one of the easier hard things I ever did and this is in big part because some years ago, a younger version of myself had to get through a lot of shift for me to be here, and I'm sending her a big hug in the past, biće bolje!

Now, this PhD thesis would not have been nearly as enjoyable and fulfilling if it weren't for the person most deserving of my deepest gratitude—my supervisor, Elisabeth Wolfrum. Danke, *Lisl*, dass du mich seit sieben Jahren auf allen Stufen meiner wissenschaftlichen Arbeit begleitet hast. Es hat mich immer fasziniert, wie du mit einer sanften, aber entschlossenen Leidenschaft so viele verschiedene Themen angehst. Du hast mir gezeigt, wie man mit Neugier einem anfangs verschwommenen Pfad folgt und daraus ein spannendes Physik-Abenteuer macht. Ich bin dir auch sehr dankbar, dass du dir jede Woche Zeit genommen hast – nicht nur, um mich zu beraten, wie ich mit meiner Arbeit vorankommen könnte, sondern auch, um sicherzustellen, dass es mir gut geht, und um mit mir über das Leben und die Welt zu sprechen. Vor allem schaue ich zu dir auf, weil du es mit deiner Art immer schaffst, Menschen zusammenzubringen und ein Gefühl der Gemeinschaft zu stärken. Danke dafür!

I am also very thankful to my Vienna supervisor, Friedrich Aumayr, who first introduced me to the topic of nuclear fusion and opened the door to the world of science to me. *Fritz*, danke dass du so früh ein Potenzial in mir erkannt hast, mich gefördert hast und mir stets die notwendigen Mittel und Möglichkeiten geboten, um mich akademisch weiterzuentwickeln – sei es durch finanzielle Unterstützung, notwendige Informationen, freundliche Erinnerungen, unkomplizierte bürokratische Lösungen oder die Förderung meiner Teilnahme an Konferenzen.

Since the moment I was born, as a baby scientist, I've had an unofficial supervisor, Micycle Dunne, who put in a lot of time and energy in the work shown in this thesis. *Mike*, I am so lucky to have you around. Thanks for always having an open door for me, for answering my many, many questions these 7 years, for adding all my missed "THEs" and

"As", for being my go-to person for any dilemma or a need to vent or just a vibe check of any situation, and thank you for your care. It was not only a pleasure to have you around to help me grow, but also a pure joy to be around your growth. You are such a wonderful human, and I am so happy and proud to call you my friend! Also, I would like to thank Frodo for being the best silly boy!

There are many more people at IPP Garching who made this work possible. Firstly, I want to thank *Marco Cavedon* for his patience and kindness teaching me all about the charge exchange diagnostics, showing me around the virtual control room and advising my very beginnings in this PhD. I'd also like to thank *Rachael McDermott*, for always being both understanding and clear, and taking her time with my questions despite the always busier schedule. *Tobias Görler* I thank for guiding me through my gyrokinetics excursion and teaching me all I know about microturbulence and making sure I always feel welcome asking questions! I am sincerely hoping for more future collaborations! Thanks also goes to *Facundo*, who started the GENE school with me, but went much further, and is now developing that branch of this project, and is also genuinly a very nice guy. I also want to thank *Clemente Angioni*, not only for performing the ASTRA simulations in this thesis, but also the lengthy discussions and lessions about transport, and for his patience with my sometimes diluted progress in that field. A big thanks to *Benedikt*! Ich habe selten so eine hilfsbereite Person kennengelernt. Es hat mir eine große Freude bereitet, mich mit dir über Plasmatransport zu unterhalten, und auch unsere Weltanschauungen bei einem oder anderem Bier nach langen Konferenztagen zu diskutieren.

The first person I'd write to each Garching visit has always been Farah, the woman, the legend! *Farah*, thank you so much for welcoming me, for your smiles, for all the lunches we've had together, for the advice on life, love, world, for your friendship! You're so great, and lovely and strong, I can't wait to see how your story goes!

A huge thank you to Branka! Jaoj *Branka*, šta bih ja bez tebe! Hvala što si takav oslonac, hvala što si me motivisala da uopšte krenem ovim putem fuzije, što si mi u Garhingu jedna balkanska vila kuma pazitelj! Joj!

Many more people have made my stays in Garching always feel homely and warm—without exception. From short greetings in the hallway to extended chats that provided a welcome distraction from the official reason I'm at IPP, and great times at conferences! I would love to thank (in no particular order) *Michael, Jonas, Tabea, Teo, Davide, Michael, Roxana, Pierre, Thomas, Andres, Alex, Andreas, Athina, Oleg*, and really... everybody! (See author list of H. Zohm et al., 2024, Nucl. Fusion).

However, I spent most of my time working on this thesis in Vienna. I consider myself incredibly lucky to be part of such a friendly research group. First and foremost, of course, I have to thank the Spaßbüro! Ihr seid so topsi!!! *Johannes*, danke für die gemeinsamen Tiraden, für das After-Work-Yoga, für das Essen holen als ich mit dem Schreiben beschäftig war, für das Lachen, für die Leg-Days, für die Mandeln und für die Cappuccinos – danke fürs gentle Snack Sein und danke für deine Unterstützung! Danke auch, *Benji*, für die interessanten Artikel und fun Facts die nur vielleicht Facts sind, für deine beruhigende Art und für all die lustigen Momente. Es freut mich sehr, dass du in der Gruppe bleibst und dass wir – wenn mir die EU Geld gibt – noch weiter Zeit miteinander verbringen werden.

RIESEN-Danke an *Martina*, die Oide! Ah Oide, du bist a Maschin'! Ich mach mir doch

gar keinen Stress im Leben, weil ich weiß: Wenn alles scheitert, sind wir in unserem Möbelgeschäft glücklich, trinken ein Bier, flippen die Platten, bohren und schleifen, fahren Rad, und lassen den Johannes Kaffee für uns machen. Die breite Zukunft liegt vor uns! Es ist ein Geschenk, so eine gute Freundin fast jeden Tag zu sehen!

And not only have I been so lucky to have such nice people in the office all these years, I also had a dream-team for all the coffee and lunch breaks! Danke, *Anna*, für deine Unterstützung bei so unterschiedlichen Problemen und vor allem dafür, dass du die Gruppe auf sowohl pragmatische als auch liebevolle Weise zusammenhältst. Danke auch, *Daniel*, dass du da bist – nicht nur, um Ratschläge für eine gesunde Wirbelsäule zu geben, sondern auch, um uns zu unterhalten, zu feiern, zu diskutieren und zu lachen! *Florian*, ich sitze immer gerne neben dir beim Mittagessen – es ist jedes Mal eine lustige Zeit! Du bist seit dem ersten Tag eine ausgezeichnete Bereicherung für die Gruppe. Und *Vicki*, so schön, dass du wieder in der Gruppe bist, so gut schnibbelst und danke für deine freundliche und angenehme Art! Und danke auch, *Kaffeelix*, dass du unser Espresso-Buddy Nummer eins bist! Ich freue mich auch, dass *Raphael* mit mir im Büro ist, auch wenn er ums Eck sitzt und ich nie weiß, ob er da ist – und dennoch stets für eine angenehme Arbeitsatmosphäre sorgt. Danke *Redl*, das du mich mit den Pranks für Martina amusierst! Danke auch Matthias, für das sorgfältige Lesen von Gerda, und dass wir mit dir keine Angst vor den Kratzer haben. Danke, *Markus*, für deine herzliche Freundlichkeit – und schön, dass du *Kendi* auch weiter als Doktorant da bist, das freut mich sehr! *Sophie*, danke, dass du in unserer „Sonstiges"-Kanban-Gruppe mit mir warst, und hoffentlich feiern wir mal gemeinsam Silvester in der Zukunft! Also, *Fil* – great to have you here, what a spicy contribution! We should zapravo practice some naš ponekad! Oh *Gyla*! Really nice to have you around, and I hope you feel the same about being here. Also, your kids were adorable this week on Zoom – you guys radiate such a great vibe together! And *Akbar*, I am very happy that you joined the group! Thank you for being such a friendly guy! And outside the group – *Luca*! Mir wird warm ums Herz, wenn ich dich sehe! Liebe Grüße an alle Diebölder!

Now, this group not only has amazing members right now, but it also has a long history of remarkable individuals. First, my fusion IPP-TU Wien family tree! Danke, *Georg*, dass du mich in die Gruppen in Wien und Garching empfangen hast und immer so eine gute Atmosphäre schaffst! Ich bin auch sehr glücklich, dass ich dabei sein konnte, um zu sehen, wie du vom lustigen Studi-Kollegen zu einem so coolen und lieben Vater wirst! Und *Florian*, danke für dein unerschöpfliches Motivieren und deine hemmungslose Leichtigkeit! Ich werde für immer in Erinnerung behalten, wie du bei meiner allerersten Konferenz immer wieder herum erzählt hast, wie stolz du auf deine wissenschaftliche kleine Schwester bist, und wie es mich ermutigt hat! *Matthias*, danke für die spannenden Gespräche, Zuspruch, Unterstützung und auch für die beste Marillenmarmelade, die ich jemals hatte! Wow!

Mein Dank geht auch an die anderen IAP AG AU Alumni: *Christian, Gabriel, Herbert, Paul, Janine und Schmu*! Ich habe die Zeit mit euch in der Gruppe in so schöner Erinnerung und freue mich immer sehr euch wiederzutreffen!

The other group seniors also have my gratitude! Danke *Martin* für deine freundliche Präsenz! Danke, *Ille*, für deine immer herzlichen Gesprächsbeiträge! Danke, *Wolfgang*, für deine genussvolle Lässigkeit! Danke, *Richard*, für dein Mitgefühl, deine Freundlichkeit

und deine Offenheit! Und vor allem danke ich dir dafür, dass du mit so vielen Gedanken und Mühen die Leitung der Gruppe übernommen hast; das schätze ich sehr!

Outside the science, I have many wonderful friends, who maybe didn't always understand what I was doing in this science thing (sometimes imagined me in a white lab coat with some chemicals), but understood very well how I am feeling, what I need, who I am!

Firstly I want to thank my life companion in Vienna for over 10 years, strong woman Jelena Čekerevac. *Čeki*, sestro, care! Hvala ti što si takva konstanta u mom životu i što me povodom mnogo stvari razumeš bolje nego iko. Kao osoba koja je od samog početka sa mnom na ovom Bečkom putovanju, jedno je veliko zadovoljstvo ploviti ovim vodama sa tobom!

The rest of my dijaspora friends have a very very special thanks. *Miljane i Slobo*, hvala za vaš humor i za to što uvek brzo vratite u meni kućanski osećaj! Jaoj *Ilija*, kumić moj, kako sam ponosna na tebe kako jedriš po Beču, kako se snašao, kakav je sjajan! Pet sa zvezdicom!

And my old WG that was emotional support in the lockdown PhD beginnings! *Mario* thank you for all the PhD talk and all the life and people and feelings talk! I miss you very much, Marina too, and I can't let go of the idea how we'd be best friends and hang out every day if we lived in the same city. But until then, can't wait to see you both again! Meine alte Mitbewohnerinnen *Klara und Jenny*! Danke, dass ihr ein Großteil meiner Doktorarbeit meine Unterstützung wart und dass ich mich mit euch über so vielen Sachen unterhalten konnte, ein immer offenes Ohr und dass ich mit euch so viel teilen konnte. Ich freue mich so sehr euch immer wiederzusehen!

I am very grateful to my friend group who support me no matter what and give me all the courage and hope for the future! Ah, die Ersatzfamilie! Danke in unbestimmter Reihenfolge: *Wanke, David, Jana, Fritz, Anna, Chris, Katrin, Konstantin, Nadine, Simon, Sophia, Sebastian, Noah, Maxi*! Und ein ganz besonderer Dank geht an Flo, der mein Projekt „Schalltaucherin" in den Monaten des Schreibens fleißig betreut hat! Leute, wirklich, ihr seid DER Grund, warum ich mich in dieser Stadt so wohl und zu Hause fühle. Die Stunden im Proberaum, im Souterrain, all die Jazz-Weihnachten, alle Schlenkztivals und all die späten Stunden mit noch einem Bier sind immer einige der wichtigsten Momente, in denen ich kaum glauben kann, dass mich so eine wundervolle Gruppe an Menschen mit so viel Selbstverständlichkeit aufgenommen hat. Ich freue mich auf die Zukunft mit euch! Danke!

I also thank my very first university friends who have been around for over 10 years, Matthias and Matthias. Ja der Matthias, der Studikollege. Na, der mit der Brille. Nein, der, der tanzt. Ah… Spaß! Matthias und Matze, selbstverständlich. Es war eine spaßige Zeit, gemeinsam zu wachsen und uns durch so viele unterschiedliche Lebensphasen immer nach vorne zu bewegen. Danke dafür!

Danke an all die Menschen in der Wiener experimentellen Musikszene, die ich kenne und die ich nicht kenne. Diese Leute waren mit ihrer Kunst mein spiritueller Hafen in dieser Zeit, haben so viel geheilt und so viel erweckt! A thanks also to the person who keeps inspiring me in this world, *nyc-noise Jessica*, thanks for being my role model and big noise sister and your words of support for my work, both in music and this thesis. I posebno hvala *Škoro*, što si mi pokazao Muziku i povezao me oko zemaljske kugle sa divnim ljudima.

I što si u pravu, ljubav i svetlost!

But before my time in Vienna, long ago, there was another time. A time during which I grew alongside some truly exceptional individuals, gems that I will cherish forever!

Tiki studio!? Kako je pametna ova moja drugarica, oštra, bistra, ko voda bistrica, sve je ona skontala! Hvala što si baš takva jer ne mogu život da zamislim bez naših konsultacija, bez da idemo u štetu, bez naših kikotanja i valjuškanja! Na vrućoj liniji sedi preko 10 godina i glavno Novosadsko sidro, najjača sugrađanka. Hvala što si tu da neguješ moju radoznalost i što se naše prijateljstvo podrazumeva!

Joj *Abu* drugarice! Mi sve volimo zajedno! Pa hvala ti mnogo što mnogo neke lepe strane tebe ponekad vidim u sebi. I hvala što si tu i što si nežna i snažna! Ti imaš neku drugu mudrost i neku i posle 15 godina tajanstvenu pesmu. Volim te puno!

Marina i *Nina*, sisters sweet! One meine posećuju svakih 6 meseci. Mi ćaskamo svakih malo malo. Vas dve ste takva moćna jedinica prijateljstva da mi je ogromna čast da me tako širokogrudo u vaš oblak uvek primite! Hvala što delite sa mnom i što me izveštavate i savetujete I slušate. Za još mnogo 6 meseci!

But i also have many friends to thank in Nürnberg, that I have been visiting more often than any other place. Danke *Mark* du lieber, danke *Yousef* du kuschliger, danke *Tasma* und *Johannes* ihr warme Menschen, danke *Amy* du Funke, und riesigen danke an die erweiterte *Familie Schwab*, die mich so herzlich aufgenommen hat!

Now you may say she has it all - great friends, amazing coworkers, and a PhD to her name. But no, no, as Beyoncé would say, I am also crazy in love! Ich bedanke mich SO SO SEHR an meine allerliebsten, meiner Mac, meiner besten und wunderbarsten *Hannah Schwab*, Frau Doktor. Jeder Tag mit dir ist ein Geschenk. Danke, dass du so eine Liebevolle bist, dass du mir so viel beigebracht hast, mich in schweren Zeiten bekocht und zugehört hast, für mich immer da bist. Wirklich immer. Es ist im Leben doch alles schöner und einfacher, wenn wir uns lieben!

In the end, I want to thank my parents and my brother! After all, these pages came out warm and fresh from my dad's printing office. Hvala *Igore* što me uvek kupiš sa stanice, što si mi porodični saradnik, što mi dozvoljavaš da izazovem tvoje stavove i što izazivaš moje. Mnogo sam ponosna na tebe! Hvala *mama i tata* što me apsolutno uvek i u svemu podržavate! Hvala što ste mi oslonac! Hvala što otvorenog duha uvek slušate sve što imam da kažem. Hvala što me prihvatate i bodrite sve strane mene i hvala za vaš trud! Hvala što znam da je vaš zagrljaj zagarantovan!

Ich wünsche uns allen jetzt mal alles Gute!